Universidade de Aveiro Departamento de Engenharia Mecânica
2015

Nelson Mineiro Souto

Desenvolvimento computacional de um teste mecânico para caracterização do material através de análise inversa

Computational design of a mechanical test for material characterization by inverse analysis

Universidade de Aveiro Departamento de Engenharia Mecânica
2015

Nelson Mineiro Souto

Desenvolvimento computacional de um teste mecânico para caracterização do material através de análise inversa

Tese em co-tutela apresentada à Universidade de Aveiro para cumprimento dos requisitos necessários à obtenção do grau de Doutor em Engenharia Mecânica pela Universidade de Aveiro e pela Université de Bretagne-Sud, realizada sob a orientação científica do Doutor António Andrade-Campos, Professor Auxiliar do Departamento de Engenharia Mecânica da Universidade de Aveiro, e da Doutora Sandrine Thuillier, Professeur des Universités, Université de Bretagne-Sud de França.

Apoio financeiro da FCT – Fundação para a Ciência e a Tecnologia, Ministério da Educação e Ciência – através da bolsa SFRH / BD / 80564 / 2011.

o júri

presidente

Prof. Dr. José Carlos da Silva Neves
professor catedrático da Universidade de Aveiro

Prof. Dr. Lionel Fourment
chercheur CNRS HDR, Ecole de Mines de Paris (France)

Prof. Dra. Marta Cristina Cardoso Oliveira
professora auxiliar da Faculdade de Ciências e Tecnologia da Universidade de Coimbra

Prof. Dr. José Luís de Carvalho Martins Alves
professor auxiliar da Universidade do Minho

Prof. Dr. Rui Miguel Barreiros Ruben
professor adjunto da Escola Superior de Tecnologia e Gestão - Instituto Politécnico de Leiria

Prof. Dr. Robertt Ângelo Fontes Valente
professor auxiliar da Universidade de Aveiro

Prof. Dra. Sandrine Thuillier
professeur des Universités, Université de Bretagne-Sud (France)

Prof. Dr. António Gil D'Orey de Andrade-Campos
professor auxiliar da Universidade de Aveiro

acknowledgements

Besides this PhD work is of an individual nature, it would not have been possible without the contribution of several persons. Therefore, I would like to express my gratitude to all those who helped me during this journey.

First of all, I start thanking Doctor António Andrade-Campos and Prof. Sandrine Thuillier for the excellent opportunity that they gave me to perform my PhD in convention between both University of Aveiro and Université de Bretagne-Sud. I want thank sincerely the friendship, dedication and availability, as well as guidelines and teachings that I have always received.

To Engineer Antony Jegat for helping me with the whole experimental part of this work.

To all my friends for the joyful moments and relaxation during my journey. In particular to Aveiro's friends and to Leo le Bourgo's family, during the time that I spent in Lorient.

To my friends from GRIDS, in special to Rui Paulo and Tiago Grilo, as well as to my friends from LIMATB, specially Jeremy Cöer and Vasco Simões.

To my family for all.

The last and most important person to thank is Marine. The life gave me the chance to meet this wonderful woman. Thank you for support me, cheer me up in the hard moments as well as share with me so much happiness since the last years of my PhD.

palavras-chave

caracterização mecânica de chapas metálicas, testes mecânicos, Método dos Elementos Finitos (MEF), conformação metálica, metodologias inversas, identificação de parâmetros, optimização de forma.

resumo

Devido ao desenvolvimento de métodos de medição global, recentes estratégias de identificação de parâmetros de material baseiam-se na informação obtida em testes mecânicos heterogéneos. Os campos de deformação desenvolvidos por estes testes permitem uma melhor caracterização mecânica de chapas metálicas, o que possibilita reduzir consideravelmente o número de testes mecânicos necessários num processo de identificação de parâmetros de modelos constitutivos complexos.

No presente trabalho, uma metodologia de design recorrendo a optimização para desenvolver testes mecânicos heterógenos é apresentada. O seu principal objectivo consistiu na concepção de um teste mecânico capaz de caracterizar o comportamento mecânico de chapas metálicas para vários estados de tensão e deformação. Para isso, este estudo foi realizado considerando um material virtual obtido a partir de dados experimentais. Além disso, um indicador capaz de caracterizar testes mecânicos foi proposto para ser posteriormente utilizado na metodologia de optimização.

Por um lado, o comportamento virtual de um aço macio foi caracterizado através de um modelo fenomenológico complexo composto pelo critério de plasticidade anisotrópico *Yld2004-18p*, combinado com uma lei de encruamento mista e com um critério macroscópico de ruptura. Para esta caracterização mecânica, um processo eficiente de identificação de parâmetros foi desenvolvido e o conjunto de parâmetros identificado foi validado comparando resultados experimentais e numéricos do processo de embutidura de um copo cilíndrico.

Por outro lado, um indicador quantitativo para avaliar a informação do campo de deformação de testes mecânicos foi formulado e a sua performance foi avaliada através da análise numérica tanto de testes mecânicos clássicos como de testes heterogéneos.

Relativamente à metodologia de optimização, duas abordagens diferentes foram consideradas para a concepção do teste mecânico heterógeno. A primeira abordagem consistiu num procedimento de etapa única projectando a forma do provete e o carregamento através da utilização de uma ferramenta. A segunda abordagem consistiu numa técnica incremental de varias etapas projectando a forma do provete e o caminho de deformação através da aplicação de carregamento por deslocamentos locais. Os resultados obtidos revelaram que a metodologia de optimização proposta permite a concepção de testes mecânicos capazes de caracterizar toda a gama de estados de deformação e níveis de deformação normalmente observados nos processos de conformação de chapas metálicas.

keywords

mechanical characterization of sheet metals, heterogeneous tests, sheet metal forming, Finite Element Method (FEM), inverse methodologies, material parameters identification, shape optimization.

abstract

With the development of full-field measurements methods, recent material parameters identification strategies call upon the use of heterogeneous tests. The inhomogeneous strain fields developed during these tests lead to a more complete mechanical characterization of the sheet metals, allowing the substantial reduction of the number of tests in the experimental database needed for material parameters identification purposes.

In the present work, an innovative design optimization process for the development of heterogeneous tests is presented. The main goal is the design of a mechanical test able to characterize the material behavior of thin metallic sheets under several stress and strain paths and amplitudes. To achieve this aim, the study was carried out with a virtual material, though derived from experimental data. An indicator of the mechanical interest of the test was proposed, and was used in an optimization procedure to design both the boundary conditions and the sample shape.

On the one hand, the virtual behavior of a mild steel was characterized using a complex phenomenological model composed by the *Yld2004-18p* anisotropic yield criterion combined with a mixed isotropic-kinematic hardening law and a macroscopic rupture criterion. An efficient material parameters identification process based on finite element model updating type was implemented and the identified parameters set was validated by performing a deep drawing test leading either to full drawing or rupture of the blank.

On the other hand, an indicator which rates the strain field of the experiment by quantifying the mechanical information of the test was formulated. The relevance of the indicator was stressed out by the numerical analysis of already known classical as well as heterogeneous tests and the results obtained were validated by a material parameter sensitivity study.

Two different optimization approaches were used for designing the heterogeneous test, namely (i) a one-step procedure designing both specimen shape and loading path by using a tool and (ii) a sequential incremental technique designing the specimen shape and the loading path of the specimen considering local displacements. The results obtained revealed that the optimization approach proposed was very promising for designing a single experiment able to fully characterize the several strain paths and amplitudes encountered in sheet metal forming processes.

mots clés

caractérisation des tôles métalliques, essais mécaniques, mise en forme, méthode des éléments finis, méthodologies inverses, identification des paramètres, optimisation de forme.

résumé

Grâce au développement des méthodes de mesure de champs, de nouvelles stratégies d'identification de paramètres matériau de lois de comportement mécanique sont proposées, fondées sur l'utilisation d'essais mécaniques hétérogènes. Les champs de déformation hétérogènes développés au cours de ces essais permettent une meilleure caractérisation du comportement mécanique des tôles métalliques et, par conséquent, de réduire considérablement le nombre d'essais nécessaires pour identifier les paramètres matériau de modèles phénoménologiques complexes. Mais comment concevoir ces essais? Dans ce travail, une méthodologie d'optimisation pour le développement d'essais mécaniques hétérogènes est présentée. L'objectif principal est la conception, par analyse inverse et en proposant un indicateur représentatif des états de déformation, d'un essai capable de caractériser le comportement mécanique des tôles métalliques pour plusieurs états de contrainte et déformation. Pour cela, cette étude a été réalisée en considérant un matériau virtuel (acier doux sous forme de tôle mince), obtenu à partir de données expérimentales. En outre, un indicateur qui caractérise les essais mécaniques a été proposé pour être utilisé dans la méthodologie d'optimisation.

D'un côté, le comportement mécanique de l'acier doux a été représenté avec un modèle phénoménologique complexe composé du critère anisotrope de plasticité *Yld2004-18p*, combiné à une loi d'écrouissage mixte et un critère macroscopique de rupture. Pour cette loi de comportement, un procédé d'identification des paramètres du matériau a été développé et le jeu de paramètres identifiés a été validé en comparant des résultats expérimentaux et numériques de l'emboutissage d'un godet cylindrique.

D'un autre côté, un indicateur quantitatif pour évaluer l'information du champ de déformation des essais mécaniques a été formulé et sa pertinence a été évaluée à travers l'analyse numérique d'essais classiques et hétérogènes de la littérature.

Concernant la méthodologie d'optimisation, deux approches différentes ont été considérées pour la conception de l'essai mécanique hétérogène. La première approche est fondée sur une procédure en une seule étape, où l'optimisation de la forme de l'éprouvette et des conditions aux limites, imposées par un outil, a été effectuée. La seconde approche est fondée sur une technique incrémentale en plusieurs étapes, en optimisant la forme de l'éprouvette et le chemin de déformation, par l'application des déplacements locaux. Les résultats obtenus sont comparés et un essai est retenu pour identifier les paramètres matériau, en utilisant le matériau virtuel comme référence, afin d'illustrer la pertinence de la démarche.

Contents

List of Tables

List of Figures

I – Outline

Chapter 1

General frame

1.1 Motivation

Sheet metal forming, in particular by drawing, is one of the most widely used processes in the manufacturing industry of thin metallic sheets. Drawing is the process where a sheet metal blank is deformed plastically, by stretching, into a desired part shape. In this stamping process, the sheet metal blank is radially drawn into a forming die by the mechanical action of a punch. The load applied by the punch forces the sheet metal to flow into the die cavity, leading to the shaping of the blank according to the design of the mating punch-die set. Commonly, a blank holder clamping the blank against the die is also included in this set-up to prevent the formation of wrinkles in the stamped part. When the length of the stamped part is equal to or greater than half of its diameter, the process is generally termed as being deep drawing.

Due to its benefits, namely, a fast production rate generally associated to very small waste of raw material and the ability of creating complex parts of superior mechanical properties, the deep drawing process is massively used for numerous industrial applications such as the production of automotive structural components, aerospace parts and home appliances.

In the past, the production of metallic parts by deep drawing was often preceded by numerous empirical trial-and-error attempts for the quest of the optimum design of the forming tools. Such attempts were mostly based on knowledge gained through experience and aimed at calibrating the stamping process parameters, such as friction and blank holder pressure, as well as to avoid undesired defects in the stamped part, such as wrinkling, earing, thinning and springback.

Nowadays, due to the great advances made both in modeling and simulation as well as in computational systems, the mechanical design of stamped parts is performed firstly by numerical simulation. Indeed, the numerical simulation of sheet metal forming, mostly based on the Finite Element (FE) method, becomes an everyday virtual tool in engineering practice. Even in the early design phases, numerical simulation is carried out. The main aims are verification of the manufacturability of the stamped parts and obtaining vital information on optimum tool design (Roll, 2007). Moreover, the numerical simulation also allows to increase the complexity and to

enhance the performance of designed metallic parts. From the economical point of view, FE simulation leads to a considerable decrease of the associated delays and costs with an optimal design of components (Kajberg and Lindkvist, 2004), allowing faster and more economical manufacturing productions. Thus, the numerical simulation of sheet metal forming processes plays a crucial role in the forming industry in order to decrease the design cycle of new products, reduce significantly the costs of preproduction and improve the product quality.

Nevertheless, reliable numerical predictions of sheet forming processes depend on the accurate modeling of the mechanical behavior of thin metallic sheets. Therefore, the success of these predictions is substantially affected by the quality of the constitutive model used for describing the analyzed material as well as by the accurateness of the input set of material parameters associated to this model (Haddadi and Belhabib, 2012).

On the one hand, the numerical simulations require the knowledge of the material behavior under several strain paths and strain amplitudes, corresponding to the paths and amplitudes encountered during the forming process. Thereby, the constitutive equations implemented in the numerical model must be able to reproduce accurately this material behavior. On the other hand, the constitutive models include several material parameters that must be determined for each material and an efficient identification of these coefficients is essential in order to achieve reliability of the numerical predictions.

Over the years, material parameters have been identified using classical mechanical tests characterized by a rather homogeneous strain distribution over the gauge area of the specimen (Andrade-Campos *et al.*, 2007; Chaparro *et al.*, 2008). This kind of tests provides stress and strain data only for a fixed stress state, being then mandatory to carry out additional tests when the chosen mechanical model depends on the information related to several stress states.

The continuous development of non-linear constitutive models with larger complexity, aiming at enhancing the material behavior description of sheet metals, led to an increase of the number of material parameters needed to be identified from experiments (Bron and Besson, 2004; Barlat *et al.*, 2005; Vegter and van den Boogaard, 2006). It imposes the use of an increasing number of classical tests and, as a consequence, the material parameters identification process becomes more expensive and time consuming. Thereby, it constitutes a serious drawback for a straightforward parameters identification of the material behavior.

Another limitation of the classical tests is the fact that the homogeneous stress and strain fields generated do not resemble the complex stress and strain fields that occur in many sheet metal forming operations. Therefore, the validity of phenomenological constitutive models is limited to situations that are comparable to the range of experiments from which the material parameters of these models are identified. Due to this, the material behavior obtained from classical tests and described by constitutive models is merely an approximation that in some cases proves insufficient for a reliable simulation of complex forming processes (Cooreman *et al.*, 2008).

In fact, sheet metals undergo multiaxial stress states during forming processes and thus, multiaxial loading experiments are highly desirable for the validation of the constitutive models used in numerical simulations (Banabic *et al.*, 2010). Thereby, to circumvent the aforementioned disadvantages of the classical tests, the material parameters identification of constitutive models demands more complex mechanical tests.

The full-field measurement (FFM) methods, which have emerged in the last years, directly provide displacement or strain field data over a surface during a mechanical test. Such measurements on the overall surface of the specimen are a crucial tool for the analysis of complex mechanical tests. This kind of methods overcomes the drawback of the strain homogeneity of classical tests by monitoring complex strain fields of heterogeneous tests. Due to this reason, recent material parameters identification strategies call upon the use of heterogeneous experiments. The inhomogeneous strain fields developed during these tests reproduce situations close to those encountered in real forming processes, regarding the variety of stress states and strain levels obtained in a single experiment (Teaca *et al.*, 2010). It is of great interest for the development of more efficient and straightforward material parameters identification processes, since (i) a smaller number of experiments (or even a single one) is required in the experimental database, (ii) these tests provide more and richer mechanical information allowing for a better material characterization of sheet metals and (iii) the quality of the identified parameters is improved (Cooreman *et al.*, 2008; Pottier *et al.*, 2011a).

1.2 Aims of this thesis

The present work deals with the development of an innovative optimization methodology for the computational design of heterogeneous mechanical tests. The main goal is to find the appropriate specimen shape and boundary conditions of the test leading to an inhomogeneous strain field which characterizes the sheet metal behavior under several strain paths and amplitudes. Hence, it is intended with this work to design a heterogeneous test able to promote an enhanced mechanical behavior characterization of thin metallic sheets.

For this purpose, two different design strategies are proposed: (i) a one-step procedure that design the specimen shape and loading path using a tool and (ii) a sequential incremental technique that design the specimen shape and the loading path of the specimen considering local displacements. Whereas the first design strategy is focused on the reproduction of the experimental reality since a tool is generally used for applying the displacement for standard testing machines, the latter one aims to understand the effect of a complex loading path in terms of multisteps as well as local displacements on the achievement of more informative strain fields.

Within this virtual design approach, an accurate description of the mechanical behavior of a sheet metal is fundamental since the reliability of the numerical simulations carried out during the optimization process depends on the constitutive model adopted and the input set of material parameters. Therefore, the first step of this work is the proper definition of a virtual material using a complex constitutive model, including anisotropy, evolution of hardening and a macroscopic rupture criterion. This virtual material must be representative of a metallic sheet used in drawing. On the one hand, this study involves an experimental database composed by several classical tests characterizing a real sheet metal in order to calibrate the complex constitutive model which reproduces virtually this chosen material. One the other hand, it includes the implementation of an inverse methodology for the identification of the hardening and anisotropic material parameters of the constitutive model as well as the calibration of the rupture criterion by a mixed experimental-numerical approach. Furthermore, the inverse

methodology of material parameters identification must be developed in order to be able to identify parameters from classical as well as heterogeneous tests.

Additionally, in the design of the mechanical test, a suitable analysis of the inhomogeneous strain field of the test is definitively a crucial point that must be carefully considered. As a result, the formulation of an indicator which rates the strain field of the experiment by quantifying the mechanical information of the test is also in the scope of this work. This quantitative indicator must be able to analyze accurately the main features of the strain field with the purpose of guiding the optimization process in the quest for the optimum design of a heterogeneous test. However, the relevance of the indicator should previously be evaluated from already known classical and heterogeneous tests in order to inquire about its performance in distinguishing and rating different tests.

Also among the objectives of this thesis is the material parameters identification of the constitutive model from one of the designed heterogeneous tests. By this way, the reliability of this identified material parameters set can be assessed and compared with the one coming from the experimental database composed by several quasi-homogeneous classical tests.

1.3 Reading guide

This work is divided into five main parts. The first part, called as *Outline*, is composed by one generic chapter (chapter 1) explaining the motivation as well as the main goals of this thesis. The second part (chapters 2 - 4) is the *Comprehensive review* and comprises a bibliographic study of the several strategies applied for material parameters identification purposes, the inverse problems formulation and the mathematical equations describing the constitutive models adopted in this work. The third part (chapters 5 and 6), designated by *Mechanical characterization of mild steel*, is related to the material parameters identification of the models used for describing a DC04 mild steel as well as to the validation of the material parameters identified. In the fourth part (chapters 7 and 8), defined as *Computational design of mechanical tests*, a quantitative indicator for evaluating the mechanical information given by the strain field of the test and the optimization methodology for designing heterogeneous mechanical tests are presented. The last part of this thesis, *Final remarks* (chapter 9), consists of the main conclusions as well as some future developments giving continuity to the present work.

After a general introduction of this thesis in chapter 1, the following chapters are described:

Chapter 2 A literature survey of the different strategies used for the material parameters identification of constitutive models describing the mechanical behavior of sheet metals is presented. These different identification strategies are investigated and discussed, taking into account the mechanical tests used for characterizing the mechanical behavior of thin metallic sheets as well as the mathematical formulations used within each one.

Chapter 3 This chapter deals with the definition and formulation of inverse problems. Both inverse problem categories, namely parameters identification and shape optimization are presented. The different types of optimization methods used in inverse problems are characterized and the optimization algorithms applied in this thesis are introduced.

Chapter 4 Some fundamental mathematical concepts applied in the formulation of the constitutive modeling as well as the phenomenological models and macroscopic rupture criteria adopted to reproduce the mechanical behavior of a DC04 mild steel are described in this chapter.

Chapter 5 The development of a global procedure for a complete characterization of sheet metal behavior, including anisotropy, evolution of hardening and rupture is presented. The initial anisotropy, evolution of hardening and rupture of a DC04 mild steel are characterized using two complex phenomenological model composed by the non-quadratic *Yld2004-18p* yield criterion combined with either an isotropic or a mixed isotropic-kinematic hardening law. Two different uncoupled macroscopic fracture criteria are also considered. An efficient inverse methodology for material parameters identification based on finite element model updating is implemented. Several classical tests considered as homogeneous are used as experimental database for identifying the material parameters of the constitutive model. Concerning the characterization of the rupture behavior, a uniaxial tensile test up to rupture is used and a mixed experimental-numerical approach to calibrate the fracture criteria is carried out.

Chapter 6 The reliability of the material parameters identified for both constitutive models as well as the critical parameters of both fracture criteria is assessed by a deep drawing test leading either to full drawing or rupture of the blank. Strain fields at several stages of the deep drawing experiment, recorded by digital image correlation, are evaluated allowing for a better comparison between the experimental observations and the results of the numerical simulation.

Chapter 7 A quantitative indicator focused on the evaluation of the strain field information of the experiments and able to distinguish and rate different mechanical tests is formulated. In order to demonstrate the relevance of this indicator, numerical simulations up to rupture of already known classical as well as heterogeneous tests are carried out and are assessed by this indicator. The performance of these tests is compared and their reliability to characterize the mechanical behavior is rated and ranked. A validation study for the proposed indicator, based on a material parameters sensitivity analysis, is also performed in this chapter.

Chapter 8 An optimization methodology focused on the computational design of heterogeneous mechanical tests for thin metallic sheets is developed. Within this approach, two different strategies, namely (i) a one-step procedure designing both specimen shape and loading path by using a tool and (ii) a sequential incremental technique designing the specimen shape and the loading path of the specimen considering local displacements, are implemented. A direct search optimization algorithm is adopted in order to design by optimization the geometrical as well as loading path conditions of both strategies. The quantitative indicator, proposed in chapter 7, is applied as cost function to guide the optimization processes. The phenomenological model composed by the non-quadratic *Yld2004-18p* yield criterion combined with a mixed isotropic-kinematic hardening law, identified in chapter 5, is used for defining the virtual material. Several design attempts are performed and the best designed heterogeneous mechanical tests of both optimization strategies are presented. Additionally, by using the inverse methodology previously

developed in chapter 5, a material parameters identification process for the constitutive model used is also carried out from one of the optimized heterogeneous tests. The reliability of this identified material parameters set is assessed and compared with the one coming from the experimental database composed by several classical tests.

Chapter 9 The main conclusions of this thesis as well as its contributions are presented. Some suggestions for future developments in the domain of the present work are also outlined.

II – Literature survey

Chapter 2

Parameters identification strategies

2.1 Introduction

Nowadays, a complete mechanical characterization of sheet metals accounting for initial anisotropy, evolution of hardening with strain, even up to rupture, and Bauschinger effect became crucial for enhanced numerical predictions of sheet forming processes. In fact, over the years, constitutive models have been continuously developed in order to include and, further, improve the numerical representation of these mechanical properties.

Most of sheet metals exhibit a significant anisotropic mechanical behavior. This anisotropy is mainly due to their crystallographic structure which results of previous thermo-mechanical processes, like rolling and annealing, and is characterized by the symmetry of the mechanical properties with respect to three orthogonal planes. Such mechanical behavior is defined as orthotropy. The intersection lines of the symmetry planes are the orthotropic axes and, in the case of rolled sheet metals, their orientations are defined as rolling (RD), transverse (TD) and normal (ND) directions, as depicted in Figure 2.1.

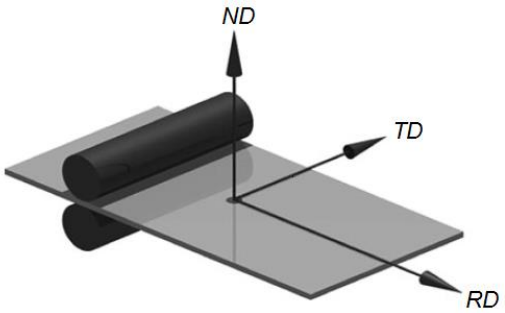

Figure 2.1 – Orthotropic axes of rolled sheet metals. RD, TD and ND stands for rolling, transverse and normal directions, respectively (Banabic, 2010).

Moreover, the anisotropy of a sheet metal during forming is a combination of its initial anisotropic behavior with the plastic deformation during the stamping operation (Yoon *et al.*,

2006). Therefore, for an accurate numerical simulation of the material behavior over a large strain range it is mandatory to take into account the hardening evolution.

Additionally, the Bauschinger effect is a main characteristics of the mechanical behavior of sheet metals and its modeling allows for improved predictions of some defects found in stamped parts, such as surface distortion and springback (Cao *et al.*, 2009). It results from the fact that representing the Bauschinger effect leads to a better determination of the internal stress distribution within the sheet metal after deformation and, consequently, it makes possible to perform more reliable springback simulations. Indeed, springback is one of the main problems influencing the final product quality in sheet forming, particularly for deep drawing, and then, taking the Bauschinger effect into account has been considered by many authors to improve the prediction of this undesired defect (Pourboghrat and Chu, 1995; Morestin *et al.*, 1996; Gau and Kinzel, 2001; Chung *et al.*, 2005).

Sheet metal forming operations often lead to complex strain paths and, as a result, several stress and strain states, as well as different strain amplitudes, occur in the sheet metal. Hence, the numerical simulations of such forming operations require the knowledge of the material behavior under these conditions.

In FE analysis, the description of the mechanical behavior of the material implies the use of a constitutive mathematical model. Constitutive equations of such a model involve several input parameters related to the mechanical properties of the material. Within a phenomenological approach, the initial anisotropy of sheet metals is quantified by anisotropic coefficients and/or initial yield stresses at different orientations to RD and at different stress states. On the one side, experimental tests performed in monotonic loading paths allow to obtain such information as well as to characterize the isotropic hardening evolution of the material. On the other side, experimental tests carried out in reversed loading path, such as tension-compression and shear-Bauschinger, allow to characterize the kinematic hardening contribution, that can represent the Bauschinger effect. This experimental data is commonly used for identifying the input parameters set of phenomenological models.

In the case of monotonic loading, several stress states can be studied such as, uniaxial and biaxial tension, uniaxial and biaxial compression, plane strain tension and simple shear. Figure 2.2 shows an overview of the classically used experimental tests and their respective stress states on the yield locus.

As it can be seen in Figure 2.2, the identification of the yield surface (transition between the elastic and plastic behaviors) through characteristic points of the yield locus can be performed considering several monotonic tests. The main stress states occurring in sheet forming processes are reproduced by these experiments. Due to the large diversity of tests proposed over the years, different ones can characterize the same stress state and, consequently, the same point of the yield locus. For instance, equibiaxial tension can be characterized by means of hydraulic bulge test, biaxial tension using cruciform specimen or disk compression test, as shown in Figure 2.2 (red point).

It is well known that the prediction capability of the forming simulations carried out by FE analysis depends not only on the constitutive model chosen but also on the suitable identification of their material parameters, which refers both to the type of the experimental tests being used and the parameters identification strategy applied (Haddadi and Belhabib, 2012).

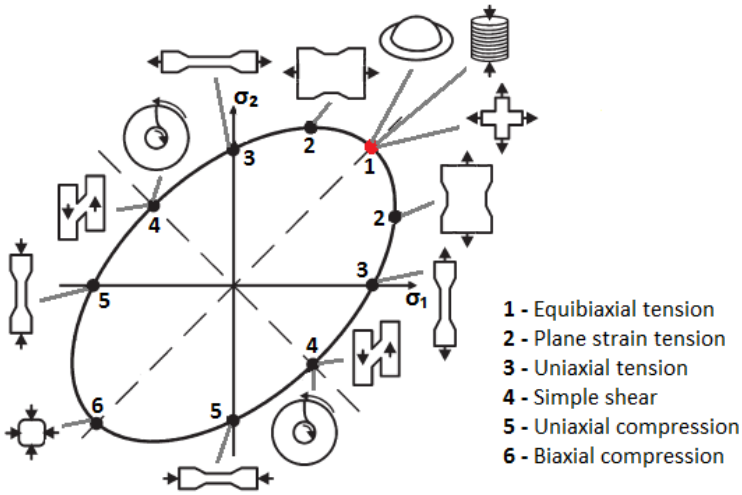

Figure 2.2 – An overview of different tests used for the mechanical characterization of sheet metals concerning the yield surface definition in terms of the major (σ_1) and minor (σ_2) stress in the sheet plane (Brosius *et al.*, 2011).

In general, the material parameters are identified by a set of classical mechanical tests developing quasi-homogeneous strain fields (Andrade-Campos *et al.*, 2007; Chaparro *et al.*, 2008; Carbonnière *et al.*, 2009; Zang *et al.*, 2011). These tests provide stress and strain data only for a fixed stress state since their design was often developed based on some assumptions in order to establish analytical formulations that give stress and strain from raw signals (Hosford and Caddell, 2007). However, some of these assumptions may not be accurate such as, true stress corrections in tensile test (Choung and Cho, 2008) or equivalent stress in hydraulic bulge test (Aretz and Keller, 2011). Additionally, these classical tests usually allow for the identification of a single material parameter (Lubineau, 2009).

Concerning simple constitutive models (Hill, 1948; Hosford, 1979; Barlat *et al.*, 1991) which involve a small number of coefficients, these classical tests seem the most suitable option to identify the material parameters. Nevertheless, when non-linear constitutive models with a larger complexity are chosen, a large number of parameters must be identified from the experiments (Bron and Besson, 2004; Barlat *et al.*, 2005; Vegter and van den Boogaard, 2006; Soare, 2007; Yoshida *et al.*, 2013). Therefore, a high number of classical tests must be used in the experimental database and it leads to more expensive and time consuming material parameters identification process.

Moreover, the homogeneous stress and strain fields provided by classical tests do not resemble the complex stress and strain fields which occur in many metal forming operations. Thereby, with the purpose of improving the quality of the parameters identification and, consequently, the numerical predictions, it seems more appropriate to characterize the mechanical behavior of sheet metals under inhomogeneous and multiaxial strain paths as the ones encountered in sheet forming processes.

Currently, the scientific community is focused on achieving a good compromise between time and material consuming as well as the number of tests. Due to this reason, complex mechanical tests allowing multi stress and strain states on a single specimen and using full-field measurement (FFM) methods (Grédiac, 2004; Grédiac and Hild, 2013) appear as a very promising

solution for a more reliable mechanical characterization of sheet metals. This approach also leads to the development of more straightforward material parameters identification processes, since a smaller number of experiments is required in the experimental database. Actually, it corresponds to the recent trend on the mechanical characterization since an increasing number of innovative tests promoting heterogeneous strain fields as well as parameters identification strategies have been proposed in the last years (Pottier *et al.*, 2011b; Zhang *et al.*, 2014).

In this chapter, the different strategies used for material parameters identification as well as the classical and heterogeneous experimental tests used for characterizing the mechanical behavior of sheet metals are investigated and discussed.

2.2 Inverse methodologies for material parameters identification

In the past, the accurate identification of the material parameters was a generalized problem for the scientific community, mainly due to the increasing complexity of the constitutive models (Kleinermann, 2000; Andrade-Campos *et al.*, 2007). At the beginning of the 1990s, the material parameters determination was simply achieved through the use of curve fitting techniques, considering simple constitutive models and experiments with the assumption of uniform distribution of the resulting strains and stresses within the whole volume of the specimen (Ponthot and Kleinermann, 2006). However, curve fitting techniques were not valid for complex constitutive models and non-homogeneous experiments. Then, Chaboche *et al.* (1991) proposed a trial-and-error procedure for the identification of material parameters. Withal, automatic methodologies based on the coupling of FE codes with optimization methods were also developed (Schnur and Zabaras, 1992; Cailletaud and Pilvin 1993, 1994; Gelin and Ghouati, 1996) and, nowadays, constitute the principal techniques adopted for the material parameters identification. This kind of techniques are commonly designated as Finite Element Model Updating (FEMU) and consists of an inverse problem where the aim is to determine the input data that lead to a final desired result that is previously known. This inverse problem can be solved using an optimization methodology whose main goal is to seek for a set of material parameters that leads to the smallest difference between the experimental observations and the numerical simulation results. In order to do this, the parameters identification framework combines an optimization algorithm, responsible for updating the material parameters, with an objective function, responsible for defining the gap between experimental and numerical data and that will control the all optimization process. During the identification procedure, the material parameters set is iteratively updated with the purpose of minimizing the objective function value. Figure 2.3 depicts a general FEMU strategy applied in material parameters identification.

An evolution relatively to the experimental data considered in the identification strategies was mainly due to the development of FFM methods. Note that FFM methods, that have emerged in the last years (c.f. an overview in Grédiac (2004)), directly provide displacement or strain field data on the overall surface of the specimen. As a result, it becomes possible to analyze complex mechanical tests developing heterogeneous strain fields. Within FFM methods, Digital Image Correlation (DIC) technique is widely used due to its simplicity and versatility (Périé *et al.*, 2009). Several works made use of DIC technique for different purposes, such as damage analysis (Tarigopula *et al.*, 2008; Périé *et al.*, 2009; Abbassi *et al.*, 2013), experimental validation of models

(Teaca *et al.*, 2010; Souto *et al.*, 2015) or identification of material parameters (Belhabib *et al.*, 2008; Cooreman *et al.*, 2008; Pottier *et al.*, 2011a; Haddadi and Belhabib, 2012; Tardif and Kyriakides, 2012; Zhang *et al.*, 2014).

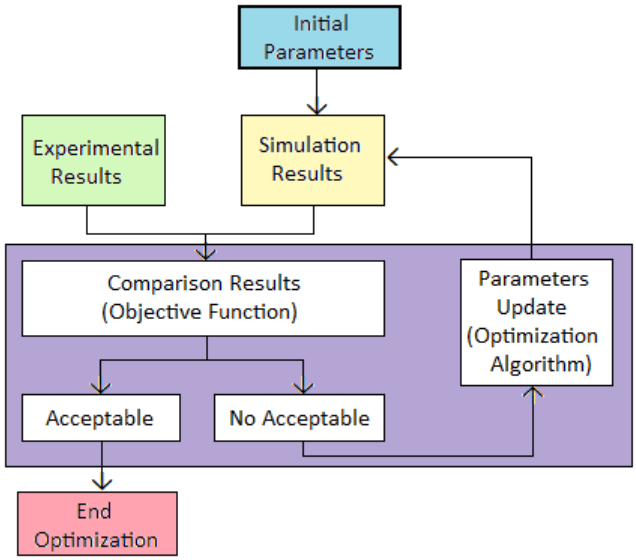

Figure 2.3 – Parameters identification framework based on FEMU strategy.

In this way, the identification strategies can be divided into two approaches, concerning the experimental data considered, namely: homogeneous and non-homogeneous. On the one hand, the homogeneous approach deals with the identification strategies which use stress-strain data obtained by classical mechanical tests, mainly performed with conventional specimens and characterized by homogeneity on the strain distribution, at least over a restricted area. Here, an analytical post-treatment of the experimental data is performed. On the other hand, the non-homogeneous approach is related to the strategies that use FFM methods applied to heterogeneous tests. These identification strategies are based on the experimental measurements of the applied load and strain field and, therefore, usually involve obtaining large amount of information data out of the experiments.

Both homogeneous and non-homogeneous identification approaches can be carried out using FEMU strategy. Indeed, this strategy consists of the most generalized and popular parameters identification process (Grédiac *et al.*, 2006). However, within the non-homogeneous approach, the increasing application of FFM methods boosted the development of other identification strategies. Thereby, several identification strategies based on full-field analysis have been developed such as, for instance, virtual field method (VFM) (Grédiac and Pierron, 2006; Pierron *et al.*, 2010; Rossi and Pierron, 2012; Kim *et al.*, 2013), equilibrium gap method (EGM) (Claire *et al.*, 2004; Périé *et al.*, 2009), constitutive equation gap method (CEGM) (Geymonat and Pagano, 2003; Latourte *et al.*, 2008; Florentin and Lubineau, 2010; Moussawi *et al.*, 2013) or reciprocity gap method (RGM) (Bui *et al.*, 2004). Detailed information about these strategies can be found in Avril *et al.* (2008a) and Grédiac and Hild (2013). The majority of these strategies also use optimization techniques for the search of parameters of non-linear elastoplastic constitutive models. Consequently, these methods can suffer from the problem of multiple solutions (Grédiac and Pierron, 2006; Avril *et al.*, 2008a).

2.2.1 Homogeneous approach

The homogeneous approach for material parameters identification is usually based on the use of a FEMU strategy and of classical mechanical tests developing quasi-homogeneous strain fields. From these tests, analytical stress and strain relations with raw test data can be defined. Indeed, it constitutes their main advantage. The several values required as input data on phenomenological models, namely, anisotropic coefficients and initial yield stress values at different orientations to RD as well as at different stress states, can also be directly calculated from these tests.

One way to identify the material parameters of the chosen phenomenological model is to adjust between several sampling experimental points and yield model predictions (Bron and Besson, 2004; Chaparro *et al.*, 2008). These sampling points correspond to the anisotropic coefficients and yield stresses obtained from the classical tests. Withal, it has been pointed out that due to the dispersion on initial yield stress as well as the evolution of anisotropy with strain, considering only initial values does not give an accurate description of the mechanical behavior (Zang *et al.*, 2011). Then, for a better prediction of the material behavior, the hardening evolution over a large strain range must also be taken into account in the material parameters identification. Therefore, the analytical stress and strain relations obtained from the classical tests must be used on the FEMU strategy. Generally, such experimental data is composed by discrete values representing a set of stress-strain measured points, as depicted in Figure 2.4. In opposition, the stress-strain numerical results obtained from FEMU are defined through a curve and interpolations for each experimental point are performed to compare both data.

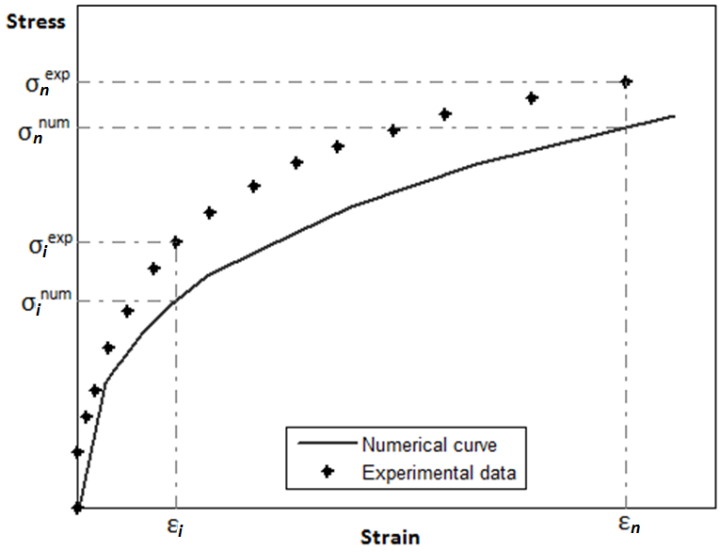

Figure 2.4 – Definition of the gap between numerical and experimental stress-strain data.

The material parameters identification procedure is guided by an objective function. In this way, the success of the optimization process demands a suitable definition of this function. Usually, the objective function consists in the sum of the squares of the differences between computed and experimental data (such as stress or strain) at the same instant of time and can be written as

$$S_{\text{obj}}^{n}(\mathbf{x}) = \frac{1}{n_{\text{p}}^{n}} \sum_{i=1}^{n_{\text{p}}^{n}} \left(\frac{Z_i^{\text{exp}}(t_i) - Z_i^{\text{num}}(\mathbf{x})}{W_{\text{abs}}^{n}} \right)^2 , \tag{2.1}$$

where $S_{\text{obj}}^{n}(\mathbf{x})$ is the objective function value for test *n* and **x** is the material parameter set to be identified. The numerator of Equation 2.1 is the quadratic difference between the experimental Z_i^{exp} and numerical Z_i^{num} values for the experimental point *i* and n_{p}^{n} stands for the number of experimental points of the test *n*. Experimental values Z_i^{exp} are recorded according to the acquisition rate and, therefore, are associated to a given time t_{i} and simulated values Z_i^{num} are calculated at the same time t_{i}. W_{abs}^{n} is a weighting factor for test *n* that should be adapted to the identification problem in order to normalize different units or scales of the data (Andrade-Campos *et al.*, 2012). The objective function becomes zero if a perfect correspondence between numerical and experimental points is obtained. However, this objective function presents more properties, such as: (i) for each test *n*, all the experimental points are taken into account and have equal opportunity to be optimized (due to the term $1/n_{\text{p}}^{n}$); (ii) when using multiple tests (*cf*. Equation 2.2), all experimental tests also have equal opportunity to be optimized, independently of the number of points of each test and (iii) different units or scales do not affect the overall performance of the optimization process by adjusting the weighting factor W_{abs}^{n}.

Although these advantages, this objective function may not be the most effective to conduct the optimization process, since a lower value of it may not necessarily means a better global reproduction of the material behavior, as shown by Andrade-Campos *et al.* (2012). Though, this objective function is one of the most commonly used in parameters identification problems (de-Carvalho *et al.*, 2011).

Nevertheless, classical mechanical tests provide stress and strain data only for a certain stress state and, as a result, usually allow for the identification of a single parameter (Lubineau, 2009). However, to warrantee the relevance of the material parameters set identified, the number of experimental data should not be lower than the number of material parameters considered in the identification process (Zhang *et al.*, 2014). Therefore, a material parameters identification process based on several classical tests is required and an optimization process must be defined. In this case, the objective function is defined by

$$S_{\text{obj}}(\mathbf{x}) = \sum_{n=1}^{n_{\text{tests}}} S_{\text{obj}}^{n}(\mathbf{x}) , \tag{2.2}$$

where n_{tests} stands for the number of tests considered in the FEMU strategy.

The main classical experiments used for parameters identification purposes are the uniaxial tension, simple shear, plane strain tension and hydraulic bulge test. However, disk compression test can also be considered mainly for determining specific data, for instance, the anisotropic biaxial coefficient r_{b}. This value is of great importance for some constitutive models that can exhibit significant difference in the biaxial tension area.

The following sections are dedicated to the description of the mechanical tests used for the homogeneous approach.

2.2.1.1 Tensile test

The uniaxial tensile test is the most commonly used experiment for sheet metal characterization mainly due to its easy preparation and reproducibility up to necking. In this experiment, a specimen is subjected to two opposite loads, applied via two crossheads, as illustrated in Figure 2.5 (Marciniak *et al.*, 2002).

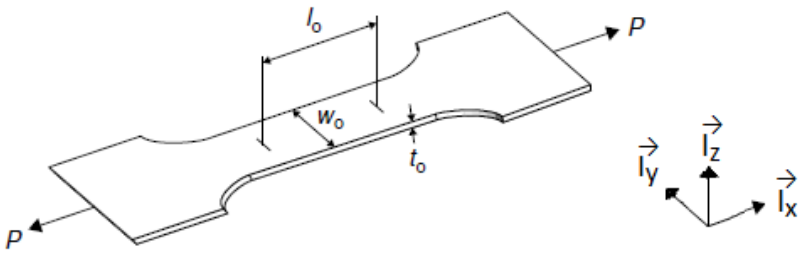

Figure 2.5 – Typical tensile test specimen used for sheet metals (Marciniak *et al.*, 2002). *P* stands for the applied loads, l_0, w_0 and t_0 correspond to the initial length, width and thickness of the gauge area.

The tensile test is standardized by several norms, such as DIN EN 10 002 (2001), ASTM E8-04 (2004) or ISO 6892-1 (2009) and it is mainly applied to determine the flow curves under uniaxial stress state at different orientations to the RD as well as the anisotropy coefficients. For that purpose, the tensile specimen is machined in different directions according to the RD. The most common tensile directions $\vec{l}_x$ used consist in the RD, 45° to the RD and TD.

The Cauchy stress **σ** and logarithmic strain **ε** tensors in the frame ($\vec{l}_x, \vec{l}_y, \vec{l}_z$) for the uniaxial tension can be written as

$$\boldsymbol{\sigma} = \begin{bmatrix} \sigma_{xx} & 0 & 0 \\ 0 & 0 & 0 \\ 0 & 0 & 0 \end{bmatrix} \qquad \boldsymbol{\varepsilon} = \begin{bmatrix} \varepsilon_{xx} & 0 & 0 \\ 0 & \varepsilon_{yy} & 0 \\ 0 & 0 & \varepsilon_{zz} \end{bmatrix}. \tag{2.3}$$

The main advantage of this test is the homogeneous deformation of the specimen until necking, allowing the accurate evaluation of the material behavior by analytical equations. Hence, it is possible to easily determine the Cauchy stress-strain curves before necking. After necking localization, this task becomes difficult due to the non-homogeneity of the gauge area, even using stress correction approaches (Choung and Cho, 2008). During the homogeneous deformation of the specimen, the logarithmic strain ε_{xx} and the Cauchy stress σ_{xx} can be obtained by assuming volume conservation and can be defined as

$$\varepsilon_{xx} = \ln\left(\frac{l}{l_0}\right) \tag{2.4}$$

and

$$\sigma_{xx} = \sigma_n \exp(\varepsilon_{xx}) = \frac{P}{w_0 t_0} \exp(\varepsilon_{xx}), \tag{2.5}$$

where l is the elongation of the gauge length and σ_n is the nominal stress.

Beyond the initial yield stress and hardening, other important material parameters usually used in the constitutive models, namely, anisotropy coefficients, can be output from the uniaxial tensile test. Indeed, the variation of the sheet metal behavior with the tensile direction in the sheet plane can be evaluated by the plastic anisotropy coefficient r_α, which can be written as

$$r_\alpha = \frac{d\varepsilon_{yy}^p}{d\varepsilon_{zz}^p}, \tag{2.6}$$

where ε_{yy}^p and ε_{zz}^p are the plastic strain components in the width and the thickness directions, respectively, and α is the angle between $\vec{l}_x$ (or tensile direction) and RD. However, for thin sheet metals it is usually calculated assuming the constant volume condition in the plastic range, *i. e.* $\varepsilon_{xx}^p + \varepsilon_{yy}^p + \varepsilon_{zz}^p = 0$. Thus, r_α can be determined as

$$r_\alpha = -\frac{d\varepsilon_{yy}^p}{(d\varepsilon_{xx}^p + d\varepsilon_{yy}^p)}. \tag{2.7}$$

Moreover, by considering the anisotropy coefficients obtained at 0°, 45° and 90° to the RD, the normal anisotropy $\bar{r}$ of the material can be defined as

$$\bar{r} = \frac{r_0 + 2r_{45} + r_{90}}{4}. \tag{2.8}$$

The normal anisotropy indicates the ability of the sheet metal to resist to the elongation when subjected to tensile and/or compression forces. Sheet metals used in deep drawing process should present a high value of normal anisotropy to prevent excessive thinning.

The variation of r_α in the sheet plane gives also useful information. This variation is evaluated by the planar anisotropy coefficient Δr by

$$\Delta r = \frac{r_0 - 2r_{45} + r_{90}}{2}. \tag{2.9}$$

The planar anisotropy coefficient indicates the difference of behavior evidenced by the material in the plane of the sheet as a function of the different directions considered. This quantity is related to the earing amplitude after cup deep drawing. When the value of the anisotropy coefficient is quite the same along all directions in the plane of the sheet, the planar anisotropy coefficient tends to be 0 and the earing phenomenon is not observed (Banabic, 2010). On the contrary, a significant planar anisotropy coefficient of the sheet metal indicates that a considerable earing phenomenon may be expected in deep drawn cups.

Despite the advantages previously enunciated, the tensile experiment has also some drawbacks. The main one is the rather small amount of homogeneous deformation obtained during the test compared with the deformation level obtained in forming processes. This

limitation occurs due to a geometric and material instability leading to the necking phenomenon. Since the analytical Cauchy stress and logarithmic strain calculations are no longer valid after the onset of necking, generally, the maximum strain achieved in homogeneous uniaxial tensile tests is 0.3 (Koç *et al.*, 2011). However, using FFM methods, such as DIC technique, it is possible to acquire strain data up to larger strains. Note that DIC technique is a non-contacting optical method that measures displacement and strain fields by comparing the random pattern of grey levels of the sample surface during deformation with an initial (reference) image taken prior to loading. In order to perform this evaluation, a region of interest (ROI) of the sample, defined by the user, is discretized into continuous finite areas. Therefore, within the ROI, the strain field data can be recorded even up to rupture of the specimen. Indeed, many authors have used DIC technique for characterizing the behavior of uniaxial tensile tests at and after strain localization or at rupture (Wattrisse *et al.*, 2001; Tardif and Kyriakides, 2012; Mishra and Thuillier, 2014).

Uniaxial compression or tension-compression tests can also be performed using uniaxial tensile specimens. Tension-compression tests have been largely used for characterizing the Bauschinger effect. However, some drawbacks are associated to this experiment. The main problems of this experimental test are the high risk of buckling due to the compression load applied in the thin specimen and the difficulty to achieve high strain levels. Often, additional support devices are required to prevent buckling.

Dietrich and Turski, in 1978, developed an experimental device for in-plane compression tests of a sheet specimen where the maximum strain is limited to 0.03 (Kuwabara, 2007). Based on the previous experimental device, Kuwabara (2007) conceived a testing apparatus which allows to reach high plastic strain values. According to the author, plastic strain about 0.16 can be obtained in this in-plane compression testing apparatus. In order to enable continuous in-plane tension-compression tests, Kuwabara *et al.* (2009) performed some updates in the previous experiment. This one is presented in Figure 2.6 and it can be seen that the lower die 1 is fixed to the lower plate of the die set and lower die 2 is positioned on a slide rail that enables the die to move smoothly in the horizontal direction. The same principle is also applied for the upper dies. The specimen is placed between the lower and upper dies and is subjected to tension and compression without buckling. However, since this experiment involves friction forces, teflon sheets must be used on both sides of the specimen. This experimental device has been used to characterize the mechanical behavior of some metals, such as copper and AA6016-T4 aluminum alloys (Kuwabara *et al.*, 2009) and DP980 steel (Saito *et al.*, 2010).

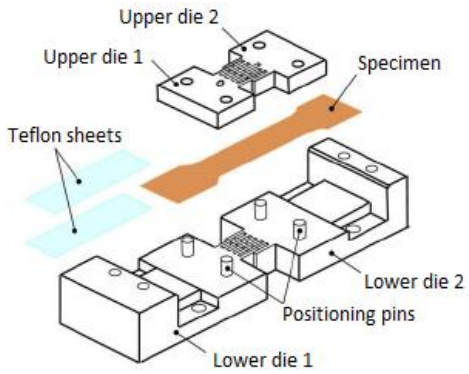

Figure 2.6 – Configuration of the tension-compression experimental apparatus developed by Kuwabara *et al.* (2009).

Yoshida *et al.* (2002) carried out experimental tension-compression tests using simultaneously specimens adhesively bonded and an anti-buckling device in order to prevent buckling phenomenon and to obtain large deformation. The specimens used consisted of five pieces of the sheet glued with an acrylic adhesive. An aluminum-killed mild steel and a dual-phase steel were tested and compressive strains up to 0.25 and 0.13 were acieved, respectively. Figure 2.7 shows the in-plane compression-tension test developed by Yoshida *et al.* (2002).

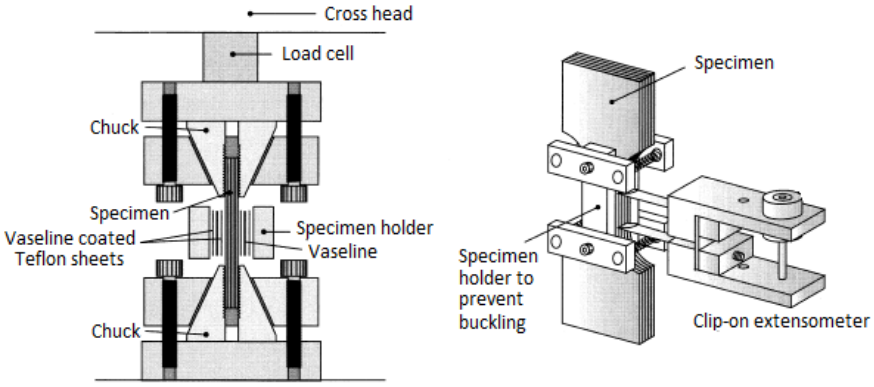

Figure 2.7 – In-plane tension-compression device proposed by Yoshida *et al.* (2002).

Boger *et al.* (2005) proposed a tension-compression test design which combines the advantages of the small specimens (large strains, continuous and reversed strain paths) with large specimens (homogeneity, self-alignment and accurate measurement of uniform stress and strain). This experiment is based on the application of solid flat plates, working as buckling constraints, and normal pressure by a hydraulic clamping system. In addition, a special tensile specimen design was developed in order to minimize three kind of buckling failure modes. Figure 2.8 a) illustrates the plate supports and final shape dimensions of this test.

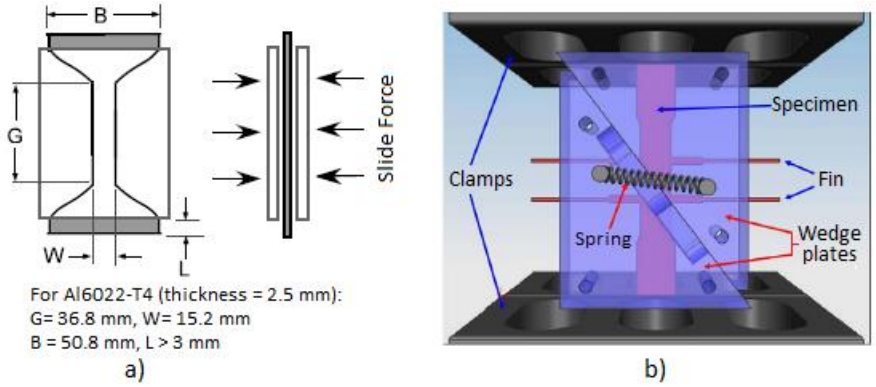

Figure 2.8 – Schematic view a) of the plates and specimen dimensions proposed by Boger *et al.* (2005) and b) tension-compression device developed by Cao *et al.* (2009).

Cao *et al.* (2009) also proposed an original testing device to carry out tension-compression tests into a universal testing machine. This device consists of four-block wedge design with pre-loaded springs, as depicted in Figure 2.8 b). It can be seen that the blocks cover the entire specimen on both sides and can freely move in the vertical direction while providing the normal support to the full length of the sample. The specimen is composed by double-side fins with the

purpose of measuring the strain. The pre-loaded spring is used on each side of the device to ensure that the edge plates are in firm contact with each other. Teflon sheets are applied between the specimen and the inner surface of the wedge plates, for the reduction of friction effects. According to the authors, (i) pre-strain levels of 0.15 and 0.09 in tension-compression and compression-tension can be respectively reached, (ii) potential buckling of the sheet specimen in compression can be prevented and (iii) the frictional force between the wedge plates and specimen can be neglected.

2.2.1.2 Shear test

The planar simple shear is a loading path particularly interesting for sheet metals since it can leads to large strains without the occurrence of plastic instability such as, flow localization and fracture (Rauch, 1998; Yoon *et al.*, 2005; Bouvier *et al.*, 2006; Thuillier and Manach, 2008). Indeed, the simple shear test allows characterizing the hardening behavior like the uniaxial tensile test, however, achieving higher level of deformation due to the absence of necking phenomenon. Furthermore, shear specimens can be machined at different orientations to the RD, such as tensile specimens, in order to characterize the anisotropic behavior in the sheet plane. From a strain state point of view, both homogeneous uniaxial tensile and simple shear tests can be seen as complementary experiments. In the case of the uniaxial tensile test, the strain state involves only diagonal components of the strain tensor while non-diagonal components of the strain tensor mainly appear in simple shear (Thuillier and Manach, 2008).

The first test reported in the literature to produce shear property data was developed by Iosipescu (1967) and is commonly called as Iosipescu shear test. Although it was developed to characterize steel metals, it has been largely used for composite materials (Adams and Walrath, 1986; ASTM, 1993). This experiment was very important to understand the different material behavior when submitted to shear deformation. However, it was revealed inadequate to characterize the material up to large strains due to the notched geometry of the shear specimen.

For this reason, Miyauchi (1984) developed a classical simple shear equipment allowing to achieve high levels of shear strain. This equipment consists of a clamping device of two rigid parts subjected to parallel movement. The device is mounted on a universal tensile machine and the specimen geometry is designed with two shear zones which are subjected to vertical displacement, as shown in Figure 2.9 a). The main advantage of this geometry, defined with two symmetric zones loaded in shear, is that both shear forces acting in the central grip of the device equilibrate each other. As a result, the friction forces decrease and it allows a better estimation of the shearing forces (Bouvier *et al.*, 2006).

An *et al.* (2009) proposed a shear test approach quite similar to the one developed by Miyauchi. FE simulations and experimental tests were carried out by the authors in order to (i) evaluate the effect of the specimen geometry on the shear distribution, (ii) study the effect of material parameters on the measured work hardening and (iii) correct the edge effect based on the geometry of the specimen. For this purpose, both specimen geometries depicted in Figure 2.9 b) were investigated. Such as the Miyauchi sample, the proposed specimens are composed by two symmetric shear zones (white zones) and are fully clamped by three sets of clamping blocks (grey zones). The authors observed in their study that (i) the strain distribution is quite homogeneous in the majority of the shear length of the rectangular specimen, while the opposite occurs for the

specimen including slits and (ii) the specimen geometry ratio (L/w) plays a critical role on the accuracy of the measured shear stress.

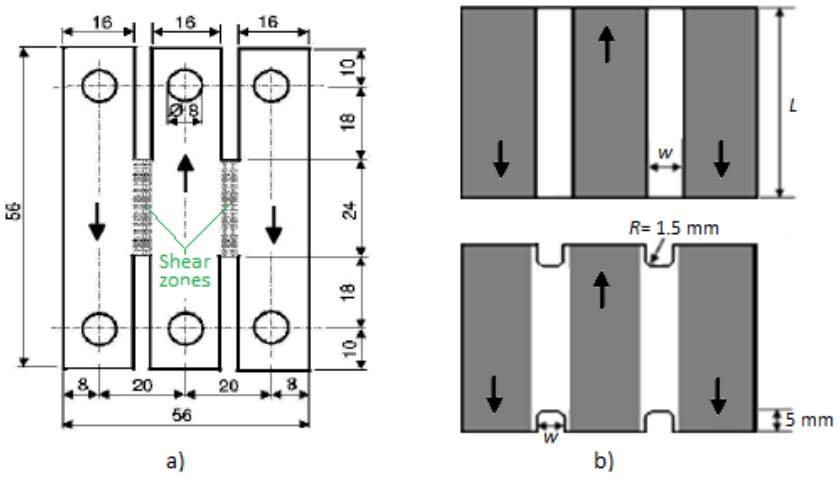

Figure 2.9 – Specimen geometries developed by a) Myiauchi (Mattiasson and Sigvant, 2004) and b) An *et al.* (2009) (rectangular specimen and specimen with slits). Dimensions are given in mm. L=55 mm and w=5 mm are the specimen length and effective shear width, respectively.

G'Sell *et al.* (1983) developed a simple shear test with only a single shear zone for polymers that was later adapted for metallic materials (Rauch and G'Shell, 1989). However, an improved version of this specimen as well as a dedicated device was developed by Genevois (1992), as shown in Figure 2.10. In this improved shear specimen, the rotation of the specimen under the action of the shearing forces is impeded by the stiffness of the machine frame (Bouvier *et al.*, 2006). Figure 2.10 shows that the dedicated device keeps the same principle of shear deformation of the equipment proposed by Miyauchi, since a parallel displacement of two lateral grips distorting a rectangular area of the specimen to a parallelogram also occurs. This dedicated device is one of the most widely used by the scientific community nowadays due to the simple rectangular geometry of the sample. Though, this simple shear test may present some drawbacks: (i) the measurement of the local strain can be difficult because of the narrowness of the shear zone, (ii) the existence of some heterogeneity of the strain state and buckling on the shear zone depends on the specimen dimensions and (iii) sliding of the sample may occur under the grips (Bouvier *et al.*, 2006; Thuillier and Manach, 2008).

Nevertheless, a numerical study conducted by Bouvier *et al.* (2006) investigated the shear strain and stress in the sample. This study shows that using $L/h \geq 10$ and $h/e \leq 3$ ratios (dimensions depicted in Figure 2.10), it is possible (i) to obtain an almost homogeneous stress state and (ii) to minimize the stress perturbation induced by clamping, avoiding buckling and premature failure. Additionally, Yoon *et al.* (2005) also carried out numerical simulations to study the effect of the shear specimen shape on the stress and strains fields. Both authors presented similar conclusions.

Despite the stress components σ_{xx} and σ_{yy} can reach considerable values near the free ends of this shear specimen, these ones can be neglected when using the dimension ratios established by Bouvier *et al.* (2006). According to this, the Cauchy stress and logarithmic strain tensors in the frame $(\vec{l}_x, \vec{l}_y, \vec{l}_z)$ can be written as

$$\boldsymbol{\sigma} = \begin{bmatrix} 0 & \sigma_{xy} & 0 \\ \sigma_{xy} & 0 & 0 \\ 0 & 0 & 0 \end{bmatrix} \qquad \boldsymbol{\varepsilon} = \begin{bmatrix} 0 & \varepsilon_{xy} & 0 \\ \varepsilon_{xy} & 0 & 0 \\ 0 & 0 & 0 \end{bmatrix} \tag{2.10}$$

within small strain assumption. For this shear test, shear stress σ_{xy} and shear strain γ can be calculated by

$$\sigma_{xy} = \frac{F}{Le} \tag{2.11}$$

and

$$\gamma = 2\varepsilon_{xy} = \frac{\Delta L}{h}, \tag{2.12}$$

where F is the applied force, ΔL is the corresponding displacement between the sheared edges, L is the length, e is the sheet thickness and h is the width of the shear zone, as illustrated in Figure 2.10. Usually, the evaluation of the shear strain directly from the relative grips displacement must be avoided due to the expected sliding of the sample. Therefore, to circumvent this, it can simply use FFM methods.

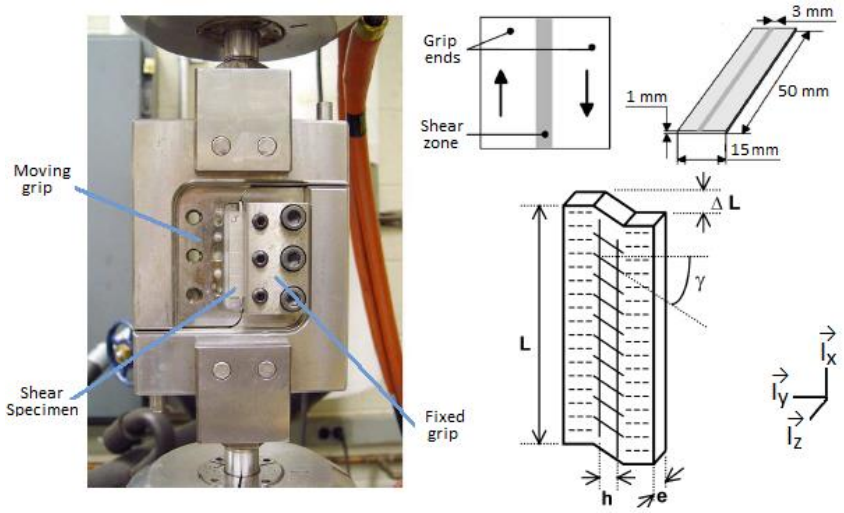

Figure 2.10 – Shear test device and specimen geometry improved by Genevois (Rauch and G'Shell, 1989; Yoon *et al.*, 2005).

Several advantages of this simple shear test must be stressed out. For instance, due to the symmetry of the stress tensor, experimental shear tests carried out at 0° and 90° to the RD are similar at the beginning of the deformation and the possible small discrepancy verified during the test results, essentially, of the induced anisotropy. Withal, the main advantage of the shear test is the possibility to also perform reversal experiments which are designated as shear-Bauschinger tests. The characterization of the kinematic work hardening in sheet metals can be a rather difficult task mainly due to the buckling in tension-compression. However, using this experiment, the loading direction can be easily reversed by simply changing the displacement direction of the

clamps. Moreover, shear-Bauschinger tests generally lead to the achievement of large strains (Hu *et al.*, 1992).

More recently, new shear test approaches have been developed for universal tensile machine without any kind of dedicated device or clamping system. Merklein and Biasutti (2011) use a modified geometry based on the specimen proposed in the ASTM B831 (2005) to carry out monotone and reverse simple shear tests in sheet metals. The obtained results with this setup were validated comparing the determined flow curves of an AA6016 aluminum alloy with similar results obtained from an optimized Miyauchi shear test device. The developed specimen and the obtained flow curves using both shear devices are shown in Figure 2.11 a). It can be seen that the proposed shear specimen promotes high strain values and also avoids sliding problems and rotation moments and reduces the experimental effort since the clamping devices are located at the upper and the lower ends, not influencing the shear zone. However, in reverse shear, buckling may occur due to the compression loads. Therefore, additional supporting devices (four plates machined out of high strength steel) must be layered on the specimen in a sandwich manner to prevent this undesirable phenomenon (Merklein and Biasutti, 2011). Nevertheless, the supporting devices are mounted without applying friction in the shear zones.

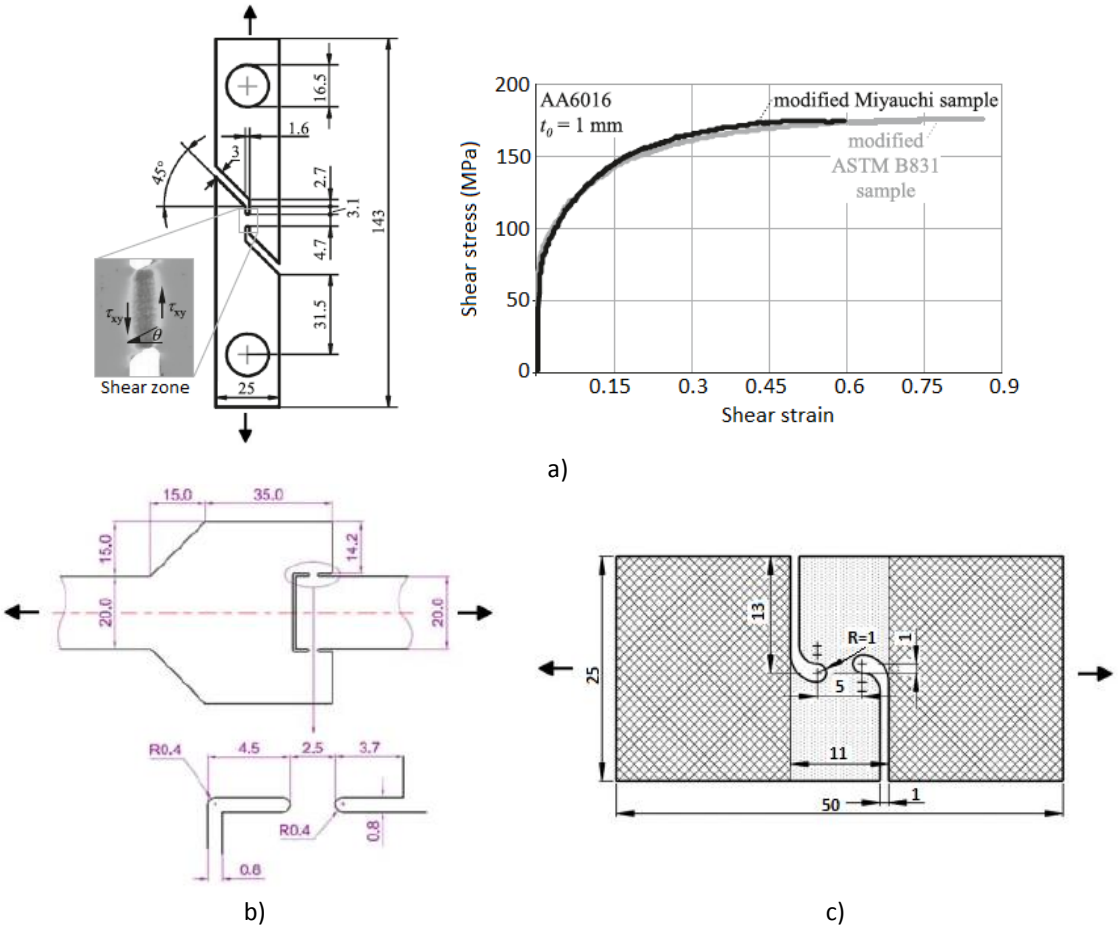

Figure 2.11 – Shear specimen proposed by a) Merklein and Biasutti (2011) and flow curves obtained by using this specimen and the one developed by Miyauchi, b) Vrh *et al.* (2011) and c) Peirs *et al.* (2011). Specimen dimensions are given in mm.

Vrh *et al.* (2011) developed a new shear specimen for a reliable identification of the hardening curve of sheet metals after the onset of necking, observed in uniaxial tensile tests. This specimen, illustrated in Figure 2.11 b), is composed by two symmetric shear regions and enables to achieve large shear strain. The contour of these shear regions was optimized by FE simulation in order to assure simple shear loading conditions.

Peirs *et al.* (2011) proposed a combined experimental-numerical approach to output the strain rate and temperature dependent mechanical behavior from high strain rate experiments. For this purpose, an in-plane shear specimen like the one shown in Figure 2.11 c) is used to study the stress-strain behavior of Ti6Al4V material. Thanks to the particular geometry, optimized for the mechanical properties of Ti6Al4V, the tensile load imposed during the experiment is converted into shear deformation in the central area of the sample. The deformation observed in the small shear zone conducts to a stress state of almost pure shear due to the non-aligned position of the notches.

Another way to obtain a shear stress state consists of the plane torsion test that was introduced by Marciniak (1961). This test uses a circular sheet sample which is clamped in the center and in the outer rim. The plane torsion is applied through the inverse rotation of both clamps and the free area is subjected to shear deformation.

Yin *et al.* (2011) proposed an experimental setup for plane torsion, as depicted in Figure 2.12 a), and determined monotonic and cyclic flow curves using optical strain measurement. The experimental setup is integrated in a universal tensile machine and is composed by a servo motor and a worm gear. The application of a torque moment on the outer clamping system produces an inhomogeneous stress and strain distribution along the radial distance to the center. In this way, the highest stress and strain is observed near the inner clamp and decreases progressively until the outer clamp. Due to this fact, the shear strain that consists of the gradient of the distorted radial line, as shown in Figure 2.12 a), cannot be directly calculated and, thus, a FFM method is required. The main advantages of this experiment are the possibility of reaching high levels of equivalent strains (up to 1.0) and obtaining multiple cyclic shear curves by using only a single specimen (Yin *et al.*, 2011). Nonetheless, the measured torque moment is an average of varying shear stress along the circumference and, consequently, an average of any effect of the material anisotropy (Yin *et al.*, 2012). Other limitations, namely, buckling and slipping can also occur in this experiment.

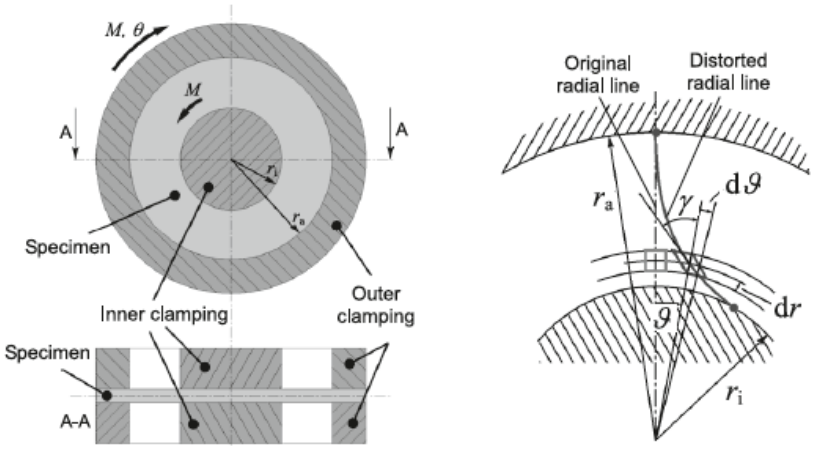

a)

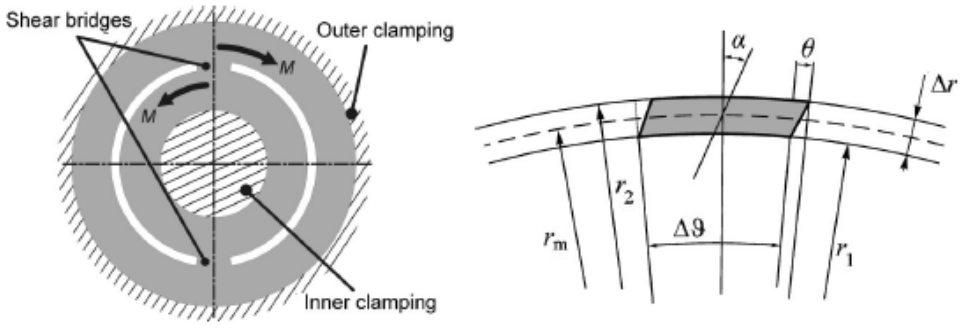

b)

Figure 2.12 – Specimen geometry and geometrical features of a) plane torsion specimen developed by Yin *et al.* (2011) and b) twin-bridge shear specimen proposed by Brosius *et al.* (2011).

Based on the plane torsion, the twin-bridge shear test presented in Figure 2.12 b) was proposed by Brosius *et al.* (2011). This test avoids the disadvantages related to plane torsion and conventional shear tests. In fact, it allows (i) the reduction of the clamping loads, (ii) the reduction of possible slipping and (iii) to avoid buckling effects especially in cyclic loading. The twin-bridge specimen consists of a circular shape with partial tangential slots. The slit geometry is responsible for strain localization in two opposite shear bridges, which are the only connection between the inner and the outer clamp zones. In addition, both bridges are arranged symmetrically to avoid any unintended resulting forces or moments (Brosius *et al.*, 2011). The principle of deformation is the same of the plane torsion test, however, the shear zone differs. For twin-bridge shear test, no occurrence of deformation in the whole free area is verified, only in the twin bridges. The use of a FFM method for obtaining the strain deformation, especially if the clamps are not adjacent to shear bridges, is recommended.

Yin *et al.* (2014) investigated the application of the twin-bridge shear, Miyauchi (Figure 2.9 a)) and modified ASTM B831 (Figure 2.11 a)) specimens on the characterization of sheet metals. The main focus of the authors was to compare the effect of these different shear test configurations, in terms of specimen geometry as well as fixtures, on the material behavior characterization under shear conditions. For this purpose, experimental strain distributions measured by DIC technique and FE simulations to evaluate the effect of the specimen geometry on the stress distributions in the shear zones were carried out for each shear test. It was concluded that (i) a good agreement between the experimental shear stress-strain curves from the different shear tests is obtained and (ii) FE simulations revealed minor discrepancies in the stress distributions.

The twin-bridge shear experiment was also applied for identifying kinematic hardening material parameters of DC06, DP600, and TRIP700 steels (Yin *et al.*, 2012). For that, the specimen dimensions r_m =21.5 mm, Δr=1 mm, Δθ=20°, t=1 mm and a radial distance of 15 mm and 30 mm, respectively for the inner and the outer clamp, were considered. Instead of using a FFM method for measuring strain data, the inverse approach for material parameters identification was implemented by using the torque and the angle data. This strategy was based on moment-angle curves and from the obtained results it was concluded that (i) these curves present the same characteristics of a material stress-strain curve and (ii) the proposed method is able to correctly predict the inhomogeneity within the shear zone.

2.2.1.3 Plane strain tensile test

The plane strain tension characterizes the material behavior between uniaxial and equibiaxial tension, as pointed out in Figure 2.2, and consists of a typical deformation path encountered in sheet metal forming. Bending of wide sheets or tension in a cylindrical cup wall are examples involving this kind of deformation. Furthermore, it was estimated that 85% of stretching failures in automotive stamping occurs near the plane strain state (Ayres *et al.*, 1978), which reveals the importance of this strain state in sheet forming operations. In plane strain tension, the Cauchy stress and logarithmic strain tensors in the frame ($\vec{l}_x, \vec{l}_y, \vec{l}_z$) can be defined by

$$\boldsymbol{\sigma} = \begin{bmatrix} \sigma_{xx} & 0 & 0 \\ 0 & \sigma_{yy} & 0 \\ 0 & 0 & 0 \end{bmatrix} \qquad \boldsymbol{\varepsilon} = \begin{bmatrix} \varepsilon_{xx} & 0 & 0 \\ 0 & 0 & 0 \\ 0 & 0 & \varepsilon_{zz} \end{bmatrix}. \tag{2.13}$$

Wagoner (1981) designed both specimen geometries shown in Figure 2.13 a) with the aim of characterizing plane strain tension. These specimens were subjected to tensile loading using a universal testing machine and near-plane strain tension was obtained in the center of the samples.

Kuwabara and Ikeda proposed an adapted cruciform specimen for characterizing plane strain tension (Kuwabara, 2007), as depicted in Figure 2.13 b). The tensile direction is parallel to the shorter arms of the specimen and the strain component of the longer arms of the specimen is maintained at zero using a closed-loop hydraulic system (Kuwabara, 2007).

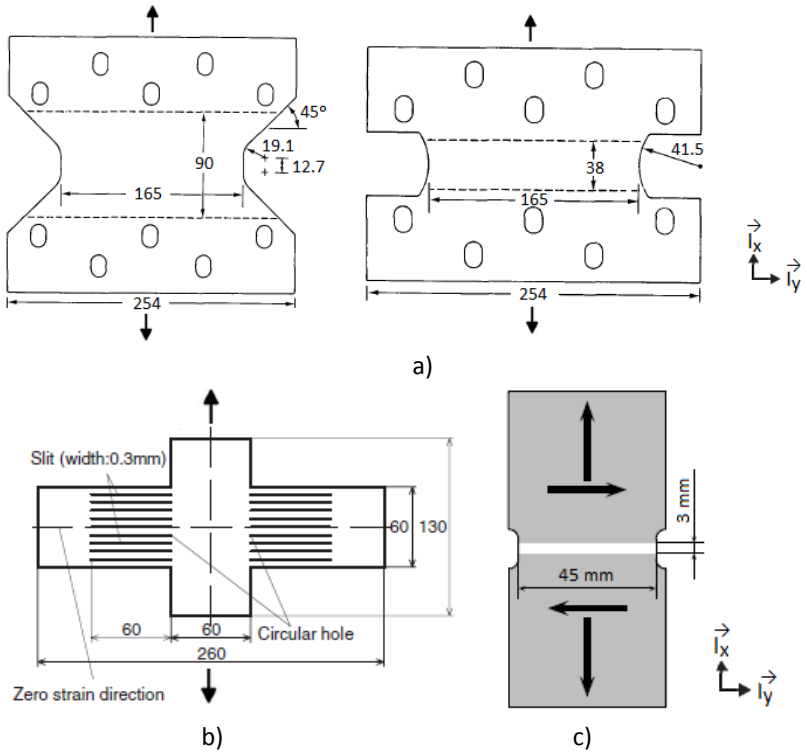

Figure 2.13 – Specimen configurations for plane strain tension test proposed by a) Wagoner (1981), b) Kuwabara and Ikeda (Kuwabara, 2007) and c) Pijlman (2001). Dimensions are given in mm.

Pijlman (2001) also developed an experiment for characterizing plane strain tension. This experiment consists of a biaxial test equipment that can combine plane strain and shear deformation. Figure 2.13 c) presents the specimen configuration used in this test. During the experimental test, the specimen is fixed between two pairs of clamps and the vertical translation of the clamps gives a plane strain deformation. The deformation zone corresponds to the small white area at the middle of the specimen. In order to obtain plane strain tension, the width of the deformation zone must be large relatively to the height. Nevertheless, it leads to high clamping loads and, usually, sliding of the specimen occurs under the grips. Due to this reason, FFM method is highly recommended for the analysis of local strains.

2.2.1.4 Hydraulic bulge test

Biaxial tests are essential to provide a reliable mechanical characterization of the material since multi-directional deformation is verified in sheet metal forming. Uniaxial tests only characterize the mechanical properties in a single direction and, usually, such experimental data is not enough to accurately describe complex sheet forming processes, like deep drawing. Biaxial tests, such as the hydraulic bulge test, are used to quantify and clarify the effects of stress biaxiality on monotonic stress-strain curves and forming limit diagrams (Makinde *et al.*, 1992).

The hydraulic bulge test is a testing method where a circular or elliptical blank is clamped around the edges and subjected to an increasing fluid pressure, as illustrated in Figure 2.14. This experiment was initially introduced by Prater and Read (Prater and Read, 1949; Dudderar *et al.*, 1977) and several improvements have since been performed, namely, a biaxial extensometer developed by Johnson and Duncan (Johnson and Duncan, 1965; Banabic *et al.*, 2010) and automated hydraulic bulge testers such as the ones developed by Golongrac (Golongrac, 1975; Kuwabara, 2007), Young *et al.* (1981) and Koh (2008). For example, the bulge testing device proposed by Young *et al.* (1981) allows to acquire true stress-strain data by controlling the strain rate deformation, while the bulge test apparatus developed by Koh (2008) allows to accommodate material strength up to 1000 MPa with plate thickness between 1.0 and 1.8 mm.

Concerning the bulge experiment, the Cauchy stress and logarithmic strain tensors in the frame ($\vec{l}_x, \vec{l}_y, \vec{l}_z$) can be written by

$$\boldsymbol{\sigma} = \begin{bmatrix} \sigma_{xx} & 0 & 0 \\ 0 & \sigma_{yy} & 0 \\ 0 & 0 & 0 \end{bmatrix} \qquad \boldsymbol{\varepsilon} = \begin{bmatrix} \varepsilon_{xx} & 0 & 0 \\ 0 & \varepsilon_{yy} & 0 \\ 0 & 0 & \varepsilon_{zz} \end{bmatrix}. \tag{2.14}$$

The hydraulic bulge test has been applied to provide flow stress properties at large strain levels as well as to determine the equibiaxial yield stress (σ_b). This test can give equivalent plastic strain levels up to 0.7 whereas the maximum achievable strain in homogeneous tensile tests is reported to be limited about of 0.3 (Gutscher *et al.*, 2004; Koç *et al.*, 2011). In addition, the experimental data are very reproducible, in particular, the pressure and local strain relation. However, for an accurate measure of biaxial stress-strain curve, the geometry of the bulge must be taken into account (Ranta-Eskola, 1979).

During the experiment, the deformation varies radially from balanced biaxial tension at the crown of the specimen to plane strain near the clamped edge (Foecke *et al.*, 2007). This effect results in a radial thickness variation and, therefore, the determination of the strain must be

based on the local thickness dimension or strain distribution measure with a FFM method. The gauge area in the bulge test is stretched by an approximately uniform biaxial membrane stress. As a consequence, the membrane theory is generally used to determine the flow stress curve and can be described as

$$\frac{\sigma_1}{\rho_1}+\frac{\sigma_2}{\rho_2}=\frac{P}{t}, \tag{2.15}$$

where σ_1 and σ_2 are the principal stresses on the sheet surface, ρ_1 and ρ_2 are the corresponding radii of the curved surface, P is the hydraulic pressure and t is the sheet thickness at the center (see Figure 2.14).

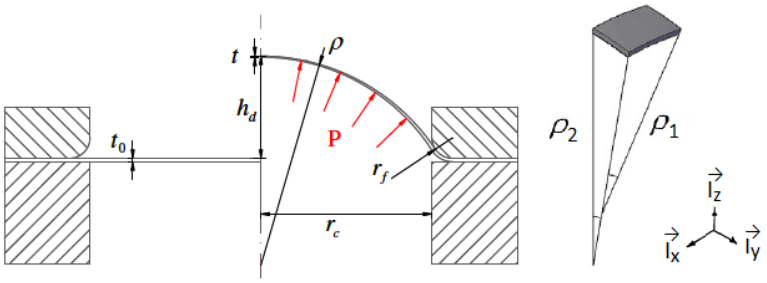

Figure 2.14 – Geometry of the bulge test (Koç *et al.*, 2011).

Considering the axi-symmetric case of the bulge test and the material isotropy assumption, $\sigma_1=\sigma_2=\sigma$ and $\rho_1=\rho_2=\rho$. Then, Equation 2.15 can be simplified to

$$\sigma=\frac{P\rho}{2t}. \tag{2.16}$$

One of the difficulties of the bulge test is the determination of the parameters t and ρ during the test when FFM methods are not used. One of the assumptions considered is that the bulge test is a portion of a sphere. In this way, the radius of the bulge can be determined by

$$\rho=\frac{r_c^2+h_d^2}{2h_d}, \tag{2.17}$$

where r_c is the die cavity radius and h_d is the dome height, as depicted in Figure 2.14. Nevertheless, such assumption consists of the main drawback of this experiment. The works of Papirno (1961) and Brown and Thompson (1949) show that the shape of the bulge is rarely spherical and is strongly dependent on the plastic deformation properties of the specimen (Dudderar *et al.*, 1977). Thus, calculations based on this assumption can lead to errors. Indeed, according to Aretz and Keller (2011), the assumption of equibiaxial stress state on bulge, assumed by Equation 2.16, may be violated due to the orthotropy of the material. For materials exhibiting r_b value significantly different from the unity, the membrane theory assumption is no longer valid due to the material anisotropy. The analysis of these authors was based on a virtual material with $r_b=0.5$ and a real one with $r_b=0.36$ and shows that an equibiaxial stress state cannot be achieved on bulge. In addition, Yoshida (2013) investigated numerically the validity of the equibiaxial stress state assumption for the bulge test in the case of material anisotropy and concluded that the stress state at the apex can deviate about 1 to 5% from the equibiaxial stress state.

2.2.1.5 Disk compression test

Barlat *et al.* (2003) proposed the disk compression test to determine the anisotropic biaxial coefficient r_b introduced in the yield function Yld2000-2d. Note that, such as in uniaxial tension, from biaxial tension it is also possible to determine an anisotropy coefficient. The so-called biaxial anisotropy coefficient r_b consists of the ratio between the principal strains in the sheet plane and is written as

$$r_b = \frac{\varepsilon_2}{\varepsilon_1}. \tag{2.18}$$

When the material is isotropic, r_b is equal to the unity. This coefficient is a direct measure of the slope of the yield locus at the equibiaxial stress state (Barlat *et al.*, 2005). Experimentally, r_b value can be determined either by using a disk compression test (Barlat *et al.*, 2003) or a biaxial tensile test with cruciform specimen (Pöhlandt *et al.*, 2002).

Concerning the disk compression test performed by Barlat *et al.* (2003), a 12.7 mm disk was compressed through the normal direction of the sheet using either dry film graphite or teflon sheets as lubrication between the faces of the specimen and contact points with the upper and lower platens of the compression test fixture. Both diameters, parallel and perpendicular to the RD, and the thickness were measured for each specimen prior to and after deformation. The strains were calculated from these measurements and the r_b coefficient was defined.

Merklein and Kuppert (2009) developed a reliable methodology for disk compression test with the aim of evaluating anisotropic materials. This methodology is based on the adaption of the experimental setup of standard compression test described in DIN 50106 (Merklein and Kuppert, 2009) and the use of two optical strain measurement systems to get experimental data along both symmetry axis. The specimen consists of stacked circular samples forming a cylindrical configuration. Both specimen and experimental device are illustrated in Figure 2.15. Teflon-foil acting as a solid lubricant is used to reduce the friction between the stacked specimen and the compression plates (Merklein and Kuppert, 2009). The optical strain measurement systems with an angle of 90° each other provide directly the major and minor strain data and the real loaded surface of the specimen. This methodology suppresses any type of assumption concerning the loaded surface or strain outside the measured area, as occurs when experimental data is only available from one axis direction.

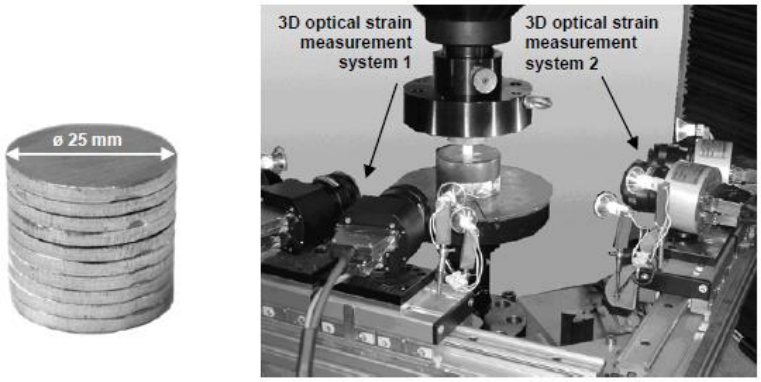

Figure 2.15 – Stacked specimen and experimental setup used by Merklein and Kuppert (2009).

The disk compression test can also be used to determine the hardening behavior in compression, having the advantage of reaching large plastic strain levels comparing with the conventional tensile test (Merklein and Kuppert, 2009). It is due to the absence of necking phenomenon in compression. However, the application of this experimental test for sheet metals is only possible staking a number of sheet samples.

2.2.2 Non-homogeneous approach

Comparing with classical testing methods, where measured global quantities are used to infer the values of constitutive parameters with the help of simple analytical solutions and under assumption of homogeneous strain and stress fields in the gauge area, FFM methods allow substantial flexibility due to the measurements of displacement and strain fields over the specimen surface (Avril *et al.*, 2008a). From this non-homogeneous approach, several parameters of a constitutive model can be identified at the same time with only one test when the experimental field information is rich enough (Zhang, 2014). Therefore, complex experiments with large strain field heterogeneity allow to extract more information from a small number of tests and to reduce considerably the experimental database required for parameters identification purposes.

2.2.2.1 FEMU identification strategy

Since sheet metal forming processes are carried out under inhomogeneous and multiaxial strain paths, heterogeneous experiments based on a new design or modified classical tests have been developed in order to evaluate the material behavior for non-homogeneous strain fields. The FEMU strategy, as described previously in section 2.2, is widely applied for the parameters identification from these heterogeneous experiments. However, because full-field measurements are considered by the non-homogeneous approach, the objective function assumes a different formulation. The most commonly used objective function consists of a weighted least-square difference between computed and experimental field data where this data can be displacement (Pottier *et al.*, 2011a; Pottier *et al.*, 2011b) or strain (Cooreman *et al.*, 2008; Güner *et al.*, 2012; Haddadi and Belhabib, 2012; Prates *et al.*, 2014; Zhang *et al.*, 2014) fields. Moreover, the quadratic difference between the experimental and numerical data can be weighted by two different ways. One way consists of dividing this difference by the corresponding experimental value of each point of the field data (Haddadi and Belhabib, 2012; Zhang *et al.*, 2014), while another way is to use the maximum experimental value of the field data (Pottier *et al.*, 2011a; Pottier *et al.*, 2011b).

In the first case, when an experimental data corresponds to a null value, an indetermination results of this division and the objective function will not be well calculated. Therefore, since the experimental field data is defined by a large number of values and some of them can be zero, this way of weighting the objective function does not seem the most suitable one. In the latter case, assuming that the maximum experimental value of the field data is different of zero (which occurs due to the specimen deformation), the objective function will be always accurately calculated during the identification process. In addition, only one weighting factor for the all field data is used and it also leads to the normalization of different units or scales of the data.

The objective function must be defined considering both field data and global reaction load as material responses in the parameters identification process, since it leads to a better suited solution when strain concentration and localized damage are involved (Avril *et al.*, 2008a). Then, for the non-homogeneous approach, the objective function $S_{\text{obj}}(\mathbf{x})$ can be defined by

$$S_{\text{obj}}(\mathbf{x}) = \sum_{i=1}^{n_{\text{im}}} \left[\left(\frac{F_i^{\text{exp}} - F_i^{\text{num}}(\mathbf{x})}{F_{\text{max}}^{\text{exp}}} \right)^2 + \frac{1}{n_{\text{p}}} \sum_{j=1}^{n_{\text{p}}} \left[\left(\frac{\varepsilon_{1,j,i}^{\text{exp}} - \varepsilon_{1,j,i}^{\text{num}}(\mathbf{x})}{\varepsilon_{1,\text{max},i}^{\text{exp}}} \right)^2 + \left(\frac{\varepsilon_{2,j,i}^{\text{exp}} - \varepsilon_{2,j,i}^{\text{num}}(\mathbf{x})}{\varepsilon_{2,\text{max},i}^{\text{exp}}} \right)^2 \right] \right] \tag{2.19}$$

where n_{p} is the number of points of the strain field, n_{im} is the number of strain fields evaluated, F_i^{exp} and $F_i^{\text{num}}(\mathbf{x})$ are the experimental and numerical load values at the strain field *i*, $F_{\text{max}}^{\text{exp}}$ is the maximum experimental load value for all the strain fields, $\varepsilon_{1,j,i}^{\text{exp}}$ and $\varepsilon_{1,j,i}^{\text{num}}(\mathbf{x})$ as well as $\varepsilon_{2,j,i}^{\text{exp}}$ and $\varepsilon_{2,j,i}^{\text{num}}(\mathbf{x})$ are the experimental and numerical major and minor principal strain values for the point *j* at the strain field *i*, respectively, $\varepsilon_{1,\text{max},i}^{\text{exp}}$ and $\varepsilon_{2,\text{max},i}^{\text{exp}}$ are the maximum experimental major and minor principal strain values at the strain field *i* and **x** is the material parameters set.

Most of the heterogeneous experiments available in the literature are based on the modification of (i) classical tensile test (Meuwissen, 1998; Meuwissen *et al.*, 1998; Kajberg and Lindkvist, 2004; Belhabib *et al.*, 2008; Cooreman, 2008; Pottier *et al.*, 2011a; Güner *et al.*, 2012; Haddadi and Belhabib, 2012) or (ii) biaxial tension test using a cruciform specimen (Cooreman *et al.*, 2008; Teaca *et al.*, 2010; Zidane *et al.*, 2010).

Heterogeneous tensile tests

Concerning the geometry of heterogeneous tensile tests, it is mainly designed by (i) adding a hole (Cooreman *et al.*, 2008; Pottier *et al.*, 2011a), (ii) notching the specimen (Belhabib *et al.*, 2008; Güner *et al.*, 2012; Haddadi and Belhabib, 2012) or (iii) promoting a shear-like tensile zone (Meuwissen *et al.*, 1998; Kajberg and Lindkvist, 2004).

Meuwissen *et al.* (1998) developed a FEMU strategy for identifying elastoplastic material parameters from the shear-like tensile tests illustrated in Figure 2.16. This procedure was performed for low strain levels of an AA1200 thin sheet. Retro-reflective markers were placed on the central area of the specimen surface and their displacements were measured optically. The displacement fields were iteratively compared with the ones coming from the numerical simulation in order to minimize an objective function. Although an overall good fit was observed between the experimental displacements and the numerical ones obtained with the identified parameters set, some discrepancies were found in the numerical prediction of the classical uniaxial tensile test, namely, an underestimation of the yield stress. The authors stated that by using a FFM method for acquiring the experimental displacements fields it is expected to improve the previous results.

Kajberg and Lindkvist (2004) proposed a FEMU strategy for characterizing the sheet metal behavior up to large strains. For that, notched samples were subjected to tension loading up to fracture and the field information for both in-plane displacements and strains was measured by digital speckle photography. The material parameters of two constitutive models were estimated by minimizing a least square cost function based on the difference between the experimental and

numerical calculated displacements, strains and loads. However, the identified parameters sets were only validated at low strains for stress-strain curves obtained from a classical uniaxial tensile test.

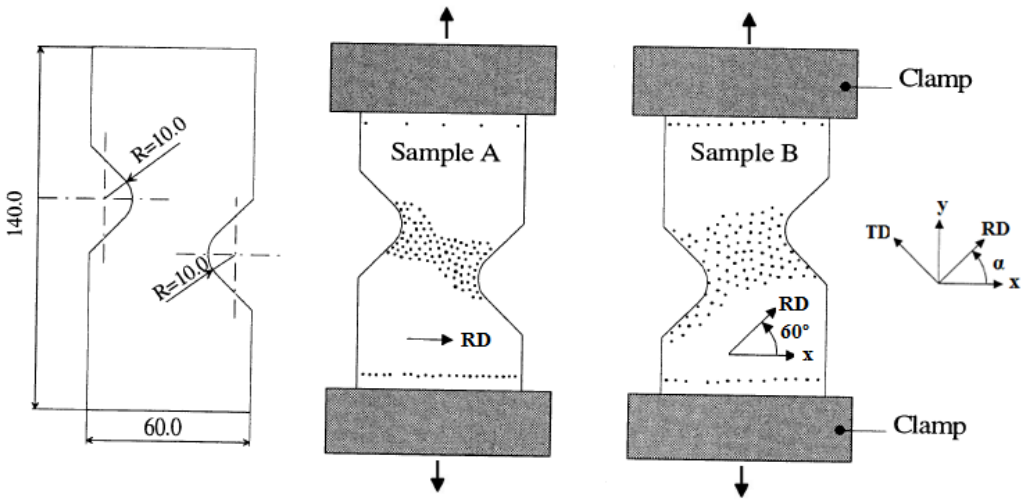

Figure 2.16 – Shear-like tensile specimens proposed by Meuwissen *et al.* (1998).

Belhabib *et al.* (2008) proposed a non-standard notched tensile test (HTT) for the identification of material parameters using FFM method. The specimen consists of a hybrid geometry between a classical tensile test (CTT) and a plane tensile test (PTT) and was designed with the aim of verifying (i) large heterogeneity of the strain in the gauge area, (ii) large strain paths diversity and (iii) good sensitivity of the strain fields to the material parameters. These tensile tests are illustrated in Figure 2.17 a). The authors showed that HTT presents large diversity of strain paths and better material parameters sensitivity of the strain fields than CTT and PTT. By this work, it was concluded that using a heterogeneous experiment, such as HTT, it is expected to improve the quality[1] of the identified material parameters.

Later, Haddadi and Belhabib (2012) developed and implemented a FEMU identification process based on both total load and full-field strain measurement obtained from the HTT test. DIC technique was used for acquiring the experimental strain data and a least-square function combining tensile load and longitudinal strain field was defined. In order to validate the material parameters identified, a comparison between the numerical and experimental strain field of the shear like-tensile test depicted in Figure 2.17 b) was carried out. The obtained results revealed that a good prediction was obtained using the identified material parameters set. In addition, this numerical strain field was also compared with the one obtained from a parameters set identified by standard tests and it was observed that a more reliable prediction is achieved by set of parameters identified with the heterogeneous HTT test.

Pottier *et al.* (2011a) compared the reliability of the material parameters identified by applying FEMU strategy and DIC technique to three sample geometries. The tests exhibit increasing strain heterogeneities and consist of a classical tension, a tension with hole and a shear-like tensile test, as shown in Figure 2.18. In order to evaluate the reliability of the three

[1] A set of material parameters for a pre-determined constitutive model is considered of better quality when it gives more reliable predictions of the material behavior and, consequently, of real forming processes.

identified parameters sets, numerical simulations of a deep drawing experiment were compared with the experimental data. The results showed that a better numerical reproduction of the deep drawing data was obtained with the material parameters set identified from the shear-like tension. According to the authors, the quality of the material parameters identified improves and the required number of experiments decreases when the heterogeneity of the strain field increases

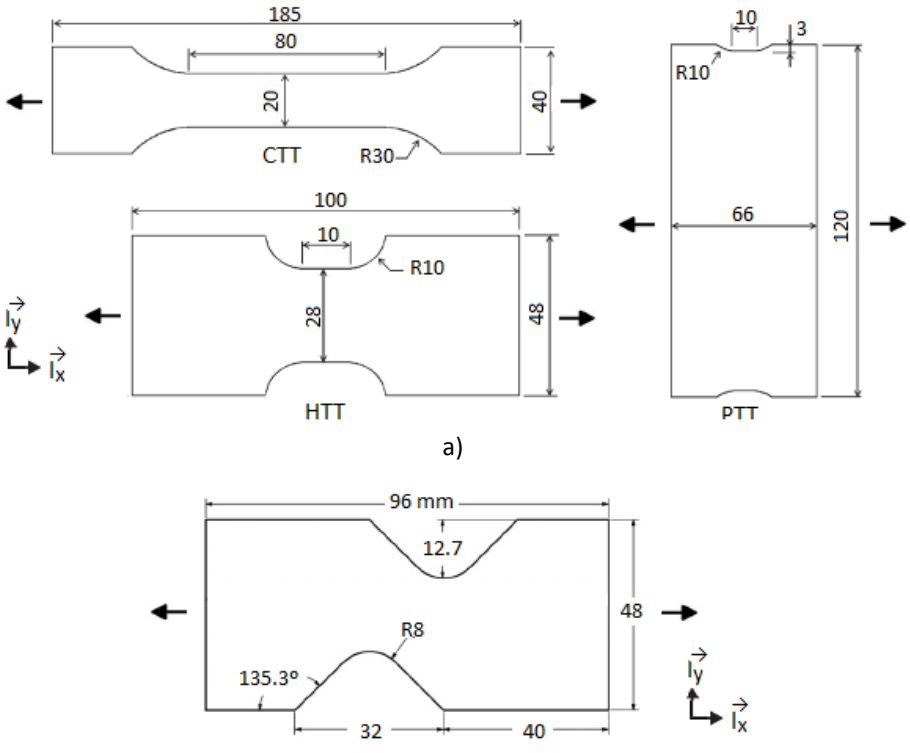

Figure 2.17 – Tensile tests with a) classical (CTT), plane strain (PTT) and heterogeneous (HTT) specimen configuration investigated by Belhabib *et al.* (2008) and b) shear-like tensile test used by Haddadi and Belhabib (2012) for material parameters validation.

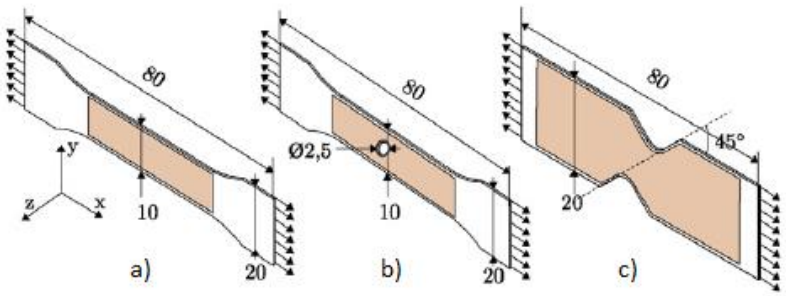

Figure 2.18 – Tensile tests a) classical, b) with a hole and c) shear-like used by Pottier *et al.* (2011a).

Güner *et al.* (2012) proposed a method to identify the planar anisotropy of sheet metals based on the evaluation of strain fields on a flat specimen with a varying cross-section. The material parameters of the constitutive model were determined by an inverse identification scheme comparing experimental and numerical strain distribution and load-displacement curves. The considered specimen geometry covered strain states between uniaxial tension and plane

strain tension and the identified parameters set was validated by comparing the experimental and numerical results of a deep drawn car hood geometry. This work pointed out that the use of the strain field distribution together with the conventionally used integral measures, such as load and displacement, improves the quality of the supplied information for an inverse parameters identification of planar anisotropy.

Biaxial tensile tests

The tensile experiments described above were designed to be subjected to uniaxial loading. However, sheet metals are subjected to multiaxial loadings during forming processes. Therefore, multiaxial loading experiments are highly desirable for the validation of the plasticity models used in numerical simulations (Banabic *et al.*, 2010). Hence, it is of great interest to consider the biaxial tensile test in the non-homogeneous approach of material parameters identification. Biaxial tensile tests are characterized by using a cruciform specimen and applying simultaneously longitudinal and transverse loads on their arms, leading to a biaxial tension in the center of the sample. This technique had been developed in the late 1960s (Shiratori and Ikegami, 1967; Mohr and Oswald, 2008) and successive improvements in the cruciform specimen shape and new testing devices have been proposed. Detailed reviews about biaxial tensile tests can be found in the works of Lebedev and Muzyka (1998) and Hannon and Tiernan (2008). The lack of a standard geometry is the main problem of this experiment in order to be used as a classical test. Due to this fact, the manner which stresses are calculated from the applied loads and the uniformity of stress and strain fields in the gauge section of the different specimen geometries influence the test results and their interpretation (Makinde *et al.*, 1992).

In addition, since a large strain heterogeneity is observed over the whole cruciform specimen surface, the biaxial tensile experiment is particularly interesting for reproducing situations close to those encountered in real forming processes, regarding the variety of stress states and strain levels obtained in a single experiment (Teaca *et al.*, 2010).

Cooreman *et al.* (2008) developed an identification strategy of material parameters based on a heterogeneous biaxial test. A perforated cruciform specimen, shown in Figure 2.19, was used by the authors and the evaluation of the strain field was carried out with DIC technique. The material parameters of a constitutive model composed by the Hill48 anisotropic yield criterion and a Swift hardening law describing a DC06 mild steel were identified by minimizing a least-square function based on the difference between the experimental and numerical 2D strain components. The material parameters identified with this non-homogeneous approach were compared with the ones obtained from a homogeneous approach considering 8 classical experiments (tension, plane strain tension and shear tests). It was observed that the results are quite similar which means that the parameters identification strategy developed with this single heterogeneous biaxial test is able to promote an identical material characterization as the one obtained from an experimental database composed by several homogeneous tests. The authors pointed out that the use of heterogeneous strain fields for material parameters identification leads to results better suited for the prediction of real forming processes than the ones based on classical homogeneous tests.

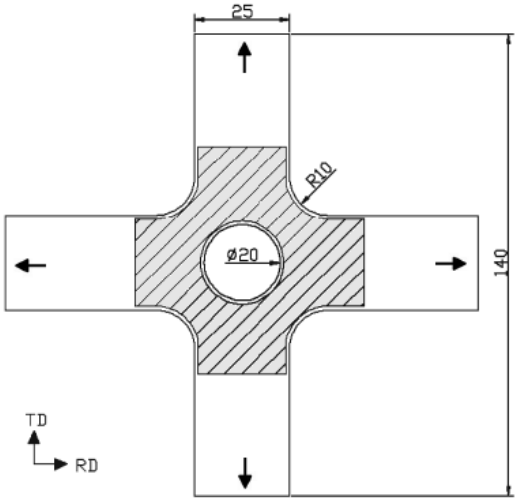

Figure 2.19 – Perforated cruciform specimen investigated by Cooreman *et al.* (2008). The shaded area is the zone in which the experimental measured strains are compared to the numerical ones. Dimensions are given in mm.

Teaca *et al.* (2010) designed two types of cruciform specimens that promotes a wide range of stress paths and a high sensitivity to the material anisotropy in order to use the obtained strain fields measure by DIC technique as input data for material parameters identification. A more accurate description of the plastic anisotropy was achieved with this strategy and, consequently, a better prediction of the strain distributions, forming limits and springback. The material characterization is performed for stress paths composed by the stress state range from uniaxial to plane strain tension using the cruciform specimen 1 depicted in Figure 2.20 a) and from uniaxial to equibiaxial tension using the cruciform specimen 2 exhibited in Figure 2.20 a). For the specimen 1, average stress states in the arms (RD region) and connecting parts between arms (DD region) are fairly close to uniaxial tension and plane strain tension, respectively. In the case of the specimen 2, stress state along RD region varies between equibiaxial tension in the center section and uniaxial tension in the central ligament of the arm. The main advantage of both experiments is the multi-stress states given in a single biaxial specimen which allows the reproduction of strain paths close to those encountered in industrial sheet forming processes.

Prates *et al.* (2014) proposed and inverse methodology for determining the material parameters of plastic constitutive models from a single biaxial tensile test using the cruciform specimen depicted in Figure 2.20 b). The geometry of this specimen was designed with the purpose of reproducing, as far as possible, inhomogeneous deformation developing strain paths commonly observed in sheet forming operations. The parameters identification strategy developed is based on the analyses of the load evolution during the test and the equivalent plastic strain distribution along the axes (RD and TD) of the sample, at a given moment of deformation; instead of following the strain fields on the specimen surface at several moments of deformation, such as carried out by the most part of the aforementioned works. This identification strategy was tested numerically considering a virtual material behavior and was compared with a homogeneous parameters identification strategy. It was shown that this proposed inverse strategy can be an efficient alternative to the homogeneous approach of material parameters identification which needs several classical tests.

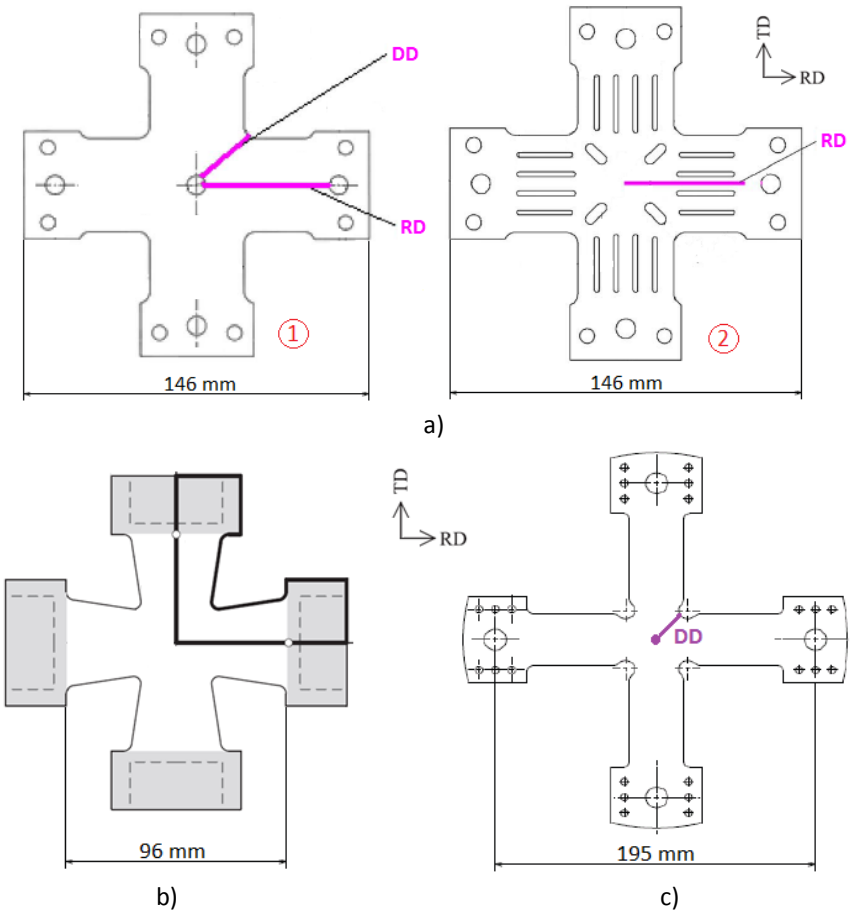

Figure 2.20 – Biaxial tensile cruciform specimens investigated by a) Teaca *et al.* (2010), b) Prates *et al.* (2014) and c) Zhang *et al.* (2014).

Zhang *et al.* (2014) also compared both homogeneous and non-homogeneous approaches of material parameters identification for calibrating the Bron and Besson (2004) anisotropic yield criterion reproducing the mechanical behavior of AA5086 aluminum alloy. Several classical experiments, namely, uniaxial tensile tests at 0°, 45° and 90° to the RD, simple shear tests at 0° and 45° to the RD and an hydraulic bulge test were used to identify the material parameters from the conventional identification strategy. Alternatively, a single biaxial tensile test using the cruciform specimen shown in Figure 2.20 c) was considered in the case of the non-homogeneous strategy. In this strategy, the principal strains along the diagonal direction of the gauge section of the cruciform sample (line DD in Figure 2.20 c)) have been evaluated and the difference between experimental results and numerical predictions was minimized. The yield contours obtained with the material parameters identified with both strategies were compared and it was observed that similar yield surface descriptions were obtained. It leads to the conclusion that a single heterogeneous test seems sufficient for identifying accurately all the material parameters of a complex yield criterion.

Other heterogeneous tests

Among the original tests that introduced a new design for the specimen and loading, the heterogeneous TIX test proposed by Pottier *et al.* (2011b) must be highlighted. This test is an

innovative testing technique for characterizing sheet metals based on the use of a uniaxial tensile device with a specimen subjected to an out-of-plane motion. In this experiment, the specimen is simultaneously deformed along two perpendicular tensile directions, two perpendicular shear directions and also in biaxial expansion, in different areas. Figure 2.21 a) shows the specimen designed by Pottier *et al.* (2011b) and the different deformation zones. This geometry presents a circular shape of 100 mm of diameter with inner grooves and leads to the development of a highly heterogeneous strain field, involving tension and shear at 0° and 90° to the RD and also biaxial tension in the center of the sample. The experimental setup of this test, shown in Figure 2.21 b), consists of a hemispherical punch with 15 mm of diameter which applies vertical displacement at the center of the specimen.

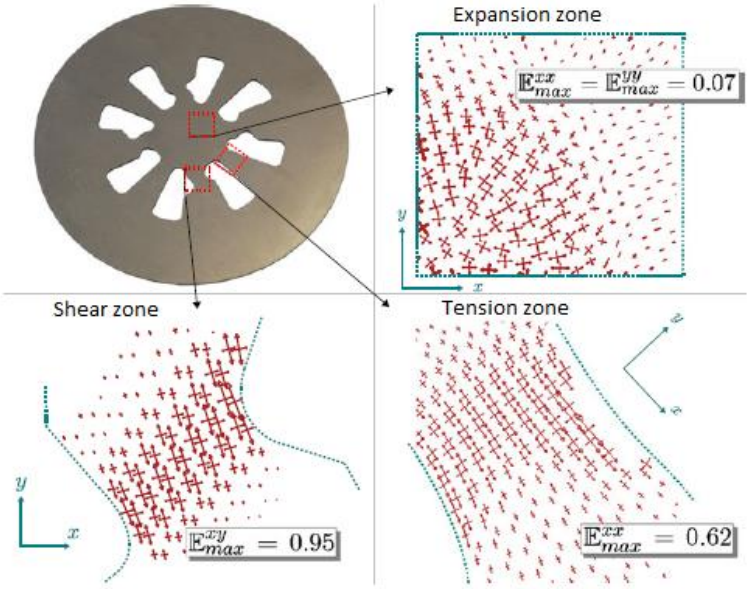

a)

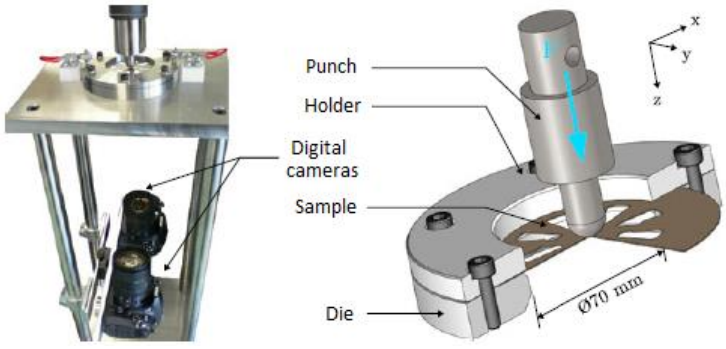

b)

Figure 2.21 – a) Specimen geometry and principal strain directions in the deformation zones and b) experimental device developed. It should be noted that E is the axial component of the Green-Lagrange strain tensor (Pottier *et al.*, 2011b).

The TIX experiment was applied for the parameters identification of a simple anisotropic constitutive model using an inverse procedure taking into account the displacement field measurements. Thus, a least-square function defining the difference between experimental and numerical (i) displacement fields along x, y, and z axis and (ii) global reaction load *F* was defined

and the gap was iteratively minimized during the parameters identification process. In order to inquire the validity of the identified material parameters, a deep-drawing test was carried out both experimentally and numerically. It was concluded that (i) a single heterogeneous test can lead to the identification of a complete material parameters set of an anisotropic plastic model and (ii) the increase of the strain field heterogeneity leads to a better assessment of the material behavior through parameter sets.

2.2.2.2 Other identification strategies

The FEMU identification procedure can become time consuming, especially if the constitutive model or the specimen geometry are complex, because at each iteration of the iterative identification process a full FE computation has to be performed. Another drawback is that often the actual boundary conditions are not perfectly reproduced in the FE model, introducing errors in the subsequent identification (Rossi and Pierron, 2012).

Therefore, other strategies have been proposed to directly evaluate the constitutive equations from the displacement and strain field measured by a FFM method, for instance, virtual field method (VFM) (Grédiac and Pierron, 2006; Pierron *et al.*, 2010; Rossi and Pierron, 2012; Kim *et al.*, 2013), equilibrium gap method (EGM) (Claire *et al.*, 2004; Périé *et al.*, 2009), constitutive equation gap method (CEGM) (Geymonat and Pagano, 2003; Latourte *et al.*, 2008; Florentin and Lubineau, 2010; Moussawi *et al.*, 2013) or reciprocity gap method (RGM) (Bui *et al.*, 2004). Among these strategies, VFM is clearly the most developed one for parameters identification of elastoplastic parameters.

The first application of the VFM to the identification of elastoplastic constitutive parameters was carried out with simulated full-field kinematic data obtained from a thin notched tensile specimen (Grédiac and Pierron, 2006). Further, experimental validations of the VFM were successfully achieved at small strains (Pannier *et al.*, 2006; Avril *et al.*, 2008b; Pierron *et al.*, 2010). Pannier *et al.* (2006) identified the material parameters of a nonlinear hardening model on a thin notched specimen showing a varying cross section. Avril *et al.* (2008b) reconstructed all the heterogeneous in-plane stress components of the stress tensor. Pierron *et al.* (2010) investigated the kinematic in addition to the isotropic hardening behavior of the material. The approach was later extended to large deformations using a thick sheet specimen with simulated data (Rossi and Pierron, 2012). More recently, VFM has been applied to characterize the post-necking strain hardening behavior of thin sheet specimens subjected to uniaxial tension (Kim *et al.*, 2013).

The VFM is based on the principle of virtual work which is, for a given solid of volume V subjected to a quasi static loading in absence of body forces, defined by (Pierron *et al.*, 2010)

$$-\int_V \boldsymbol{\sigma} : \boldsymbol{\varepsilon}^+ \mathrm{d}V + \int_{\mathrm{d}V_\mathrm{f}} \mathbf{T}.\mathbf{u}^+ \mathrm{d}S = 0\,, \tag{2.20}$$

where $\boldsymbol{\sigma}$ is the actual stress tensor, $\boldsymbol{\varepsilon}^+$ is the virtual strain tensor, $\mathbf{T}$ is the distribution vector of loading tractions acting on the boundary, $\mathrm{d}V_\mathrm{f}$ is the part of the solid boundary where the tractions are applied and $\mathbf{u}^+$ is the virtual displacement vector. A virtual displacement field is actually a test function, defined across volume V, for which the Equation 2.20 is verified. The virtual strain tensor is the strain tensor derived from the given virtual field displacement. An important feature is the fact that $\mathbf{u}^+$ must be kinematically admissible (Grédiac *et al.*, 2006). It means that $\mathbf{u}^+$ must be

continuous and differentiable across the whole volume and it must be null or constant over boundaries where the reaction traction distributions are unknown, in order to involve only the measured resultant loads in the equations (Pierron *et al.*, 2010). The choice of the virtual fields is a key issue in the method. Indeed, their number and their type depend on the nature of the constitutive equations. When these constitutive equations are nonlinear functions describing the elastoplastic behavior of the material, the equation derived from the principle of virtual work is also non-linear with respect to unknown material parameters (Grédiac and Pierron, 2012). In this case, the stress tensor only depends implicitly on the unknown material parameters through the evolution of plastic strains (Grédiac *et al.*, 2006). Due to this reason, an iterative procedure which minimizes a cost function is required for determining the material parameters. However, this iterative problem remains rather easy and fast to solve comparing with the one defined by FEMU strategy (Grédiac and Pierron, 2012). The main drawback of this identification strategy is related to the choice of the optimum virtual fields when complex constitutive models are considered.

RGM relies on situations where full-field measurements are available on the boundary. In this strategy, a reciprocity gap function is defined from the principle of virtual work using the Maxwell–Betti reciprocity theorem (Avril *et al.*, 2008a). An adjoint state is defined and the reciprocity gap between this adjoint state and the experimental one is minimized in order to obtain the parameters. The RGM can be seen as a variation of the VFM where kinematical fields are known only on the boundary. Nevertheless, there is no method for extrapolating the displacement field from known boundary values. Thus, the RGM method has not been applied to material parameters identification using experimental field data (Avril *et al.*, 2008a). Most applications deal with hidden crack identification, however, the technique is also theoretically applicable to retrieve constitutive coefficients governing elastic linear constitutive equations (Ikehata, 1993; Grédiac and Pierron, 2012).

The EGM strategy is based on the discretization of the equilibrium equations. In this way, the equilibrium equations are prescribed between elements on a discretized domain. Therefore, the EGM strategy requires full-field displacement data from which a finite element method is set up so that its nodes are coincident with the measurement grid points (Avril *et al.*, 2008a). This strategy allows determining heterogeneous elastic or damage fields by minimizing the equilibrium gap. Indeed this strategy has been applied to the identification of damage heterogeneity in composite materials (Claire *et al.*, 2004, 2007; Azzouna *et al.*, 2011).

The CEGM strategy is based on the minimization of a constitutive equation gap functional which provides the identified values of constitutive parameters (Avril *et al.*, 2008a). The CEGM measures the difference between a given stress field and another stress field computed through a constitutive model from a given displacement field. This strategy does not specifically need full-field measurements and can be applied to any kind of over determined data (Avril *et al.*, 2008a). In the case of an elastoplastic problem, the constitutive equation gap is defined by both *F* (associated to the standard formulation) and *G* (associated to the incremental formulation) functionals (Latourte *et al.*, 2008)

$$F(\boldsymbol{\tau},\mathbf{B}^{S}) = \frac{1}{2}\int_{\Omega}\left(\boldsymbol{\tau}-\mathbf{B}^{S}:\boldsymbol{\varepsilon}(\mathbf{u}^{*})\right)^{T}:\mathbf{B}^{S\text{-}1}:\left(\boldsymbol{\tau}-\mathbf{B}^{S}:\boldsymbol{\varepsilon}(\mathbf{u}^{*})\right)\,d\Omega \tag{2.21}$$

and

$$G(\Delta\boldsymbol{\tau},\mathbf{B}^{t}) = \frac{1}{2}\int_{\Omega}\left(\Delta\boldsymbol{\tau}-\mathbf{B}^{t}:\boldsymbol{\varepsilon}(\Delta\mathbf{u}^{*})\right)^{T}:\mathbf{B}^{t-1}:\left(\Delta\boldsymbol{\tau}-\mathbf{B}^{t}:\boldsymbol{\varepsilon}(\Delta\mathbf{u}^{*})\right)\,d\Omega\,, \tag{2.22}$$

where $\mathbf{u}^{*}$ is the in-plane displacement field measured on a given region of interest Ω of the specimen, $\boldsymbol{\tau}$ and $\Delta\boldsymbol{\tau}$ are the standard and incremental stress fields, $\mathbf{B}^{s}$ and $\mathbf{B}^{t}$ are the secant and tangent tensors and $\boldsymbol{\varepsilon}(\mathbf{u}^{*})$ and $\boldsymbol{\varepsilon}(\Delta\mathbf{u}^{*})$ are the strain related to the measured displacement and to the incremental displacement, respectively. In order to perform the numerical minimization of these functionals, by an iterative optimization process, a FE method is required to obtain an appropriate description of displacement, stress and material properties in the region of interest Ω. The CEGM strategy was initially applied in dynamics in the context of model updating of vibrational data (Ladeveze *et al.*, 1994), then was adapted for the identification of elastic properties (Geymonat and Pagano, 2003; Florentin and Lubineau, 2010; Moussawi *et al.*, 2013) and of elastoplastic parameters in the context of a small strain hypothesis and plane stress assumption for quasi-static loadings (Latourte *et al.*, 2008). More recently, it has been used for identifying the nonlinear damage behavior of composite materials (Merzouki *et al.*, 2014).

2.3 Conclusion

A literature review concerning both homogeneous and non-homogeneous approaches used to identify material parameters of constitutive models applied to thin metallic sheets was presented in this chapter. The parameters identification strategies behind both approaches were formulated and discussed.

It was stated that the material parameters are mainly identified based on a finite element model updating (FEMU) strategy which is applied to both homogeneous and non-homogeneous approaches. This strategy consists of an inverse problem where an optimization algorithm performs an iterative updating of the material parameters to minimize an objective function which computes the difference between experimental observations, coming from mechanical tests, and numerical predictions, usually obtained by FE simulation. Moreover, other identification strategies were also proposed in the case of the non-homogeneous approach. Within these strategies, just the VFM has been sufficiently developed to be applied to the material parameters identification of elastoplastic constitutive models. Nevertheless, due to the difficulty in choosing the optimum virtual fields, this strategy has not yet been largely used for identifying parameters of anisotropic elastoplastic constitutive models.

In addition, the classical and heterogeneous mechanical tests characterizing the sheet metal behavior which are respectively used by the homogeneous and non-homogeneous approach were introduced. These ones consist of the uniaxial tension, simple shear, plane strain tension, hydraulic bulge test and disk compression test, in the case of classical experiments, whereas tensile tests with notched specimen, a hole or shear-like tensile zone in the specimen and biaxial tensile tests using cruciform samples are the most common heterogeneous experiments.

It was pointed out that several works using the strain or displacement field measurements of a single heterogeneous test for identifying the material parameters from a non-homogeneous approach led to a similar or a better suited numerical prediction of the material behavior than

using the material parameters identified from an homogeneous approach based on the analytical stress-strain relations of several quasi-homogeneous classical tests. These results highlight that the time and material consuming as well as experimental database for material parameters identification purposes can be significantly reduced with a simultaneous enhancement of the quality of the material parameters when a heterogeneous experiment developing multi-stress and -strain sates is used. Due to this reason, the main goal of this thesis is the design of a mechanical test leading to a more complete mechanical characterization of the sheet metal behavior.

Since both homogeneous and non-homogenous approaches consist of an inverse optimization strategy, the formulation of an optimization problem and the different types of optimization methods are introduced in the next chapter.

Chapter 3

Parameter and shape optimization

3.1 Introduction

Optimization is the act of obtaining the best result under given circumstances. In design, construction and maintenance of any engineering system, technological and managerial decisions at several stages must be taken. The aim of these decisions is either to minimize the effort required or to maximize the desired benefit. Since the effort required or the benefit desired in any practical situation can be expressed as a function of certain decision variables, optimization can be defined as the process of finding the conditions that give the maximum or minimum value of a function (Rao, 1996).

Focusing on sheet metal forming, the design of metallic parts is no longer performed by trial-and-error procedures, mostly for economical and competitive reasons. Today, the numerical simulation by FE method is largely applied for testing virtually sheet forming processes in order to optimize the process parameters. However, numerical simulation of sheet metal forming is a complex process controlled by input coefficients describing the material behavior, blank shape, geometry of the tools, blank-holder pressure, friction, etc. Due to its complexity, involving the combination of all these input variables, optimization procedures are crucial tools for the proper design of sheet forming process as well as for the prediction and correction of undesirable forming defects (de-Carvalho *et al.*, 2012). Indeed, the optimization by numerical simulation of sheet forming processes and respective design of metallic parts is, currently, fundamental in the forming industry for decreasing the design cycle of new products, reduce substantially the associated costs and enhance the product quality.

Therefore, in the current chapter, the optimization problems found in sheet metal forming processes are defined and the different optimization methods generally used for solving these problems are characterized. Additionally, the optimization methods used in this work are introduced.

3.2 Optimization problem

In order to obtain accurate stress and strain fields, an effective FE numerical simulation requires reliable input data such as geometry, mesh, non-linear material model, contact and friction models, etc. This sort of problems can be defined as direct problems, in which the quality of the results relies on the quality of the input data that are however not always available. In order to overcome these difficulties, a possible approach are the inverse problems, for instance, with the definition of input parameters to be used in geometric or constitutive models for numerical simulations, based on experimental data (de-Carvalho *et al.*, 2011).

Hence, inverse problems deal with the determination of unknown parameters inherent to mathematical formulations of physical problems by comparing the measured real responses with the calculated numerical ones of the physical system. Taking into account the type of parameters needing to be determined, inverse problems can be divided in parameters identification and initial shape optimization problems (Kleinermann and Ponthot, 2003).

The aim of the parameters identification problem is to estimate the parameters of the constitutive model describing the mechanical behavior of the material. This optimization problem relies on the knowledge of material behavior coming from experimental data and its iterative comparison to results (for the same experiments) provided by numerical simulation models. Mathematically, the goal is to minimize the difference between experimental and simulation-based results defined by an objective function in order to found a reliable input constitutive parameters set. Note that this kind of inverse problem was already discussed in chapter 2.

The initial shape optimization problem intends to determine the initial shape of the blank and/or the shape of the forming tools when the final shape of the part is already known. In most forming process designs, such as in deep drawing, the final geometry of the part to be formed is prescribed. Moreover, the forming process must be designed to ensure that, after deformation, the blank will reach this prescribed shape (Ponthot and Kleinermann, 2006). However, this task becomes difficult due to the non-linearities that are inherent to the forming process, such as contact, non-homogeneous strain fields, large deformation and structural defects onset, such as wrinkling, thinning, earing and springback after the tools removal (Valente *et al.*, 2010). Due to this reason, an automatic design of the initial shape of the blank and/or the forming tools shape by performing optimization is essential in order to provide the desired final part geometry after forming process. In such an optimization procedure, the blank shape to be optimized is defined by a finite number of input parameters. An objective function evaluating the gap between the desired final part shape and the final one obtained by numerical simulation is iteratively minimized with the purpose of determining the optimal initial shape of the blank and/or tools.

Nevertheless, regarding the modification of the blank shape during the optimization process, another kind of optimization problem can be distinguished. This one consists in the shape optimization problem. Shape optimization problems do not belong to the class of inverse problems but are not so different. The general shape optimization problem tries to find a geometry or shape that is optimal, in the sense that it minimizes a certain objective function while satisfying given constraints (de-Carvalho *et al.*, 2012). Thereby, the only difference with the corresponding inverse problem is that in the inverse one the final shape is already known. This

shape optimization problem is the approach used for the computational design of the mechanical test proposed in this thesis, as can be seen further in chapter 8.

The concept of modern design optimization in engineering has been introduced by Schmit (1960). Zienkiewicz and Campbell (1973) combined the FE method with shape optimization concepts. In metal forming, Park *et al.* (1983) were pioneers presenting a methodology to calculate the optimum design of a forging preform. Later, Maniatty and co-workers (Maniatty and Zabaras, 1989, 1994; Maniatty and Chen, 1996) contributed significantly with sensitivity analysis for steady processes of metal forming inverse problems. Fourment and co-workers (Fourment *et al.*, 1996; Fourment and Chenot, 1996) generalized the design optimization in metal forming by suggesting a shape optimization method for a non-linear and non-steady-state metal forming problem. These authors proposed an inverse approach in order to optimize the initial shape of the part as well as the shape of the preform tool during a two-step forging operation, for which the shape of the second operation was previously known.

Concerning the optimization of mechanical tests for characterizing the material behavior of sheet metals, usually, only parametric studies related to the geometrical dimensions of the specimen are carried out in order to improve the performance of such tests (Zidane *et al.*, 2010; Dunand and Mohr, 2011; Tiernan and Hannon, 2014). However, note that Makris *et al.* (2010) implemented a shape optimization process with the aim of finding the optimal design of a cruciform specimen used in biaxial tension. These authors coupled a numerical optimization technique with FE analysis and the geometrical dimensions of the specimen were optimized in order to (i) maximize the region of strain uniformity in the biaxial loaded zone, (ii) minimize the strain concentration outside the test zone of interest and (iii) make specimen failure in the biaxial loaded zone.

Both parameters identification and shape optimization problems can be formulated as

$$\begin{aligned} &\text{minimize} && S_{\text{obj}}(\mathbf{x}) \\ &\text{subjected to:} && g_m(\mathbf{x}) \leq 0, && m = 1, \ldots, M \\ & && h_l(\mathbf{x}) = 0, && l = 1, \ldots, L \\ & && x_i^{\min} < x_i < x_i^{\max} && i = 1, \ldots, r. \end{aligned} \tag{3.1}$$

Here, $\mathbf{x}=[x_1, x_2, \ldots, x_r]$ with $r \in \mathbb{N}$ is the optimization variables tensor of the problem, S_{obj} is the objective function to be minimized, M is the number of inequalities constraints $g_m(\mathbf{x})$ and L is the number of equalities constraints $h_l(\mathbf{x})$ (Polak, 1997). In the case of both inverse problems, the objective function is usually written as (Valente *et al.*, 2010)

$$S_{\text{obj}}(\mathbf{x}) = \frac{1}{M_{\text{q}}} \sum_{j=1}^{M_{\text{q}}} [\text{gap}_j(\mathbf{x})]^2 , \tag{3.2}$$

while, in the case of the standard shape optimization problem, S_{obj} is generally defined by (Valente *et al.*, 2010)

$$S_{\text{obj}}(\mathbf{x}) = \frac{1}{M_{\text{q}}} \sum_{j=1}^{M_{\text{q}}} F_j(\mathbf{x}, \boldsymbol{\sigma}, \boldsymbol{\varepsilon}, \ldots). \tag{3.3}$$

Both objective functions expressed by Equations 3.2 and 3.3 are evaluated at the M_{q} instants of observation. Concerning the inverse problems, the objective function (Equation 3.2) calculates the gap between desired results and numerical predictions, as mentioned before. Alternatively, in the standard shape optimization problem, the objective function (Equation 3.3) is based on a functional F_j that characterizes the geometric shape as a function of structural properties such as, for instance, stress $\boldsymbol{\sigma}$ and strain $\boldsymbol{\varepsilon}$ fields.

An important aspect in design optimization is the fact that the optimization techniques used for minimizing the objective function are not able to evaluate the physical relevancy of the numerical model. Such optimization techniques just search for the design variables set which promote a best approximation between the numerical and expected results. However, the search space of design optimization problems is generally limited due to the physical admissible bounds of the different optimization variables. Therefore, the optimization variables should fill in this search space and, for this purpose, boundaries or inequality constraints for the design parameters value are commonly included in the optimization process. In the case of constrained optimization problems, the search space is limited by considering lower and upper admissible boundary sets for the optimization variables as defined in the last expression of Equation 3.1. Nevertheless, in the case of using unconstrained optimization methods, the design variables can be transformed as follows (Andrade-Campos, 2011)

$$x \geq x_0 \left[1 + (x^{\max} - 1) \left(1 - \exp\left(\frac{1 - x}{x^{\max} - 1} \right) \right) \right], \tag{3.4}$$

where $x_0 \geq 1$ is the initial value of x for an existing $x^{\max}$ and x normalized. A similar equation is formulated for $x_0 < 1$ using $x^{\min}$. In this way, lower and upper boundaries are imposed to the optimization variables.

Moreover, non-linear inequality constraints that represent complex relations among the design variables can also be imposed to the optimization process by the form of penalization terms (penalty method). These terms are added to the objective function with the aim of discouraging constraint violations. As a result, the optimization problem to be minimized can be defined by (Andrade-Campos *et al.*, 2007; Andrade-Campos, 2011)

$$S_{\text{obj}}^{\text{P}}(\mathbf{x}) = S_{\text{obj}}(\mathbf{x}) + \sum_{m=1}^{M} [\alpha_{\text{m}} \max\{0, g_{\text{m}}(\mathbf{x})\}]^2 , \tag{3.5}$$

where α_{m} are penalty coefficients and the second term of the equation is an exterior penalty function which leads to the evolution of the optimization process.

3.2.1 Optimization methods

The solution for the aforementioned optimization problems cannot be achieved analytically and is carried out with the aid of iterative numerical techniques designated as optimization methods.

These optimization methods are applied to update the variables **x** during the optimization procedure, with the purpose of minimizing the objective function value.

However, it must be pointed out that during the optimization process several local minima can be reached and some of the optimization methods do not have mechanisms to avoid this drawback. In this way, the selection of the optimization method assumes a great importance because it controls the efficiency of the parameters identification process (Cailletaud and Pilvin, 1994).

A large number of optimization methods can be used to solve inverse problems, generally, these belong to three main groups: (i) classic gradient-based, (iii) direct-search and (iii) evolutionary methods (Chong and Zak, 2001; Nocedal and Wright, 2006; Weise, 2008).

The classic gradient-based methods are characterized by using the information of the derivative of the objective function to successively update the solution until a criterion is satisfied. These methods usually converge quickly in the vicinity of the solution and then, are very interesting in terms of convergence rate (Chaparro *et al.*, 2008). Nonetheless, the results obtained with this type of optimization methods are characterized for being dependent on the initial set of parameters, since these methods do not have mechanisms that hinder the convergence for local minima (Polak, 1997; Andrade-Campos *et al.*, 2007). Thereby, the skills of the user on the definition of the initial guess solution may present a crucial role for the success of the optimization process. However, classic gradient-based methods are widely used in optimization due to their very good relationship between efficiency and required computational time (Chaparro *et al.*, 2008).

Among the several classic gradient-based methods, the most popular one applied to inverse optimization problems is the Levenberg–Marquardt least-square algorithm (Levenberg, 1944; Marquardt, 1963). Withal, other traditional optimization methods, such as the conjugate gradient or Broyden-Fletcher-Goldfarb-Shanno (BFGS) (Polak, 1997), as well as the convex approximation methods, such as the convex linearization (CONLIN) (Fleury, 1989), the method of moving asymptotes (MMA) (Svanberg, 1987) and the sequential quadratic programing (SQP) were also successfully used in optimization problems (Andrade-Campos *et al.*, 2007).

The direct search methods are generally based on simple strategies that only use function evaluations without needing the calculation of derivatives of the objective function. These optimization methods undergo the problem of converging to local minimums and are also user-dependent (Chaparro *et al.*, 2008). Their convergence can be very time-consuming and involves the comparison of each trial solution with the best previous solution. Several direct search methods can be mentioned, such as pattern search (Nocedal and Wright, 2006), Rosenbrock (Rao, 1996) and Nelder-Mead (Lagarias *et al.*, 1998). This kind of methods is popular, mostly the Nelder-Mead algorithm, due to its simplicity, flexibility and reliability. Additionally, these methods are less sensitive to numerical noise than the gradient-based methods.

Evolutionary method is a generic definition used to indicate any population-based optimization algorithm that makes use of some mechanism to improve the initial solutions (Chaparro *et al.*, 2008). Among the evolutionary optimization methods, the nature-inspired algorithms can be distinguished. These are probabilistic optimization methods based on biological evolution mechanisms, such as the reproduction or natural selection (Andrade-Campos *et al.*, 2007). These algorithms, which resort to a population where each individual can be a possible

solution, are very robust. Their search is initiated with a set of possible solutions only using the information of the objective function value (Furukawa and Yagawa, 1997), however, these algorithms require a large number of evaluations and, consequently, their convergence can be very time-consuming. In the following, the 2 algorithms used in this work are detailed.

3.2.1.1 Levenberg-Marquardt algorithm

One of the most used optimization methods in material parameters identification process is the Levenberg-Marquardt (L-M) gradient-based algorithm (Levenberg, 1944; Marquardt, 1963). This algorithm is an evolution of the classical least-square Newton method and calculates a search direction between the Gauss-Newton direction and the steepest descent direction (Chong and Zak, 2001). The L-M algorithm is characterized by alternating between a slow descent when moved away from a minimum and a quick convergence when in the neighborhood of a minimum. This feature associated to the excellent relationship between efficiency and required computational calculation time constitutes the main reason for the wide application of the L-M algorithm in optimization problems.

The L-M gradient-based algorithm uses the first order derivative of the residuals of the objective function. This algorithm starts on an initial point and creates a quadratic approach of the objective function using the values of first order of the derivative in this point. The L-M algorithm for an iteration k can be written as (Kleinermann, 2000; Andrade-Campos *et al.*, 2007)

$$\left([\mathbf{J}(\mathbf{x}_k)]^{\mathrm{T}} \mathbf{J}(\mathbf{x}_k) + \lambda \mathrm{diag}\left([\mathbf{J}(\mathbf{x}_k)]^{\mathrm{T}} \mathbf{J}(\mathbf{x}_k) \right) \right) \mathbf{h}_k^{\mathrm{LM}} = -[\mathbf{J}(\mathbf{x}_k)]^{\mathrm{T}} \mathbf{R}(\mathbf{x}_k), \tag{3.6}$$

where $\mathbf{J}(\mathbf{x}_k)$ is the Jacobian matrix of the objective function defined as a sum of squares of residuals, λ is the Levenberg-Marquardt parameter, $\mathbf{h}_k^{\mathrm{LM}}$ corresponds to the step given for the algorithm in each iteration k and $\mathbf{R}(\mathbf{x}_k)$ is the vector of the residuals between the experimental results and the numerical predictions obtained with the optimization variables tensor $\mathbf{x}$ at the iteration k. The parameter λ promotes different behaviors in the method influencing the direction and size of the algorithm step $\mathbf{h}_k^{\mathrm{LM}}$.

3.2.1.2 Nelder-Mead algorithm

The direct search Nelder-Mead algorithm is based on a spatial approximation to achieve the minimum of the objective function. Since this algorithm does not use any kind of derivative information of the objective function, it is suitable for problems that are not smooth or have a number of discontinuities and it tends to be very robust and efficient (Coleman *et al.*, 1999; González, 2001).

The Nelder-Mead algorithm is based on the definition of a non-degenerate[2] simplex. For an objective function of r optimization variables, this simplex consists of a geometric figure of non-zero volume which is the convex hull of $r+1$ vertices (Lagarias *et al.*, 1998). At each iteration of the optimization process, this algorithm removes the vertex with worst objective function value and replaces it with another vertex with a better value. The new vertex is obtained by reflecting, expanding or contracting the simplex along the line joining the worst vertex with the centroid of

[2] A simplex is non-degenerate if its vertices are not coplanar.

the remaining vertices. When it is not possible to find a better vertex in this way, then, only the vertex of the best objective function value is retained and the simplex is shrunk by moving all the other vertices toward this value (Nocedal and Wright, 2006).

For a given iteration k, the $r+1$ vertices v_1^k, …, v_{r+1}^k are ordered, such that (Nocedal and Wright, 2006)

$$S_{\text{obj}}(v_1^k) \leq S_{\text{obj}}(v_2^k) \leq \ldots \leq S_{\text{obj}}(v_{r+1}^k) \tag{3.7}$$

and the centroid of the best r^k vertices can be denoted by

$$\bar{v}^k = \sum_{i=1}^{r} v_i^k \ . \tag{3.8}$$

Since the goal is the minimization of the objective function, v_1^k corresponds to the best vertex while v_{r+1}^k is the worst one. Points along the line joining v_{r+1}^k and $\bar{v}^k$ are denoted by

$$\bar{v}(d) = \bar{v}^k + d(\bar{v}_{r+1}^k - \bar{v}^k) \,, \tag{3.9}$$

where d is a scalar.

Figure 3.1 illustrates the spatial approximation principle used by the Nelder-Mead algorithm by considering a two dimensional example. From this figure, the current simplex configuration defined by the three vertices as well as the possible replacement configurations, for instance, (i) reflection point $\bar{v}(-1)$, expansion point $\bar{v}(-2)$, inside contraction point $\bar{v}(1/2)$, outside contraction point $\bar{v}(-1/2)$ and shrunken simplex defined by the grey region. Note that the worst current vertex consists of v_3.

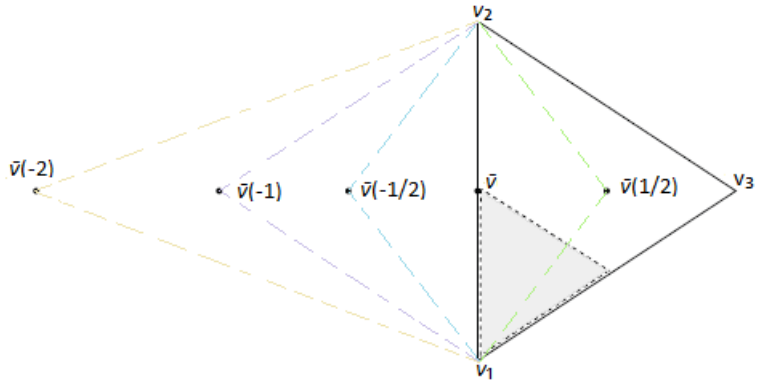

Figure 3.1 – Simplex (solid triangle with vertices v_1, v_2 and v_3) defined by the Nelder-Mead algorithm.

3.3 Conclusion

In this chapter, both types of optimization problems covered in this thesis, namely material parameters identification and shape optimization, were defined and discussed.

In fact, the shape optimization consists of the main purpose of the current work by the development of an innovative optimization methodology for the computational design of

heterogeneous mechanical tests. Alternatively, the material parameters identification problem appears due to the need of calibrating numerically the mechanical behavior of the DC04 mild steel in order to become the virtual material in the previous mentioned shape optimization problem.

In addition, the classic gradient-based L-M and the direct search Nelder-Mead optimization algorithms which are used, respectively, in the material parameters identification and shape optimization problems, were introduced. On the one side, the L-M algorithm was selected for the material parameters identification procedure due to its excellent relationship between efficiency and required computational time. On the other side, the Nelder-Mead algorithm was chosen for the shape optimization problem due to the fact that it is suitable for problems that are not smooth or have a number of discontinuities. It is the case of the optimization problem formulated for designing a heterogeneous mechanical test.

The following chapter deals with the mathematical formulation of the constitutive model chosen for reproducing the mechanical behavior of DC04 mild steel.

Chapter 4

Mechanical model up to rupture

4.1 Introduction

The constitutive model of the mechanical behavior of sheet metals is a decisive input of the FE simulations in order to obtain accurate numerical predictions. As a consequence, the quality of the constitutive model chosen for describing the material behavior plays a crucial role for the success of these predictions.

Therefore, with the aim of obtaining a reliable virtual material to be used on the optimization design of the heterogeneous mechanical test, a complex constitutive model involving anisotropy, evolution of hardening also including Bauschinger effect and macroscopic rupture must be considered for describing accurately the mechanical behavior of the DC04 mild steel.

Thus, in the current chapter, a brief review concerning the fundamental concepts that are used in the description of the macroscopic mechanical behavior of solids is presented. For instance, the main topics of the continuum mechanics theory of a material body as well as the constitutive modeling of phenomenological plasticity within the large strain framework are explained. Furthermore, the phenomenological constitutive models and macroscopic rupture criteria chosen to reproduce the mechanical behavior of DC04 mild steel are described.

4.2 Continuum mechanics

The continuum mechanics theory ignores inhomogeneities of the matter such as molecular, grain or crystal structures and thus, supposes that a material body is a continuum (Belytschko *et al.*, 2001). In this way, it considers that the material can be modeled by assuming that the matter is continuously distributed and fills the entire space region occupied by the material body. This assumption allows for the modeling of physical phenomena of the material body with high accurateness when length scales much greater than that of interatomic distances are taken into account.

In this context, the material body can be continually sub-divided into infinitesimal material particles over which the local heterogeneity of the stresses and strains are neglected and averaged quantities can be used. In this case, the effects of the heterogeneities act only indirectly through a certain number of internal variables (Chaboche, 2008).

Forming processes change the initial configuration of a material body by imposing a displacement field which results in large deformations. The deformation of the material body can be divided into several components: stretch, rigid body rotation and translation. The stretch implies the change in shape and/or size of the material body between the initial configuration and the current (deformed) configuration (Dunne and Petrinic, 2005).

Deformable bodies occupy regions in three dimensional Euclidean space **Ψ**, and a given body which consists of a continuous set of particles defined by the spatial points **P** will occupy different regions at different times. The subsets of **Ψ** occupied by a body **β** are defined as its configurations. The motion of a continuum body **β** is a continuous time sequence of mapping displacements **ρ** between the initial configuration and the current configuration. The domain of the body **β** in the initial configuration at time $t = 0$ is denoted by Ω_0 and usually coincides with the reference configuration. The reference configuration is the configuration where the geometry and physical state of the body **β** are known and other configurations of the body at different times can be characterized by comparing them with this one. Figure 4.1 exemplifies a general motion of a deformable body **β**.

The material body **β** can be seen as a continuous set of particles defined by the spatial points **P** that are labeled by the coordinates **X**, with respect to the Cartesian coordinate system, at their initial positions at time t=0.

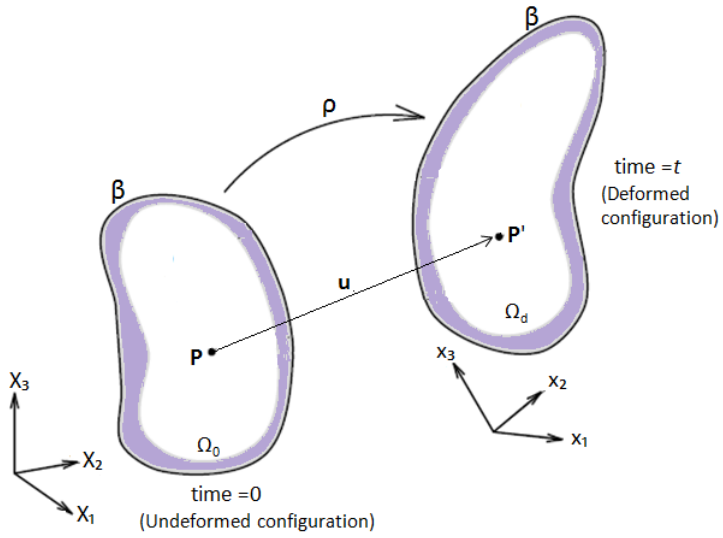

Figure 4.1 – General representation of a general motion of a deformable body **β**.

The motion **ρ** of a material particle can be expressed by two distinct formulations: Eulerian (or spatial) and Lagrangian (or material). In the Lagrangian description, the independent variables are the position **X** (material coordinates) at time $t = 0$ and the time t. The motion can be expressed as (Belytschko *et al.*, 2001; Banabic, 2010)

$$\boldsymbol{\rho} = \boldsymbol{\rho}(\mathbf{X}, t). \tag{4.1}$$

In the Eulerian description, the independent variables are the time *t* and the current position **x** (spatial coordinates) of the particle that occupied the point **X** at time *t*=0**.** This kind of description is focused in a given region in space instead of a certain particle of a continuum and can be described as (Belytschko *et al.*, 2001; Banabic, 2010)

$$\boldsymbol{\rho} = \boldsymbol{\rho}(\mathbf{x}, t). \tag{4.2}$$

The Eulerian or spatial description is largely used in fluid mechanics, because it is often impossible and unnecessary to describe the motion with respect to the reference configuration. Generally, in these problems the attention is focused on a certain region in space, which enables the analysis of a flow in a considered point (Banabic, 2010).

The Lagrangian description is more suitable for solid and structural mechanics due to the history-dependence. Indeed, the stresses generally depend on the history deformation and an undeformed (reference) configuration must be specified to define the strain (Belytschko *et al.*, 2001). In a FE context, the primary variables in the Lagrangian formulation are displacements, while in the Eulerian formulation they are velocities (Banabic, 2010).

Deformation gradient and strain measurement

The description and definition of deformation constitutes an essential part of nonlinear continuum mechanics. An important tensor in the finite deformation analysis is the deformation gradient **F** which can be defined by

$$\mathbf{F} = \frac{\partial \mathbf{x}}{\partial \mathbf{X}}. \tag{4.3}$$

Note that **F** transforms vectors in the reference configuration into vectors in the current configuration establishing a description of deformation components, for instance, rigid body movement and stretch. Therefore, it is common to express the deformation gradient as function of the displacement gradients. Considering that the displacement **u** can be obtained by (Dunne and Petrinic, 2005; Banabic, 2010)

$$\mathbf{x} = \mathbf{X} + \mathbf{u} \tag{4.4}$$

thus, the deformation gradient **F** can assume the form of (Banabic, 2010)

$$\mathbf{F} = \frac{\partial \mathbf{x}}{\partial \mathbf{X}} = \mathbf{I} + \frac{\partial \mathbf{u}}{\partial \mathbf{X}}, \tag{4.5}$$

where **I** is the second order identity tensor. The deformation gradient definition obtained by Equation 4.5 is particularly interesting for describing the Green-Lagrange strain tensor **E**, defined by (Banabic, 2010)

$$\mathbf{E} = \frac{1}{2}\left(\mathbf{F}^{\mathrm{T}}\mathbf{F} - \mathbf{I}\right). \tag{4.6}$$

It must be highlighted that many different measures of strain are used in nonlinear continuum mechanics, such as the Almansi, logarithmic or Green-Lagrange strain tensors.

Velocity gradient and rate of deformation

The velocity gradient, that describes the spatial rate of change of velocity **v**, is defined by (Dunne and Petrinic, 2005)

$$\mathbf{L} = \frac{\partial \mathbf{v}}{\partial \mathbf{x}} = \dot{\mathbf{F}}\mathbf{F}^{-1}. \tag{4.7}$$

The velocity gradient **L** can be decomposed into symmetric (stretch related) and skew-symmetric (rotation related) components as (Dunne and Petrinic, 2005; Banabic, 2010)

$$\mathbf{L} = \mathbf{d} + \mathbf{w}. \tag{4.8}$$

The symmetric component **d** is called as the rate of the deformation tensor and can be described by

$$\mathbf{d} = \frac{1}{2}\left(\mathbf{L} + \mathbf{L}^{\mathrm{T}}\right), \tag{4.9}$$

while the skew-symmetric component **w** is the continuum spin tensor and is formulated as

$$\mathbf{w} = \frac{1}{2}\left(\mathbf{L} - \mathbf{L}^{\mathrm{T}}\right). \tag{4.10}$$

4.3 Anisotropy and hardening modeling

The mechanical behavior of a material can be mathematically expressed by a constitutive formulation which gives the stress as a function of the deformation history of the body. Usually, it is modeled by two sets of constitutive equations, according to the elastic and plastic deformation. For metallic materials, the first set consists of a linear stress-strain relation governed by Hooke's law, where the deformation applied by a load is reversible and, consequently, the initial shape of the material is recovered. However, when the elastic limit or initial yield stress σ_0 is overcome, irreversible deformation begins and the material will be permanently deformed.

According to the plasticity theory, elastoplastic constitutive models can be based on the additive decomposition of the rate of deformation tensor **d**,

$$\mathbf{d} = \mathbf{d}^{\mathrm{e}} + \mathbf{d}^{\mathrm{p}}, \tag{4.11}$$

where $\mathbf{d}^{\mathrm{e}}$ and $\mathbf{d}^{\mathrm{p}}$ are the elastic and plastic parts of the rate of deformation tensor, respectively. From Equation 4.11, the stress dependency of the plastic deformation can be written as

$$\dot{\boldsymbol{\sigma}} = \mathbf{D} : (\mathbf{d} - \mathbf{d}^{p}), \tag{4.12}$$

where **D** is the elastoplastic modulus tensor. In the case of elasticity, the coefficients of **D** are determined by using the elastic Young modulus E and the Poisson coefficient υ and **D** is given by

$$\mathbf{D} = \frac{E}{(1+\upsilon)(1-2\upsilon)} \begin{bmatrix} (1-\upsilon) & \upsilon & \upsilon & 0 & 0 & 0 \\ \upsilon & (1-\upsilon) & \upsilon & 0 & 0 & 0 \\ \upsilon & \upsilon & (1-\upsilon) & 0 & 0 & 0 \\ 0 & 0 & 0 & \frac{(1-2\upsilon)}{2} & 0 & 0 \\ 0 & 0 & 0 & 0 & \frac{(1-2\upsilon)}{2} & 0 \\ 0 & 0 & 0 & 0 & 0 & \frac{(1-2\upsilon)}{2} \end{bmatrix}. \tag{4.13}$$

The transition from the elastic to plastic material behavior is determined by the yield surface. This surface defines the boundary between the elastic and plastic domains. Figure 4.2 illustrates the elliptical yield surface according to the von Mises criterion and shows the stress states in plane stress ($\sigma_3 = 0$) at which yielding occurs. The points located inside the yield surface correspond to the elastic stress levels, while the points belonging to the surface are related to the elastoplastic state. Points outside the surface have no physical meaning. In order to describe the yield surface, yield functions are adopted and these ones can be defined using two distinct approaches: micromechanical or phenomenological.

On the one hand, the micromechanical approach is based on the mechanism of plastic deformation, e.g. slip (and twinning) in metallic crystals, and on averaging procedures over a large number of grains. The crystallographic texture is the main input to this approach but other parameters, such as grain shape, can also be included. Usually, micromechanical models are very powerful to describe the mechanical behavior of materials (Banabic, 2007). However, these models are complex and often expensive in terms of computational effort. Detailed information concerning micromechanical models can be obtained, for instance, in Banabic *et al.* (2000b) and Habraken (2004).

On the other hand, the phenomenological approach corresponds to the macroscopic description of the mechanical behavior. In this approach, the internal variables of the material particle are directly associated with the dissipative behavior observed at the macroscopic level in terms of continuum quantities. By comparison with the micromechanical approach, the phenomenological one presents: (i) a simpler mathematical form, (ii) an easy implementation into FE codes, (iii) a better relationship between numerical simulation and computational calculation time and (iv) may present some poor accuracy under multiaxial and non-proportional loading conditions (Banabic, 2010).

The plastic behavior of metallic materials described by phenomenological models can be defined by three major concepts: the yield criterion, the associated flow rule and the hardening law. Note that though non-associated plasticity has regained recently some interest, only associated plasticity is considered in this work.

The yield criterion establishes the relationship between the stress components at the moment when plastic yielding occurs and is defined taking into account important macroscopic phenomena such as incompressibility condition and independency to the hydrostatic stress (Dunne and Petrinic, 2005). In addition, the yield surface described must be closed, smooth and convex (Banabic, 2010). Over the years, several anisotropic yield functions have been developed to characterize the planar anisotropy and stress directionality of the material. Hill (1948), Hosford (1979), Yld91 (Barlat *et al.*, 1991), Karafillis and Boyce (1993), BBC (Banabic *et al.*, 2000a), Bron and Besson (2004), *Yld*2004-*18p* (Barlat *et al.*, 2005), Vegter and van den Boogaard (2006) and, more recently, Yoshida *et al.* (2013) are some of the anisotropic yield functions presented in the literature. An extensive and comprehensive survey about yield functions can be found in Banabic *et al.* (2010).

Hill (1948), introduced a quadratic yield function which is a generalization of the von Mises isotropic criterion (von Mises, 1913) for anisotropic materials. Nowadays, this criterion is one of the most well-known anisotropic yield criteria and, due to its simplicity, remains as one of the most used in the description of the behavior of orthotropic metals, mainly steels. It presents a reduced number of material parameters which can be determined by uniaxial tensile tests at 0°, 45° and 90° to the RD. However, the reduced number of material parameters and experimental database constitutes a limitation to obtain an accurate reproduction of the mechanical behavior of advanced metal sheets. Indeed, this drawback of the Hill48 yield criterion can be shown by the four ears when using it in axisymmetric deep drawing processes whereas, in practice, different numbers of ears are observed (Banabic *et al.*, 2000b).

Comparatively to quadratic phenomenological models, constitutive models composed by a complex non-quadratic yield function are more suitable to accurately represent the material anisotropy of the sheet metal. In fact, non-quadratic yield functions, such as *Yld2004-18p* function, have been developed with the purpose of well describing the anisotropic behavior of metallic alloys with different crystallographic texture. These yield functions generally lead to a finer description of the plastic anisotropy. Nonetheless, these ones incorporate a large number of coefficients and, therefore, an increasing experimental database is required to determine the material parameters.

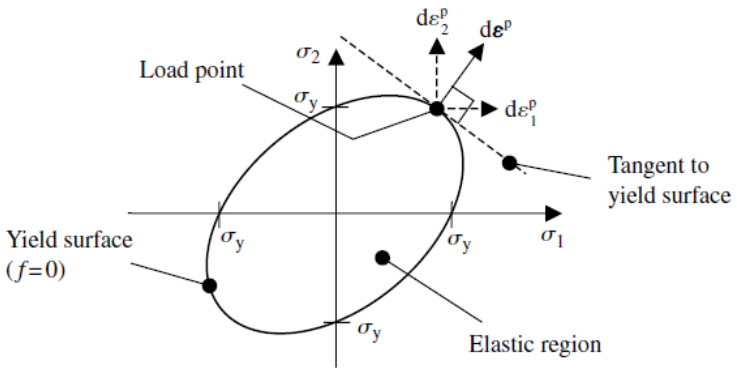

Figure 4.2 – Representation of the von Mises yield surface, in the major (σ_1) and minor (σ_2) stress in the sheet plane, showing the increment of plastic strain $d\boldsymbol{\varepsilon}^p$ in a normal direction to the tangent to the surface (Dunne and Petrinic, 2005).

The associated flow rule is responsible for establishing the relationship between the strain rate and stress tensors. In other words, the associated flow rule allows the determination of the evolution of the plastic deformation after the occurrence of plastic yielding. To do this, the normality condition of plasticity is considered stating that the increment of the plastic strain tensor is normal to the yield surface at the load point (Dunne and Petrinic, 2005), as depicted in Figure 4.2.

The hardening law describes the evolution of the yield surface during the deformation. The evolution of the yield surface can be a function of the accumulated plastic strain and may involve expansion, translation, rotation or distortion to which correspond isotropic, kinematic, rotational and distortional hardening, respectively. Usually, the combination of different hardening types is considered for a better description of the material behavior. Among such combinations, the most popular one that takes Bauschinger effect into account consists of considering simultaneously the isotropic and kinematic hardening behaviors. In the case of the isotropic hardening, the change of size of the yield surface is updated leading to a homothetic expansion. The isotropic hardening is mainly formulated by means of exponential or power laws. In the case of the kinematic hardening, the translation of the yield surface can be investigated by reverse loading, *cf*. chapter 2. Such a model aims at taking into account the Bauschinger effect, which is characterized by a lower yield stress under strain reversal, further transient behavior that corresponds to the smooth elastic-plastic transition with a rapid change of strain hardening rate, and for some materials a hardening stagnation, the magnitude of which depends on the pre-strain and eventually permanent softening characterized by a stress offset (Zang *et al.*, 2011). The kinematic hardening can be formulated by (i) single surface models, e.g. Prager-Ziegler, Armstrong-Frederick or Chaboche and (ii) multi- or bounding surface models, e.g. Mróz, Geng and Wagoner or Yoshida and Uemori (Cao *et al.*, 2009).

It is important to highlight that the hardening behavior of most metals is well modeled by combining isotropic and kinematic hardening formulation. On the one side, constitutive models only composed by isotropic hardening over-estimates the hardening component by missing the Bauschinger effect. On the other side, constitutive models with pure kinematic law under-estimates the hardening component and over-estimates the Bauschinger effect (Thuillier and Manach, 2008). As a result, with the purpose of predicting correctly both effects, it is highly recommended to adopt constitutive models with simultaneous contribution of isotropic and non-linear kinematic hardening behavior (Gau and Kinzel, 2001; Geng and Wagoner, 2002; Li *et al.*, 2002; Yoshida *et al.*, 2002; Gosling *et al.*, 2008; Cao *et al.*, 2009).

In the present work, a phenomenological model based on the framework of mixed isotropic-kinematic hardening is adopted. In this case, the yield condition F is defined by the generic form,

$$F(\boldsymbol{\sigma},\boldsymbol{\alpha},\bar{\varepsilon}^{\mathrm{p}}) = \overline{\eta}(\boldsymbol{\sigma}-\boldsymbol{\alpha}) - \sigma_{\mathrm{Y}}(\bar{\varepsilon}^{\mathrm{p}}) = 0, \tag{4.14}$$

where $\overline{\eta}$ is the equivalent stress which is a function of the tensor $\boldsymbol{\eta}$, defined by $\boldsymbol{\eta} = \boldsymbol{\sigma} - \boldsymbol{\alpha}$. Here, $\boldsymbol{\alpha}$ is a backstress tensor that describes the kinematic hardening, σ_{Y} is the yield stress related to the isotropic hardening and $\bar{\varepsilon}^{\mathrm{p}}$ is the equivalent plastic strain according to the conservation of plastic work.

The isotropic hardening, controlling the size of the yield surface is defined by an exponential law written as (Simo, 1988)

$$\sigma_Y(\bar{\varepsilon}^p) = \sigma_0 + (\sigma_\infty - \sigma_0).\left[1 - \exp(-\delta.\bar{\varepsilon}^p)\right] + \beta.\bar{\varepsilon}^p, \tag{4.15}$$

where σ_0, σ_∞, δ and β are material parameters.

The kinematic hardening law is based on the additive contribution of several backstress components such as proposed by Chaboche and Rousselier (1983). This formulation defines the evolution of the backstress tensor as

$$\dot{\boldsymbol{\alpha}} = \sum_{i=1}^{3} \dot{\boldsymbol{\alpha}}_i = \sum_{i=1}^{3} \left(\frac{C_i}{\bar{\eta}} \boldsymbol{\eta} - \gamma_i . \boldsymbol{\alpha}_i \right) \dot{\bar{\varepsilon}}^p, \tag{4.16}$$

where C_i and γ_i, with i = 1,…, 3, are material parameters related to the kinematic hardening behavior, $\boldsymbol{\alpha}_i$ are the backstress components and $\dot{\bar{\varepsilon}}^p$ is the equivalent plastic strain rate. Comparing with a kinematic hardening model composed by only one backstress component, this expression allows for a more extensive strain domain and a better description of the soft transition between elasticity and the onset of plastic flow (Chaboche, 2008). However, this kinematic formulation is not able to perform an accurate description of the work hardening stagnation observed after cyclic loading (Zang *et al.*, 2011).

The associated flow rule determines the plastic strain increment, e.g. presented in Yoon *et al.* (2006), as

$$\dot{\boldsymbol{\varepsilon}}^p = \dot{\lambda} \frac{\partial \bar{\eta}}{\partial \boldsymbol{\eta}}, \tag{4.17}$$

where λ is the plastic multiplier. From the work-equivalent principle for incremental deformation theory it can be stated that $\dot{\bar{\varepsilon}}^p = \dot{\lambda}$ (Chung *et al.*, 2005; Yoon *et al.*, 2006). The determination of the plastic multiplier is based on the consistency condition. This condition implies that during plastic loading the stress point remains on the yield surface (Dunne and Petrinic, 2005).

The present work accounts for the advanced non-quadratic *Yld2004-18p* anisotropic yield criterion (Barlat *et al.*, 2005). This criterion is defined by

$$\bar{\eta}(\boldsymbol{\eta})^a = \sum_{i=1,j=1}^{3} \left| \tilde{\mathbf{S}}_i^{(1)} - \tilde{\mathbf{S}}_j^{(2)} \right|^a = 4\sigma_Y{}^a, \tag{4.18}$$

where a is the yield criterion exponent. In this equation, $\tilde{\mathbf{S}}_i^{(k)}$, k=1, 2 and i,j = 1 ,…, 3, are the eigenvalues of the tensors $\tilde{\mathbf{S}}^{(k)}$ and are given by a similar linear transformation of $\mathbf{S}$, the deviatoric part of the tensor $\boldsymbol{\eta}$,

$$\tilde{\mathbf{S}}^{(k)} = \tilde{\mathbf{L}}^{(k)} : \mathbf{S}, \quad k = 1,\ 2, \tag{4.19}$$

where $\tilde{\mathbf{L}}^{(k)}$ are given by

$$\tilde{\mathbf{L}}^{(k)} = \begin{bmatrix} 0 & -c_{12}^{(k)} & -c_{13}^{(k)} & 0 & 0 & 0 \\ -c_{21}^{(k)} & 0 & -c_{23}^{(1)} & 0 & 0 & 0 \\ -c_{31}^{(k)} & -c_{32}^{(k)} & 0 & 0 & 0 & 0 \\ 0 & 0 & 0 & c_{44}^{(k)} & 0 & 0 \\ 0 & 0 & 0 & 0 & c_{55}^{(k)} & 0 \\ 0 & 0 & 0 & 0 & 0 & c_{66}^{(k)} \end{bmatrix}, \quad k = 1,\ 2\,, \tag{4.20}$$

using the Voigt notation. The two linear transformations provide 18 anisotropic coefficients for a general three-dimensional stress state.

When all coefficients are equal to one, the *Yld2004-18p* anisotropic yield criterion is reduced to Hershey's isotropic yield criterion, proposed to reproduce the yield surface calculated with a self-consistent polycrystal model (Barlat *et al.*, 2005). It must be mentioned that these coefficients have no real physical meaning. Additionally, the exponent *a* of the yield criterion depends on the material crystallographic texture and can be adjusted in function of the material structure type.

Based on polycrystal theories and experimental results it was verified that quadratic yield criteria are not able to perform reliable yield surface descriptions of some metallic materials of cubic structure, namely, body-centered cubic (bcc) and face-centered cubic (fcc) materials. For this reason, non-quadratic yield criteria are more flexible for the mechanical behavior description of most metallic materials. Logan and Hosford (1980) showed that the most indicated values for the exponent of non-quadratic yield criteria are 6 and 8 in order to reproduce the mechanical behavior of bcc and fcc materials, respectively.

According to Barlat *et al.* (2005), the coefficients of *Yld2004-18p* can be identified from tensile tests at every 15° to the RD, biaxial test, disk compression test and four more additional data characterizing the out-of-plane properties. The out-of-plane experiments referred by the authors are needed for characterizing the crystallographic texture of the material. However, when these out-of-plane tests cannot be carried out and texture or any other microstructural information is not available, it is recommended to assume the out-of-plane properties equal to the isotropic values. In this case, the coefficients $c_{44}^{(k)}$ and $c_{55}^{(k)}$ with k=1, 2 must be considered equal to one.

The anisotropic *Yld2004-18p* yield criterion was chosen in this work due to the fact that, as a non-quadratic yield function, it is more suitable to accurately represent the material anisotropy of the sheet metal. This yield criterion involves a large number of coefficients, which gives a high flexibility to adjust the yield surface to the experimental data. Indeed, the use of a high number of coefficients directly leads to an excellent prediction of the mechanical behavior of highly anisotropic metals, such as AA2090-T3 aluminum alloy (Yoon *et al.*, 2006). This model has also proved its capability to provide an accurate prediction of the planar variations of the uniaxial yield stresses and plastic anisotropy coefficients as well as to predict the occurrence of six and eight ears in the process of cup drawing (Barlat *et al.*, 2005; Banabic, 2010).

Although the large flexibility and accuracy on the description of the yield surface, the Yld2004-18p anisotropic yield criterion assumes much more complexity than other criteria, such as Hill48, *Yld*91, etc., mainly due to the large number of material parameters which must be

identified. As a consequence, a large number of experimental tests for an appropriate material identification procedure is required.

In the present work, the anisotropic plastic behavior of a DC04 mild steel is characterized using two phenomenological constitutive models. Both ones are composed by the non-quadratic *Yld2004-18p* anisotropic yield criterion combined (i) with an isotropic hardening model defined by Equation 4.15, and (ii) with a mixed isotropic-nonlinear kinematic hardening model, defined by Equations 4.15 and 4.16. These are denominated as '*Yld2004-Iso*' and '*Yld2004-Mixed*' models, respectively.

Though *Yld2004-Iso* model does not take into account the Bauschinger effect, it was considered with the purpose of adjusting the material parameters identification process since it needs a smaller number of parameters to be identified, comparatively to *Yld2004-Mixed* model.

4.4 Macroscopic rupture criteria

The study of the rupture assumes great importance in forming industry, especially in automotive industry, due to the necessity of performing crash simulations and also predicting energy absorption of the materials. Thus, fracture ductility is also a relevant phenomenon, insofar consists of the ability of a material to reach high amount of deformation without rupture. In this work, the rupture has to be predicted, in order to validate the maximum strain level reached during the design of a new experiment. The rupture behavior can be analyzed considering two different approaches: (i) uncoupled fracture criteria, which neglect the effects of damage on the yield surface of materials and (ii) coupled fracture criteria, which consists in ductile damage models coupled with plasticity (Li *et al.*, 2011).

The coupled fracture criteria incorporate the damage accumulation and allow the modification of the yield surface by damage-induced density change (Li *et al.*, 2011). The degradation of the mechanical properties is taken into account in the constitutive equations up to the final rupture. These criteria are usually based on micromechanical phenomena of initiation and growth of voids followed by coalescence. The coupled fracture criteria tend to give a more reliable description of the fracture behavior than the uncoupled fracture criteria. However, these coupled criteria are usually complex and difficult to implement into FE codes. Gurson-Tvergaard-Needleman (GTN) and continuum damage mechanics (CDM) models are examples of coupled fracture criteria. An extensive description about this kind of fracture criteria can be found in Besson (2010).

The uncoupled fracture criteria are formulated considering an empirical or semi-empirical rupture parameter based on some macroscopic variables such as, the equivalent plastic strain, principal and hydrostatic stresses and more recently the Lode angle, since these variables are the most relevant to fracture initiation and propagation (Li *et al.*, 2011). Several uncoupled fracture criteria have been proposed, for instance, Cockroft and Latham (1968), Brozzo *et al.* (1972), Rice and Tracey (1969), Oyane *et al.* (1990), Xue-Wierzbicki (Wierzbicki *et al.*, 2005). Although there is a limitation of not representing the deterioration of the mechanical properties related to damage, these fracture criteria are widely adopted due to their easy implementation into FE codes and easy calibration (Wierzbicki *et al.*, 2005).

In this work, the rupture behavior of a DC04 mild steel is evaluated considering both Cockroft and Latham (CL) and Rice and Tracey (RT) uncoupled fracture criteria. The definition of CL criterion is taken as the one given in (Li *et al.*, 2011)

$$W_{\mathrm{CL}} = \int_0^{\bar{\varepsilon}_{\mathrm{f}}^{\mathrm{p}}} \frac{\sigma_I}{\bar{\eta}} \mathrm{d}\bar{\varepsilon}^{\mathrm{p}} \leq W_{\mathrm{CL}}^{\mathrm{f}} \ , \tag{4.21}$$

where σ_{I} is the maximum principal stress. Fracture is expected to occur when the rupture parameter W_{CL} reaches the critical value $W_{\mathrm{CL}}^{\mathrm{f}}$, leading to the determination of the equivalent plastic strain at rupture $\bar{\varepsilon}_{\mathrm{f}}^{\mathrm{p}}$. The RT criterion is described by (Li *et al.*, 2011)

$$W_{\mathrm{RT}} = \int_0^{\bar{\varepsilon}_{\mathrm{f}}^{\mathrm{p}}} \exp\left(\frac{3\sigma_{\mathrm{H}}}{2\bar{\eta}}\right) \mathrm{d}\bar{\varepsilon}^{\mathrm{p}} \leq W_{\mathrm{RT}}^{\mathrm{f}} \ , \tag{4.22}$$

where σ_{H} is the hydrostatic stress and the critical parameter is defined as $W_{\mathrm{RT}}^{\mathrm{f}}$.

Both CL and RT fracture criteria were adopted in this work due to their simple calibration which can be obtained from a single test. Moreover, CL fracture criterion was chosen because it is a widely used macroscopic rupture criterion (Zhalehfar *et al.*, 2013; Björklund *et al.*, 2014). Alternatively, RT criterion was selected since it takes into account the stress triaxiality ratio ($\sigma_{\mathrm{H}}/\bar{\eta}$) in its formulation and the stress triaxiality is, besides the strain intensity, the most important factor that controls initiation of ductile fracture, e.g. Bao and Wierzbicki (2004).

The calibration of the uncoupled fracture criterion parameters is generally performed comparing experiments leading to rupture, such as the tensile test, with FE simulation. Takuda *et al.* (1999) applied the combination of uncoupled ductile fracture criteria with FE simulation in order to predict the fracture initiation and, consequently forming limits. The predictions were performed for deep drawing experiment and accurate results were obtained by the authors. Ozturk and Lee (2004) presented a complete determination of forming limit diagram (FLD) by using several uncoupled fracture criteria. For this purpose, tensile tests up to rupture and numerical simulation were used by the authors in order to calibrate the fracture criterion parameters. Zhalehfar *et al.* (2013) predicted the effect of strain path change on the FLD at rupture by using a numerical approach and the uncoupled CL fracture criterion. Björklund *et al.* (2013) also adopted the uncoupled CL criterion and performed a comparison between experimental results coming from simple mechanical tests and FE simulations, to calibrate the criterion. Tarigopula *et al.* (2008) used DIC technique on shear test up to rupture and calibrated the parameter of the CL fracture criterion through FE simulation. In addition, Wierzbicki *et al.* (2005) presented the calibration and evaluation of several uncoupled fracture criteria by using numerical simulation.

4.5 Conclusion

In this chapter, some mathematical concepts of the continuum mechanics, which constitute the foundation of the constitutive models used in FE simulation, and the phenomenological constitutive models adopted in this study were presented. Both phenomenological models chosen

for representing the anisotropic plastic behavior of a DC04 mild steel consist of the *Yld2004-18p* anisotropic yield criterion combined with either an isotropic hardening law (*Yld2004-Iso*) or a mixed isotropic-nonlinear kinematic hardening law (*Yld2004-Mixed*).

In addition, two different uncoupled fracture criteria namely, Cockroft and Latham (CL) and Rice and Tracey (RT), were adopted in order to calibrate the macroscopic rupture behavior of the mild steel. The main purpose of using a fracture criterion is to validate the heterogeneous mechanical test further developed in chapter 8. Such criterion will be the end condition to stop the numerical optimization approach used on the design of the heterogeneous mechanical test.

III – Mechanical characterization of mild steel

Chapter 5

Material parameters identification and rupture

5.1 Introduction

The accurate description of the mechanical behavior of a DC04 mild steel involves considering deformation up to large strains including rupture. Therefore, an efficient procedure that leads to a complete mechanical characterization of the sheet metal behavior, including anisotropy, evolution of hardening and rupture, is proposed in this chapter.

The focus of the global procedure presented here is to identify the anisotropic and hardening material parameters of both *Yld2004-Iso* and *Yld2004-Mixed* phenomenological models and also to calibrate the macroscopic rupture behavior of a DC04 mild steel by considering both RT and CL fracture criteria. To do this, an inverse methodology for material parameters identification was developed based on FEMU and several classical tests considered as homogeneous were used in the experimental database. Furthemore, a mixed experimental-numerical approach to calibrate the fracture criteria was performed. Such approach consisted in the comparison of the experimental strain distribution, obtained by DIC technique, of a tensile test carried out up to rupture with the numerical results obtained by FE simulation.

5.2 Parameters identification process

5.2.1 General structure

Since a FEMU technique was adopted for identifying the material parameters of the phenomenological modes, the parameters identification process was performed using a combination of the FE code ABAQUS (Abaqus, 2009) and the optimization software code SdL[3] (Andrade-Campos, 2011). While ABAQUS is responsible for the numerical simulations of the

[3] SdL is a non-commercial optimization software designed for material parameters identification and engineering shape optimization problems. It is currently developed at Limatb (University of Bretagne-Sud) and Grids (University of Aveiro) research groups.

classical tests, SdL updates the material parameters at each evaluation of the identification process with the purpose of minimizing the objective function and, eventually, stops the optimization. The communication between these two programs was ensured by a FORTRAN interface which compares the experimental and numerical results and writes the updated parameters on the ABAQUS input file after each evaluation. Figure 5.1 depicts the flow diagram of the identification process implemented.

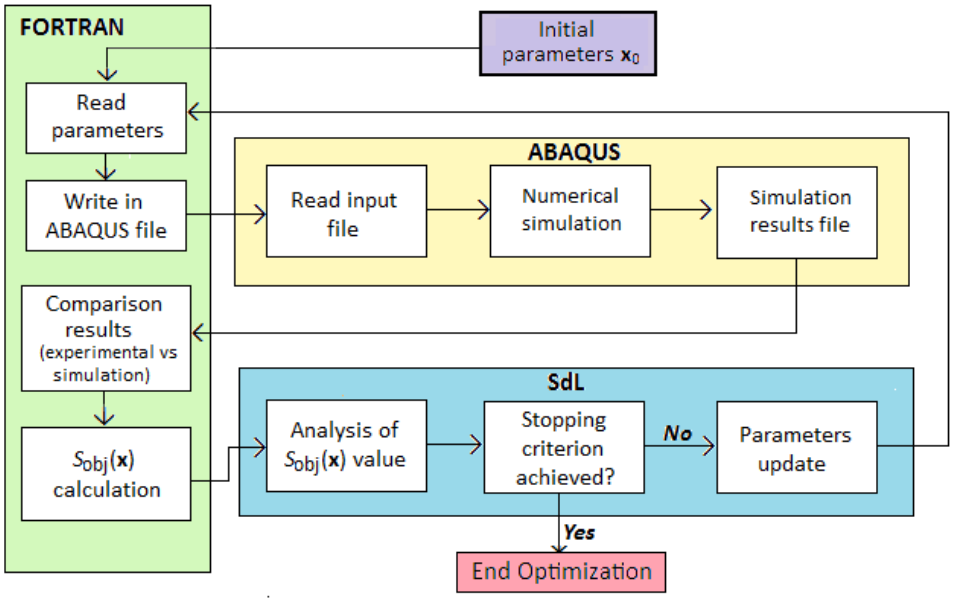

Figure 5.1 – Scheme of the parameters identification process developed.

DC04 mild steel used in this work presents a thickness e = 0.7 mm and its mechanical behavior was characterized by Le Port (2012) and Zang *et al.* (2011) under different stress and strain states. The experiments carried out consisted of: (i) uniaxial tensile and simple shear tests at 0°, 22°, 45°, 77° and 90° to the RD; (ii) hydraulic bulge test and (iii) three shear-Bauschinger tests in the RD, consisting of unloading and reloading in the reverse direction after a pre-strain of 0.13, 0.21 and 0.33. The stress levels in uniaxial tension are quite close whatever the orientation, except at 45°/RD, where it is lower than the others. Concerning the plastic anisotropy coefficients, the minimum value, equal to 1.68, was measured at 0°/RD and it then increases when the angle between the tensile direction and RD also increases, up to 2.25 at 90°/RD. It leads to an average coefficient, characterizing the normal anisotropy, of 1.93 and a planar anisotropy characterized by a coefficient of 0.08. Concerning bulge test, the evolution during the test of the two strain components, in the RD and TD, were measured by DIC technique, and these two values are very close, with a relative gap lower than 5% (Zang *et al.*, 2011).

The experimental database used in the identification process was composed by the stress-logarithmic strain curves (σ-ε) in uniaxial and biaxial tension, shear stress-strain curves (τ-γ) in simple shear and transverse strain-longitudinal strain curves (ε_{11}-ε_{22}) for the several uniaxial tensile tests and bulge test.

All experiments were used in the material parameters identification of the *Yld2004-Mixed* model. Whereas, in the material parameters identification of the *Yld2004-Iso* model, shear-

Bauschinger tests were not considered due to the fact that this model does not account for the kinematic hardening.

5.2.2 Objective function

According to the experimental database available and the definition of an objective function for a test *n* (introduced in Equation 2.1), the experiments were divided into 4 main groups and the global objective function was defined as

$$S_{\text{obj}}(\mathbf{x}) = \sum_{\alpha} S_{\text{obj}}^{\text{TU-S}}(\mathbf{x}) + \sum_{\alpha} S_{\text{obj}}^{\text{TU-E}}(\mathbf{x}) + \sum_{\alpha,Baus} S_{\text{obj}}^{\text{Shear-S}}(\mathbf{x}) + S_{\text{obj}}^{\text{BT-S}}(\mathbf{x}). \tag{5.1}$$

Superscript 'TU-S' stands for the stress level in tension, 'TU-E' for the width strain in tension, 'Shear-S' for the stress level in simple shear and finally 'BT-S' stands for the stress level in bulge test. The sums over α gathers for all tests at a given orientation α to RD and Bauschinger tests in simple shear where also accounted for (subscript '*Baus*'). These 4 main groups were defined in order to apply a same normalized weighting factor W_{abs}^{h} for each one of the experiments belonging to the group, instead of attributing an individual weighting factor for each test *n* as suggested in Equation 2.1. In this way, for each group *h*, the parameter W_{abs}^{h} was calculated according to the following equation,

$$W_{abs}^{h} = \frac{\max\left((Z_{\max}^{\exp})^{n}, n = 1,\ldots,n_t^h\right)}{\sum_{i=1}^{n_{\text{h}}} \max\left((Z_{\max}^{\exp})^{n}, n = 1,\ldots,n_t^h\right) \times n_t^h}, \tag{5.2}$$

where n_t^h is the number of tests belonging to the same group *h*, n_{h} is the number of groups (equal to 4 in this work) and $(Z_{\max}^{\exp})^{n}$ is the maximum output data from each experiment for a given test *n* of a group *h*. The different W_{abs}^{h} values used for both *Yld2004-Iso* and *Yld2004-Mixed* models are given in Table 5.1. The sum of W_{abs}^{h}, with k=1, …, 4 is equal to 1 to normalize the objective function values obtained by each group of experiments.

Table 5.1 - Number of tests and W_{abs} values of each group for both constitutive models.

	TU-S	Shear-S	BT-S	TU-E	
W_{abs}	$1.05\text{x}10^{-1}$	$5.95\text{x}10^{-2}$	$1.75\text{x}10^{-1}$	$7.78\text{x}10^{-5}$	*Yld2004-Iso*
n_{t}	5	5	1	6	
W_{abs}	$8.93\text{x}10^{-2}$	$5.05\text{x}10^{-2}$	$1.48\text{x}10^{-1}$	$6.60\text{x}10^{-5}$	*Yld2004-Mixed*
n_{t}	5	8	1	6	

5.2.3 Numerical simulation of the tests

Concerning the numerical modeling of the material behavior, the phenomenological formulation of *Yld2004-18p* yield criterion with the Armstrong-Frederick kinematic hardening model,

composed by one backstress tensor, was implemented by Grilo *et al.* (2013c) in a user-defined material subroutine UMAT of the FE code ABAQUS (Abaqus, 2009). Nevertheless, this phenomenological model is not the most suitable one to perform a better numerical description of DC04 kinematic hardening. Thereby, the kinematic hardening formulation was modified in the UMAT subroutine adopting the kinematic hardening model proposed by Chaboche and Rousselier (1983) which is defined by Equation 4.16. The implementation of this kinematic hardening model in a UMAT subroutine as well as its validation was detailed in appendix A.

Note that the implemented kinematic hardening model is composed by the additive contribution of a set of three Armstrong-Frederick terms leading to a hardening law defined by three backstress tensors. As a consequence, it leads to an improved description of the Bauschinger effect and more flexibility since it can be reduced to the previous hardening formulation using only one backstress tensor. In Figure 5.2, the hardening evolution ($\boldsymbol{\alpha}_T$) described by the kinematic hardening model proposed by Chaboche and Rousselier (1983) with three Armstrong-Frederick hardening terms ($\boldsymbol{\alpha}_1$, $\boldsymbol{\alpha}_2$ and $\boldsymbol{\alpha}_3$) is illustrated. This figure shows the advantage of using a kinematic formulation based on multiple individual backstress tensors, because the additive contribution of each backstress allows a more complex Bauschinger modeling.

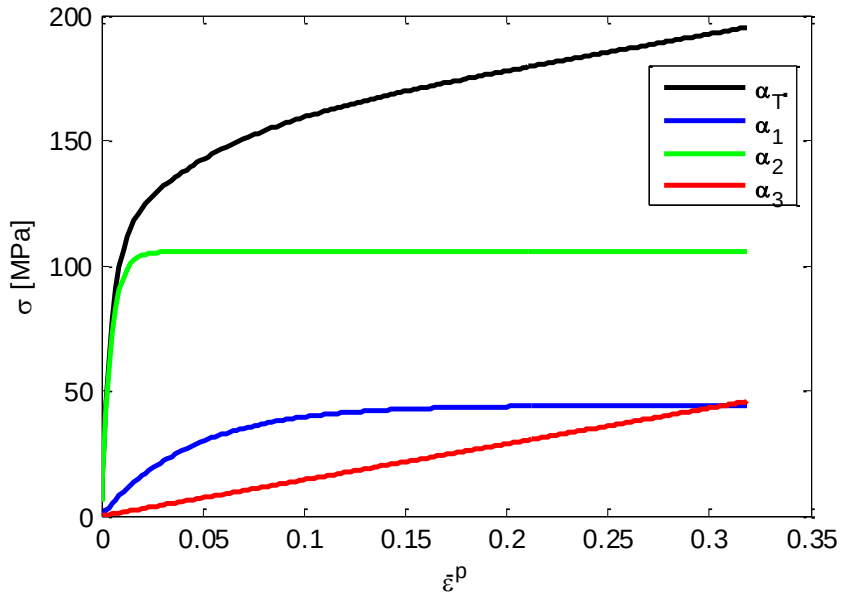

Figure 5.2 – Evolution of the individual backstress tensors ($\boldsymbol{\alpha}_1$, $\boldsymbol{\alpha}_2$ and $\boldsymbol{\alpha}_3$) that compose the kinematic hardening formulation ($\boldsymbol{\alpha}_T=\boldsymbol{\alpha}_1+\boldsymbol{\alpha}_2+\boldsymbol{\alpha}_3$) implemented in this work. Kinematic hardening described by the identified material parameters listed in Table 5.2.

Concerning the numerical modeling of the tests, tridimensional models with one single 8 node element with linear interpolation and reduced integration (C3D8R) were used to reproduce these experiments. Boundary conditions were applied in order to obtain a homogeneous stress and strain states over the element, in the uniaxial tension and simple shear. In the case of biaxial tension, to save calculation time, only the central area of the bulge specimen was considered and an equibiaxial strain state was imposed on the element. Figure 5.3 illustrates the boundary conditions applied for the numerical simulations.

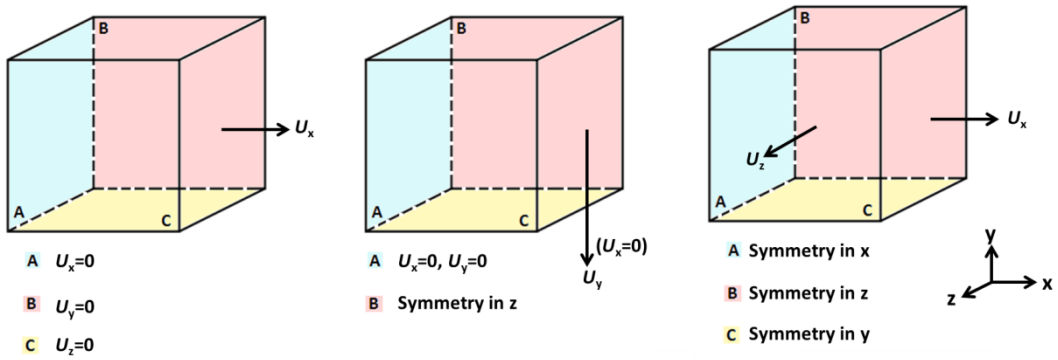

a) Tensile test b) Shear test c) Biaxial strain

Figure 5.3 – Boundary conditions applied on the numerical model of each test. *U* stands for displacement.

It must be pointed out that, for simple shear and uniaxial tension, the definition of 1-element model is justified by the homogeneous strain distribution verified during the experiment. In the case of bulge test, the simplification is only valid if the 1-element model reproduces the same conditions experimentally verified in the center of the bulge specimen, as shown in appendix B.

According to the membrane theory for hydraulic bulging, defined by Equation 2.15, and considering the axisymmetric case of the bulge test and material isotropy, the longitudinal and transverse stress components σ_{11} and σ_{22} must be similar. Thus, based on Equation 2.16, a single stress component was calculated from the experimental pressure, using the radius of curvature of a small area centered at the specimen apex.

The numerical simulation of the bulge test was carried out applying a same displacement in both 1 and 3 direction, as shown in Figure 5.3 c). This situation leads to the same numerical strain components ε_{11} and ε_{22} during the test. Such an assumption was justified by the fact that, experimentally, the evolution during the bulge test of the two strain components leads to a very close equibiaxial strain state. This assumption was checked by comparing the 1-element simplified model with 3D model of hydraulic bulging, as detailed in appendix B.

5.2.4 Process parameters

Some conditions related to the optimization process of material parameters identification must be defined. For instance, the stopping criterion to end the optimization process consisted of a stagnation value of 10^{-7}, in terms of the objective function value between two consecutive evaluations. The Jacobian (partial derivatives) of the objective function was calculated numerically through a forward finite difference scheme with a perturbation value of $5.0\text{x}10^{-3}$. Additionally, the L-M algorithm was used with a maximum number of evaluations limited to 500.

In the parameters identification framework, some material parameters were considered constant like the elastic parameters *E* and υ, the exponent *a* as well as the anisotropic coefficients $c_{44}^{(k)}$ and $c_{55}^{(k)}$, with $k=1,2$ of the *Yld2004-18p* yield function. As previously referred in section 4.3, these four anisotropic coefficients of the yield function are related to out-of-plane properties of

the sheet material and, as the experimental database available does not allow the identification of this kind of properties, these ones were assumed constants and equal to 1 (isotropic value). The exponent *a* was considered equal to 6 since DC04 mild steel is a bcc material and this exponent value is the more appropriate for this material crystallographic structure. In the case of the elastic properties of DC04 mild steel, the constant values of *E*=176 GPa (calculated from tensile tests) and *υ*=0.29 were considered.

It was also considered that the initial stress of the isotropic hardening law ($\sigma_Y(0)$), *cf*. Equation 4.15, must be equal to the initial yield stress σ_0 in uniaxial tension at the RD. Therefore, based on the uniaxial tension state at the RD, $\boldsymbol{\sigma} = \left[\sigma_{xx} \quad 0 \quad 0 \quad 0 \quad 0 \quad 0\right]$, and Equations 4.18-4.20 the following condition was also taken into account in the identification process,

$$\frac{\sigma_{xx}}{\sigma_Y(0)} = \left(\frac{4}{\varphi}\right)^{\frac{1}{a}} = 1\,, \tag{5.3}$$

where φ is defined by

$$\begin{aligned}\varphi = &\left|\frac{1}{3}\left(c_{12}^1 + c_{13}^1 - c_{12}^2 - c_{13}^2\right)\right|^a + \left|\frac{1}{3}\left(c_{12}^1 + c_{13}^1 + 2c_{21}^2 - c_{23}^2\right)\right|^a + \left|\frac{1}{3}\left(c_{12}^1 + c_{13}^1 + 2c_{31}^2 - c_{32}^2\right)\right|^a + \\ &\left|\frac{1}{3}\left(-2c_{21}^1 - c_{23}^1 - c_{12}^2 - c_{13}^2\right)\right|^a + \left|\frac{1}{3}\left(-2c_{21}^1 + c_{23}^1 + 2c_{21}^2 - c_{23}^2\right)\right|^a + \left|\frac{1}{3}\left(-2c_{21}^1 + c_{23}^1 + 2c_{31}^2 - c_{32}^2\right)\right|^a + \\ &\left|\frac{1}{3}\left(-2c_{31}^1 + c_{32}^1 - c_{12}^2 - c_{13}^2\right)\right|^a + \left|\frac{1}{3}\left(-2c_{31}^1 + c_{32}^1 + 2c_{21}^2 - c_{23}^2\right)\right|^a + \left|\frac{1}{3}\left(-2c_{31}^1 + c_{32}^1 + 2c_{31}^2 - c_{32}^2\right)\right|^a .\end{aligned} \tag{5.4}$$

5.3 Numerical results

In this section, the identified material parameters that characterize the mechanical behavior of DC04 mild steel considering both *Yld2004-Iso* and *Yld2004-Mixed* phenomenological models are presented.

Table 5.2 shows the initial and the optimal identified parameters, the respective initial and final values of the objective function and the number of evaluations carried out by both identification procedures. The anisotropy coefficients to determine are 14 whereas the hardening parameters are 10 for *Yld2004-Mixed* model and 4 for *Yld2004-Iso* model. Then, the total number of parameters to identify is 24 and 18, respectively.

The initial values for the anisotropy coefficients were chosen equal to 1 in order to start the identification process from material isotropy, describing the Hershey isotropic yield surface. From values found in the literature using the same yield criterion for several sheet metals, it came that the coefficients $c_{ij}^{(k)}$ where *i*, *j* = 1, 2, 3 and *k*= 1, 2 all found lying within the range [-2.2, 2.2]. The initial value for σ_0 was defined from the initial yield stress in uniaxial tension at the RD and the initial σ_∞ and δ values came from an estimation from the tensile stress-strain curve in the RD considering isotropic hardening. The lower bound of 100 MPa was set to prevent the L-M optimization algorithm to decrease drastically the initial yield stress, in order to compensate the contribution coming from the kinematic hardening (*Yld2004-Mixed* model), in particular the rapidly saturating term $Xsat_2$ (Carbonnière *et al.*, 2009). This lower bound value seemed

acceptable from a physical point of view. Concerning the parameters for the kinematic contribution of *Yld2004-Mixed* model, $Xsat_i$ and γ_i, with $i = 1, 2, 3$, these ones were chosen in order to ensure three saturating rates very different, without any overlapping. Indeed the following relation $\gamma_3 < \gamma_1 < \gamma_2$ was always satisfied regarding the upper and lower bounds. The initial guesses for these parameters were chosen approximately in the middle of the range. Note that the ratio C_i/γ_i, with $i = 1, 2, 3$ was optimized because it corresponds to the saturating value (*Xsat*) and therefore setting bounds for it was easier.

Table 5.2 - Material parameters identified for DC04 mild steel.

	Yld2004-Iso		*Yld2004-Mixed*			
Parameters	Initial	Optimal	Initial	Optimal	Limits	Units
$c_{12}^{(1)}$	1.0	1.114	1.0	1.264	-2.2 / 2.2	-
$c_{13}^{(1)}$	1.0	1.019	1.0	0.974	-2.2 /2.2	-
$c_{21}^{(1)}$	1.0	1.228	1.0	1.242	-2.2 / 2.2	-
$c_{23}^{(1)}$	1.0	0.664	1.0	1.049	-2.2 /2.2	-
$c_{31}^{(1)}$	1.0	0.319	1.0	0.579	-2.2 / 2.2	-
$c_{32}^{(1)}$	1.0	0.913	1.0	0.708	-2.2 /2.2	-
$c_{66}^{(1)}$	1.0	1.476	1.0	1.365	-2.2 / 2.2	-
$c_{12}^{(2)}$	1.0	0.989	1.0	0.792	-2.2 /2.2	-
$c_{13}^{(2)}$	1.0	0.458	1.0	0.672	-2.2 / 2.2	-
$c_{21}^{(2)}$	1.0	0.613	1.0	0.838	-2.2 /2.2	-
$c_{23}^{(2)}$	1.0	0.964	1.0	0.929	-2.2 / 2.2	-
$c_{31}^{(2)}$	1.0	0.959	1.0	0.996	-2.2 /2.2	-
$c_{32}^{(2)}$	1.0	0.656	1.0	0.768	-2.2 /2.2	-
$c_{66}^{(2)}$	1.0	0.509	1.0	0.678	-2.2 /2.2	-
σ_0	128.0	164.0	141.2	100.0	100.0 / 170.0	MPa
σ_∞	250.0	332.7	261.0	210.3	160.0 / 800.0	MPa
δ	10.5	14.07	10.5	5.92	1.0 / 100.0	-
β	150.0	259.9	160.0	102.8	100.0 / 900.0	MPa
$Xsat_1$	-	-	25.0	44.57	5.0 / 50.0	MPa
γ_1	-	-	90.0	22.85	10.0 / 150.0	-
$Xsat_2$	-	-	100.0	106.2	70.0 / 300.0	MPa
γ_2	-	-	300.0	258.38	500 / 1200	-
$Xsat_3$	-	-	5000	5629.7	2500 / 7500	MPa
γ_3	-	-	0.02	0.0258	0.001 / 4.0	-
$S_{obj}(\mathbf{x})$	1.04×10^7	6.67×10^4 (-99.4%)	8.14×10^6	1.05×10^6 (-87.1%)		-
Evaluations		416		500		-

Generally speaking, using a gradient-based algorithm makes the solution dependent on the initial guess of parameters. Local minimums can be reached, which may depend on the initial

parameter set. Therefore, after finding a set leading to a good description of all the tests in the database, several initial guesses were tried for both models, in order to investigate the robustness of these solutions and the algorithm converged each time toward almost the same solutions, presented in Table 5.2.

Comparing the initial and final objective function values, given at the bottom of Table 5.2, it can be seen that a reduction of 99.4% for *Yld2004-Iso* and 87.1% for *Yld2004-Mixed* models were achieved. Despite the optimization method adopted may conduct the optimization process to a local minimum of the objective function, these results show a great efficiency of L-M algorithm.

Figure 5.4 depicts the evolution of the objective function value during the identification process for both constitutive models. The first initial decrease, over 19 and 25 evaluations (for *Yld2004-Iso* and *Yld2004-Mixed* models, respectively), correspond to the variations of each initial parameters in order to numerically calculate the sensitivity matrix. Then, a considerable reduction of S_{obj} occurred before the first 100 evaluations, and subsequently, a stabilization of S_{obj} value is seen. This type of evolution is due to the fact that L-M algorithm always seeks the best descent direction, thus accelerating to the converged state. However, when the optimization process is close to a possible solution (minimum of the objective function), the objective function value tends to stabilize until the end condition is satisfied. Thereby, considering the relationship between required calculation time and obtained results, it is important to point out that, in both material parameter identifications, approximately 200-250 evaluations could be enough to obtain similar results comparatively to those achieved by the identification procedures performing 416 (*Yld2004-Iso*) and 500 (*Yld2004-Mixed*) evaluations.

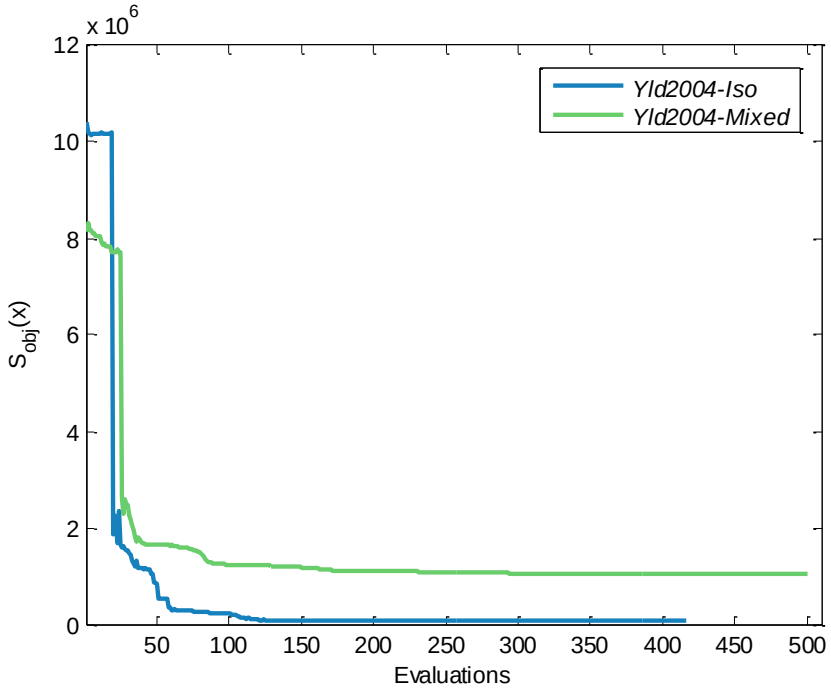

Figure 5.4 – Evolution of the objective function S_{obj} during the material parameters identification process for both *Yld2004-Iso* and *Yld2004-Mixed* models for DC04 mild steel.

First of all, the normalized projection of the yield surface in the plane ($\sigma_{XX}/\sigma_Y(0)$, $\sigma_{YY}/\sigma_Y(0)$) was plotted in Figure 5.5 for the identified material parameters listed in Table 5.2. For comparison

purposes, experimental data as well as yield surface projections obtained by Le Port (2012) and Zang *et al.* (2011) using Hill48 anisotropic yield criterion were added in Figure 5.5. Comparing the yield surface projections for both models, it is observed that the one of *Yld2004-Mixed* model is very close to the experimental data. The yield surface of *Yld2004-Iso* model tends to be more stretched still, lies between Hill48 surfaces obtained by Le Port (2012) and Zang *et al.* (2011).

With the set of material parameters identified for both phenomenological models, τ-γ/σ-ε curves for simple shear/uniaxial tension and ε_{11}-ε_{22} curves for uniaxial tension in the five different orientations to RD were predicted, as shown in Figures 5.6 to 5.10. Note that in Figure 5.6, it is also depicted the numerical prediction relative to bulge test. It should be emphasized that the bulge test data was plotted by using ε_{11}, instead of an equivalent strain, leading to a falsely exaggerated gap between uniaxial tensile and biaxial stress levels.

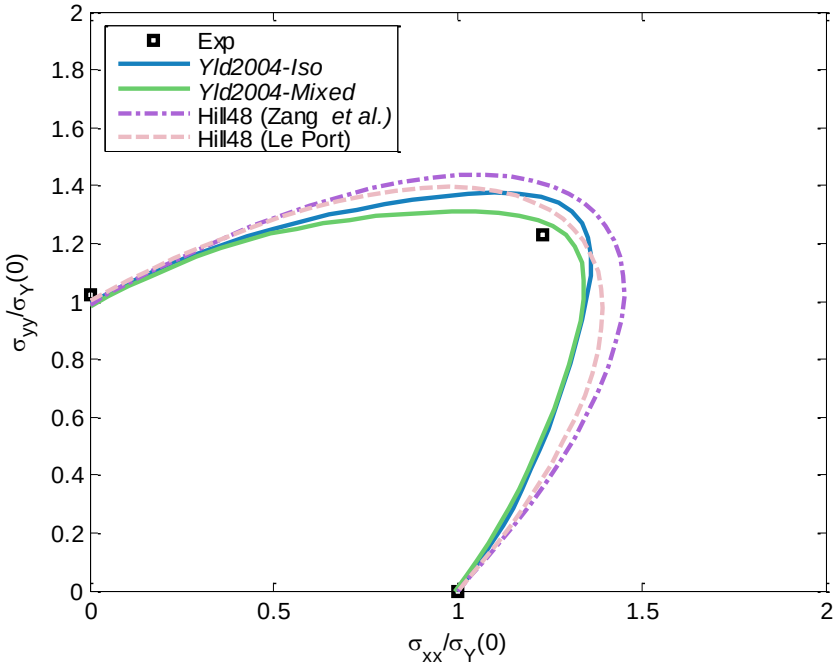

Figure 5.5 – Projection of the yield surface in the plane ($\sigma_{XX}/\sigma_Y(0)$, $\sigma_{YY}/\sigma_Y(0)$) for the identified material parameters given in Table 5.2.

Comparing the experimental and predicted results of both models exhibited in Figures 5.6 to 5.10, it can be seen that an overall good description of the mechanical behavior was obtained. However, a numerical over-estimation of σ-ε curve of the last experimental points occurs for the bulge test, depicted in Figure 5.6. In the case of the simple shear experiment at 45° to RD, depicted in Figure 5.8, τ-γ curve was also over-predicted by both numerical models. In addition, it can be seen that almost all τ-γ numerical curves in simple shear predicted by *Yld2004-Mixed* model tend to overestimate the stress level close to the initial yield stress. It may come from the choice of the hardening law, in the first loading, the kinematic contribution described by rapidly evolving terms (*cf*. Equation 4.16) leading to such phenomenon.

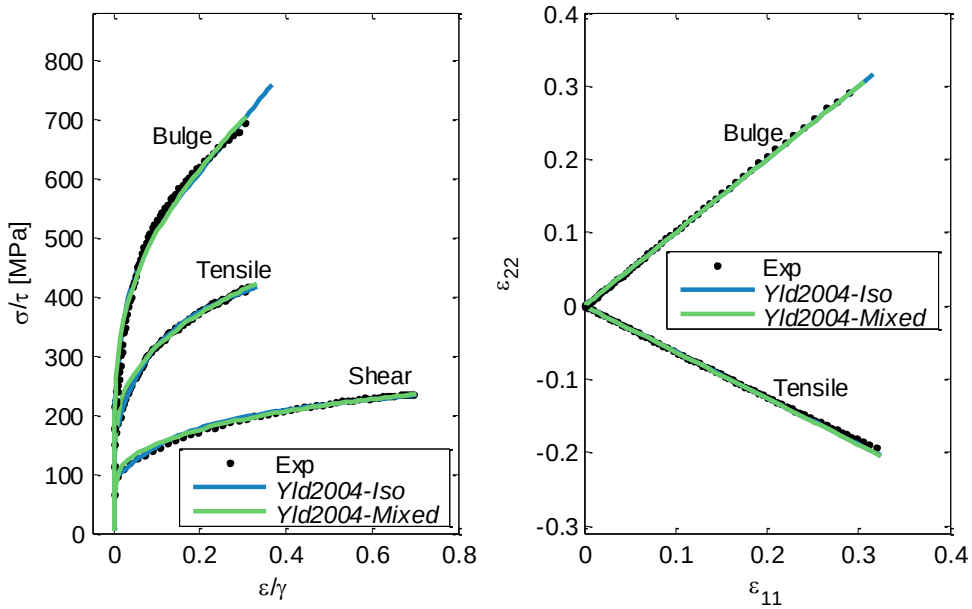

Figure 5.6 – Experimental and numerical (i) τ-γ curve for simple shear and σ-ε curves for bulge and uniaxial tension to 0°/RD and (ii) ε_{11}- ε_{22} curves for bulge and uniaxial tension to 0°/RD.

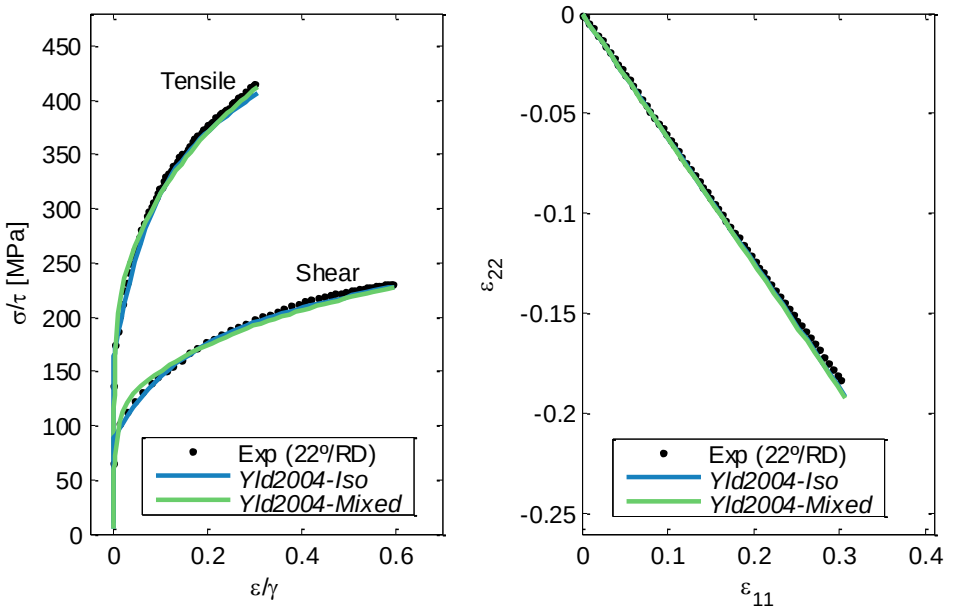

Figure 5.7 – Experimental and numerical (i) τ-γ and σ-ε curves for simple shear and uniaxial tension to 22°/RD and (ii) ε_{11}- ε_{22} curve for uniaxial tension to 22°/RD.

In Figure 5.11, the numerical reproduction of τ-γ curves with reverse loading at 0.13, 0.21 and 0.33 of pre-strain are presented for both *Yld2004-Iso* and *Yld2004-Mixed* models. As expected, the numerical *Yld2004-Iso* model was not able to perform an acceptable reproduction of such *τ-γ* curves since kinematic hardening formulation was not included in this model. Concerning the numerical Bauschinger curves predicted by *Yld2004-Mixed* model, it can be seen that the kinematic material parameters give a generally good description of the Bauschinger

effect with the exception of the rounded yield point and work hardening stagnation. It must be noted that a transient behavior and hardening stagnation are experimentally observed for DC04 mild steel and the kinematic formulation adopted on *Yld2004-Mixed* model does not include the prediction of this phenomenon.

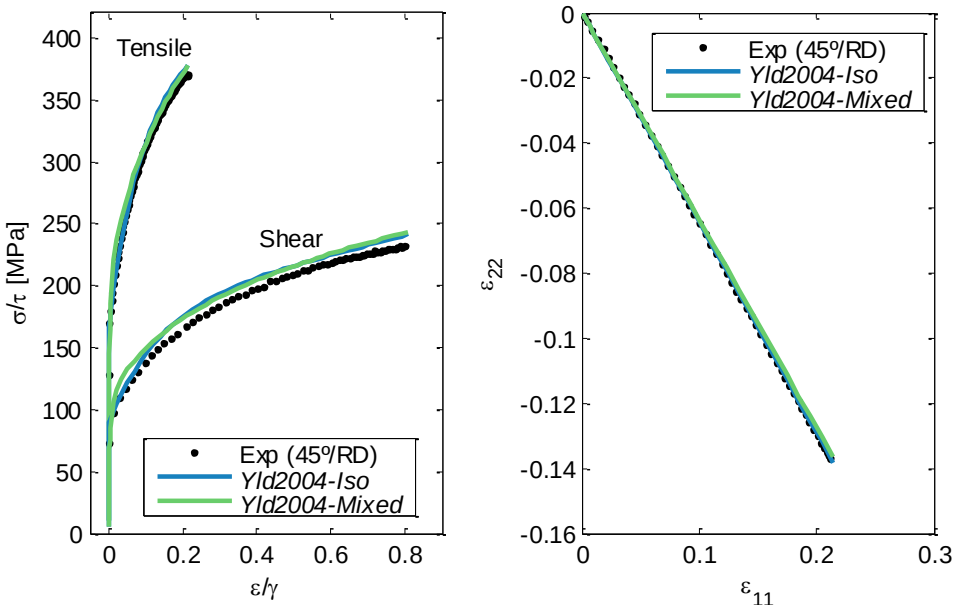

Figure 5.8 – Experimental and numerical (i) τ-γ and σ-ε curves for simple shear and uniaxial tension to 45°/RD and (ii) ε_{11}- ε_{22} curve for uniaxial tension to 45°/RD.

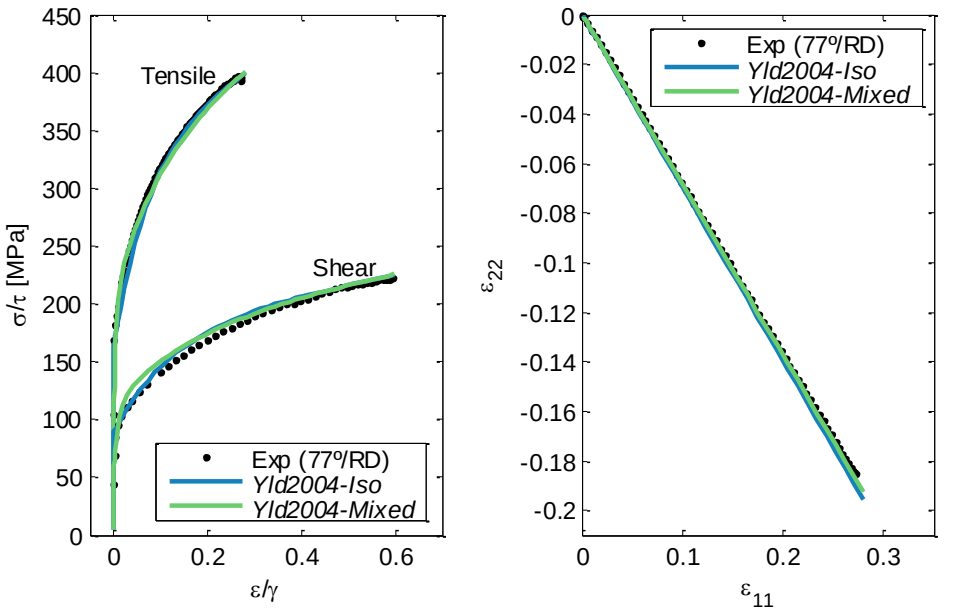

Figure 5.9 – Experimental and numerical (i) τ-γ and σ-ε curves for simple shear and uniaxial tension to 77°/RD and (ii) ε_{11}- ε_{22} curve for uniaxial tension to 77°/RD.

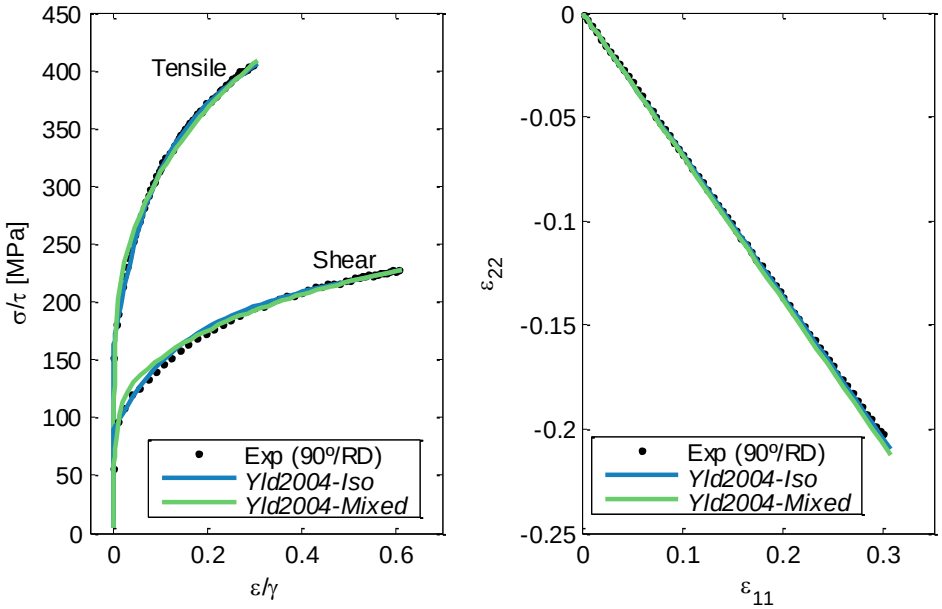

Figure 5.10 – Experimental and numerical (i) τ-γ and σ-ε curves for simple shear and uniaxial tension to 90°/RD and (ii) ε_{11}- ε_{22} curve for uniaxial tension to 90°/RD.

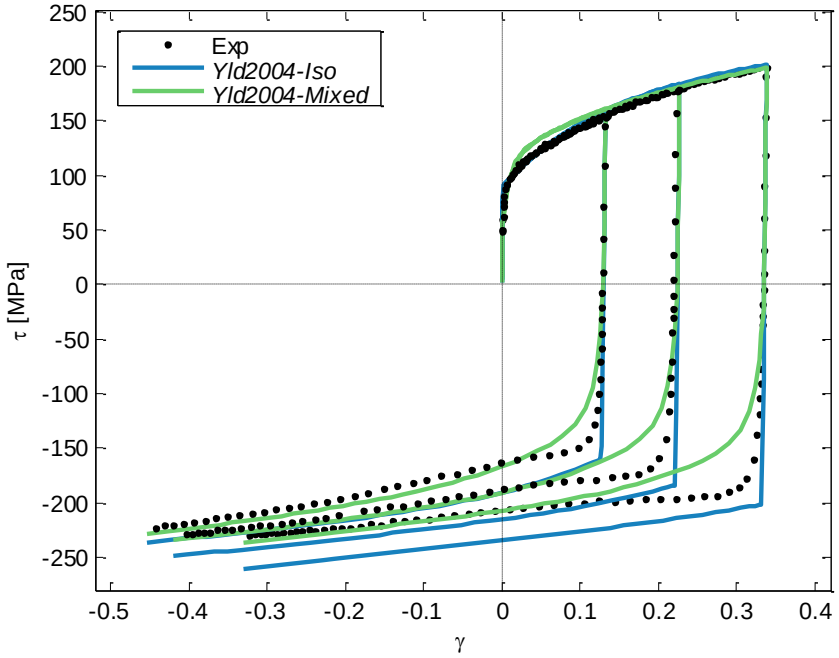

Figure 5.11 – Experimental and numerical τ-γ Bauschinger curves obtained with the identified parameters of both *Yld2004-Iso* and *Yld2004-Mixed* models for DC04 mild steel.

The visual comparison of the numerical results with the experimental behavior is always mandatory in order to ascertain the real quality of the identified material parameters. Based on this, it is stated that both sets of material parameters identified from the several tests lead to a good representation of the mechanical behavior of DC04 mild steel, under monotonic loading conditions.

5.4 Macroscopic rupture calibration

As reported in section 4.4, the calibration of uncoupled fracture criteria parameter is usually performed comparing experiments leading to rupture, such as the tensile test, with FE simulation. Therefore, this kind of experimental-numerical approach is adopted for evaluating the macroscopic rupture in DC04 mild steel.

Uniaxial tensile tests were carried out up to rupture and the critical parameters of RT and CL criteria were directly determined by comparing the numerical simulation with the experiment in terms of the critical deformation level reached. Both experimental and numerical nominal stress-displacement curves were compared up to the experimental rupture displacement. The critical value of the fracture criteria was determined for this displacement by the numerical simulation.

According to Xue (Xue, 2008), the number of experiments needed for the calibration of uncoupled fracture criteria is equal to the number of material parameters. Hence, a single experiment and FE simulation can be used to determine the critical W_{CL}^{f} and W_{RT}^{f} values. However, based on the results of Li *et al*. (Li *et al.*, 2011), calibrate uncoupled fracture criteria using a single test may not be enough for a reliable prediction of fracture in other plastic deformation process even under similar forming conditions.

5.4.1 Experimental data

The uniaxial tensile test up to rupture is adopted for the characterization of the rupture behavior of DC04 mild steel. This test is easy to carry out and gives specific data in the fracture zone using DIC technique. Another reason for its selection is related to the fact that RT and CL criteria are able to correctly predict the fracture onset and location in experiments with localized deformation, like necking. Indeed, uncoupled fracture criteria are able to easily capture the plastic deformation mode as well as failure initiation when localized deformation occurs (Li *et al.*, 2011).

In this work, four uniaxial tensile tests up to rupture in RD were conducted under displacement control with Instron 8033 testing machine, at a displacement rate of the grips of 10 mm/min and at room temperature. Rectangular specimens were machined. A slight grinding of the long edge was made in the middle, in order to ensure necking and subsequent rupture in the center of the sample. Figure 5.12 shows the sample geometry and dimensions of the adopted uniaxial tensile specimen.

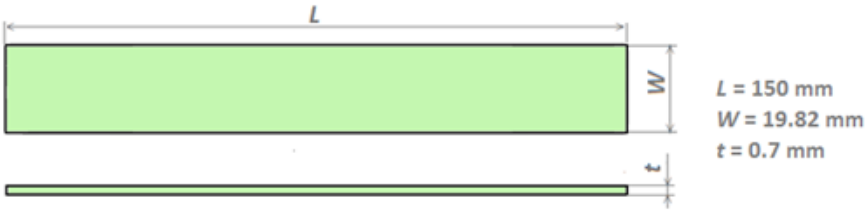

Figure 5.12 – Geometry of the specimen applied in tensile test experiment.

The deformation was measured by DIC technique, with Aramis system developed by GOM (2009), as well as an extensometer. Figure 5.13 a) depicts Cauchy and nominal stress-logarithmic strain curves obtained with DIC technique for all experiments. The experimental curves were

plotted up to rupture and it was verified that a good reproducibility was achieved between all the tests. Thus, test 3 was selected as the reference one. Figure 5.13 b) compares the stress-logarithmic strain curves recorded by both DIC and extensometer techniques. Additionally, the uniaxial tensile σ-ε curve in RD obtained by Zang *et al.* (2011) from the same DC04 mild steel was also included in this figure. This test corresponds to the one used in the database for parameters identification. The comparison between the experimental curve recorded and the one obtained by Zang *et al*. allows to ascertain if the aging time between the tensile test carried out by Zang *et al*. and the presented one may influence the mechanical behavior of DC04 mild steel. Analyzing Figure 5.13 b), it was observed that σ-ε curves obtained by using both measurements techniques as well as by Zang *et al.* (2011) are identical. It reveals that no aging phenomena affected DC04 mild steel sheet during the time between the presented test and the one performed by Zang *et al.* (2011). In addition, the ultimate tensile strength (UTS), that defines the limit between the uniform plastic deformation and the plastic instability, was also added in Figure 5.13 b).

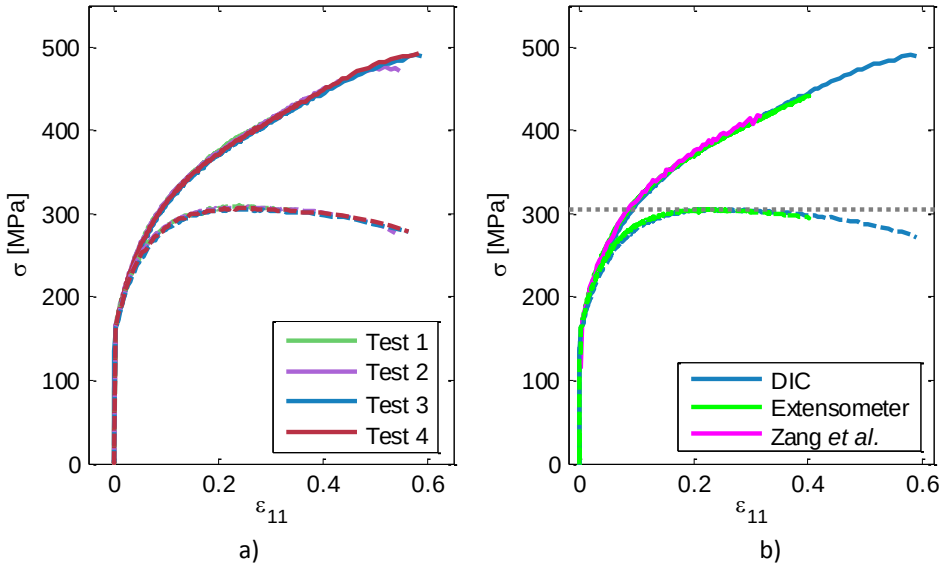

Figure 5.13 – Cauchy (solid line) and nominal (dashed line) stress-logarithmic strain curves a) of the different tensile tests up to rupture obtained by DIC technique and b) of the tensile test up to rupture used as reference. Note that gray line define the UTS value of 305.3 MPa.

A detailed analysis of the rupture phenomenon can be carried out by analyzing additional data coming from DIC measurement technique. Indeed, logarithmic strain field over the whole sample surface can be recorded up to rupture, defined by the breaking into two parts. These data are very useful to understand and characterize the neck geometry and subsequent fracture and, by comparison with the numerical simulation, may be used to calibrate the parameters of the fracture criteria.

For computation, DIC analysis was performed with digital images subdivided into square facets of 13x13 pixels with a 5 pixel overlapping area (facet step equal to 8 pixels). From each valid facet, a measuring point results after computation. The accuracy of the resulting measuring point improves with the increase of facet size. However, more computation time is required and local effects within the facet size cannot be captured. Conversely, the increase of the facet step leads to a decrease of the measuring point density and less computation time is required (GOM,

2009). Then, the value defined for both parameters constitutes a compromise between accuracy and computation time. The influence of the facet size on the calculated local strain values was investigated, leading to this choice, which corresponds to rather stable values (independent of the facet size) and a reasonable computational time. The considered facet step and size, for this experiment, led to the discretization in square elements with a mesh defined by 3 facets per mm.

In order to perform a robust comparison between experimental and numerical rupture, the following data was output: (i) nominal stress-displacement curve (σ_{nom}-Δl) up to rupture considering the displacement between two equidistant points from the specimen center (points 1 and 2 depicted in Figure 5.14), (ii) ε_{11}-Δl and ε_{22}-Δl curves with strain components calculated in the rupture zone (region of 2x1.5 mm^2 shown in Figure 5.14) and (iii) ε_{11} strain distribution in the center of the specimen along direction $\vec{1}$ (section 0°/RD) and along direction $\vec{2}$ (section 90°/RD) at the moment just before rupture. Mention that this moment just before rupture was defined as the one corresponding to DIC image taken before the specimen breaking into two parts. In this experiment, the capture time, between two consecutive images, used by DIC was 1.05 seconds. Figure 5.15 presents these results. The initial distance between the equidistant points 1 and 2 was 7 mm and at the moment of rupture was 13.65 mm, which means that the fracture was obtained for a relative displacement of 6.35 mm. The relative displacement between these two points is taken as reference for comparison with the numerical data.

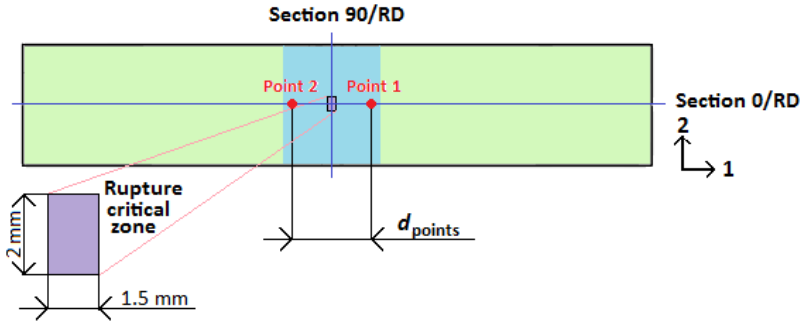

Figure 5.14 – Illustration of areas used for strain field output.

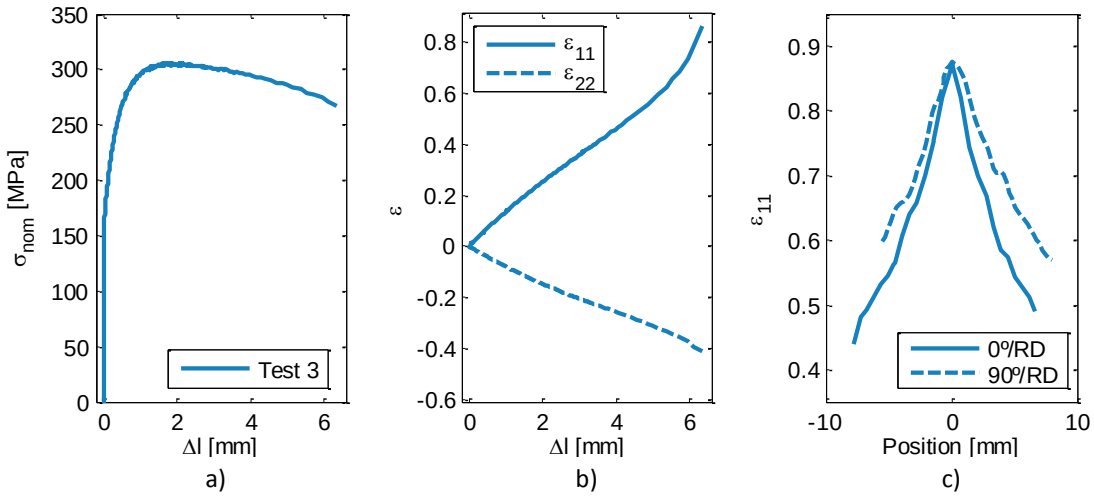

Figure 5.15 – a) σ_{nom}-Δl curve, b) ε_{11}- Δl and ε_{22}- Δl curves and c) ε_{11} strain distribution along the sections 0° and 90° to RD at the moment just before rupture.

From the digital images taken by DIC technique, a visual distribution of the experimental deformation was recorded. Figure 5.16 shows ε_{11} isovalue distribution just before and after rupture for the tensile test used as reference. By Figure 5.16 a) it is possible to realize the non-uniformity of ε_{11} distribution and the appearance of the strain critical zone in the center of the specimen just before rupture. This region constitutes the origin of the fracture, as shown in Figure 5.16 b).

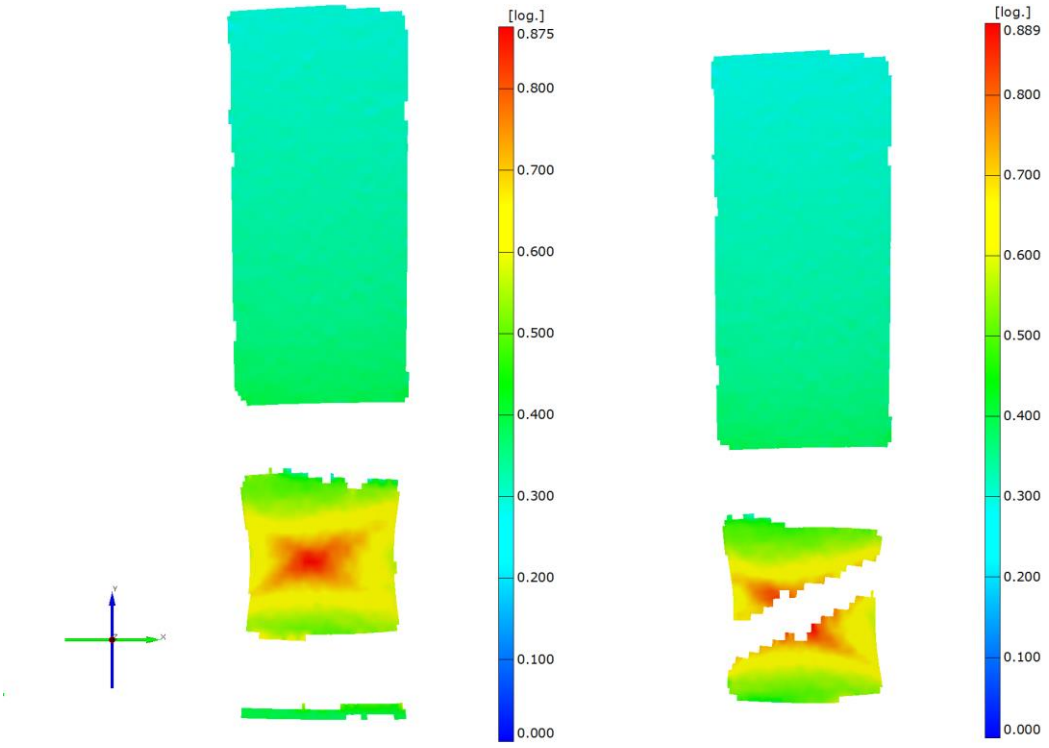

a) b)

Figure 5.16 – Strain distribution ε_{11} a) just before and b) after rupture recorded by DIC technique. The gaps close to the center specimen (without strain distribution) are due to the extensometer device.

5.4.2 Numerical modeling

The computational analysis of the tensile test up to rupture was evaluated by using the FE code ABAQUS, within the implicit scheme. The numerical model consists in one fourth of the specimen, considering symmetry in the thickness and in the width; the total length in-between the grips was considered. Displacement, of equal magnitude d_1, in $\vec{1}$ and $-\vec{1}$ directions was applied at both extremities of the sample, as depicted in Figure 5.17.

The mesh was structured and 3D 8-node linear isoparametric elements with reduced integration (C3D8R) and with hourglass control were used. With the purpose of evaluating the mesh dependency, different mesh sizes were considered. By this way, two distinct regions (A and B) as well as a transition region were defined, as depicted in Figure 5.17, and three different mesh refinements were considered in region A. Table 5.3 depicts the features of each mesh. It should be emphasized that mesh 2 is defined in region A with the same facet size used with DIC system in the experiment.

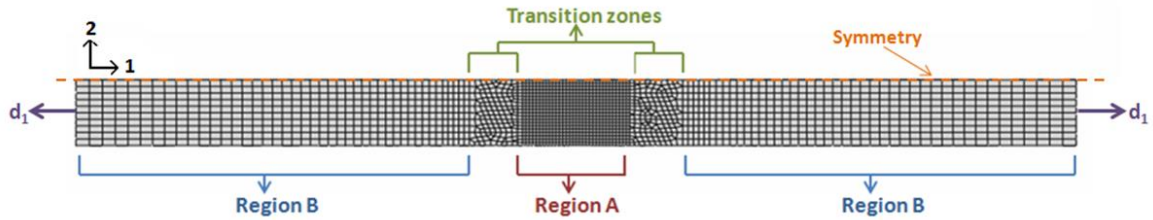

Figure 5.17 – Different sub-regions defined over the numerical model of the tensile sample, for mesh refinement.

Numerical simulations were carried out for both *Yld2004-Iso* and *Yld2004-Mixed* models and both CL and RT fracture criteria were evaluated. These fracture criteria were implemented in ABAQUS code as user-defined output variable subroutine (UVARM).

Table 5.3 - Features of the different meshes used in the numerical simulation of tensile specimen.

	Region			
Mesh	A	B	Thickness (el)	Nº elements (el)
1	2 el/mm	1 el/mm (along *y*) 1 to 0.5 el/mm (along *x*)	2	3630
2	3 el/mm		2	5898
3	4 el/mm		2	9394

5.4.3 Critical value determination

The critical value of the uncoupled fracture criteria is calibrated comparing the experimental and numerical data up to rupture displacement. However, an accurate reproduction of the experimental data by the numerical simulation can be difficult when uncoupled fracture criteria are adopted. Indeed, while the experimental data up to rupture may be influenced by damage, leading to a decrease of the stress level, the plastic response of the numerical model was not influenced when using uncoupled fracture criteria. As a consequence, the simulation can lead to a larger plastic deformation than the one observed experimentally.

Therefore, in order to assure the best numerical description using these uncoupled fracture criteria, it must be verified whether the material parameters were identified within the same deformation range as the one investigated in the tensile test up to rupture. Figure 5.18 depicts the equivalent plastic strain evolution for the uniaxial tensile test up to rupture and for the conventional tests used in the material parameters identification process. As the strain rate effect was not taken into account in the constitutive equations, all the numerical simulations were carried out for a total time of 1 s. The time increment used in Figure 5.18 is a normalized evolution parameter. From this figure, it can be seen that the maximum equivalent plastic strain $\bar{\varepsilon}^{p}$ reached in the tensile test up to rupture is similar to the one achieved at the end of the bulge test.

However, the numerical prediction of the bulge experiment using both *Yld2004-Iso* and *Yld2004-Mixed* models shows (Figure 5.19) an overestimation of the stress level for an equivalent plastic strain greater than 0.6. For this reason, a modification of the isotropic hardening law was

considered in order to improve the mechanical description for a plastic strain above 0.6. In this way, the modified isotropic hardening law was defined by

$$\sigma_Y(\bar{\varepsilon}^p)=\begin{cases}\sigma_0+(\sigma_\infty-\sigma_0)\left[1-\exp(-\delta\bar{\varepsilon}^p)\right]+\beta\bar{\varepsilon}^p & \text{for } \bar{\varepsilon}^p\le 0.6\\ \sigma_0+(\sigma_\infty-\sigma_0)\left[1-\exp\left(-\delta\bar{\varepsilon}^p_{0.6}\right)\right]+\beta\bar{\varepsilon}^p_{0.6}+\beta_2\left(\bar{\varepsilon}^p-0.6\right) & \text{for } \bar{\varepsilon}^p>0.6\end{cases}, \quad (5.5)$$

where $\bar{\varepsilon}^p_{0.6}$ = 0.6 and β_2 is an extra material parameter obtained by adjusting the predicted stress level of the bulge test to the experimental values, with a trial-and-error procedure. The phenomenological models with this isotropic hardening formulation were named as *Yld2004-Iso*$_{Mod}$ and *Yld2004-Mixed*$_{Mod}$. Parameter β_2 assumed the values of 220.9 MPa and 59.6 MPa for *Yld2004-Iso*$_{Mod}$ and *Yld2004-Mixed*$_{Mod}$ models, respectively. Note that $\sigma_Y(\bar{\varepsilon}^p)$ for $\bar{\varepsilon}^p \le 0.6$ consisted of the isotropic hardening law defined by Equation 4.15 and the parameter values are the ones listed in Table 5.2. Thereby, the modification introduced in the hardening law does not alter the previous identification results.

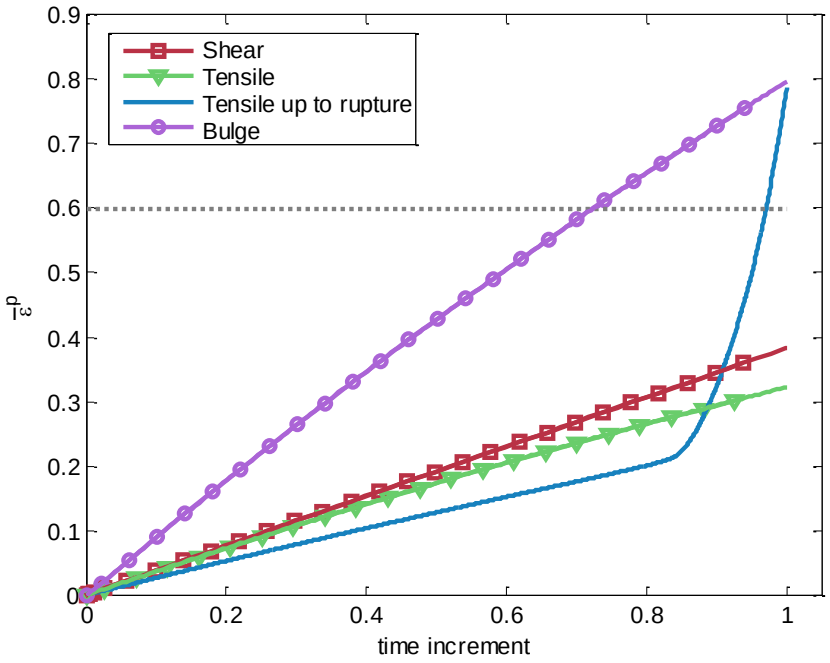

Figure 5.18 – Evolution of the equivalent plastic strain for the conventional tests and tensile test up to rupture using *Yld2004-Iso* model. Note that the numerical simulations were stopped for the same deformation value (ε or γ) observed at the end of the corresponding experimental test.

Figure 5.19 shows the experimental and numerical σ-ε cuves of the bulge test using both *Yld2004-Iso* and *Yld2004-Iso*$_{Mod}$ and both *Yld2004-Mixed* and *Yld2004-Mixed*$_{Mod}$ models. By this figure, it can be seen that a closer description of the bulge test data is attained using the modified isotropic hardening law because a decrease of the slope is obtained in the latter deformation stage ($\bar{\varepsilon}^p \ge 0.6$) comparatively to the prediction with *Yld2004-Iso* and *Yld2004-Mixed* models.

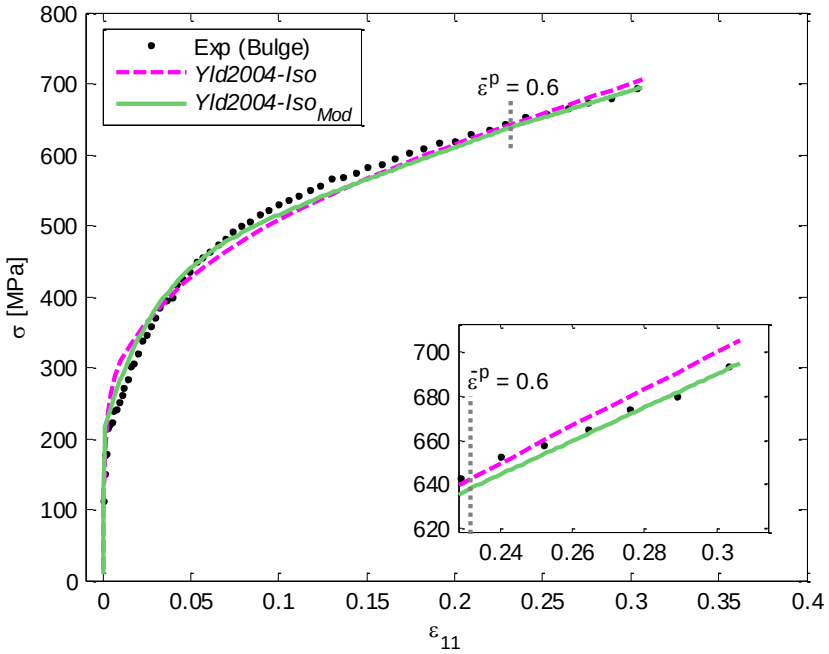

a) *Yld2004-Iso and Yld2004-Iso*$_{Mod}$

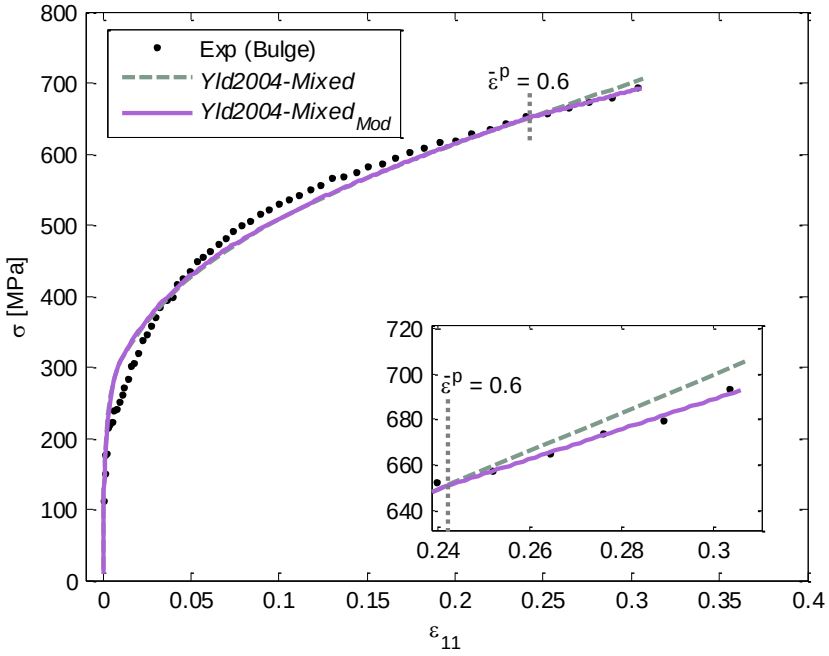

b) *Yld2004-Mixed and Yld2004-Mixed*$_{Mod}$

Figure 5.19 – Experimental and numerical σ-ε curves of the bulge test using the initial and the modified hardening formulation. Numerical simulation performed using 1-element model.

The improvement of the results using the modified hardening formulation can be observed by comparing the experimental and numerical rupture data using both *Yld2004-Iso* and *Yld2004-Iso*$_{Mod}$ models. Thus, the experimental and numerical σ_{nom}-Δl and ε-Δl curves up to rupture as well as ε_{11} strain distribution at the center of specimen along the sections 0°/RD and 90°/RD at the moment just before rupture, obtained using mesh 2, are depicted in Figures 5.20 and 5.21.

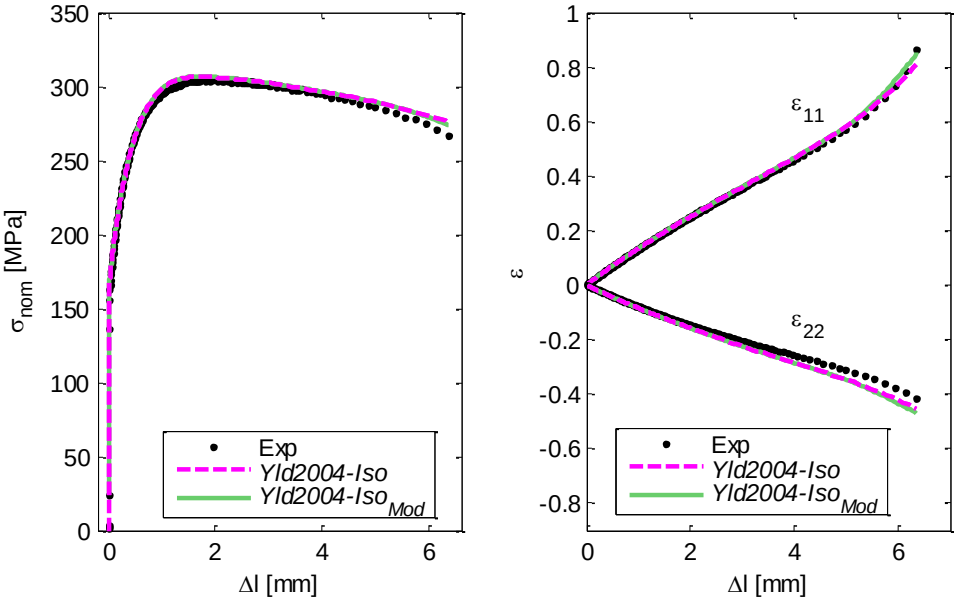

Figure 5.20 – Experimental and numerical a) σ_{nom}-Δl curves and b) ε_{11}-Δl and ε_{22}-Δl curves obtained up to rupture, using mesh 2, for *Yld2004-Iso* and *Yld2004-Iso*$_{Mod}$ models.

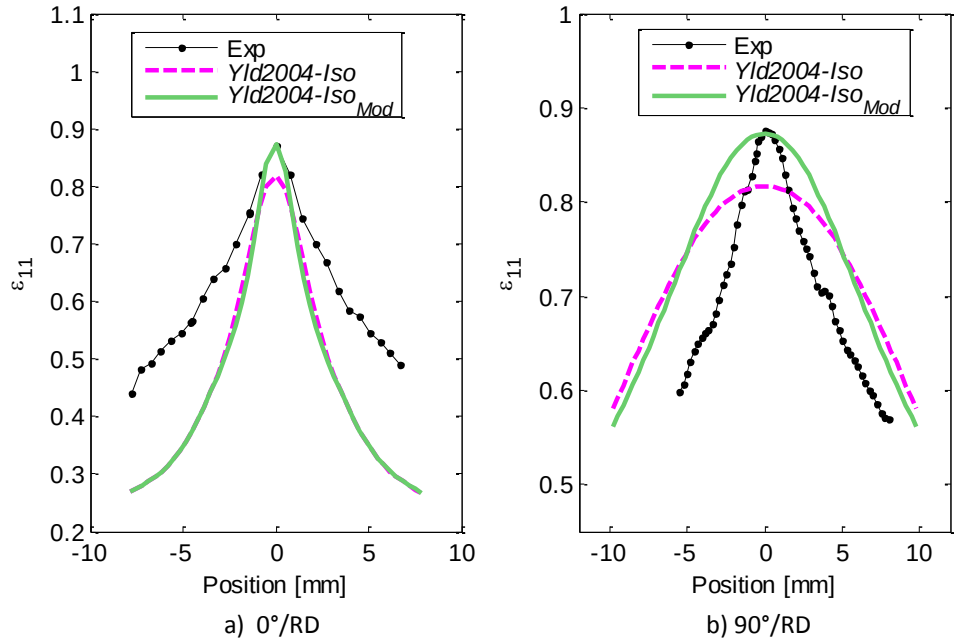

Figure 5.21 – Experimental and numerical ε_{11} strain distribution along the sections a) 0°/RD and b) 90°/RD at the moment just before rupture, using mesh 2, for *Yld2004-Iso* and *Yld2004-Iso*$_{Mod}$ models.

By comparing the experimental and numerical data illustrated in Figure 5.20, it was observed that the nominal stress-displacement curve σ_{nom}-Δl up to rupture and the ε_{22}-Δl curve were overestimated by both *Yld2004-Iso* and *Yld2004-Iso*$_{Mod}$ models. It may come from the non-taking into account of the effect of damage on the plastic response of the material by the uncoupled fracture criteria (Li *et al.*, 2011). However, huge differences between the numerical

results of both *Yld2004-Iso* and *Yld2004-Iso*$_{Mod}$ models were pointed out. In fact, a reliable reproduction of ε_{11}-Δl curve was achieved by using *Yld2004-Iso*$_{Mod}$. In addition, concerning ε_{11} strain distribution crossing the center of the specimen along the sections 0°/RD and 90°/RD (Figure 5.21), the results obtained by *Yld2004-Iso*$_{Mod}$ model were closer to experimental data than *Yld2004-Iso*. ε_{11} strain distribution at the center of the specimen was well reproduced for both 0°/RD and 90°/RD sections while the global distribution was not too coincident. Nonetheless, the most important zone was accurately reproduced since the necking and consequent fracture occurs at the center of the specimen.

Due to the previous analysis, the numerical simulations were then carried out for both *Yld2004-Iso*$_{Mod}$ and *Yld2004-Mixed*$_{Mod}$ models using both CL and RT fracture criteria and considering the different meshes presented in Table 5.3.

Figures 5.22 and 5.23 illustrate the numerical and experimental σ_{nom}-Δl and ε-Δl curves obtained up to rupture and ε_{11} distribution along the two sections at 0° and 90° to RD at the moment just before rupture for the different meshes listed in Table 5.3. The numerical results with mesh 2 were the ones that give a good representation of DC04 mechanical behavior up to rupture, in particular the maximum ε_{11} value was well predicted, as shown in Figure 5.23. Indeed, FE simulation with mesh 2 was defined with the same element size used by DIC technique during the experiment. Additionally, it was also possible to verify that the numerical models with mesh 2 of both *Yld2004-Iso*$_{Mod}$ and *Yld2004-Mixed*$_{Mod}$ models present a similar prediction.

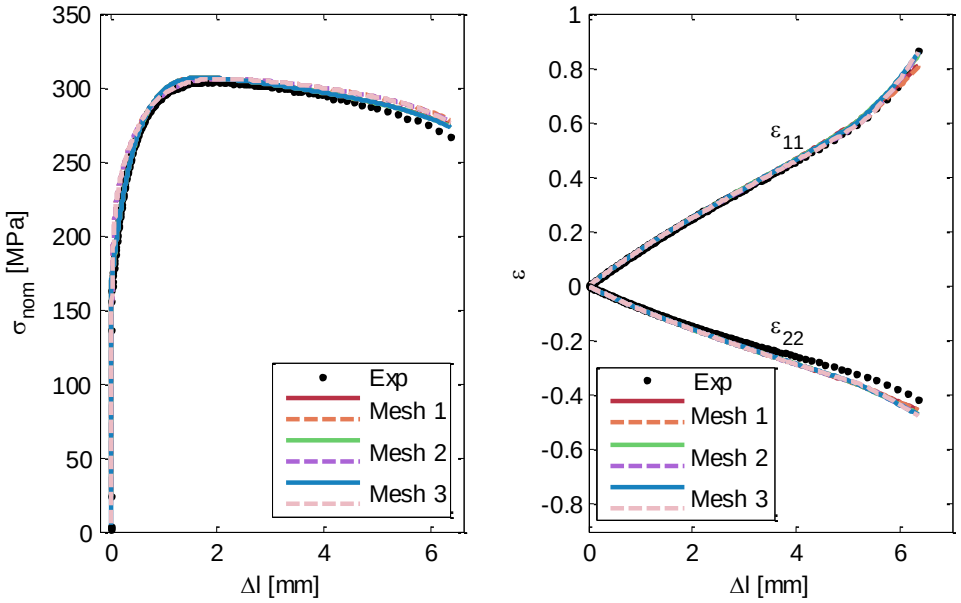

Figure 5.22 – Experimental and numerical a) σ_{nom}-Δl curves and b) ε_{11}-Δl and ε_{22}-Δl curves obtained up to rupture for the different meshes considered using both *Yld2004-Iso*$_{Mod}$ (solid line) and *Yld2004-Mixed*$_{Mod}$ (dashed line) models.

Based on the numerical results of Figures 5.22 and 5.23, the critical value of CL and RT criteria were determined from the FE simulation with mesh 2 for both *Yld2004-Iso*$_{Mod}$ and *Yld2004-Mixed*$_{Mod}$ models.

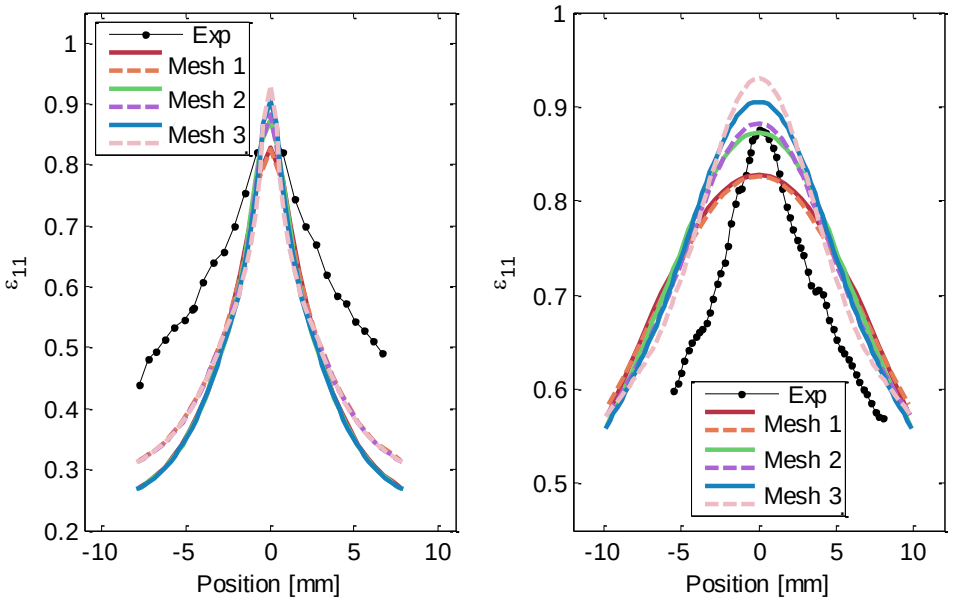

Figure 5.23 – Experimental and numerical ε_{11} strain distribution along the sections a) 0° and b) 90° to RD at the moment just before rupture for the different meshes considered using both *Yld2004-Iso*$_{Mod}$ (solid line) and *Yld2004-Mixed*$_{Mod}$ (dashed line) models.

In Figure 5.24, the experimental and numerical ε_{11} distributions over the tensile specimen at the moment just before rupture can be compared. It can be seen that the numerical simulations have some difficulty in describing perfectly the cross shape localization in the fracture zone, leading therefore to the differences observed in Figure 5.23. However, *Yld2004-Mixed*$_{Mod}$ model allowed a better prediction of the cross shape localization than *Yld2004-Iso*$_{Mod}$. Note that it is mandatory to obtain a good prediction by the FE model since the mesh may affect the calibration of the fracture criteria.

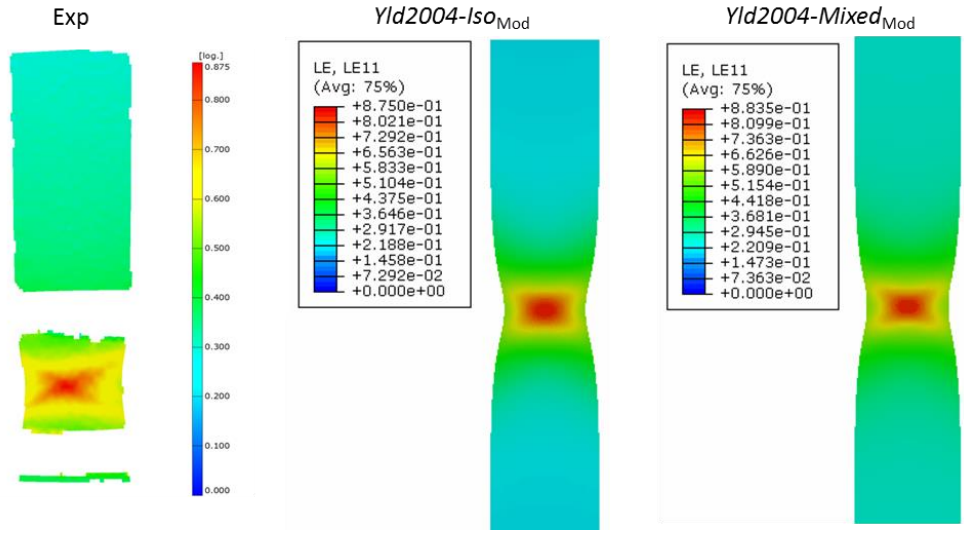

Figure 5.24 – Experimental (Exp) and numerical (*Yld2004-Iso*$_{Mod}$ and *Yld2004-Mixed*$_{Mod}$) ε_{11} distribution over the tensile specimen at the moment just before rupture, by using FE model with mesh 2.

Figure 5.25 shows the W_{CL} distribution on the specimen at the moment just before rupture using both *Yld2004-Iso*$_{Mod}$ and *Yld2004-Mixed*$_{Mod}$ models. From this figure, it was observed that W_{CL} distribution achieved larger values at the center of the sample, predicting accurately the fracture zone. In addition, it was verified that W_{CL} distribution using *Yld2004-Mixed*$_{Mod}$ model tends to define the cross shape that appeared on the experimental ε_{11} distribution at the center of the specimen. Moreover, W_{RT} distributions using *Yld2004-Iso*$_{Mod}$ and *Yld2004-Mixed*$_{Mod}$ models similar to the ones obtained with W_{CL} criterion were also observed.

In Table 5.4 the critical values of W_{RT}, W_{CL} and stress triaxiliaty (χ) are listed. These values were calculated in the region of 2 x 1.5 mm^2 depicted in Figure 5.14. The comparison of W_{RT}, W_{CL} and χ values shows that a huge difference exists between the values obtained for both constitutive models. The reason of such difference is related to $\bar{\eta}$ inherent to each constitutive model. Although the principal stresses σ_1, σ_2 and σ_3 were almost identical for both *Yld2004-Iso*$_{Mod}$ and *Yld2004-Mixed*$_{Mod}$ models, in the case of $\bar{\eta}$, a different evolution was obtained, as shown in Figure 5.26. This figure exhibits the evolution of the principal stress components and $\bar{\eta}$ during the tensile test up to rupture. It can be seen that $\bar{\eta}$ value of *Yld2004-Mixed*$_{Mod}$ was approximately half of the $\bar{\eta}$ value obtained for *Yld2004-Iso*$_{Mod}$ model. The difference between both $\bar{\eta}$ values comes from the kinematic hardening contribution of *Yld2004-Mixed*$_{Mod}$ model.

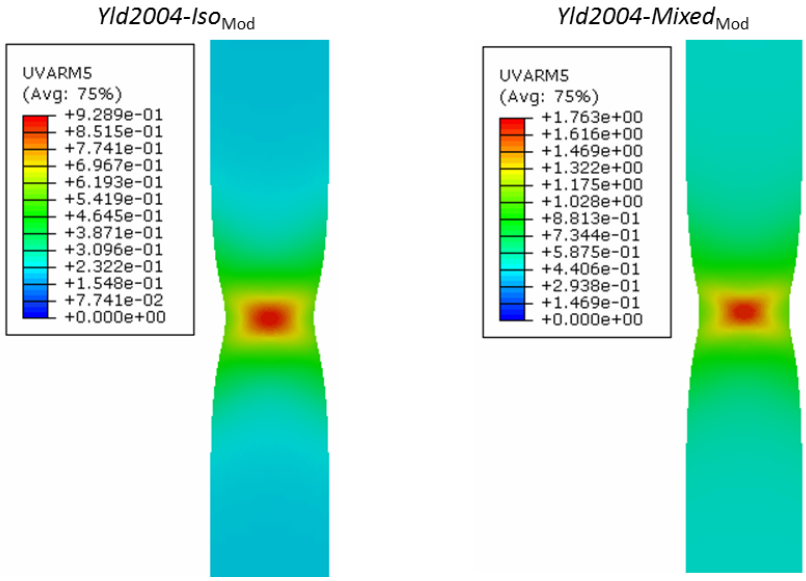

Figure 5.25 – Numerical (*Yld2004-Iso*$_{Mod}$ and *Yld2004-Mixed*$_{Mod}$) W_{CL} distribution of the tensile test at the moment just before rupture. UVARM5 stands for W_{CL}.

Table 5.4 - Critical values of W_{RT} and W_{CL}, and χ (χ=$\sigma_h/\bar{\eta}$, where σ_h is the hydrostatic stress) obtained for both *Yld2004-Iso*$_{Mod}$ and *Yld2004-Mixed*$_{Mod}$ models using FE model with mesh 2.

	W_{RT}^f	W_{CL}^f	χ
Yld2004-Iso$_{Mod}$	1.52	0.90	0.49
Yld2004-Mixed$_{Mod}$	2.51	1.68	0.94

Table 5.4 puts in evidence the influence of the constitutive model in the definition of the stress triaxility χ. For material isotropy, such as using von Mises yield criterion, it has been

analytically proven that for uniaxial tensile state $\chi \approx 0.33$ and for biaxial state $\chi \approx 0.67$. However, the anisotropy of the material leads to different χ values. It can be checked through Figure 5.27, which depicts the stress triaxiality evolution of the bulge and tensile test up to rupture for (i) *Yld2004-Iso*$_{Mod}$, (ii) *Yld2004-Mixed*$_{Mod}$ and (iii) a constitutive model composed by von Mises isotropic yield criterion with the modified isotropic hardening law, called as vonMises_Iso$_{Mod}$. The latter model was defined in the UMAT subroutine reducing all the coefficients of *Yld*2004-18p criterion to 1 and adjusting the exponent *a* to 2.

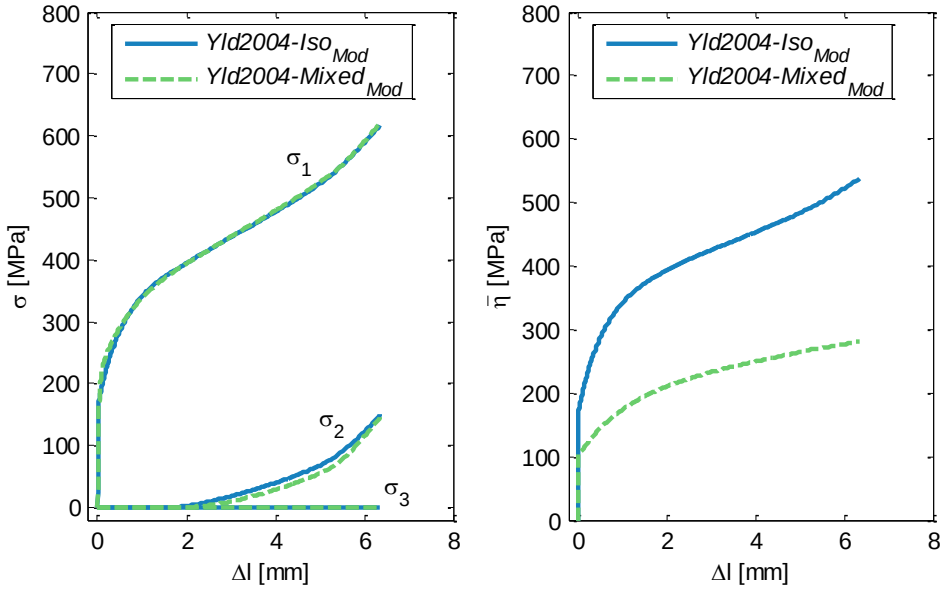

Figure 5.26 – Evolution of a) principal stress σ_1, σ_2, σ_3 and b) $\bar{\eta}$ during the tensile test up to rupture for both *Yld2004-Iso*$_{Mod}$ and *Yld2004-Mixed*$_{Mod}$ models.

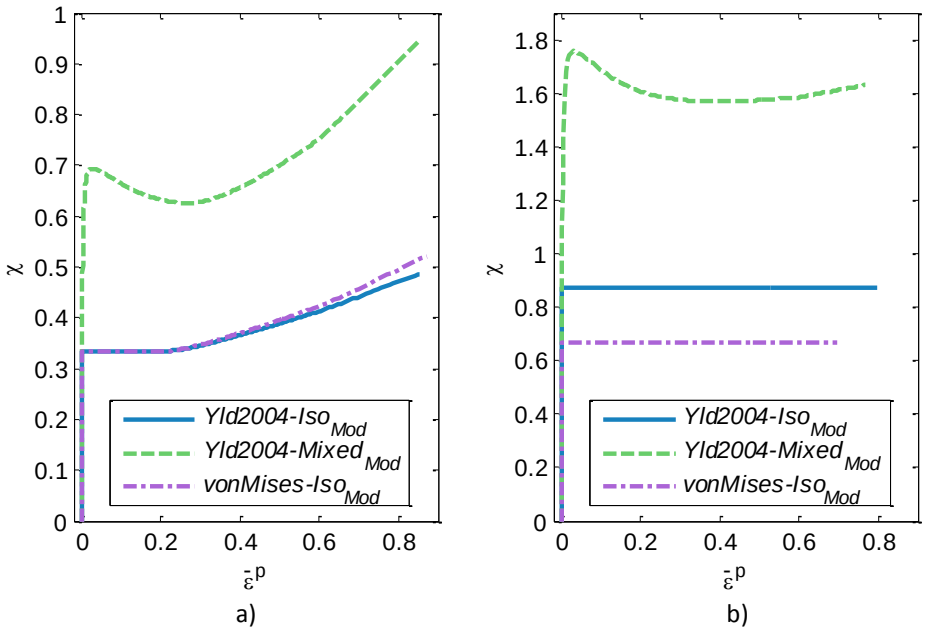

Figure 5.27 – Evolution of χ with the equivalent plastic strain during the a) tensile test up to rupture and b) bulge test for *Yld2004-Iso*$_{Mod}$, *Yld2004-Mixed*$_{Mod}$ and vonMises_Iso$_{Mod}$ models.

Analyzing Figure 5.27, it can be seen that vonMises_Iso$_{Mod}$ model achieved the theoretical expected χ values for both uniaxial tensile (up to necking) and biaxial state, while different values were obtained for both *Yld2004-Iso*$_{Mod}$ and *Yld2004-Mixed*$_{Mod}$ models. It appears that the stress triaxiality is dependent on the constitutive model and, consequently, the theoretical χ values cannot be used as reference when anisotropic yield criteria are considered.

5.5 Conclusion

In order to characterize the mechanical behavior of a DC04 mild steel, a large experimental database composed by (i) uniaxial tensile and simple shear tests at 0°, 22°, 45°, 77° and 90° to RD, (ii) bulge test and (iii) three shear-Bauschinger tests reversed at 0.13, 0.21 and 0.33 of pre-strain was used. In the case of the *Yld2004-Mixed* model, all the mentioned experiments were considered in the parameters identification process. While, in the case of *Yld2004-Iso* model, the shear-Bauschinger tests were not taken into account. Despite the large number of experimental tests, the implemented optimization process was able to identify a set of material parameters leading to a global accurate characterization of the DC04 mechanical behavior. However, concerning the shear-Bauschinger tests, the identified kinematic parameters for *Yld2004-Mixed* model give a global correct description of the Bauschinger effect with the exception of the rounded yield point and work hardening stagnation.

In addition, CL and RT uncoupled fracture criteria were adopted in order to calibrate the macroscopic rupture behavior of the mild steel. The calibration of these criteria was performed considering an experimental-numerical approach. The experimental data obtained during the experiment was recorded by using DIC system. Several numerical and experimental data were compared up to rupture displacement: (i) nominal stress-displacement curve (σ_{nom}-Δl) up to rupture, (ii) ε_{11}-Δl and ε_{22}-Δl curves with strain components calculated in the rupture zone and (ii) ε_{11} strain distribution in the center of the specimen along the directions at 0° and 90° to RD at the moment just before rupture. The numerical simulations presented some difficulty in describing perfectly the cross shape localization in the fracture zone. Nevertheless, *Yld2004-Mixed*$_{Mod}$ model allowed a better prediction of the cross shape localization than *Yld2004-Iso*$_{Mod}$. Moreover, both W_{CL} and W_{RT} distributions achieved larger values at the center of the sample, predicting accurately the fracture zone.

Chapter 6

Validation in deep drawing

6.1 Introduction

With the purpose of validating the material parameters identified for both *Yld2004-Iso*$_{Mod}$ and *Yld2004-Mixed*$_{Mod}$ models as well as W_{CL}^{f} and W_{RT}^{f} critical values, a deep drawing test was carried out. A schematic view of the experiment with detailed dimensions of the blank and tools is shown in Figure 6.1.

Experimental and numerical force-displacement curves and final diameter of the blank were assessed. In addition, a visual comparison of the major strain distribution was also performed at different stages of the deep drawing test. The acquisition of strain fields using DIC technique constituted an important tool to promote a better validation of the numerical results.

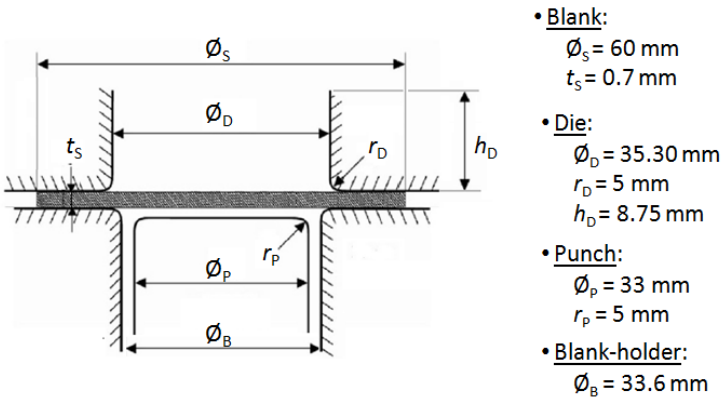

Figure 6.1 – 2D projection of the set-up of the deep drawing experiment (revolution symmetry).

6.2 Deep drawing experiment

The material DC04 is a mild steel, and therefore extreme conditions must be taken into account to promote rupture of the blank for the adopted cylindrical cup test. Thereby, the validation of the

material parameters can be carried out by an experiment leading to full drawing, while CL and RT fracture criteria can be validated by an experiment that leads to premature rupture of the blank. Then, for full drawing of the blank, the experiment was carried out considering a blank-holder force $F_{holder} = 15$ kN and lubrication was used. To obtain the experimental strain distribution data on the cylindrical cup using DIC system, a polypropylene film was applied on the blank surface in order to avoid damaging the black and white paint deposited on the blank surface (Coër, 2013).

To reach a premature rupture of the blank, a blank-holder force $F_{holder} = 90$ kN was applied. Moreover, neither lubrication nor the polypropylene film was used. Additionally, all surfaces of the tools and blank were carefully cleaned. The occurrence of the premature rupture in this experiment for DC04 mild steel was only possible under these severe conditions. Indeed, several experimental conditions were tested for this purpose, as depicted in Figure 6.2. It can be seen that just one condition was able to promote the premature rupture of the blank.

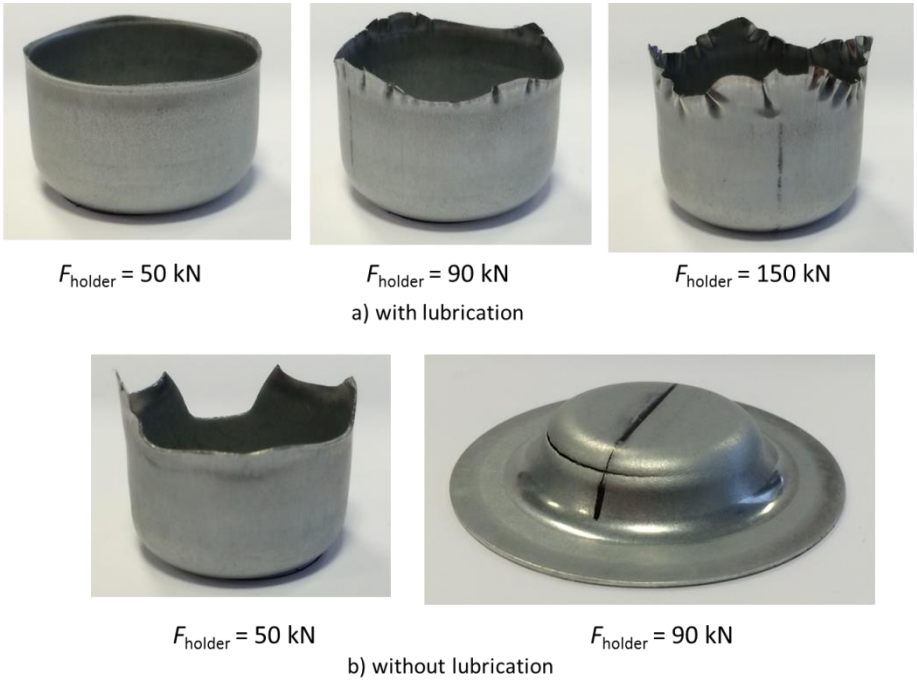

Figure 6.2 – Cylindrical cups obtained under several conditions tested to reach premature rupture on the blank for DC04 mild steel.

It should be also emphasized that an increase of F_{holder} was not enough to provoke a premature rupture of the blank. The small amount of lubrication applied also needed to be removed.

The friction coefficient μ is a crucial parameter in sheet forming simulation and then its accurate definition is mandatory for reliable predictions of the process. Thereby, due to the special conditions applied to promote rupture on the cylindrical cup test, another experiment with the same friction condition, *i.e*. without lubrication and polypropylene film, but using $F_{holder} = 15$ kN was performed. This additional test helped to obtain a better determination of the friction coefficient for the experiment that leads to premature rupture of the blank.

The experiments were carried out using a displacement rate of the punch of 1 mm/s. In the case of the experiment leading to premature rupture of the blank, a crack sensitivity criterion was

considered in order to stop the test after a load drop of 200 N after the maximum value. The blank-holder forces (F_{holder}) of 15 and 90 kN corresponds to a blank-holder pressure approximately of 7.7 and 46.4 MPa, respectively. Figure 6.3 depicts the experimental force-displacement curve obtained for each deep drawing experiment. Three tests were carried out for each drawing experiment and reproducible results were obtained. From Figure 6.3, it can be seen that both experiments with $F_{holder} = 15$ kN led to full drawing of the cylindrical cup, however, the one without lubrication required larger load effort. Concerning the experiment with $F_{holder} = 90$ kN, it led to premature rupture of the blank. Nevertheless, this test needed a significant higher load effort than the other two tests with $F_{holder} = 15$ kN, as can be seen by comparing the initial slope of these experiments. Figure 6.4 shows the final blank shape obtained for each one of these experiments. By this figure it can be pointed out that almost no earing phenomenon is observed for both tests leading to full drawing of the cup, namely, the tests with $F_{holder} = 15$ kN. In the case of the test with $F_{holder} = 90$ kN, it can be seen that the rupture was reached for an earlier deformation stage of the blank.

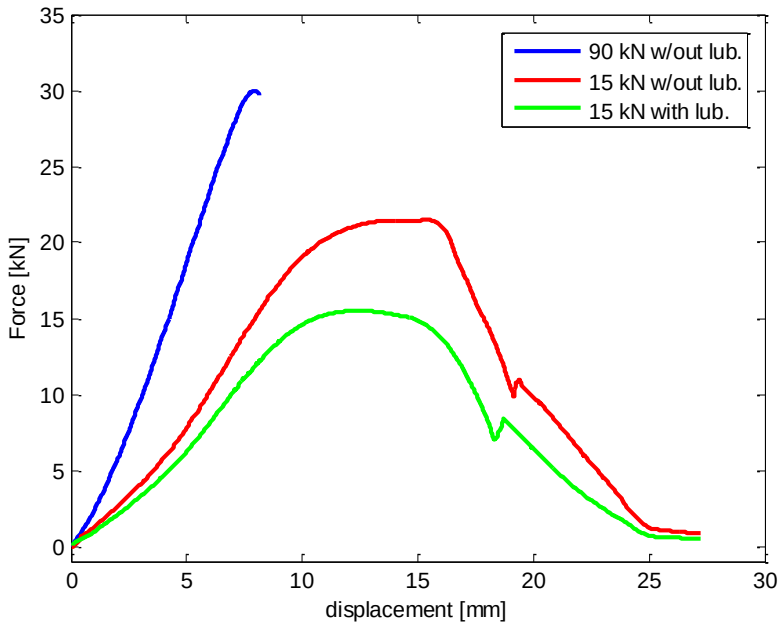

Figure 6.3 – Experimental force-displacement curves of the cylindrical cup tests carried out for DC04 mild steel.

The experimental acquisition of the strain field on part of the outer surface of the cylindrical cup can be seen as challenging due to several limitations present in this type of forming process. First of all, it cannot be obtained continuously during the experiment due to the device configuration. Thus, for acquiring these experimental data, a procedure that consists in the capture of an image of the blank before and after the experiment was adopted. In this way, this procedure imposed that several test experiments must be performed when strain fields at different punch displacements (d_{punch}) are desired (Coër, 2013). Consequently, for obtaining the strain field distribution at different punch displacements, several experiments, either leading to full drawing or to rupture, must be repeated. For instance, in the case of the test leading to full drawing, the data acquisition was carried out for d_{punch} equals to 7.6 and 15 mm, and also up to

the end of drawing, while in the case of the test that led to premature rupture, the data acquisition was performed for d_{punch} equals to 7.6 and 8.2 mm. This last value corresponded to the final value when rupture occurred.

Figures 6.5 and 6.6 illustrate the force-displacement curves including the major strain distribution obtained in the tests leading to full drawing (F_{holder} = 15 kN with lubrication and polypropylene film) and premature rupture (F_{holder} = 90 kN without lubrication nor polypropylene film), respectively.

The procedure adopted for acquiring the strain field information in this experiment depends on placing correctly the blank for capturing the images. The same blank position for the initial and final images recorded by DIC is required in order to be possible to establish an accurate correlation between the initial and final pattern of grey levels of the blank surface.

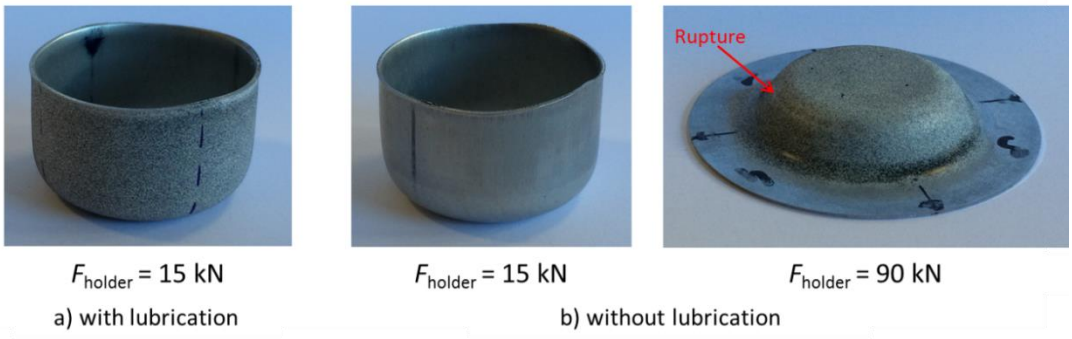

Figure 6.4 – Blank shapes obtained for the cylindrical cup test considering different experimental conditions.

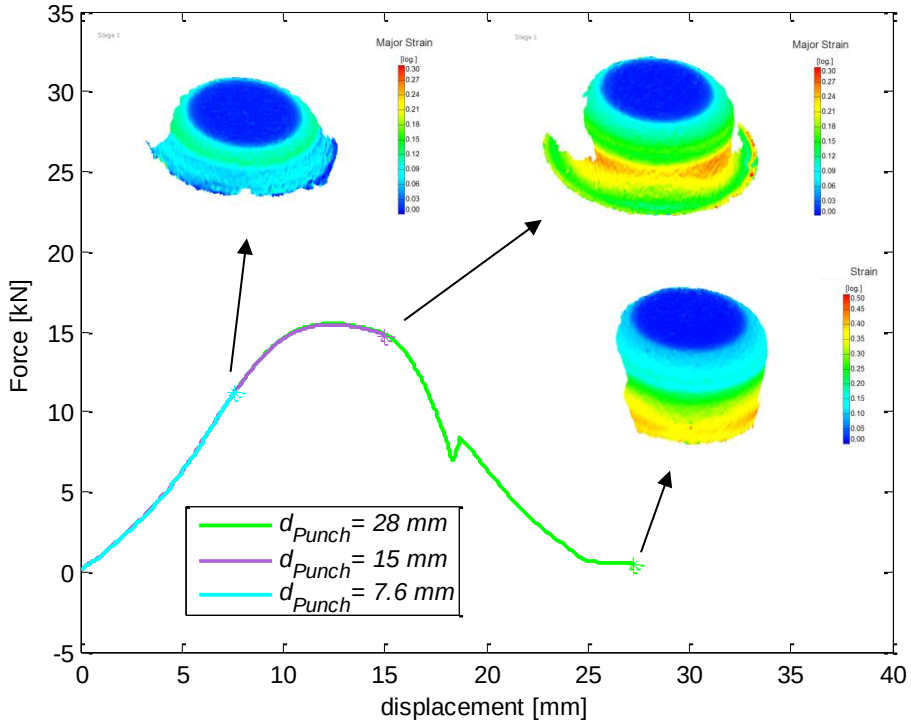

Figure 6.5 – Experimental force-displacement curves using F_{holder} = 15 kN and major strain distribution of the cylindrical cup test leading to full drawing for the different displacements (d_{punch}) considered.

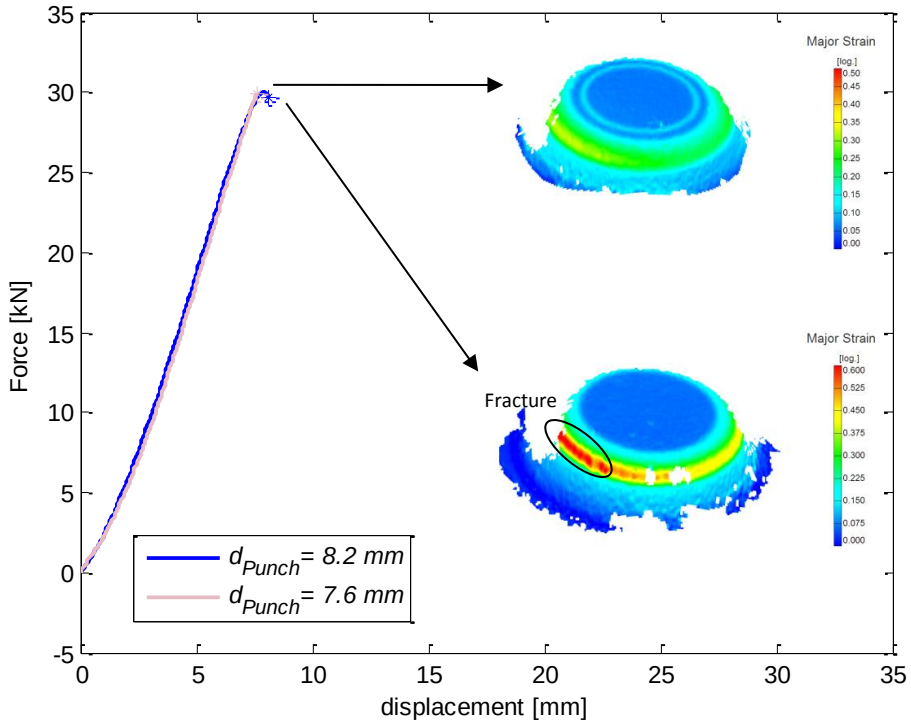

Figure 6.6 – Experimental force-displacement curves using F_{holder} = 90 kN and major strain distribution of the cylindrical cup test leading to premature rupture for the different displacements considered.

The damage of the painting was inherent to the contact of the blank surface with the tools and led to another limitation of the procedure. This limitation can be successfully avoided by adding a polypropylene film between the blank painted surface and the tools, which made possible the preservation of the painting. For this reason, in the experiment leading to full drawing, a polypropylene film was included. In the case of the experiment leading to premature rupture of the blank, even though the severe conditions considered, the strain field can be acquired without using the polypropylene film since the drawing up to rupture did not destroy the painting.

Additional data information was output concerning the cylindrical cup test leading to rupture. The final diameter ($L_{draw\text{-}in}$) of the blank at 0° and 90° to RD when rupture occurred was measured. Figure 6.7 illustrates the measurement of the final diameter and these values are further listed in Figure 6.11. Comparing the measured $L_{draw\text{-}in}$ values with the initial diameter of the blank (60 mm) it can be stated that no significant drawn-in occurred during the test up to rupture of the blank.

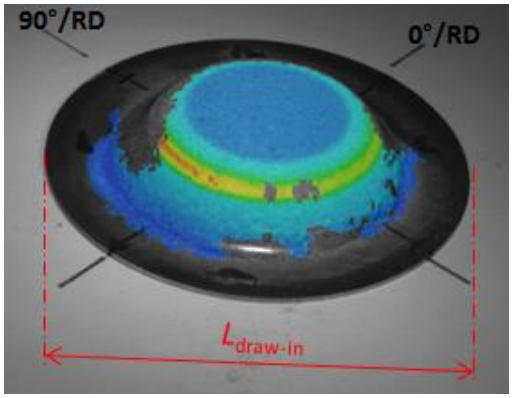

Figure 6.7 – Experimental image of the blank at the rupture captured by DIC system.

6.3 Numerical modeling

The numerical simulation of the cylindrical cup test was performed considering implicit time integration scheme using ABAQUS/Standard. Only one quarter of the blank was modeled due to the material and process symmetries and it was meshed with 3D 8-node linear isoparametric elements with reduced integration (C3D8R). Concerning the tools, namely, die, punch and blank-holder, these were modeled as analytical rigid surfaces. The mesh size defined for the blank was in agreement with the mesh selected for the numerical simulation of the tensile experiment up to rupture. This is a crucial point because W_{CL}^{f} and W_{RT}^{f} are valid for a given mesh size. Figure 6.8 shows the mesh adopted for FE simulation. The number of element layers used in the thickness was 4 and the blank was meshed with a total of 13348 elements.

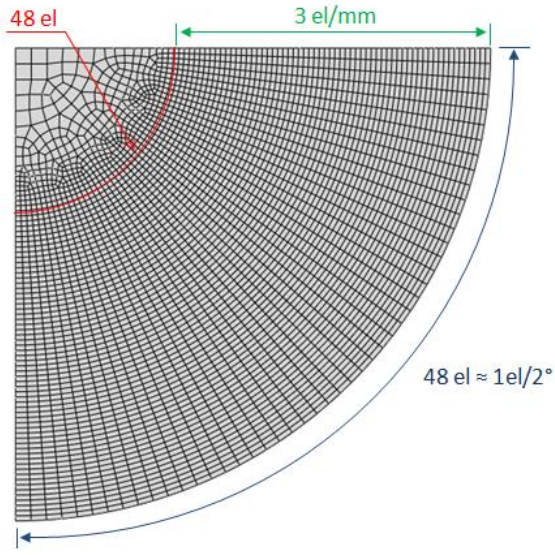

Figure 6.8 – Blank mesh used for the deep drawing simulation.

Analyzing Figure 6.8, it can be seen that two different mesh densities were chosen. Coarse and fine meshes were defined in the center zone and in the rest of the blank, respectively. On one side, the coarse mesh was defined in the zone which is in contact with the bottom of the punch and where no significant deformation occurs. On the other side, the fine mesh, with a density of 3

el/mm (such as mesh 2 of the numerical model of the tensile experiment up to rupture), was defined in the blank region subjected to high strains.

The contact between the blank and the tools was modeled with the Coulomb's law for friction, using a friction coefficient $\mu = 0.06$ for the experiment with lubrication and $\mu = 0.22$ for the experiments without lubrication. These values were fixed in order to have a good compromise between experimental and numerical results within a reasonable μ range. In Figure 6.9, the assembly of the test device composed by the blank and tools is illustrated.

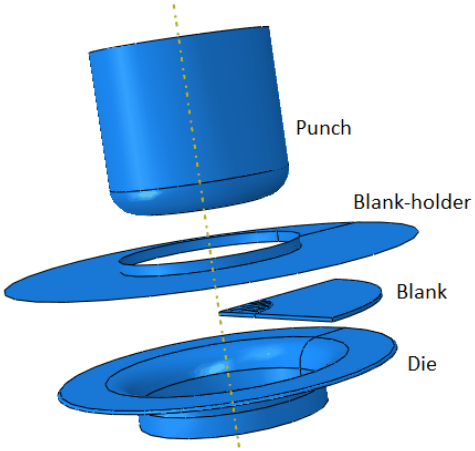

Figure 6.9 – Numerical assembly of the cylindrical cup device.

6.4 Results

In this section, the experimental and numerical results obtained for the cylindrical cup test of DC04 mild steel were compared with the aim of validating the material parameters as well as the fracture values calibrated for both *Yld2004-Iso*$_{Mod}$ and *Yld2004-Mixed*$_{Mod}$ models.

Figure 6.10 depicts the experimental and numerical force-displacement curves obtained both for the full cup drawing ($F_{holder} = 15$ kN) and rupture ($F_{holder} = 90$ kN) of the blank using both *Yld2004-Iso*$_{Mod}$ and *Yld2004-Mixed*$_{Mod}$ models. From this figure, it is shown that a very reliable prediction of the force-displacement curves relative to the experiments leading to full drawing of the blank ($F_{holder} = 15$ kN, either with or without lubrication) is obtained using both models. In the case of the experiment leading to premature rupture of the blank ($F_{holder} = 90$ kN), some discrepancy between experimental and numerical force-displacement evolution was observed. This discrepancy may result from some residual blank material adhesion on the tools, which was observed during the experiment. It was not considered in the numerical simulation. Moreover, the absence of lubrication in this experiment also increased the difficulty of its numerical prediction since in this condition the contact property was hard to properly define.

The experimental and numerical final diameters of the blank for the experiment leading to rupture of the blank were also compared. Figure 6.11 presents the experimental and numerical $L_{draw\text{-}in}$ values measured for both *Yld2004-Iso*$_{Mod}$ and *Yld2004-Mixed*$_{Mod}$ models. It can be seen that the numerical simulations using both *Yld2004-Iso*$_{Mod}$ and *Yld2004-Mixed*$_{Mod}$ models underestimate the experimental $L_{draw\text{-}in}$ values. Numerically, a larger displacement of the blank region in contact with the blank-holder and the die was verified comparing with the experimental observations.

Thus, the numerical simulations allowed the material to flow more in the die cavity than occurred experimentally. It also highlights that the contact property was not properly defined.

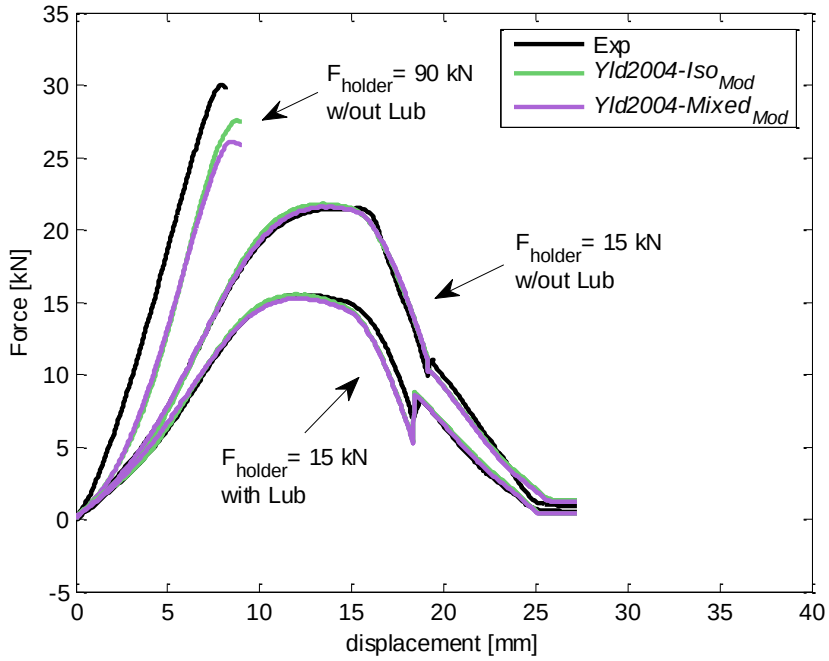

Figure 6.10 – Experimental and numerical force-displacement curves obtained for the deep drawing experiments using both *Yld2004-Iso*$_{Mod}$ and *Yld2004-Mixed*$_{Mod}$ models.

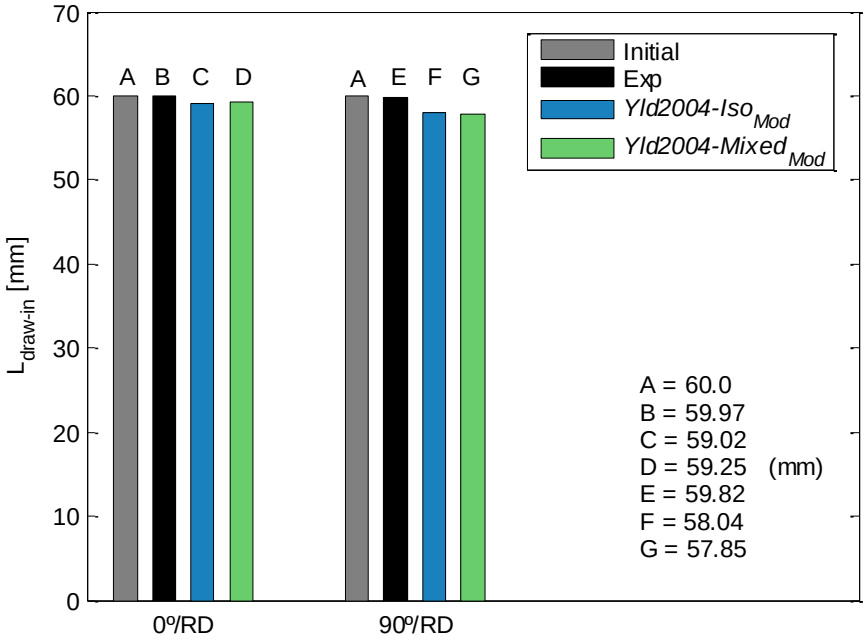

Figure 6.11 – Experimental and numerical $L_{draw\text{-}in}$ values measured in the blank at 0° and 90° to RD.

The major strain distribution over the blank for several punch displacements (7.6, 15 mm and at the end of the drawing) was numerically predicted for the experiment with F_{Holder} = 15 kN and using lubrication. These results were compared with the experimental ones, as illustrated in

Figure 6.12. This figure shows that an overall accurate representation of the experimental distributions was obtained with both *Yld2004-Iso*$_{Mod}$ and *Yld2004-Mixed*$_{Mod}$ models. Concerning the major strain distribution for a punch displacement of 7.6 mm, it can be seen that the larger major strain value was about of 0.18 and it was reached on the blank region which was in contact with the punch radius zone. Note that the blank zone in-between blank-holder and die was not captured by DIC image. The numerical major strain distribution obtained with both models was identical and is in agreement with the experimental observation. The punch displacement of 15 mm corresponds approximately to the displacement at the middle of the drawing experiment and its major strain distribution revealed a maximum level of strain about of 0.27. It was achieved for the blank region in contact with the radius die zone. Such a zone corresponds to the one where the blank was subjected to the highest starching at this deformation stage. Both numerical models were able to predict the experimental major strain distribution, also presenting similar results. Relatively to the major strain distribution at the end of the drawing, it can be observed that the largest strain was about 0.45. The numerical major strain distributions of both *Yld2004-Iso*$_{Mod}$ and *Yld2004-Mixed*$_{Mod}$ models were able to describe the experimental results, however, the blank zone with higher major strain distribution was less pronounced than the experimental one. Note that no significant differences were observed between the major strain distributions predicted by both *Yld2004-Iso*$_{Mod}$ and *Yld2004-Mixed*$_{Mod}$ models. Indeed, the main difference between these two models is the fact that *Yld2004-Mixed*$_{Mod}$ accounts for the kinematic hardening. Nonetheless, such contribution is not observed in these experimental results and, therefore, it was expected to achieve similar predictions using both numerical models.

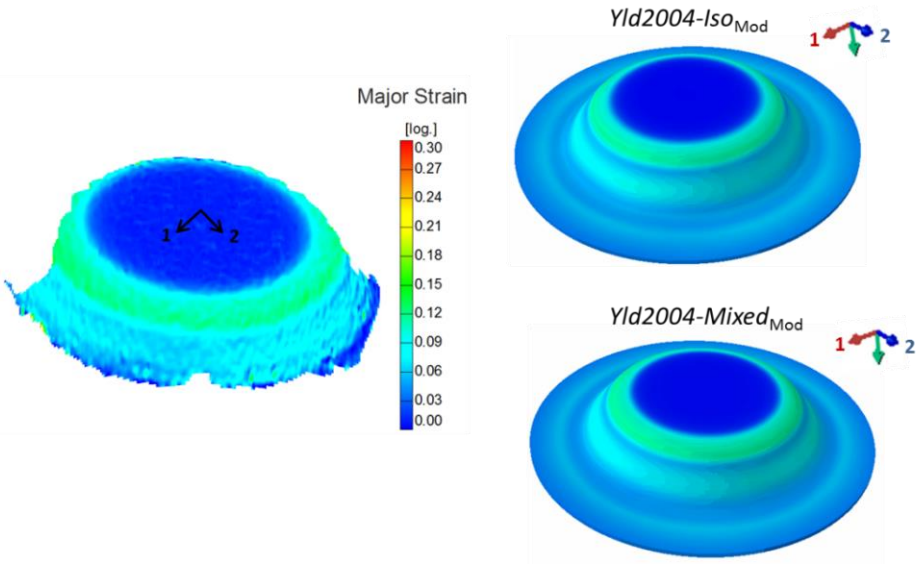

a) d_{punch} = 7.6 mm

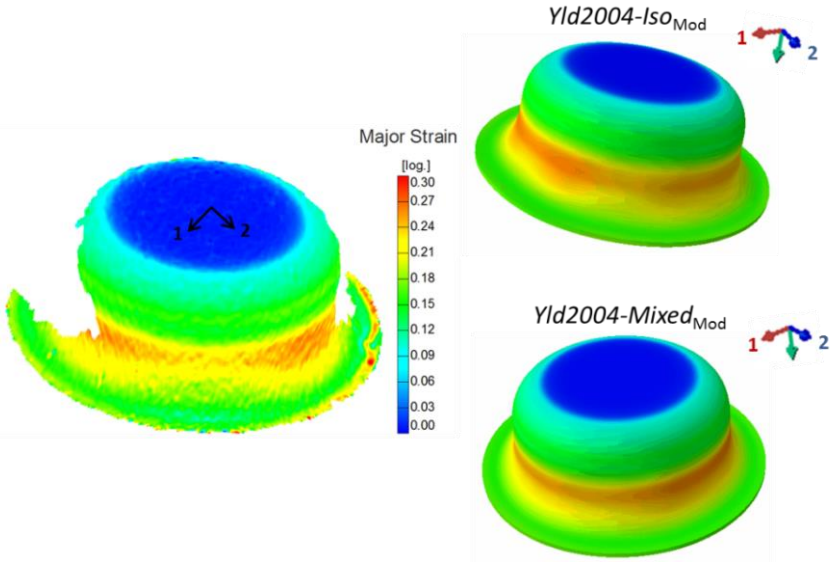

b) d_{punch} = 15 mm

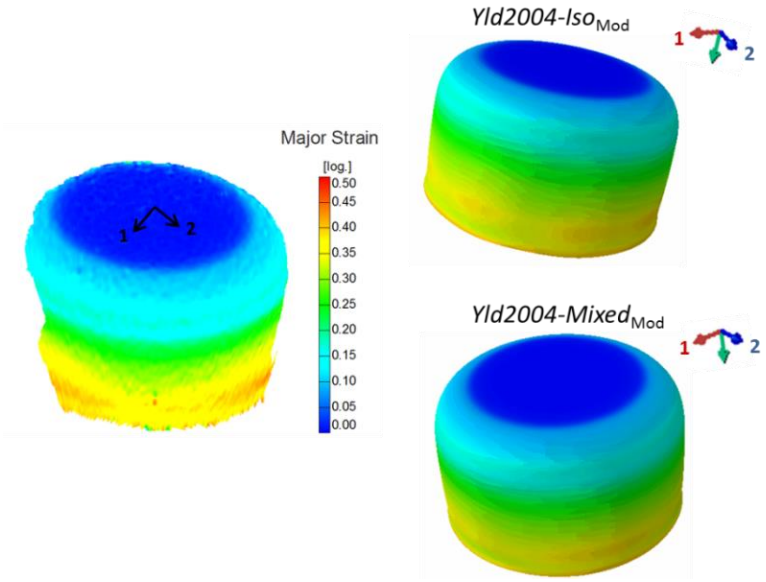

c) End of drawing

Figure 6.12 – Experimental and numerical major strain distribution for several punch displacements obtained in the experiment leading to full drawing, F_{holder} = 15 kN using lubrication.

For the experiment relative to the end of the drawing, experimental and numerical major and minor strain evolutions were compared for different sections of the blank, as shown in Figure 6.13. Taking the major strain at 45° to RD, which corresponds to the lowest value, as the reference, the relative gap between the major strain in RD (at 90°/RD respectively) and the reference was calculated from the experimental results and numerical predictions. For the section at 3 mm from the cup rim, these gaps are 10% from the experiments whereas the numerical simulations for both models lead to lower values of 5%, approximately. The same underestimation of the simulation was found for the section lying at 7 mm from the cup rim. The earing amplitude of deep drawing cups is related to planar anisotropy and these results revealed a less pronounced one by the numerical models, however, the same evolution was predicted.

Concerning the experiment leading to rupture of the blank, a visual comparison of the experimental and numerical major strain distribution was performed for d_{punch} equals to 7.6 and 8.2 mm (rupture), as shown in Figure 6.14. It can be seen that the experimental fracture zone is accurately detected by both numerical models, with an accurate representation of the experimental distributions with exception of the fracture zone, where the major strain was underestimated. The difference between the experimental and numerical major strain distribution in the fracture zone of the cylindrical cup could be expected due to the previous discrepancy observed in the force-displacement curve, shown in Figure 6.10.

CL and RT fracture distributions at rupture of the blank (d_{punch} equal to 8.2 mm) are represented in Figure 6.15. It can be highlighted that the critical value for CL and RT criterion using both *Yld2004-Iso*$_{Mod}$ and *Yld2004-Mixed*$_{Mod}$ models were reached in the fracture zone of the blank. Therefore, the fracture parameters were calculated and these values are listed in Table 6.1. Additionally, the critical ones (W_{CL}^{f} and W_{RT}^{f}), calibrated by the tensile test up to rupture, as well as the stress triaxility values were also listed in Table 6.1.

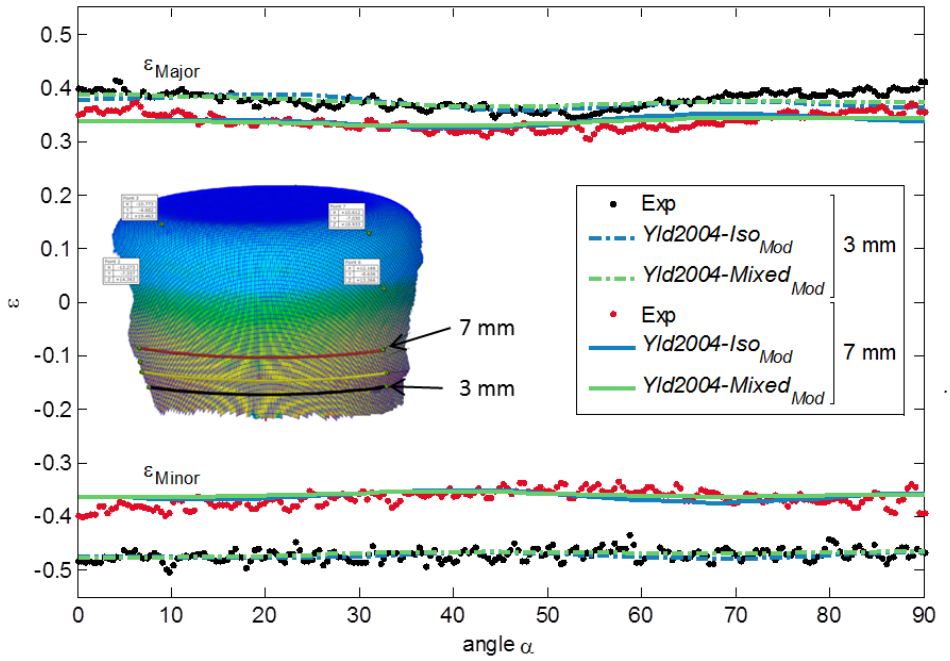

Figure 6.13 – Experimental and numerical major and minor strain evolution at the end of the drawing (sections at 3 and 7 mm to the base of the blank) obtained in the experiment with F_{holder}=15 kN and using lubrication.

It can be seen that W_{RT} fracture parameters obtained for the cylindrical cup test using both *Yld2004-Iso*$_{Mod}$ and *Yld2004-Mixed*$_{Mod}$ models were over-predicted while W_{CL} parameters were both under-predicted. In the case of RT fracture criterion, the rupture parameter was already exceeded W_{RT}^{f} critical value when the numerical rupture in the cylindrical cup test occurs. Conversely, in the case of CL fracture criterion, the rupture parameter has not reached yet its critical value W_{CL}^{f} when rupture occurs numerically in the blank. Based on the numerical results

obtained for the experiment leading to rupture of the blank, it was verified that the prediction of the fracture parameter with lower relative gap is achieved for CL criterion using *Yld2004-Mixed*$_{Mod}$ model. For this model, W_{CL} fracture value was predicted with a relative gap of 13%. In addition, the reference and the obtained stress triaxility χ values were also compared, as shown in Table 6.1. In the case of both numerical models, χ values obtained in the cup drawing test are far to the reference ones coming from the tensile test up to rupture. Therefore, the triaxility ratio χ is different for both tensile test up rupture and cylindrical cup experiments and the discrepancy verified between the critical (W_{CL}^{f} and W_{RT}^{f}) and fracture values (cylindrical cup test) suggests that CL and RT criterion may not be able to perform reliable predictions in this χ range.

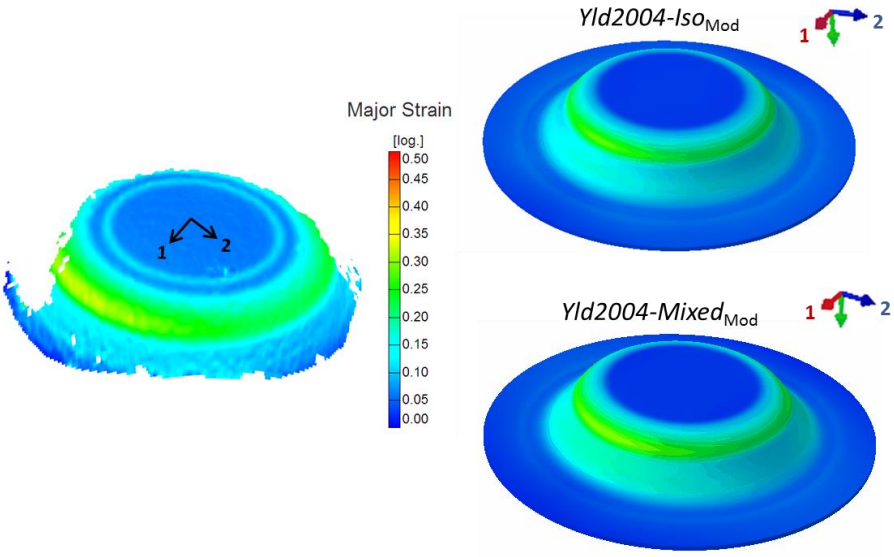

a) d_{punch} = 7.6 mm

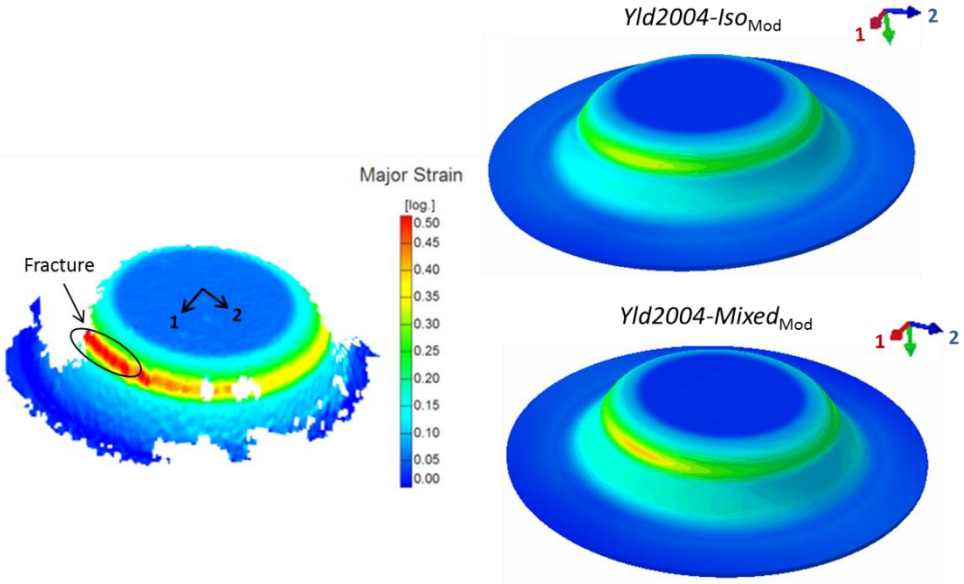

b) d_{punch} = 8.2 mm

Figure 6.14 – Experimental and numerical major strain distributions obtained in the experiment leading to rupture, F_{holder}=90 kN without lubrication.

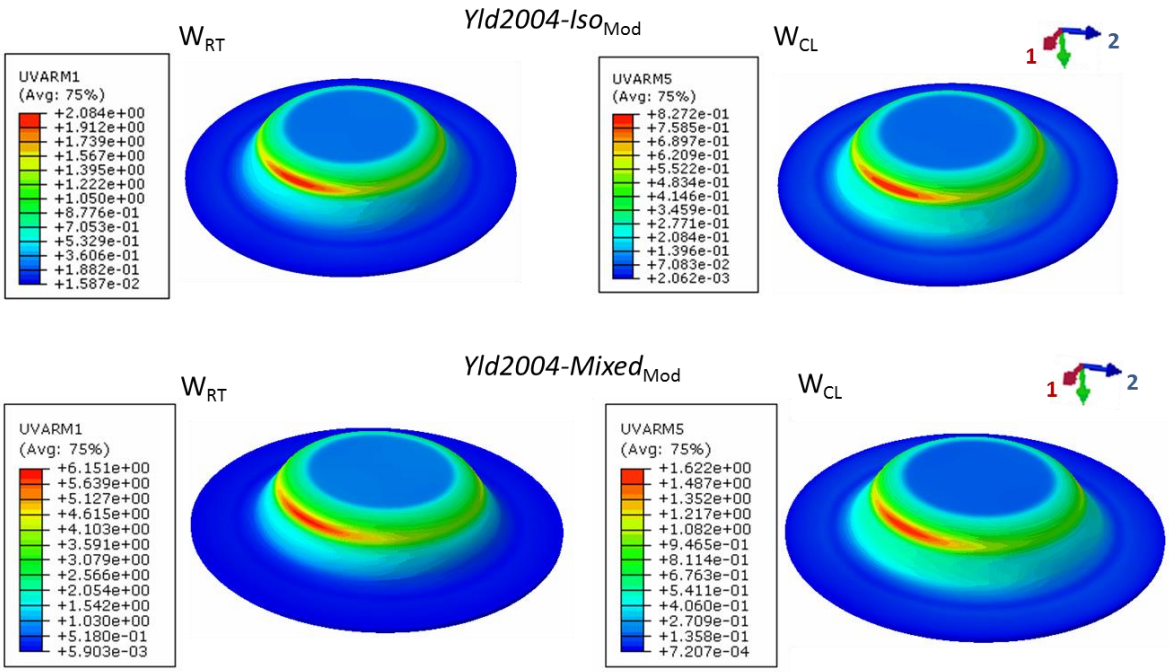

Figure 6.15 – Fracture criteria distribution at the moment of rupture (d_{punch} = 8.2 mm) using both *Yld2004-Iso*$_{Mod}$ and *Yld2004-Mixed*$_{Mod}$ models.

Table 6.1 – Critical and numerical W_{RT} and W_{CL} values and stress triaxiality (χ) calculated in the experiment leading to rupture using both *Yld2004-Iso*$_{Mod}$ and *Yld2004-Mixed*$_{Mod}$ models.

	Critical	*Yld2004-Iso*$_{Mod}$	Critical	*Yld2004-Mixed*$_{Mod}$
W_{CL}	0.90	0.73	1.68	1.46
W_{RT}	1.52	1.83	2.51	5.55
χ	0.49	0.81	0.94	1.43

In order to investigate the strain state in the fracture zone at the rupture of the blank, the ratio between the minor and major principal strains ($\varepsilon_2/\varepsilon_1$) in the sheet plane was numerically evaluated. Note that the formability of sheet metals is related to the strain state and such strain state is commonly defined by the combination of these major ε_1 and minor ε_2 principal strains. As a consequence, this ratio allows to distinguish for different strain states. Therefore, the numerical evolutions of $\varepsilon_2/\varepsilon_1$ ratio over the blank for d_{punch} equals to 4, 5, 6, 7 and 8.2 mm using both *Yld2004-Iso*$_{Mod}$ and *Yld2004-Mixed*$_{Mod}$ models were investigated and are illustrated in Figure 6.16. The results obtained for both numerical models reveal that $\varepsilon_2/\varepsilon_1$ ratio tends near zero with the increase of the equivalent plastic strain, which means that the strain state at the rupture of the blank corresponds to near plane strain state. In addition, the results depicted in Figure 6.16 also give information concerning the maximum equivalent plastic strain reached at the moment of rupture. It can be seen that both numerical models achieved different values. In the case of *Yld2004-Iso*$_{Mod}$ model the maximum equivalent plastic strain was about of 0.74, while in the case of *Yld2004-Mixed*$_{Mod}$ model, the equivalent plastic strain was approximately 0.8.

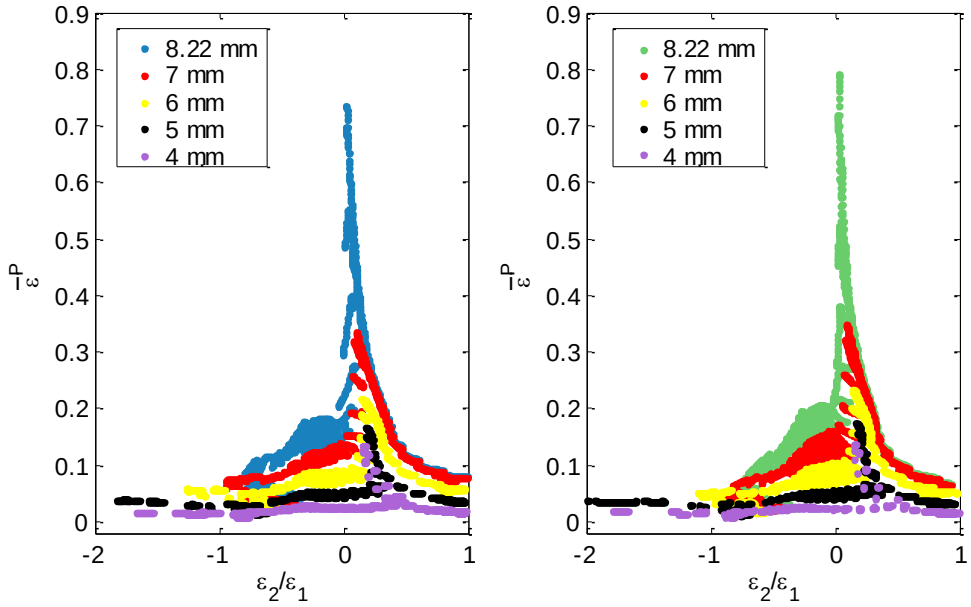

Figure 6.16 – Numerical $\varepsilon_2/\varepsilon_1$ evolution over the blank for several d_{punch} values in the experiment leading to rupture using a) *Yld2004-Iso*$_{Mod}$ and b) *Yld2004-Mixed*$_{Mod}$ models.

6.5 Conclusion

The purpose of this chapter was the validation of the material parameter sets presented in chapter 5, as well as the RT and CL critical values, by considering a deep drawing experiment. A cylindrical cup test was carried out, considering different conditions in order to obtain (i) full drawing of the blank, to validate the material parameters, and (ii) premature rupture of the blank, to validate CL and RT fracture criteria. Experimental and numerical force-displacement curves, final diameter of the blank and major strain distribution over the blank for several punch displacements were assessed.

In the case of the experiment leading to full drawing, a reliable reproduction of the experimental force-displacement curve and major strain distributions over the blank was obtained using both numerical models. In consequence, the material parameters identified for both *Yld2004-Iso*$_{Mod}$ and *Yld2004-Mixed*$_{Mod}$ models were successfully validated.

Concerning the experiment leading to premature rupture of the blank, some discrepancy between the experimental and numerical force-displacement curve was observed for both phenomenological models. The experimental and numerical major strain distributions over the blank were compared for punch displacements of 7.6 and 8.2 mm (rupture). The results stressed out that the experimental fracture zone was accurately detected by both numerical models and a good prediction of the experimental distributions with exception to the fracture zone, where the major strain distribution is underestimated, was obtained.

CL and RT fracture distributions at rupture of the blank (d_{punch} equal to 8.2 mm) were also evaluated. W_{RT} values obtained in the cylindrical cup test were over-predicted while W_{CL} values were under-predicted when compared with the critical ones (W_{CL}^{f} and W_{RT}^{f}) determined using a

tensile test up to rupture. In the case of *Yld2004-Mixed*$_{Mod}$ model, W_{CL} fracture value was predicted with a relative gap of 13%. The stress triaxiality was also investigated in the experiment leading to rupture of the blank using both numerical models. It was observed that the triaxility ratio was different for the tensile test up to rupture (reference) and cylindrical cup tests. The discrepancy observed between the critical (W_{CL}^{f} and W_{RT}^{f}) and fracture parameters obtained suggests that CL and RT criterion may not be able to perform reliable predictions due to the different stress triaxiality range.

Though some difference in the validation of W_{CL}^{f} using *Yld2004-Mixed*$_{Mod}$ model, it was considered that such difference remained acceptable, mainly due to the substantial difficulty in reproducing the experimental friction conditions of the cylindrical cup test leading to rupture but also regarding the different stress triaxiality range. Therefore, knowing that the anisotropy and hardening behavior of DC04 mild steel was successfully validated then, *Yld2004-Mixed*$_{Mod}$ model and CL criterion, by considering its critical W_{CL}^{f} value, will be used on the design of the computational mechanical test.

IV – Computational design of mechanical tests

Chapter 7

Development of an indicator

7.1 Introduction

The main goal of this PhD is the optimized design of a mechanical test able to promote a thorough reproduction of the sheet metal behavior. For that, such a test must congregate most of the several strain paths and amplitudes encountered in classical mechanical tests. Therefore, during the optimization process of its design, each of these features needs to be accurately evaluated in order to achieve an improved experiment most suitable for material parameters identification.

Due to this reason, the purpose of this chapter is the development of an indicator able to assess, quantitatively, the main features of mechanical tests. This indicator is decisive for determining, during the optimization procedure, if a given mechanical test provides more information for the characterization of the material behavior than another one. In this way, it is possible to satisfy the current aims of the mechanical characterization, for instance, to find a non-homogeneous strain field that (i) promotes the identification of large sets of material parameters and (ii) improves the quality of the identified parameters. Thus, by ranking the information provided by the tests, the proposed indicator can be used to guide the design of the mechanical test.

Thereby, in this chapter, the formulation of an indicator focused on the mechanical behavior of sheet metal is presented and applied considering classical as well as heterogeneous tests presented in chapter 2. The performance of these several tests is compared and their reliability on the mechanical behavior characterization is rated and ranked. Moreover, with the aim of validating the results obtained with the proposed indicator, a material parameter sensitivity study is carried out for the chosen tests.

It must be highlighted that, in a first step, strain path change is not considered in the formulation of the indicator and, as a consequence, only monotonic experiments are evaluated. Nonetheless, according to Schmitt et al. (1985) the parameter Θ can be used to describe strain path changes. This parameter is defined as the cosine of the angle in the strain space between the strain rate tensors during the pre-strain $\mathbf{D}_1^P$ and the subsequent strain path $\mathbf{D}_2^P$,

$$\Theta = \frac{\mathbf{D}_1^P : \mathbf{D}_2^P}{\left\|\mathbf{D}_1^P\right\| \cdot \left\|\mathbf{D}_2^P\right\|}, \tag{7.1}$$

where $\Theta \in [-1,1]$ assumes value 1, -1 and 0 for monotonic, reversed and orthogonal strain path, respectively. This parameter is useful in two-stage tests, however, sheet metal forming processes usually do not consist of two monotonic strain paths. Multistep deep drawing processes can exhibit such changes, but single-step deep drawing processes show continuous strain path changes and a clear distinction of individual strain paths cannot be made (van Riel and van den Boogaard, 2007; Thuillier *et al.*, 2010).

7.2 Features of the indicator

In order to properly formulate the indicator, it is mandatory to define a list of the main features and mechanical phenomena observed in sheet metal forming that should be covered. Only in this way, will it be possible to develop a quantitative indicator able to show that one mechanical test is more informative[4] than another one. Hence, the indicator must be an evaluation criterion rating the difference between tests and should include the following aims:

- recognize and quantify all distinct strain states presented in the mechanical test, favoring tests that cover larger strain state range with a minor number of gaps.
- analyze the deformation heterogeneity of the specimen during the test, promoting tests with large non-homogeneity.
- evaluate the maximum strain achieved for the most important strain states, promoting the increase of these values.
- quantify the average strain level, taking into account the geometry, and favoring large values of this average strain.
- promote a continuous evaluation of the test up to rupture.
- promote the unicity of the solution when identification strategies are used.

The listed features should be quantified to define the indicator and must be continuously evaluated during the test up to rupture. These can be arranged in the following two groups: (i) strain state range and heterogeneity and (ii) strain level.

In addition, the proposed indicator must be evaluated from both real (experiments) as well as virtual (numerical simulation) tests. For that purpose, since strain level is considered, it is just necessary take into account a definition of equivalent plastic strain $\bar{\varepsilon}^P$. As example, in the case of experimental data, the elastic strain ε^e can be neglected comparatively to the plastic strain ε^P because $\varepsilon^P >> \varepsilon^e$ and a von Mises equivalent strain definition can be adopted. Concerning numerical results, an equivalent plastic strain can be defined based on von Mises criterion or on the yield criterion used to characterize the material behavior.

[4] A mechanical test is considered more informative if a larger number of mechanical phenomena and stress/strain states are covered.

7.2.1 Strain state range and heterogeneity

Several strain states are expected during sheet metal forming processes. Due to this, the strain state range of the test must be taken into account by the indicator. The ratio between the minor ε_2 and major ε_1 principal strains in the sheet plane can be considered in order to analyze the strain state range. Indeed, this ratio is commonly used to evaluate the formability of sheet metals by means of Forming Limit Diagram (FLD). Note that due to the incompressibility condition, only two principal strains are required and, consequently, the ratio $\varepsilon_2/\varepsilon_1$ leads to a different value for each strain state. Figure 7.1 shows the most relevant strain states observed in sheet metal forming as well as their $\varepsilon_2/\varepsilon_1$ ratio considering material isotropy. In this way, the strain state range $(\varepsilon_2/\varepsilon_1)_R$ covered by the mechanical test can be calculated by using the maximum and minimum $\varepsilon_2/\varepsilon_1$ values achieved in the test as

$$\left(\frac{\varepsilon_2}{\varepsilon_1}\right)_R = \left(\frac{\varepsilon_2}{\varepsilon_1}\right)_{max} - \left(\frac{\varepsilon_2}{\varepsilon_1}\right)_{min} . \tag{7.2}$$

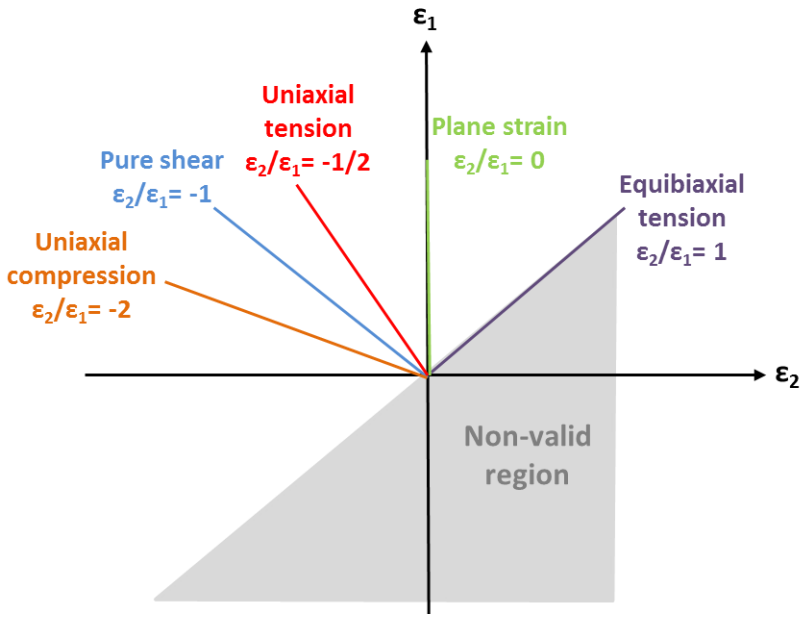

Figure 7.1 – Range of $\varepsilon_2/\varepsilon_1$ values of the most relevant strain states observed in sheet metal forming, considering material isotropy.

However, $(\varepsilon_2/\varepsilon_1)_R$ may not be able to characterize fully the strain state range information. Indeed, the diversity of the mechanical information obtained by the strain state range is not characterized by Equation 7.2, since large strain state bounds do not necessarily means large diversification of the mechanical information provided by the test. A practical example of this situation consists in the conventional simple shear test using rectangular specimen. Indeed, most part of the specimen region corresponds to a simple shear strain state ($\varepsilon_2/\varepsilon_1 = -1$) and the remaining small regions near the free edges exhibit distinct strain states (tension and compression) (Bouvier *et al.*, 2006). Nevertheless, this test can be considered as quasi-homogeneous within the central area. The diversification of the mechanical information given by the test is a relevant feature that must be considered and can be evaluated measuring the strain

state range variation of the specimen during the test. In this work, such a variation of the strain state range was determined by the standard deviation (*Std*) of $\varepsilon_2/\varepsilon_1$ values obtained for the specimen during the test. Note that *Std* is a statistical function that shows how much dispersion from the average exists. A low *Std* value indicates that the data points tend to be very close to the mean (which is the case for homogeneous experiments) while a high *Std* value indicates that the data points are spread out over a large range of values, expected for heterogeneous experiments. $Std(\varepsilon_2/\varepsilon_1)$ is defined as

$$Std\left(\frac{\varepsilon_2}{\varepsilon_1}\right)=\sqrt{\frac{\sum_{i=1}^{n}[(\varepsilon_2/\varepsilon_1)_i-\mu_{\varepsilon_2/\varepsilon_1}]^2}{n-1}}, \tag{7.3}$$

where $(\varepsilon_2/\varepsilon_1)_i$ is the ratio $\varepsilon_2/\varepsilon_1$ for subarea or element *i* of the mesh, $\mu_{\varepsilon_2/\varepsilon_1}$ is the mean value of $\varepsilon_2/\varepsilon_1$ of the specimen and *n* is the number of elements or subareas. Indeed, histograms representing $\varepsilon_2/\varepsilon_1$ distribution of subareas of the sample or the elements of the meshed specimen, when using DIC measurements or FE analysis, are an easy way to visualize the applicability of $Std(\varepsilon_2/\varepsilon_1)$. Figure 7.2 shows two histograms with distinct $\varepsilon_2/\varepsilon_1$ distributions. In both cases, the same strain state range is covered. However, the diversity of the mechanical information provided differs significantly. A large distribution of element sets with similar number of elements in each set corresponds to a high diversity of the mechanical information leading to a high $Std(\varepsilon_2/\varepsilon_1)$, since a large quantity of elements is far from $\mu_{\varepsilon2/\varepsilon1}$, as illustrated by Figure 7.2 a). On the contrary, when the majority of the elements presents similar $\varepsilon_2/\varepsilon_1$ values, a lower $Std(\varepsilon_2/\varepsilon_1)$ for the test is obtained since the majority of the elements is close to $\mu_{\varepsilon2/\varepsilon1}$, as shown in Figure 7.2 b).

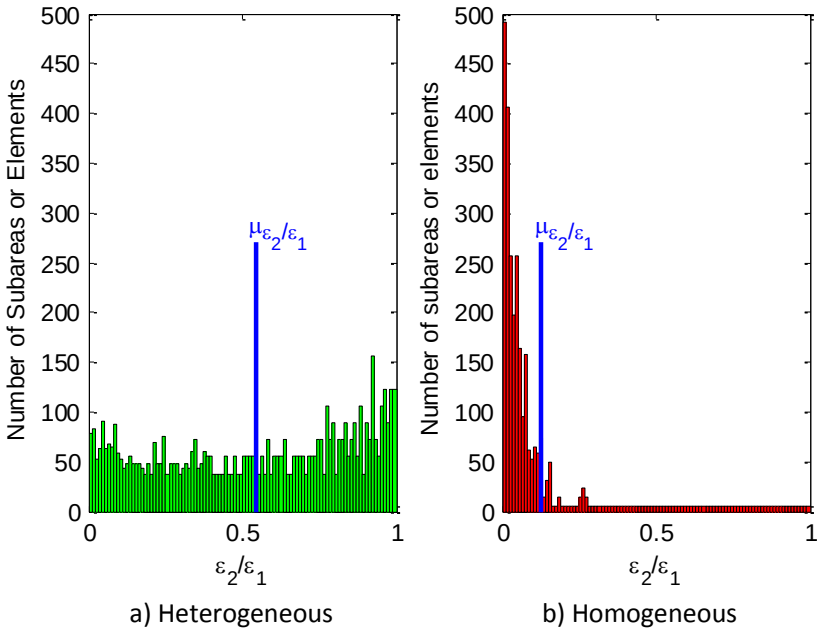

a) Heterogeneous b) Homogeneous

Figure 7.2 – Histograms representing $\varepsilon_2/\varepsilon_1$ distribution in finite subareas or elements in the specimen.

Additionally, it is well known that the non-homogeneity of the specimen deformation is also a crucial factor for the larger diversification of the mechanical information of the test. Consequently, the deformation heterogeneity of the specimen was also taken into account in the formulation of the indicator. In that respect, the non-homogeneity of the strain field during the test was evaluated through the variation of the equivalent plastic strain $\bar{\varepsilon}^{\mathrm{P}}$ by assessing $Std(\bar{\varepsilon}^{\mathrm{P}})$, such as

$$Std\ \left(\bar{\varepsilon}^{\mathrm{P}}\right)=\sqrt{\frac{\sum_{i=1}^{n}(\bar{\varepsilon}_i^{\mathrm{P}}-\mu_{\bar{\varepsilon}^{P}})^2}{n-1}}, \tag{7.4}$$

where $\bar{\varepsilon}_i^{\mathrm{P}}$ is the equivalent plastic strain of the specimen subarea or element i and $\mu_{\bar{\varepsilon}^{P}}$ is the mean $\bar{\varepsilon}^{\mathrm{P}}$ value of the sample at a given time.

7.2.2 Strain level

One of the main goals considered in the development of tests for material parameters identification is to reach the same deformation level as the one recorded in sheet metal forming processes. Hence, the strain $\bar{\varepsilon}_{\mathrm{Max}}^{\mathrm{P}}$ achieved during the test is a crucial data that must be evaluated by the indicator. $\bar{\varepsilon}_{\mathrm{Max}}^{\mathrm{P}}$ was calculated taking into account the maximum $\bar{\varepsilon}^{\mathrm{P}}$ value obtained for the test ($\bar{\varepsilon}_{\mathrm{test}}^{\mathrm{P}}$) as well as the $\bar{\varepsilon}^{\mathrm{P}}$ values for the most relevant strain states (*cf*. Figure 7.1), namely, equibiaxial tension ($\bar{\varepsilon}_{\mathrm{biaxial}}^{\mathrm{P}}$), simple shear ($\bar{\varepsilon}_{\mathrm{shear}}^{\mathrm{P}}$), uniaxial tension ($\bar{\varepsilon}_{\mathrm{tens}}^{\mathrm{P}}$), plane strain tension ($\bar{\varepsilon}_{\mathrm{plane}}^{\mathrm{P}}$) and uniaxial compression ($\bar{\varepsilon}_{\mathrm{comp}}^{\mathrm{P}}$), and can be written as

$$\bar{\varepsilon}_{\mathrm{Max}}^{\mathrm{P}}=\frac{\bar{\varepsilon}_{\mathrm{test}}^{\mathrm{P}}+\bar{\varepsilon}_{\mathrm{tens}}^{\mathrm{P}}+\bar{\varepsilon}_{\mathrm{shear}}^{\mathrm{P}}+\bar{\varepsilon}_{\mathrm{biaxial}}^{\mathrm{P}}+\bar{\varepsilon}_{\mathrm{comp}}^{\mathrm{P}}+\bar{\varepsilon}_{\mathrm{plane}}^{\mathrm{P}}}{6}. \tag{7.5}$$

Note that Equation 7.5 was defined by giving equal importance to each term and, then, $\bar{\varepsilon}_{\mathrm{Max}}^{\mathrm{P}}$ consists of an average value of the $\bar{\varepsilon}^{\mathrm{P}}$ values. It was considered that any strain state is not more relevant than the other ones. It is rather difficult to assume that, for example, uniaxial tension is more important than simple shear and, consequently, to attribute different weights for these strain states. Actually, from a strain state point of view, uniaxial tension and simple shear are complementary since the first one only involves diagonal components of the strain tensor while the second one involves non-diagonal components of the strain tensor.

Additionally, the average deformation obtained in the specimen was also considered on the definition of the indicator since this feature points out the global level of deformation imposed during the test. Larger values of the average deformation contribute to a more informative test. The average deformation $Av_{\bar{\varepsilon}^{\mathrm{P}}}$ of the test is calculated by

$$Av_{\bar{\varepsilon}^{\mathrm{P}}} = \frac{\sum_{i=1}^{n} \bar{\varepsilon}_i^{\mathrm{P}} v_i}{v_{\mathrm{T}}}, \tag{7.6}$$

where v_i is the volume of the element or subarea i and v_T is the total volume of the specimen. Note that, in order to normalize the average deformation to the specimen geometry, $Av_{\bar{\varepsilon}^{\mathrm{P}}}$ is defined accounting for the volume of the specimen. In this way, $Av_{\bar{\varepsilon}^{\mathrm{P}}}$ values for experiments with different specimen geometries can be compared.

7.3 Mathematical formulation

The indicator is formulated based on Equations 7.2-7.6 which characterize the strain state range and heterogeneity as well as strain level features. However, some considerations must be taken into account for its formulation.

For instance, the indicator must be based on a continuous evaluation of the strain field up to rupture. Though plastic instabilities can occur before achieving rupture for some tests, these phenomena may provide useful additional information for a better characterization of the material behavior. Cockroft and Latham (1968) fracture parameter $W_{\mathrm{CL}}^{\mathrm{f}}$ was used as an end condition to stop the numerical simulation.

Within the characterized features, $\bar{\varepsilon}_{\mathrm{Max}}^{\mathrm{P}}$ and $Av_{\bar{\varepsilon}^{\mathrm{P}}}$ consist of cumulative data of the test. As a result, just the values obtained at the end of the test were considered in the indicator calculation.

Nevertheless, $(\varepsilon_2/\varepsilon_1)_{\mathrm{R}}$, $Std(\bar{\varepsilon}^{\mathrm{P}})$ and $Std(\varepsilon_2/\varepsilon_1)$ are not cumulative and may change in subsequent increments of the test mostly due to the heterogeneity. As a consequence, the mean values of $Std(\bar{\varepsilon}^{\mathrm{P}})$ and $Std(\varepsilon_2/\varepsilon_1)$ calculated over the whole test time were considered in the definition of the indicator. Nonetheless, in the case of $(\varepsilon_2/\varepsilon_1)_{\mathrm{R}}$, just the value obtained at the end of the test was taken into account. This choice was made considering that $(\varepsilon_2/\varepsilon_1)_{\mathrm{R}}$ is dependent on the heterogeneity and, generally, the large heterogeneity of the test occurs at the rupture.

By considering the previous assumptions, the proposed indicator I_T was defined as

$$I_{\mathrm{T}} = w_{\mathrm{r1}} \frac{\mathrm{Mean}\left[\mathrm{Std}\left(\varepsilon_2/\varepsilon_1\right)\right]}{w_{\mathrm{a1}}} + w_{\mathrm{r2}} \frac{\left(\varepsilon_2/\varepsilon_1\right)_{\mathrm{R}}}{w_{\mathrm{a2}}} + w_{\mathrm{r3}} \frac{\mathrm{Mean}\left[\mathrm{Std}\left(\bar{\varepsilon}^{\mathrm{P}}\right)\right]}{w_{\mathrm{a3}}} + w_{\mathrm{r4}} \frac{\bar{\varepsilon}_{\mathrm{Max}}^{\mathrm{P}}}{w_{\mathrm{a4}}} + w_{\mathrm{r5}} \frac{Av_{\bar{\varepsilon}^{\mathrm{P}}}}{w_{\mathrm{a5}}}, \tag{7.7}$$

where w_{ri} and w_{ai} with i=1, …, 5 are relative and absolute weighting factors. Table 7.1 shows w_{ri} and w_{ai} values adopted for I_T.

Table 7.1 – Weighing factors used on the definition of I_T.

w_{a1}	w_{a2}	w_{a3}	w_{a4}	w_{a5}
1	4	0.25	1	1
w_{r1}	w_{r2}	w_{r3}	w_{r4}	w_{r5}
0.3	0.03	0.17	0.4	0.1

The absolute weighting factors w_{ai} correspond to the maximum achievable value for each one of the indicator terms. Therefore, these weighting factors are based on a physical meaning. The weights w_{a4} and w_{a5} were defined assuming that the maximum and average $\bar{\varepsilon}^{P}$ values that can be obtained are 1 whatever the test, which is a reasonable value regarding thin sheet metals. Concerning w_{a1} and w_{a3}, these absolute weighting factors were selected based on the mean values of $Std(\bar{\varepsilon}^{P})$ and $Std(\varepsilon_2/\varepsilon_1)$ obtained for the different tests considered further in section 7.4. In the case of w_{a2}, this one was defined limiting the strain state range between equibiaxial state ($\varepsilon_2/\varepsilon_1 = 1$) and a compression state presenting $\varepsilon_2/\varepsilon_1 = -3$, therefore, $w_{a2} = 4$. These bounds were imposed to the numerical analysis of $(\varepsilon_2/\varepsilon_1)_R$ since high negative values can be obtained, as can be seen in Figure 7.1. Moreover, the main strain states are covered by this range and in sheet metal forming it is not expected to obtain relevant compression states, due to buckling. The purpose of w_{ai} factors was to normalize each term of the indicator between 0 and 1, which is very useful for evaluating the several indicator contributions.

In the case of the relative weighting factors, these w_{ri} values can be defined by the user taking into account the importance attributed to each contribution. The indicator was formulated by the sum of five different terms and w_{ri} factors must be considered in order to (i) scale, for any mechanical test, the indicator value between 0 and unity and (ii) adjust the importance of each term in the calculation of the indicator. Note that, though each indicator term defines a different feature, some of these features are related.

For example, without deformation heterogeneity (Equation 7.4) it is not possible to obtain different strain states on the specimen (Equation 7.2). Nevertheless, high deformation heterogeneity does not lead inevitably to relevant strain states variation. It is observed when necking appears in the uniaxial tensile test since substantial strain heterogeneity occurs in the center of the sample but, the strain states covered remains almost the same. In addition, as pointed out in section 7.2.1, both features defined by Equations 7.2 and 7.3 are required for a full characterization of the strain state range information. Since, the strain state range value defined by Equation 7.2 may not be directly related with the diversification of the mechanical information provided by the test (Equation 7.3). Furthermore, the average strain level of the specimen (Equation 7.6) contributes for a more informative test. Notwithstanding, such feature can be considered less important than the maximum strain achieved on the test (Equation 7.5) because one of the main goals considered in the development of mechanical tests is to reach the same deformation level as the one recorded in sheet metal forming processes.

Considering the inherent relation between some of the indicator features, relative weighting factors are needed for defining the importance of each term. Thus, the focus of the relative weighting factors is adjusting the contributions of each one of the indicator terms aiming at a suitable calculation of I_T. Then, w_{ri} factors were defined attributing equal importance to the contributions of both strain state range/heterogeneity ($w_{r1} + w_{r2} + w_{r3} = 0.5$) and strain level ($w_{r4} + w_{r5} = 0.5$), which seems a reasonable decision. According to this, the several w_{ri} values listed in Table 7.1 were adjusted empirically. Additionally, for scaling the indicator value between 0 and unity, the sum of the several w_{ri} values is equal to 1. Then, the maximum I_T value that can be reached by a certain experiment is unity.

7.4 Numerical tests evaluation

Several tests were considered for evaluating the indicator I_T given by Equation 7.7: (i) uniaxial tensile test, (ii) plane strain tension test (Wagoner, 1981), (iii) simple shear test (Thuillier and Manach, 2008), (iv) classical biaxial test using cruciform specimen (Prates *et al.*, 2014), (v) equibiaxial bulge test (Sousa *et al.*, 2007), (vi) TIX test (Pottier *et al.*, 2011b), (vii) biaxial tensile test using a perforated cruciform sample (Teaca *et al.*, 2010) and (viii) tensile test using a shear-like tensile specimen (Haddadi and Belhabib, 2012). The reason for such a selection is the fact that these tests reproduce different types of stress/strain states. Additionally, it must be highlighted that these ones consist of classical or quasi-homogeneous (i, …, v) as well as heterogeneous tests (vi, …, viii) and their performance characterizing the material behavior can be compared. Indeed, by calculating I_T for each test it was possible to establish a raking, hence rating the importance of each one. This analysis allows inquire for the most informative test among the selected ones. Figures 7.3 and 7.4 show, respectively, the specimen geometries of the classical and heterogeneous tests. It must be noticed that the width of the plane strain specimen (Figure 7.3 d)) was increased for obtaining a more accentuated plane strain state in this test, since the original plane strain specimen proposed by Wagoner (1981) only promotes near-plane strain tension (as stated before in section 2.2.1.3).

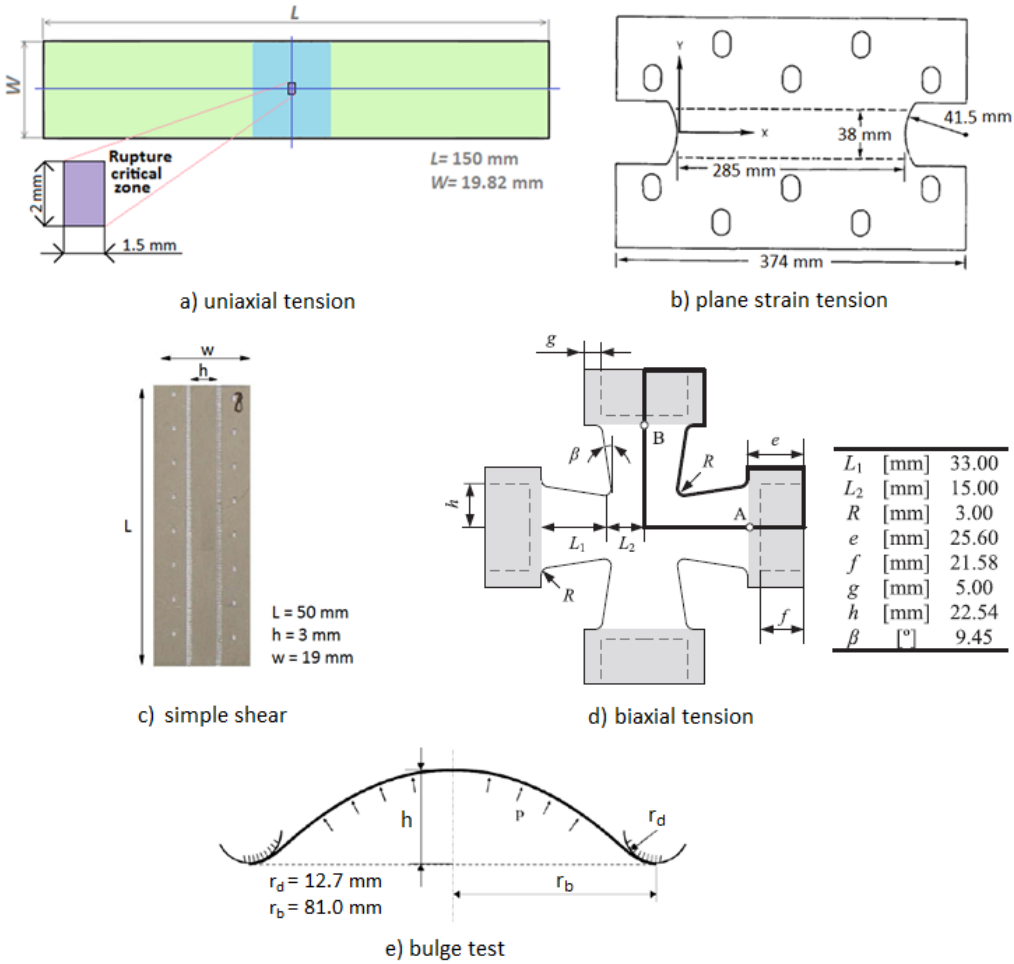

Figure 7.3 – Sample geometries of the classical tests.

The different tests adopted were generally discussed in chapter 2. However, it must be stressed out that the uniaxial tensile test considered corresponds to the tensile test used in chapter 5 for calibrating the rupture behavior of DC04 mild steel.

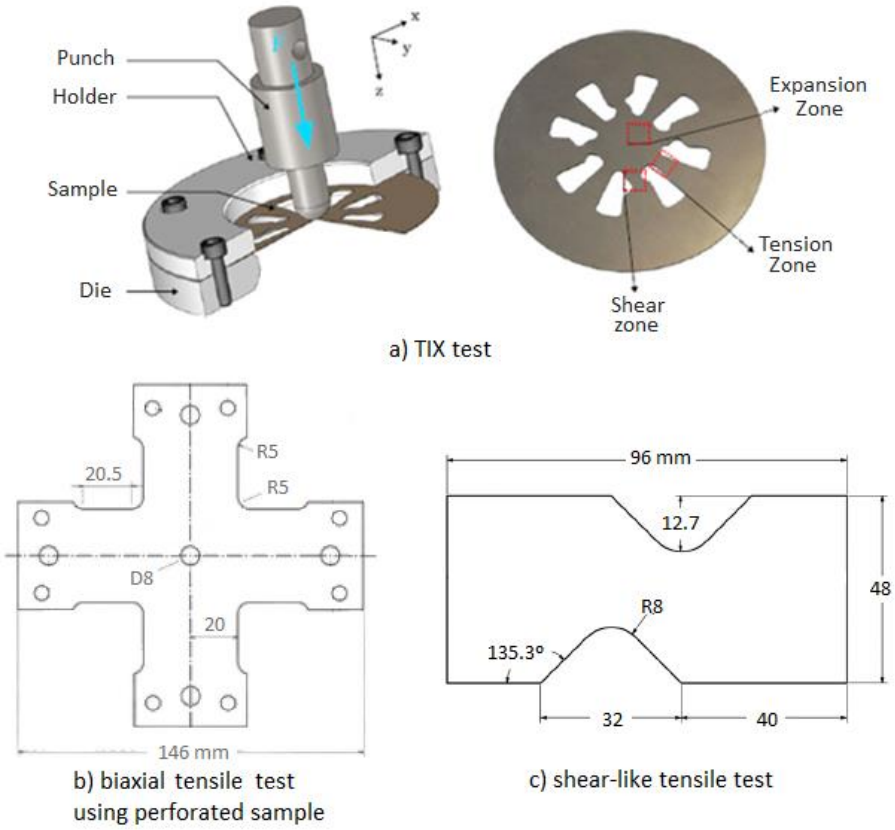

Figure 7.4 – Sample geometries of the heterogeneous tests.

The computational analysis was carried out considering implicit time integration scheme by using ABAQUS/Standard FE code. The tests were modeled with 3D 8-node linear isoparametric elements with reduced integration (C3D8R) and with hourglass control. Symmetry conditions were used for uniaxial tensile, bulge, biaxial tensile and plane strain tests with the purpose of saving computational time. Only one fourth of uniaxial tensile (symmetry in the thickness and width), bulge and biaxial tension geometries were modeled while half specimen was considered in the case of plane strain test. Figure 7.5 shows the boundary conditions for all the tests. It must be mentioned that the punch of TIX test was defined as an analytical rigid surface and the lubrication coefficient taken into account was 0.25, as suggested by Pottier *et al.* (2011b).

The numerical simulations were carried out using the material parameters identified for *Yld2004-Mixed*$_{\text{Mod}}$ model and also W_{CL}^{f} fracture parameter. A mesh density of 3 elements per mm was used for all the tests. Additionally, samples were meshed with 3 elements along the thickness. The specimens of the several mechanical tests were defined with a thickness of 0.7 mm. Note that this thickness value is the same of DC04 mild steel sheet used for identifying the material parameters of the constitutive model adopted.

The analysis of the tests for calculating I_{T} was carried out considering the evaluation of the specimen surface. Such as in DIC technique, a region of interest (ROI) of the sample was defined

and the strain field was post-treated only in this region. In the case of uniaxial tensile, plane strain tension, shear-like tensile and biaxial tensile tests all the deformed geometry was taken into account. However, for simple shear, bulge and TIX tests, a ROI was defined to avoid local effects such as the contact with the tools or to avoid regions that cannot be measured experimentally by DIC. The ROI are illustrated in Figure 7.5 as red zones.

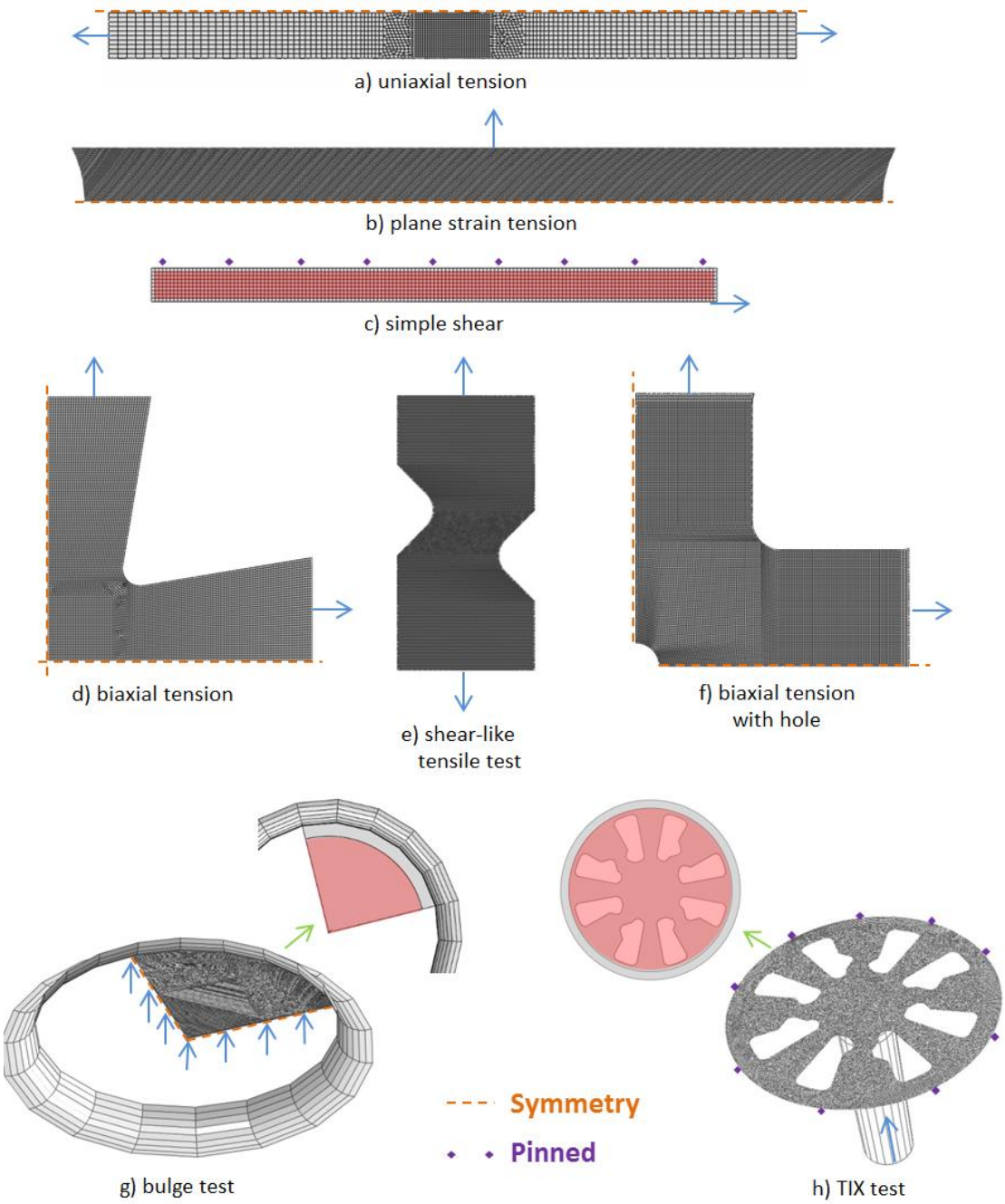

Figure 7.5 – Numerical model of the tests.

Concerning $\varepsilon_2/\varepsilon_1$ analysis, this ratio was defined by calculating the eigenvalues and eigenvectors for each finite element in order to determine accurately the major ε_1 and minor ε_2 principal strains in the sheet plane. A python script was developed to perform the $\varepsilon_2/\varepsilon_1$ analysis in

post-processing, after the numerical simulation. $\varepsilon_2/\varepsilon_1$ ratio was only determined for elements exhibiting a certain amount of equivalent plastic strain, i.e. with $\bar{\varepsilon}^P \geq 10^{-3}$.

Relatively to $\bar{\varepsilon}^P$ values obtained for the test as well as for the most relevant strain states, it must be pointed out that $\bar{\varepsilon}^P_{test}$ was calculated by defining the average of the 15 elements (region with approximately 1.5x1 mm^2) with highest $\bar{\varepsilon}^P$ value while $\bar{\varepsilon}^P$ of the different strain states was calculated as the average value for all elements having $\varepsilon_2/\varepsilon_1$ range depicted in Table 7.2. Note that due to DC04 material anisotropy, $\varepsilon_2/\varepsilon_1$ values characterizing the uniaxial tensile and uniaxial compression states are -0.627 and -1.595, respectively.

Table 7.2 – $\varepsilon_2/\varepsilon_1$ range characterizing the different strain states considered for I_T calculation.

Strain State	$\varepsilon_2/\varepsilon_1$ range
Uniaxial tension	-0.627 ± 0.03
Simple shear	-1 ± 0.03
Plane strain tension	0 ± 0.03
Equibiaxial tension	1 (0.94 - 1)
Uniaxial compression	-1.595 ± 0.03

7.5 Results

The different terms used in I_T formulation were analyzed for the several tests adopted. The calculation of I_T and its robustness to the variation of the relative weighting factors were also presented in this section.

7.5.1 Main characteristics of the tests

With the aim of obtaining a visual description of $\bar{\varepsilon}^P$ evolution during the test, histograms showing its distribution at normalized times 0.5, 0.75 and 1 (end of the test) are depicted in Figures 7.6 and 7.7. The histograms represent $\bar{\varepsilon}^P$ distribution on element sets divided in 100 equal intervals. By the analysis of these element sets it is possible to evaluate the level of heterogeneity of each test. Note that accurate $\bar{\varepsilon}^P$ distributions using histograms are only possible considering a constant element size for the whole mesh. Otherwise element sets would not represent equally the area of the specimen. Additionally, $\bar{\varepsilon}^P$ distribution over the specimen is included in Figures 7.6 and 7.7. These contours show the location of the heterogeneity regions as well as $\bar{\varepsilon}^P$ value obtained on the sample.

Large element set distribution with a similar number of elements and, consequently, heterogeneity, is verified for biaxial tension tests using classical cruciform specimen and also perforated sample, as can be seen in Figures 7.6 d) and 7.7 c). On the contrary, a narrow distribution of element sets composed of a high number of elements indicates non-heterogeneity, as observed in the case of uniaxial tensile, TIX and shear-like tensile tests before strain localization (histograms at times $t = 0.5$ and $t = 0.75$) illustrated, respectively, in Figures 7.6 a), 7.7 b) and 7.7 d). It must be highlighted that TIX and shear-like tension are heterogeneous tests, however, their heterogeneity occur in rather small areas of the ROI. In the case of plane strain tension, simple shear and bulge test, shown in Figures 7.6 b), 7.6 c) and 7.7 a), it can be seen that the heterogeneity tends to increase during the test. For these experiments, a narrow element sets

distribution is observed for the histogram at time $t = 0.5$, however, the element sets distribution enlarges up to end of the test (histograms at times $t = 0.75$ and $t = 1$). Note that though simple shear consists of a quasi-homogeneous experiment, the ROI defined for this test comprises non-homogeneous zones of the sample and, therefore, heterogeneity is observed from the analysis of its histograms.

Similarly, histograms reproducing $\varepsilon_2/\varepsilon_1$ distribution on the specimen during the test as well as $\varepsilon_2/\varepsilon_1$ contours were analyzed, as shown in Figures 7.8 and 7.9. These figures show that $\varepsilon_2/\varepsilon_1$ range covered by each test is almost constant during the experiment since no significant changes occur on the element set distribution. The tests that present some smooth $\varepsilon_2/\varepsilon_1$ range variation between half time (t=0.5) and the end (t=1) of the test are the uniaxial tensile and the bulge test. Indeed, the strain state ratio of the uniaxial tensile test was comprised between -0.64 and -0.62 before strain localization (up to t=0.75) and after necking phenomenon the strain state range covered was $-0.64 < \varepsilon_2/\varepsilon_1 < -0.54$ ($t = 1$), as shown in Figure 7.8 a). Taking into account that the total strain state range available is in-between -3 and 1, the increase of $\varepsilon_2/\varepsilon_1$ range observed in uniaxial tensile test is not substantial.

The larger is the strain state range covered, the larger is the diversity of the mechanical state information given by the test. As expected, classical tests such as uniaxial tension, simple shear or bulge test provide mainly uniaxial tensile ($\varepsilon_2/\varepsilon_1 = -0.627$), shear ($\varepsilon_2/\varepsilon_1 = -1$) and equibiaxial ($\varepsilon_2/\varepsilon_1 = 1$) strain states, as can be seen in Figures 7.8 a), 7.8 c) and 7.9 a), respectively. However, several strain states are covered by biaxial tension tests using classical cruciform specimen or perforated sample (Figures 7.8 d) and 7.9 c)), TIX test (Figure 7.9 b)) and shear-like tensile test (Figure 7.9 d)).

In the case of biaxial tension test using classical cruciform sample (Figure 7.8 d)), strain state range between uniaxial and equibiaxial tensions is characterized. Hence, plane strain state ($\varepsilon_2/\varepsilon_1 = 0$) is also included in this test. A similar $\varepsilon_2/\varepsilon_1$ range is achieved using the perforated cruciform sample (Figure 7.9 c)). Note that the test is similar, however, the hole at the center of the sample hinders the propagation of the biaxial strain state. Thereby, this strain state is localized in small regions of the specimen, as shown by $\varepsilon_2/\varepsilon_1$ contour. In fact, this test was suggested by Teaca *et al.* (2010) to characterize a strain state range between uniaxial to plane strain tension, as can be seen in section 2.2.2.1. Concerning shear-like tensile test, it can be seen in Figure 7.9 d) that this test exhibits uniaxial compressive and tensile strain states. A large $\varepsilon_2/\varepsilon_1$ range is covered by this test comparatively to uniaxial tensile test (Figure 7.8 a)). However, the covered $\varepsilon_2/\varepsilon_1$ strain range is not continuous due to the observed gap between compressive and tensile states. It results not only from the specimen design but also from the imposed condition to determine $\varepsilon_2/\varepsilon_1$ ratio for elements with $\bar{\varepsilon}^p \geq 10^{-3}$ as well. Consequently, grey regions on $\varepsilon_2/\varepsilon_1$ contour of shear-like tensile test means that the imposed condition was not satisfied.

The TIX test is the only one covering all principal strain states, namely, uniaxial compression, shear, uniaxial, plane strain and equibiaxial tensions, as illustrated in Figure 7.9 b). However, excluding uniaxial tension, the remaining strain states were localized in very small regions, as shown by $\varepsilon_2/\varepsilon_1$ contour. As for the shear-like tensile test, $\varepsilon_2/\varepsilon_1$ ratio was not calculated for some areas of TIX specimen.

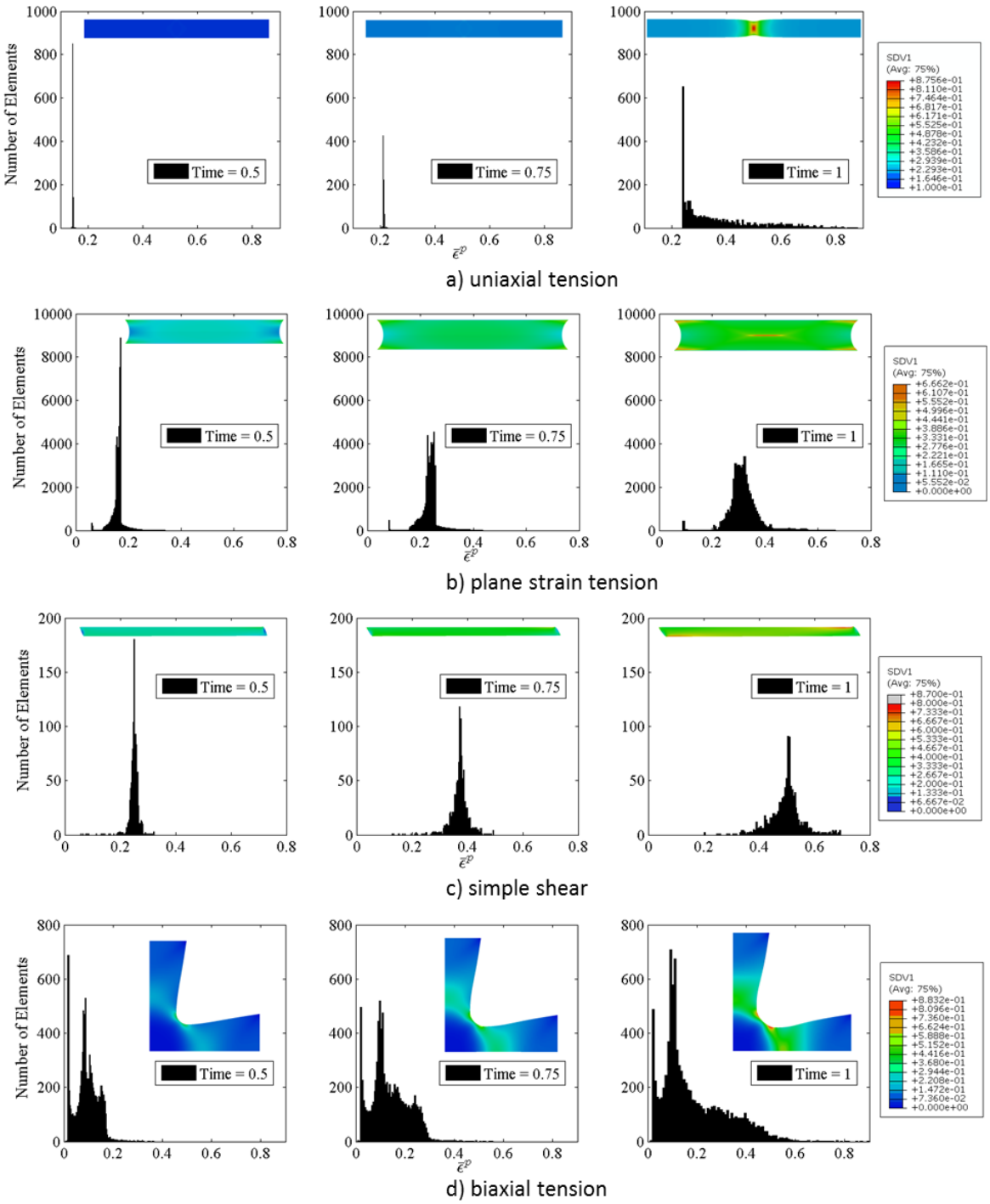

Figure 7.6 – Histograms representing $\bar{\varepsilon}^P$ distribution of the elements for a) uniaxial tension, b) plane strain tension c) simple shear and d) biaxial tension. SDV1 stands for $\bar{\varepsilon}^P$.

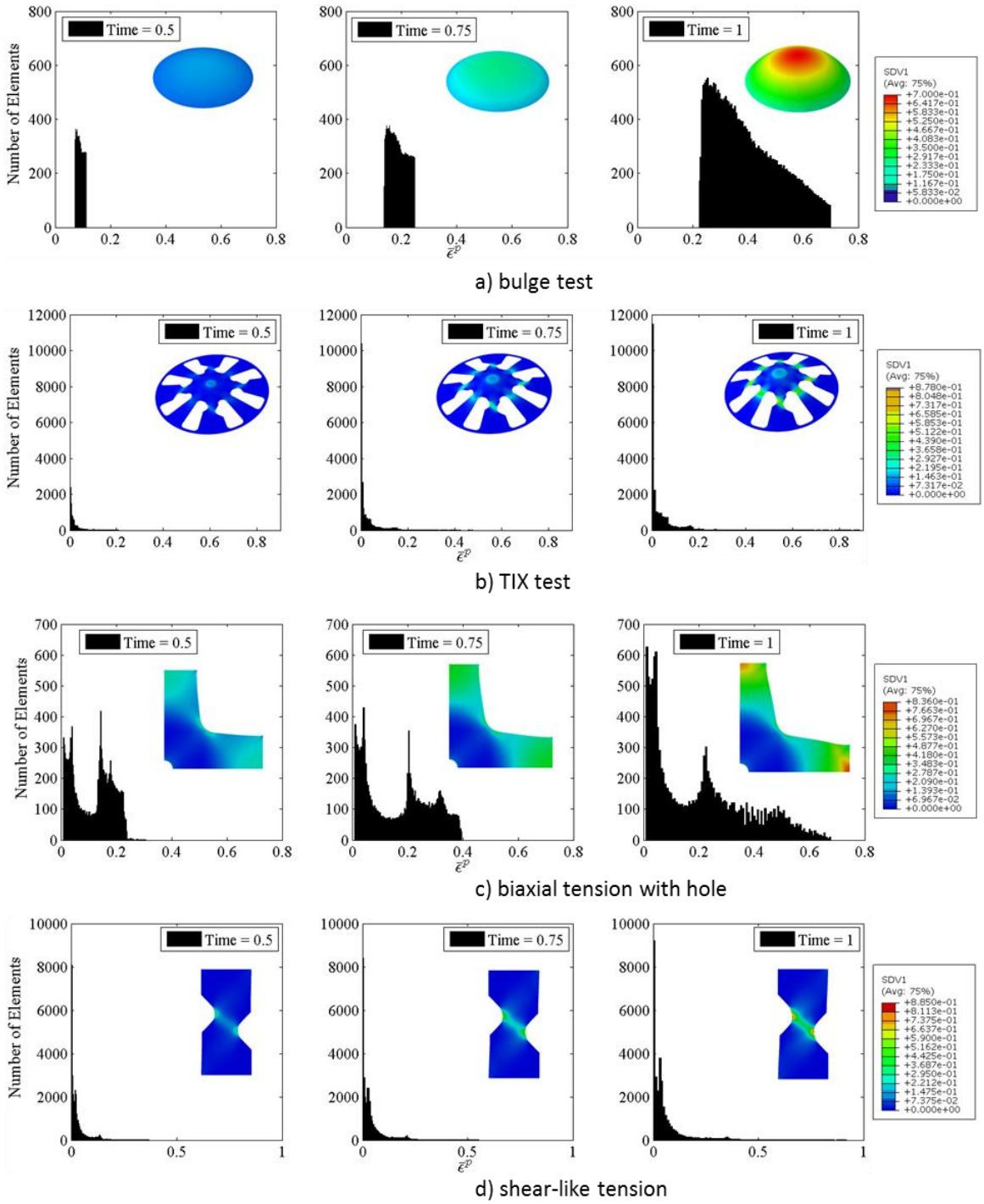

Figure 7.7 – Histograms representing $\bar{\varepsilon}^{P}$ distribution of the elements for a) bulge test, b) TIX test c) biaxial tension with hole and d) shear-like tension. SDV1 stands for $\bar{\varepsilon}^{P}$.

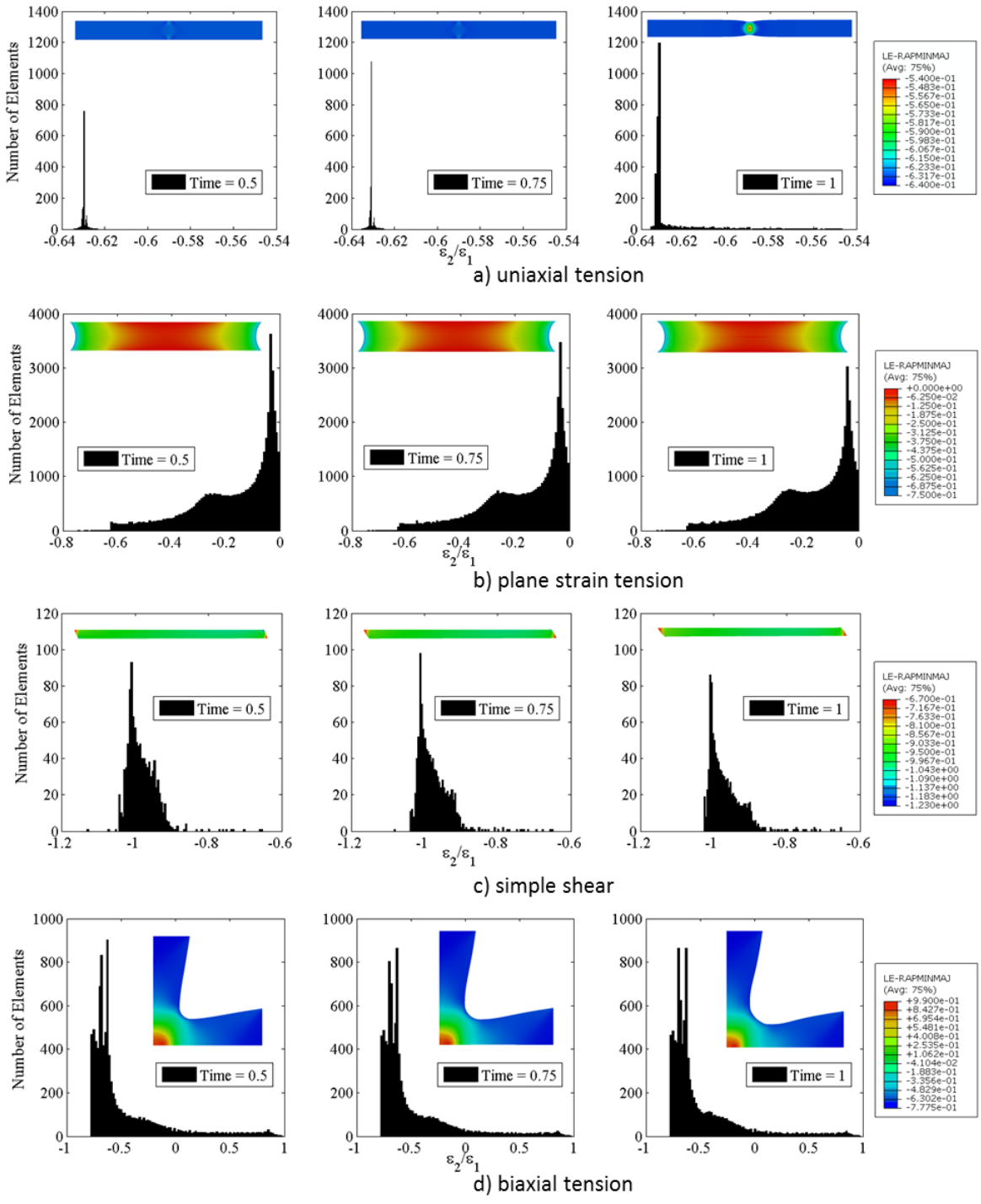

Figure 7.8 – Histograms representing $\varepsilon_2/\varepsilon_1$ distribution of the elements for a) uniaxial tension, b) plane strain tension c) simple shear and d) biaxial tension. LE-RAPMINMAJ stands for $\varepsilon_2/\varepsilon_1$.

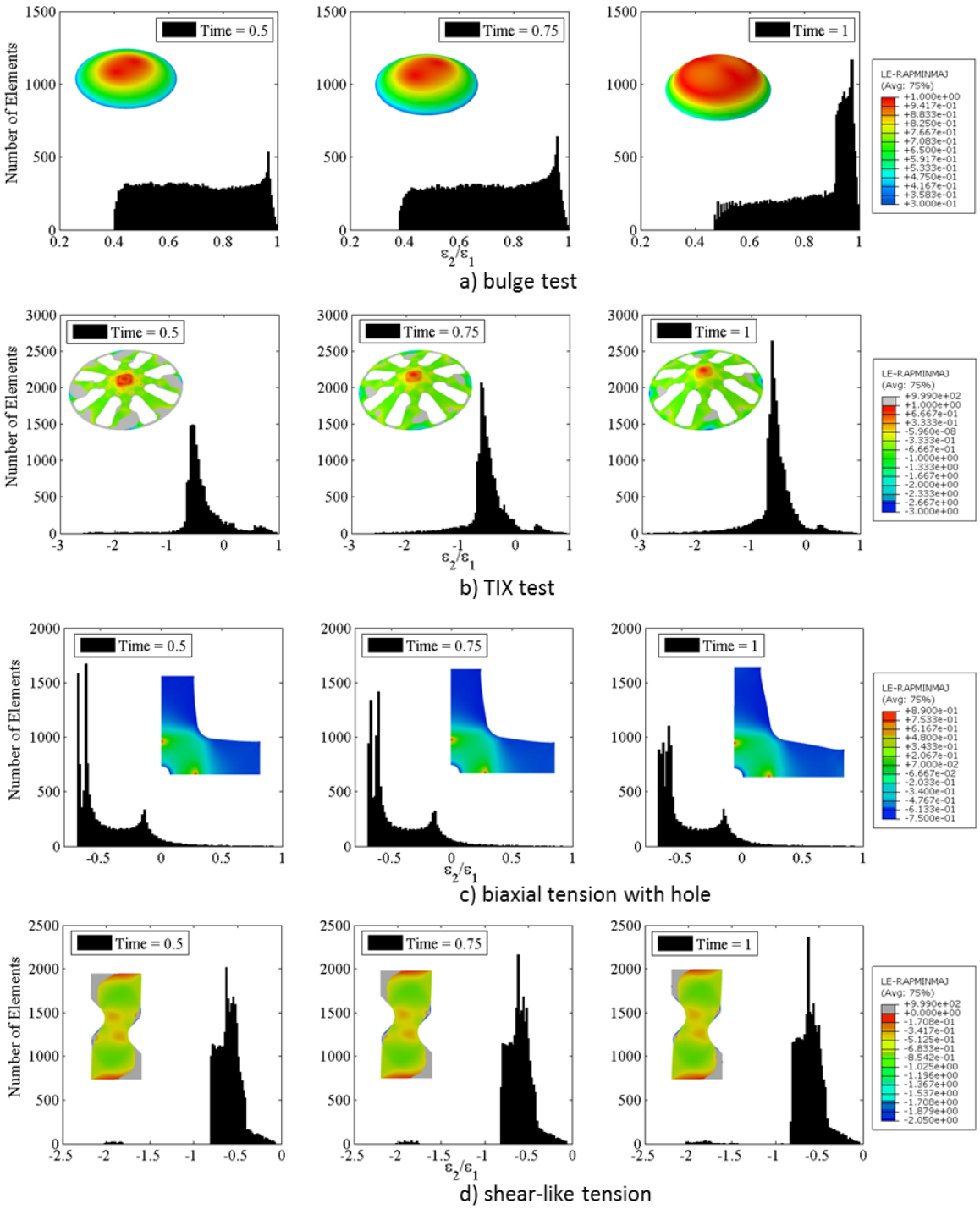

Figure 7.9 – Histograms representing $\varepsilon_2/\varepsilon_1$ distribution of the elements for a) bulge test, b) TIX test c) biaxial tension with hole and d) shear-like tension. LE-RAPMINMAJ stands for $\varepsilon_2/\varepsilon_1$.

7.5.2 Calculation of the indicator

The evolution of $Std(\bar{\varepsilon}^P)$ and $Std(\varepsilon_2/\varepsilon_1)$ for each test is depicted in Figures 7.10 and 7.11, respectively. In addition, $\bar{\varepsilon}^P$ and $\varepsilon_2/\varepsilon_1$ evolution for all elements belonging to the ROI of the sample are included in these figures, providing supplementary information.

Analyzing $\bar{\varepsilon}^P$ evolution, it can be stated that, generally, a continuous increase of $Std(\bar{\varepsilon}^P)$ occurs during the tests. The displacement imposed as boundary condition during the test leads to the specimen deformation where some regions are more deformed than the remaining ones. Consequently, a significant variation of $\bar{\varepsilon}^P$ on the sample surface may occur. In this way, the deformation heterogeneity of the specimen can be accurately measured by $Std(\bar{\varepsilon}^P)$. An example of $Std(\bar{\varepsilon}^P)$ functionality can be seen for the uniaxial tensile test depicted in Figure 7.10 a). Due to the homogeneity of this test, $Std(\bar{\varepsilon}^P)$ remains equal to almost zero until necking starts. However, after necking, the increase of $Std(\bar{\varepsilon}^P)$ is verified. Moreover, analyzing the mean value of $Std(\bar{\varepsilon}^P)$, it can be seen that both biaxial tension tests present the higher values (Figures 7.10 d) and 7.11 c)) among the several tests investigated. Indeed, it is in agreement with the results obtained from Figures 7.6 and 7.7, since it was observed that these two tests were the ones presenting large heterogeneity.

On the contrary, the analysis of $Std(\varepsilon_2/\varepsilon_1)$ evolution reveals that a continuous increase is not observed. Indeed, $Std(\varepsilon_2/\varepsilon_1)$ evolution tends to a stabilized value which is verified during the major part of the test. This is in agreement with the observations of Figures 7.8 and 7.9, where it can be seen that no considerable change occurs on the covered $\varepsilon_2/\varepsilon_1$ range. Thereby, no substantial variations of $Std(\varepsilon_2/\varepsilon_1)$ value are verified along the test. In addition, from $\varepsilon_2/\varepsilon_1$ evolution for all elements belonging to the ROI, it is shown that though the tests are non-homogenous in space they are rather uniform in time. It is also observed that biaxial tension and TIX test, shown in Figures 7.10 d) and 7.11 b), are the tests with large mean value of $Std(\varepsilon_2/\varepsilon_1)$ and it is in agreement with the fact that both tests are the ones covering a large strain state range.

$Std(\varepsilon_2/\varepsilon_1)$ evolution is mainly influenced by the design of each test such as, for instance, the boundary conditions and specimen geometry. However, it is clear that strain localizations, such as the ones observed for uniaxial tensile (Figure 7.10 a)), TIX (Figure 7.11 b)) or shear-like tensile test (Figure 7.11 d)), promote $Std(\varepsilon_2/\varepsilon_1)$ variations during the test.

In Figures 7.12 and 7.13, the evolution of $(\varepsilon_2/\varepsilon_1)_{max}$, $(\varepsilon_2/\varepsilon_1)_{min}$, $\bar{\varepsilon}^P$ for the most relevant strain states and the distribution of W_{CL} at the rupture are shown for all the tests. Note that $\bar{\varepsilon}^P$ value for the relevant strain states was calculated as an average considering the elements presenting $\varepsilon_2/\varepsilon_1$ ranges depicted in Table 7.2. W_{CL} contours were presented in order to show the expected localization of the rupture for each test. For uniaxial tensile, simple shear, bulge and shear-like tensile tests, experimental and numerical rupture localization is in agreement. Concerning the remaining tests, no experimental data is available to proceed to such a comparison.

In the case of uniaxial tension, plane strain tension, biaxial tension test using classical cruciform sample, bulge test and biaxial tension test using perforated sample (Figures 7.12 a), 7.12 b), 7.12 d), 7.13 a) and 7.13 c), respectively), $(\varepsilon_2/\varepsilon_1)_{max}$ and $(\varepsilon_2/\varepsilon_1)_{min}$ values tend to be rather constant during the whole test. For simple shear, TIX and shear-like tensile tests (Figures 7.12 c), 7.13 b) and 7.13 d), respectively), $(\varepsilon_2/\varepsilon_1)_{max}$ is constant, however, variations on $(\varepsilon_2/\varepsilon_1)_{min}$ are observed. Relatively to $(\varepsilon_2/\varepsilon_1)_{min}$ evolution for simple shear test, it can be seen that this value starts from the compressive state and reaches shear state which is then the dominant strain state

over all the specimen. In both TIX and shear-like tensile tests, the decrease of $(\varepsilon_2/\varepsilon_1)_{min}$ value during the test is due to the occurrence and evolution of compression zones in the sample.

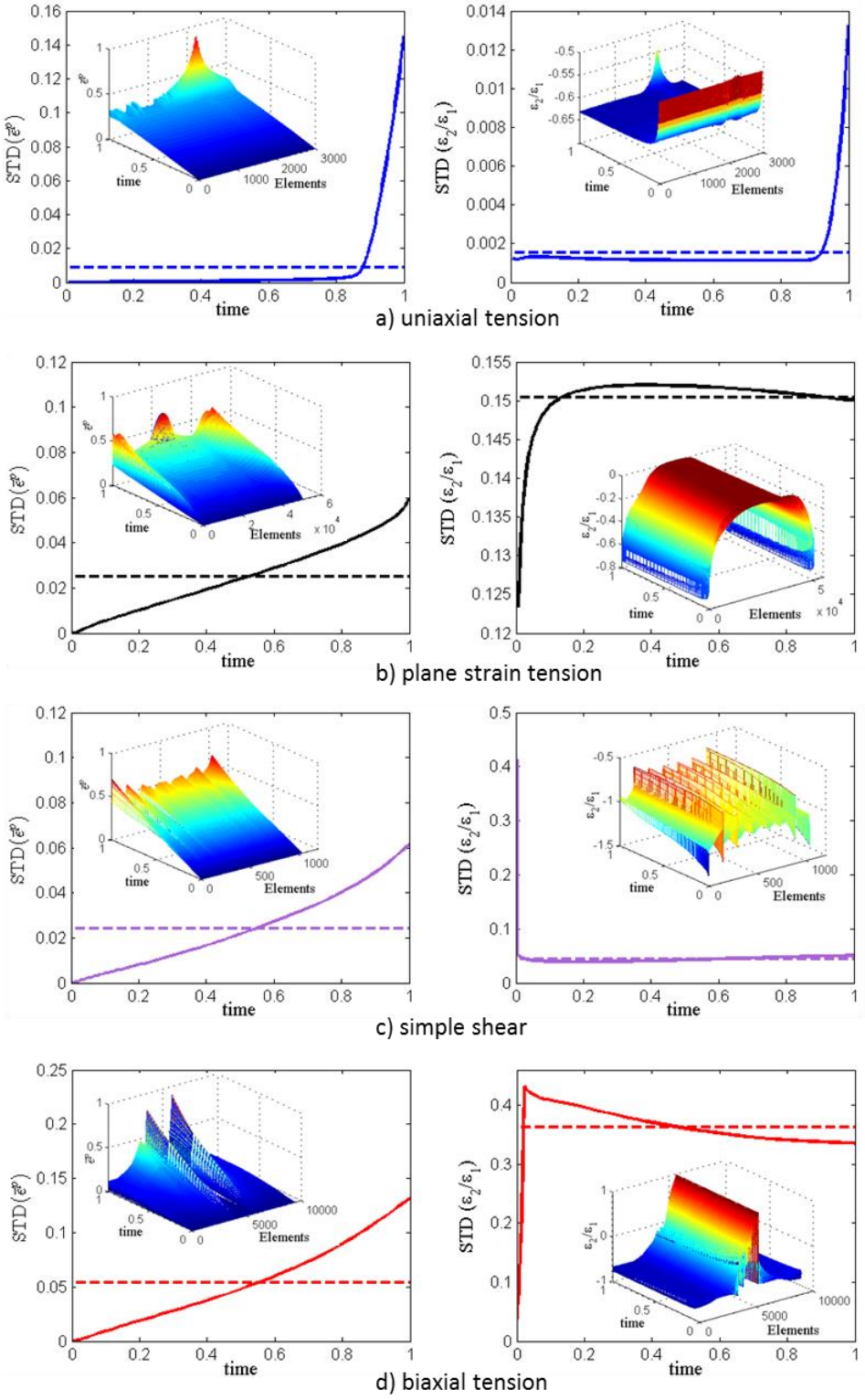

Figure 7.10 – Evolution of $Std(\bar{\varepsilon}^P)$ (left) and $Std(\varepsilon_2/\varepsilon_1)$ (right) for a) uniaxial tension, b) plane strain tension c) simple shear and d) biaxial tension. Dashed lines are the mean values of $Std(\bar{\varepsilon}^P)$ and $Std(\varepsilon_2/\varepsilon_1)$.

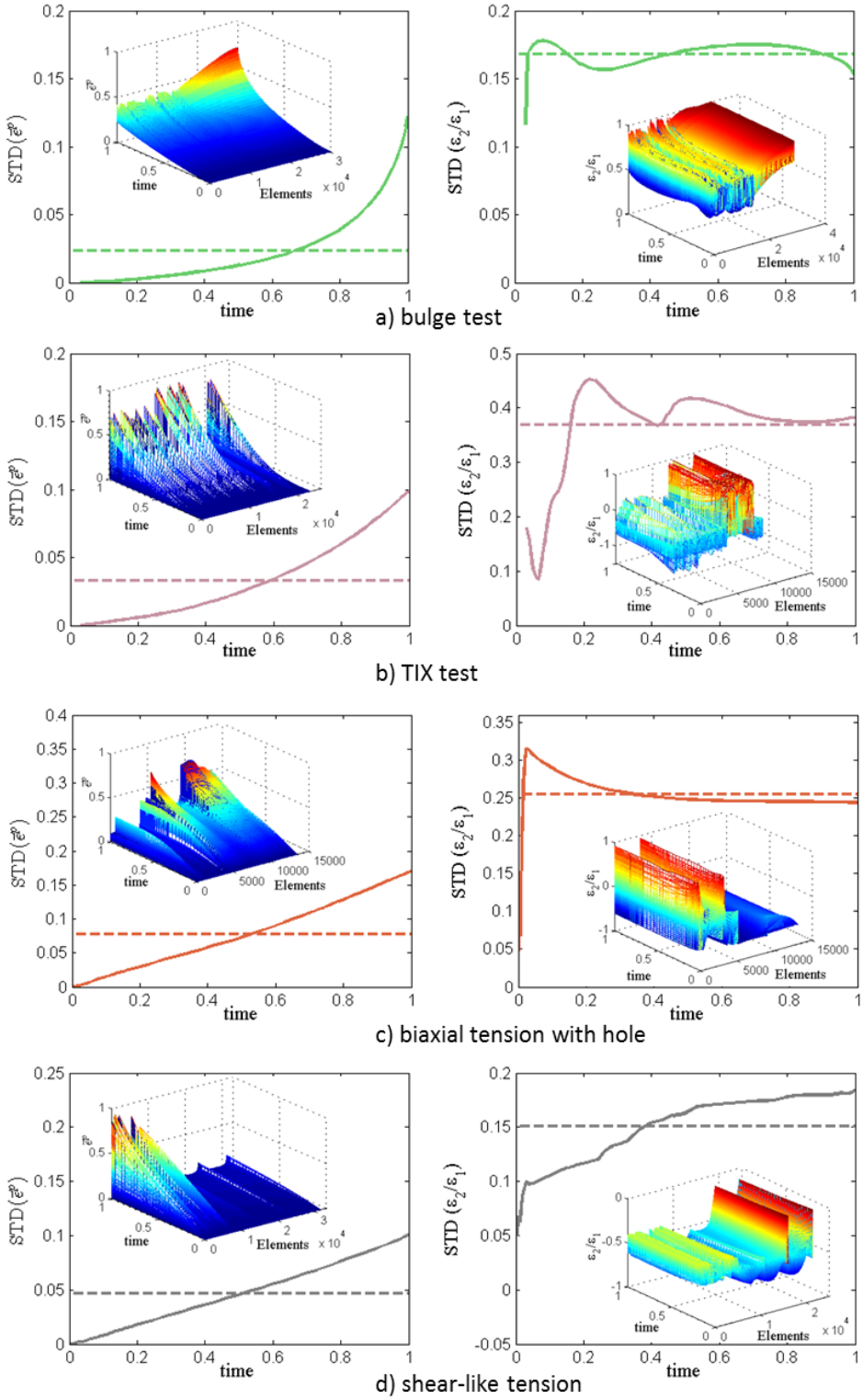

Figure 7.11 – Evolution of $Std(\bar{\varepsilon}^P)$ (left) and $Std(\varepsilon_2/\varepsilon_1)$ (right) for a) bulge test, b) TIX test c) biaxial tension with hole and d) shear-like tension. Note that dashed lines correspond to the mean $Std(\bar{\varepsilon}^P)$ and $Std(\varepsilon_2/\varepsilon_1)$ values.

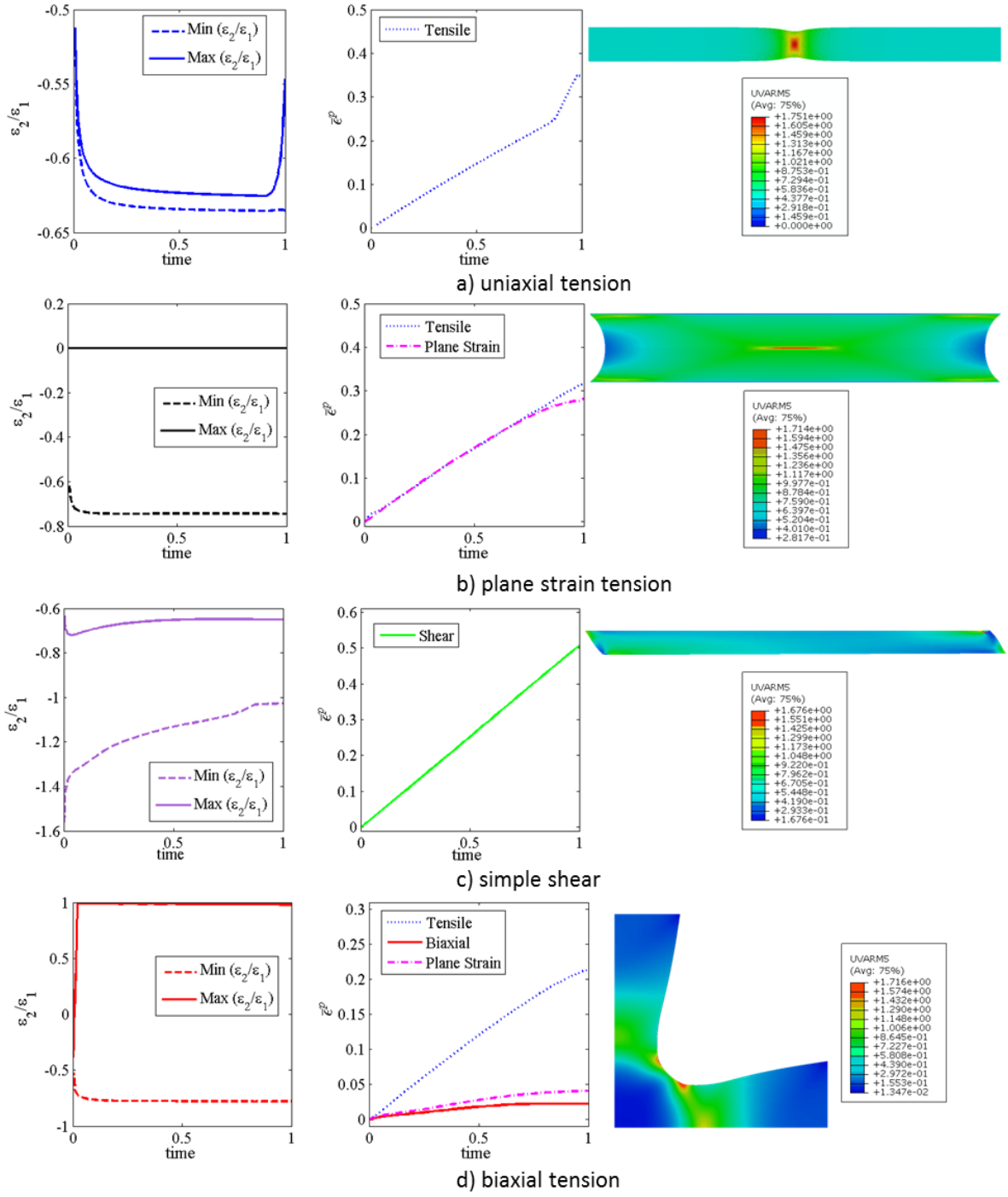

Figure 7.12 – Evolution of maximum and minimum $\varepsilon_2/\varepsilon_1$ values (left), maximum $\bar{\varepsilon}^p$ value of the different strain states (center) and W_{CL} distribution at the rupture (right) for a) uniaxial tension, b) plane strain tension c) simple shear and d) biaxial tension.

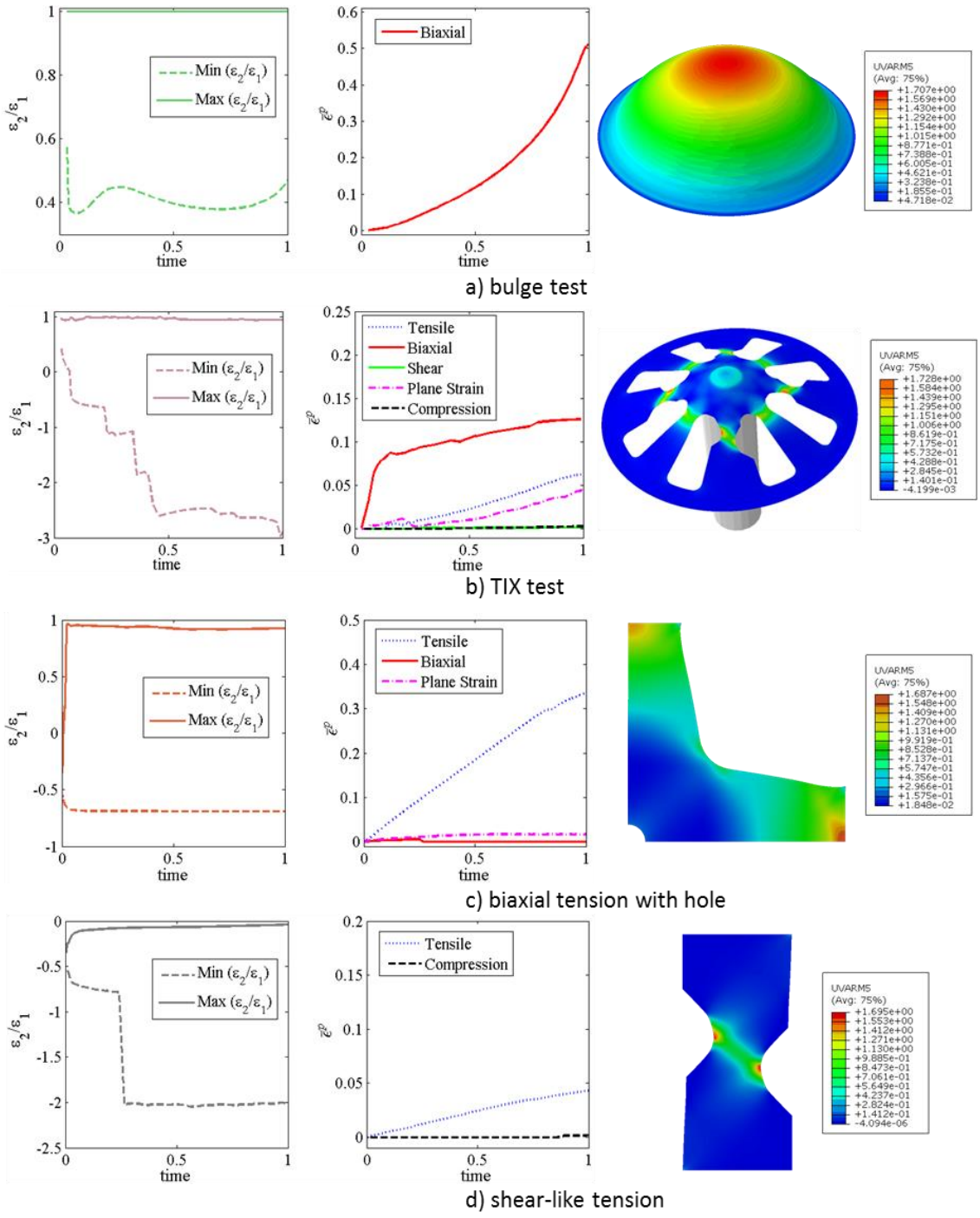

Figure 7.13 – Evolution of maximum and minimum $\varepsilon_2/\varepsilon_1$ values (left), maximum $\bar{\varepsilon}^p$ value of the different strain states (center) and W_{CL} distribution at the rupture (right) for a) bulge test, b) TIX test c) biaxial tension with hole and d) shear-like tension.

In order to evaluate the maximum and the average deformation achieved in the several tests, $\bar{\varepsilon}^{P}_{test}$ as well as $Av_{\bar{\varepsilon}^P}$ values are illustrated in Figure 7.14. In the case of $\bar{\varepsilon}^{P}_{test}$, it can be observed that most part of the tests achieve the same level of maximum equivalent plastic strain at the end of the test. However, for $Av_{\bar{\varepsilon}^P}$, distinct values are obtained for the several tests. This is due to the fact that $Av_{\bar{\varepsilon}^P}$ is related to the overall deformation of the specimen and, depending of their design, strain localization occurs leading to high values for $\bar{\varepsilon}^{P}_{test}$ but rather low values for $Av_{\bar{\varepsilon}^P}$, *e.g.* the TIX test.

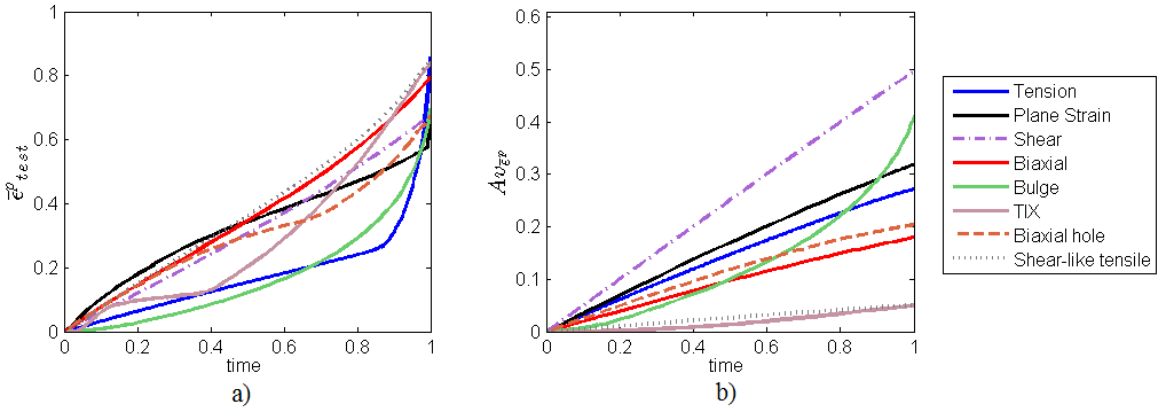

Figure 7.14 – Evolution of a) maximum $\bar{\varepsilon}^{P}$ value achieved during the test and evolution of b) $Av_{\bar{\varepsilon}^P}$.

The different contributions used for I_T calculation as well as the I_T values obtained for all tests are listed in Table 7.3. Based on the I_T results, a rating scale ordering the several experiments by order of importance is presented in Figure 7.15.

According to the proposed indicator, uniaxial tension is the test giving the lowest information concerning the mechanical behavior of the material. This test is limited by the small $\varepsilon_2/\varepsilon_1$ range as well as by the necking phenomenon, which leads to high level of deformation only in a localized zone of the specimen. The shear-like tensile and simple shear tests provide more significant mechanical information than uniaxial tensile test. Next, plane strain tension and bulge test appear providing even more mechanical information than the previous tests. It must be noted that this rating shows that plane strain tension is more interesting for material characterization than simple shear or uniaxial tension. It is related to the fact that this test covers a large $\varepsilon_2/\varepsilon_1$ range with a substantial level of deformation. Biaxial tension test using perforated sample, TIX test and biaxial tension test using classical cruciform specimen consist of the best three tests giving richer mechanical information. I_T indicates that biaxial tests provide more information than uniaxial ones. Indeed, these three tests are the ones covering higher $\varepsilon_2/\varepsilon_1$ range. It is interesting to note that the biaxial tension test using classical cruciform specimen leads to a better mechanical information than the other heterogeneous tests. In fact, it must be noted that even though TIX test was developed in order to promote shear and tensile strain in RD and TD directions as well as equibiaxial strain, small deformation levels are obtained for these strain states and for the overall specimen.

Table 7.3 – Obtained values for the several contributions of I_T and I_T values for the different tests.

	Tensile	Plane strain	Shear	Biaxial	Bulge	TIX	Biaxial hole	Shear-like tensile
$\mathrm{Mean}\left[\mathrm{Std}\left(\varepsilon_2/\varepsilon_1\right)\right]$	0.001	0.150	0.044	0.363	0.168	0.369	0.255	0.151
$\left(\varepsilon_2/\varepsilon_1\right)_{\min}$	-0.636	-0.743	-1.026	-0.777	0.471	-2.898	-0.693	-2.030
$\left(\varepsilon_2/\varepsilon_1\right)_{\max}$	-0.547	0	-0.651	0.981	0.999	0.945	0.925	-0.039
$\left(\frac{\varepsilon_2}{\varepsilon_1}\right)_R$	0.089	0.743	0.375	1.758	0.528	3.843	1.618	1.991
$\mathrm{Mean}\left[\mathrm{Std}\left(\bar{\varepsilon}^P\right)\right]$	0.009	0.025	0.024	0.054	0.023	0.033	0.078	0.047
$\bar{\varepsilon}^P_{\mathrm{test}}$	0.859	0.667	0.679	0.794	0.699	0.842	0.674	0.852
$\bar{\varepsilon}^P_{\mathrm{tens}}$	0.348	0.317	-	0.214	-	0.063	0.336	0.043
$\bar{\varepsilon}^P_{\mathrm{shear}}$	-	-	0.507	-	-	0.002	-	-
$\bar{\varepsilon}^P_{\mathrm{plane}}$	-	0.283	-	0.040	-	0.046	0.017	-
$\bar{\varepsilon}^P_{\mathrm{biaxial}}$	-	-	-	0.020	0.508	0.126	-	-
$\bar{\varepsilon}^P_{\mathrm{comp}}$	-	-	-	-	-	0.003	-	0.001
$Av_{\bar{\varepsilon}^P}$	0.272	0.318	0.496	0.179	0.410	0.049	0.204	0.050
I_T	0.115	0.184	0.161	0.248	0.192	0.239	0.231	0.157

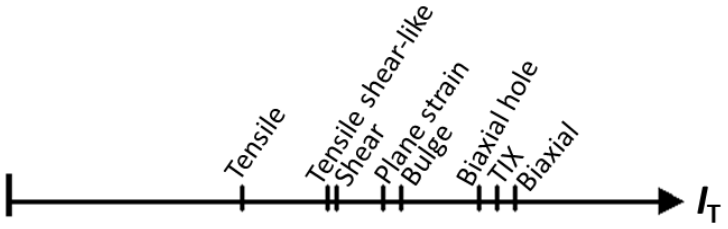

Figure 7.15 – Ranking of the different tests by using I_T indicator.

7.5.3 Robustness of the indicator

It must be emphasized that the obtained I_T values are influenced by the relative weighting factors w_r adopted. Different w_r sets may change I_T rating and, therefore, a parametric study comparing three distinct w_r sets was performed with the aim of assessing the robustness of the proposed indicator. Table 7.4 lists w_r sets used for this analysis.

The weighting factors w_{r1}, w_{r2} and w_{r3} are related to the I_T terms that evaluate strain state range/heterogeneity while w_{r4} and w_{r5} are related to the strain level. The three w_r sets were defined imposing (i) 50%-50%, (ii) 65%-35% and (iii) 35%-65% of importance for strain range/heterogeneity and strain level, as can be seen in Table 7.4. It must be highlighted that $I_{T(50\text{-}50)}$ consists in the reference indicator calculated in the previous section.

Table 7.4 – Different w_r sets selected for I_T robustness study.

	$I_{T\,(50\text{-}50)}$	$I_{T\,(65\text{-}35)}$	$I_{T\,(35\text{-}65)}$	
w_{r1}	0.3	0.36	0.22	Strain range/ Heterogeneity
w_{r2}	0.03	0.05	0.04	
w_{r3}	0.17	0.24	0.09	
w_{r4}	0.4	0.23	0.5	Strain level
w_{r5}	0.1	0.12	0.15	

Figure 7.16 shows the I_T calculations for all the tests using the different w_r sets. Analyzing these results, it can be observed that the variation of w_r values leads to almost identical I_T ratings.

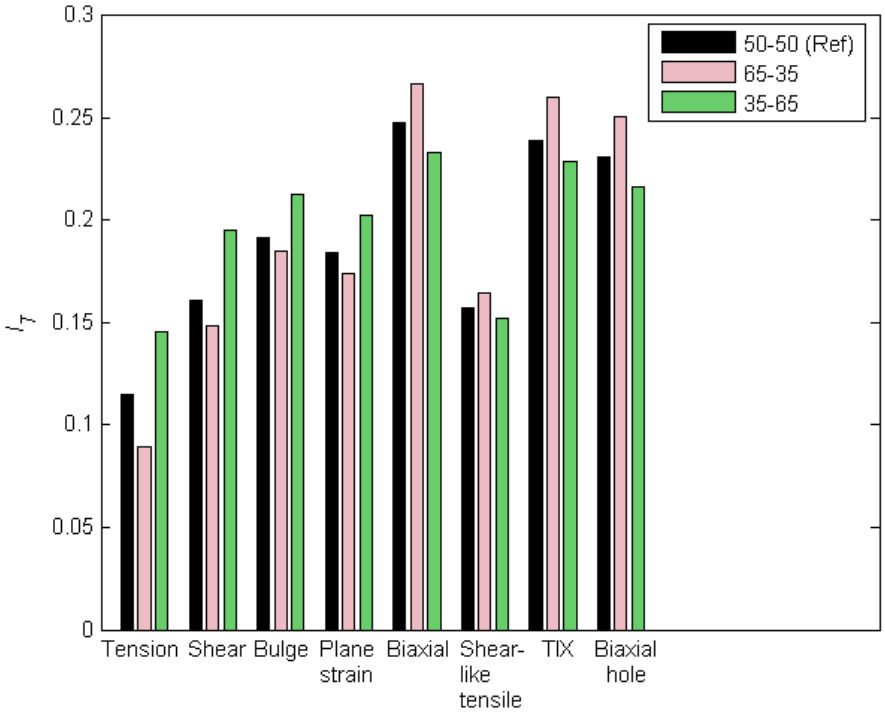

Figure 7.16 – I_T results obtained considering the different w_r sets.

By comparing $I_{T\,(65\text{-}35)}$ results with the reference ones ($I_{T\,(50\text{-}50)}$), it can be seen that the ranking of the several tests is quite the same, just changing the order of shear-like tensile with the simple shear test. With $I_{T\,(65\text{-}35)}$, shear-like tensile test provides some more mechanical information than simple shear. However, it must be stressed out that in the ranking obtained with the reference indicator ($I_{T\,(50\text{-}50)}$), shown in Figure 7.15, no substantial difference exists between the amount of mechanical information given by these two tests since they have obtained very close $I_{T(50\text{-}50)}$ values. Therefore, knowing that shear-like tensile test promotes more heterogeneous strain fields than simple shear, the increase of importance of the strain state range/heterogeneity group (65%) led to the re-ordering of these two tests. Withal, the general results suggest the achievement of similar rating when considering an I_T calculation that gives more importance to the strain range/heterogeneity contribution.

Alternatively, the comparison of the results obtained by $I_{T\,(35\text{-}65)}$ with the reference ones shows that an equal rating scale ordering the several tests was achieved. Nevertheless, it must be

highlighted that the classical tests with significant level of deformation, such as bulge test, plane strain tension or simple shear, tend to reach higher indicator values and such values became closer to the ones obtained for the best tests, namely, the TIX and the biaxial tension tests using perforated and classical cruciform samples. Hence, it can be more difficult to distinguish the mechanical information of the several tests when a large importance to the strain achieved on the test is attributed.

According to the results obtained for the several I_T configurations tested, it can be stated that the robustness of I_T was demonstrated. Moreover, it is expected to reach a reliable reproducibility of the I_T rankings when choosing w_r values for a range comprised in-between [35% - 65%] of importance of both strain state range/heterogeneity and strain level groups. Outside of this interval, I_T results tend to promote considerable changings on the ranking of the several tests.

7.6 Material parameters sensitivity

With the purpose of validating the results obtained using I_T, the analysis of the material parameters sensitivity (Belhabib *et al.*, 2008) of the tests was carried out. This methodology gives a comparison of the several tests, searching for the one presenting a larger sensitivity to the strain field. It should be mentioned that this analysis is dependent on the constitutive model, material parameter set and definition of the cost function.

The material parameters sensitivity of the test expresses the sensitivity of the strain field to the parameters of the material model (Belhabib *et al.*, 2008). In this way, it is possible to evaluate the contribution of each test mainly when complex material models are used. Thus, tests with more sensitivity to the material parameters have a greater contribution on the prediction of the strain field.

As in Belhabib *et al.* (2008), in order to quantify this sensitivity, a cost function S_{sen} is defined by the least-square difference between a reference and a perturbed data given as

$$S_{sen} = S_F + S_{\varepsilon_{xx}} + S_{\varepsilon_{yy}} , \tag{7.8}$$

with

$$S_F = \sqrt{\frac{1}{n_{im}} \sum_{i=1}^{n_{im}} \left(\frac{F_i(\mathbf{P}_0) - F_i(\mathbf{P})}{F_i(\mathbf{P}_0)} \right)^2} , \tag{7.9}$$

$$S_{\varepsilon_{xx}} = \sqrt{\frac{1}{n_{im}} \sum_{i=1}^{n_{im}} \left[\frac{1}{n_{el}} \sum_{j=1}^{n_{el}} \left(\frac{\varepsilon_{xx,i,j}(\mathbf{P}_0) - \varepsilon_{xx,i,j}(\mathbf{P})}{\varepsilon_{xx,i,j}(\mathbf{P}_0)} \right)^2 \right]} , \tag{7.10}$$

and

$$S_{\varepsilon_{yy}} = \sqrt{\frac{1}{n_{im}}\sum_{i=1}^{n_{im}}\left[\frac{1}{n_{el}}\sum_{j=1}^{n_{el}}\left(\frac{\varepsilon_{yy,i,j}(\mathbf{P}_0)-\varepsilon_{yy,i,j}(\mathbf{P})}{\varepsilon_{yy,i,j}(\mathbf{P}_0)}\right)^2\right]}, \tag{7.11}$$

where n_{im} and n_{el} are the number of strain fields evaluated and elements of the test, $F_i(\mathbf{P}_0)$ and $F_i(\mathbf{P})$ are the load values at the increment i obtained with the reference ($\mathbf{P}_0$) and the perturbed ($\mathbf{P}$) parameter set values, $\varepsilon_{xx,i,j}(\mathbf{P}_0)$ and $\varepsilon_{xx,i,j}(\mathbf{P})$ as well as $\varepsilon_{yy,i,j}(\mathbf{P}_0)$ and $\varepsilon_{yy,i,j}(\mathbf{P})$ are the strain values for the element j at the strain field i obtained using $\mathbf{P}_0$ and $\mathbf{P}$ set parameters, respectively. Both load and strain data are taken into account in the definition of S_{sen} since it leads to a better suited solution when strain concentration and localized damage are involved (Avril *et al.*, 2008a).

Note that the sensitivity of S_{sen} to each parameter is not dependent on the reference term of S_{sen} because this term is constant. It is the perturbed term responsible to distinguish between different values of the parameter (Valente *et al.*, 2014).

The reference parameter set $\mathbf{P}_0$ consists of the material parameters describing *Yld2004-Mixed*$_{Mod}$ model, while $\mathbf{P}$ set is obtained by perturbating one of the parameters of $\mathbf{P}_0$ by -10%. Therefore, numerical simulations were carried out for all the tests perturbing individually each parameter listed in Table 5.2. Hence, 24 perturbed set parameters were used on this sensitivity analysis. The reference and perturbed data were analyzed in ROI of the tests up to the maximum deformation level of $\bar{\varepsilon}^P = 0.35$ by comparing 6 strain fields ($n_{im} = 6$). The strain fields were obtained at maximum levels of $\bar{\varepsilon}^P = [0.1, 0.15, 0.2, 0.25, 0.3, 0.35]$ for each test. The sensitivity results of the cost function for the several material parameters are depicted in Figures 7.17 to 7.19.

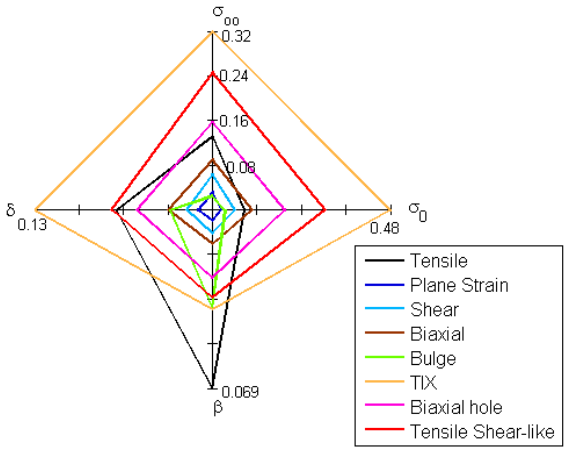

Figure 7.17 – Sensitivity of S_{sen} to the isotropic hardening parameters.

Figure 7.17 shows the sensitivity of the cost function to the isotropic hardening parameters. It can be seen that the cost function is highly sensitive to variations of σ_0 and σ_∞ while, in the case of β, the sensitivity of S_{sen} is less expressive. Among the several tests, biaxial tension test using perforated sample, shear-like tensile and TIX test show the greatest sensitivity to the isotropic hardening parameters. Note that these tests consist of the heterogeneous ones and, thereby, the results illustrated in Figure 7.17 seem to indicate that large strain field heterogeneity leads to more sensitivity to the hardening parameters.

Concerning the variations of the kinematic hardening parameters, it is verified in Figure 7.18 that, generally, these material parameters lead to lower sensitivity of S_{sen} than the isotropic hardening parameters. It is justified by the fact that the contribution of the kinematic hardening is more significant when reverse strain path is considered. However, reverse strain is not verified in the tests used for this study. With exception to γ_3 and $X\text{sat}_3$ where uniaxial tensile test presents higher S_{sen} sensitivity, it is observed that biaxial tension test using perforated sample, shear-like tensile and TIX test show greatest sensitivity for the remaining kinematic hardening parameters. Nonetheless, a considerable difference exists between the sensitivity to the kinematic hardening parameters obtained for the TIX test and the remaining mechanical tests. In order to understand the meaning of this occurrence, the evolution of strain path change by Θ (*cf*. Equation 7.1) was evaluated for this test. It was observed that some smooth strain path variation occurs in TIX test, explaining these results.

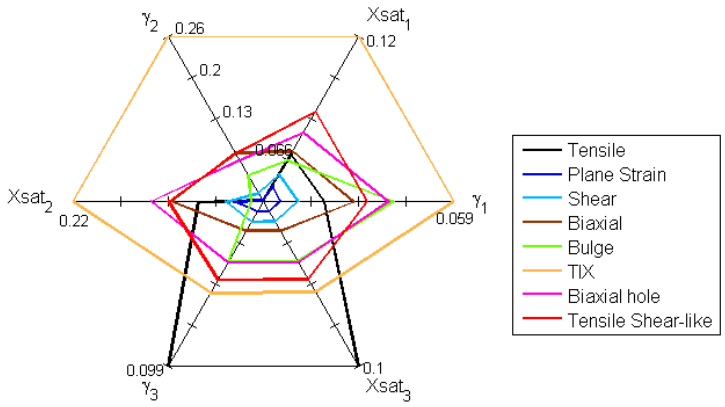

Figure 7.18 – Sensitivity of S_{sen} to the kinematic hardening parameters.

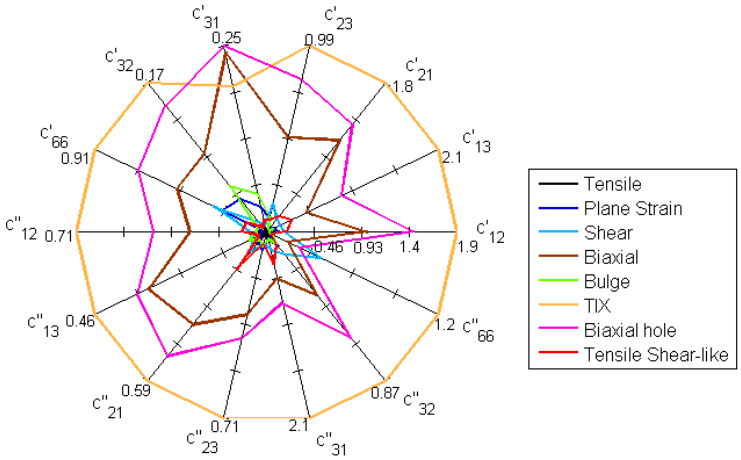

Figure 7.19 – Sensitivity of S_{sen} to the yield function coefficients.

It can be stressed out that biaxial tension test using perforated sample, shear-like tensile and TIX test are the mechanical tests that contribute the more for the prediction of the work hardening, because these tests present strain fields with the highest sensitivity to the variations of the isotropic and kinematic hardening parameters.

The sensitivity of S_{sen} to the yield criterion parameters is illustrated in Figure 7.19. It can be pointed out that the variations performed for these material parameters lead to the major variations of the strain field due to the larger S_{sen} values obtained. In this way, these results highlight the large influence of the coefficients of *Yld2004-18p* anisotropic yield criterion on the prediction of the strain field. In addition, it is verified that the TIX test as well as both biaxial tension tests are the ones most sensitive to the anisotropy of the material since these tests present higher S_{sen} values. Thereby, concerning the large diversity of strain paths required by *Yld2004-18p* yield criterion it seems clear that these tests are the most indicated to characterize larger strain state ranges.

The global evaluation of the results shows that the TIX test is the most sensitive test to the mixed work hardening as well as material anisotropy. Therefore, the material parameters sensitivity carried out indicates that this test is one of the tests that can contribute more significantly for the prediction of the material model adopted. In part, it may due to the fact that the TIX experiment reproduces a considerable number of the strain fields used for identifying the input parameters of this constitutive model, for instance, uniaxial tensile and simple shear at 0° and 90° to RD and also biaxial tensile state.

Moreover, it can be stated that a general agreement is observed between the results obtained by the validation study and by the proposed indicator. Both methodologies highlighted the same three tests (the TIX and both biaxial tension tests) as the best ones promoting the mechanical behavior characterization of the material.

On the one hand, by a qualitative analysis of the mechanical tests, it seems clear that the tests involving multiaxial stresses as well as larger heterogeneity must provide a better mechanical characterization of the material behavior. On the other hand, since the material model adopted to reproduce the DC04 mild steel behavior corresponds to a complex phenomenological model based on several stress states as well as mechanical phenomena, the sensitivity of the material parameters tends to reflect the ability of the tests in reproducing these several stress states and mechanical phenomena.

7.7 Conclusion

In this chapter, a quantitative indicator able to distinguish, rate and rank mechanical tests was proposed. This indicator, called I_T, was designed to include the analysis of strain state range covered by the test, the deformation heterogeneity of the specimen as well as the strain level achieved up to rupture. For that, a continuous evaluation of the strain fields up to rupture was considered.

One of the main advantages of I_T is the fact that all its contributions have physical meaning. These contributions were based on strain characteristics and, in addition, can be obtained by using FFM techniques.

In order to evaluate the performance of I_T, classical mechanical tests as well as modern heterogeneous tests were carried out numerically using the virtual behavior of DC04 mild steel. The several I_T terms were calculated for each test and a ranking of all the tests was defined. The qualitative analysis of the mechanical tests adopted indicated that the tests involving multiaxial stresses as well as larger heterogeneity provide a more complete mechanical characterization of

sheet metals. The obtained I_T ranking confirmed this trend and it revealed that the indicator is able to perform an accurate quantification of the mechanical information provided by the tests. Moreover, the robustness of the I_T results was also investigated and identical ratings ordering the several tests were achieved.

The indicator performance was only investigated for single-step tests. However, the inclusion of the parameter Θ (*cf*. Equation 7.1) in the indicator formulation was mentioned as suggestion for the analysis of multi-step tests evidencing strain path changes, in a future work.

With the purpose of comparing results and validate I_T, a material parameter sensitivity study was performed. In this analysis, a cost function was defined based on load and strain data for each test and the sensitivity of the strain field was evaluated by perturbing each material parameter. According to the obtained results as well as its validation, it was shown that the proposed indicator consists of an efficient strategy for choosing the most appropriate heterogeneous test when it comes to the identification of material parameters. Therefore, I_T can be used for guiding the design of the computational mechanical test in order to find an ideal strain field able to promote better mechanical characterization of the material behavior.

Chapter 8

Design of mechanical tests

8.1 Introduction

Aiming at better descriptions of the sheet metal behavior, the design of different classical experiments trying to reproduce individually the stress and strain states encountered in sheet forming processes had been considered by the scientific community in the past. Nowadays, thanks to FFM methods, the design of non-classical experiments based on the heterogeneity of the strain field became the focus of several recent studies. Alternatively to the classical experiments, where homogeneous stress and strain fields are provided, these heterogeneous experiments search for reproducing the complex stress and strain fields which generally occur in sheet metal forming operations.

The main goal on the design of heterogeneous experiments is to define a sample geometry and boundary conditions leading to an ideal strain field that develops several stress and strain states and amplitudes. However, such a task imposes to have no idea concerning the initial shape, boundary conditions and loading path of the experiment. For this reason, the most common specimen optimization approaches described in the literature are mainly based on (i) the shape improvement of existent classical experiments (Belhabib *et al.*, 2008; Teaca *et al.*, 2010; Dunand and Mohr, 2011; Tiernan and Hannon, 2014), usually by performing parametric studies for some geometrical parameters and (ii) trial-and-error attempts in the shape design of specimens inspired in previous experiments (Shouler and Allwood, 2010; Brosius *et al.*, 2011; Pottier *et al.*, 2011b; Yin *et al.*, 2011; Yin *et al.*, 2012).

The classical experiments mostly used to re-design the specimen shape consist of classical uniaxial tensile test (Meuwissen, 1998; Meuwissen *et al.*, 1998; Kajberg and Lindkvist, 2004; Belhabib *et al.*, 2008; Cooreman, 2008; Pottier *et al.*, 2011a; Güner *et al.*, 2012; Haddadi and Belhabib, 2012) and biaxial tensile test using a cruciform specimen (Cooreman *et al.*, 2008; Makris *et al.*, 2010; Teaca *et al.*, 2010; Zidane *et al.*, 2010; Zhang *et al.*, 2014), as previously described in section 2.2.2.1.

Concerning the shape specimen design based on trial-and-error attempts, twin bridge shear test (Yin *et al.*, 2012) and TIX test (Pottier *et al.*, 2011b) must be highlighted (Figures 2.12 and 2.21). The twin bridge shear specimen was based on the plane torsion test (Yin *et al.*, 2012), while the TIX test was inspired from Nakazima tests (Pottier, 2010). The TIX test was developed with the purpose of increasing the variety of strain paths. It imposed the (i) reproducibility of the boundary conditions, (ii) minimization of friction phenomena and (iii) existence of strain localization and, by trial-and-error attempts, a specimen generating shear, uniaxial and biaxial tensile zones was designed.

In the present chapter, a different approach, based on the strain field as well as loading path optimization, is considered. This innovative procedure was developed without taking into account any kind of specimen geometry or loading path of existent experiments. Its main purpose is to understand what can be the best geometry and loading conditions that promote a strain field more sensitive to the mechanical information. To accomplish this, an optimization methodology based on a direct search method[5] was developed in order to optimize the geometry as well as loading path conditions. The quantitative indicator, proposed in chapter 7, which rates the strain field of the experiment by quantifying the mechanical information of the test was used, as cost function, to guide the optimization process. Within this approach, two different strategies were developed: (i) a one-step procedure optimizing both the specimen initial shape and the loading path by using a rigid tool, (ii) a sequential incremental technique optimizing the specimen shape and the loading path of the specimen considering local displacements. In both strategies, no friction phenomenon takes place, avoiding the difficulties related to the choice of friction coefficients. In addition, a material parameters identification using one of the designed heterogeneous tests was carried out considering the virtual DC04 mild steel identified from the conventional tests as reference material. Furthermore, the experimental curves obtained for these conventional tests were predicted using the parameters set identified from the heterogeneous test with the purpose of evaluating the quality of the material parameters determined by this non-homogeneous inverse approach.

Note that the quantitative indicator assumes a crucial role in the innovative procedure developed. Its application and robustness to the design of a mechanical test is evaluated in this chapter as well as its pertinence for the design of novel mechanical tests.

8.2 Strain field optimization

In order to design an experiment able to promote a more complete material characterization of sheet metals, it is mandatory to determine the strain field that gives a rich mechanical information. The best way to achieve this objective is to implement an efficient optimization procedure that evaluates the strain field information. However, the main question relies in the initial shape, boundary conditions and loading path that must be taken into account in the modeling.

The use of existent experiments or specimen geometries in the quest for the best strain field consists in a constraint imposed to the optimization process, since the assumption that such

[5] Direct search methods are not dependent on the gradient of the cost function and are less time consuming than evolutionary algorithms (*cf*. chapter 3).

experiment or specimen geometry is the one that leads to the best results is made. Therefore, this kind of approach constrains the optimization process. Nevertheless, the goal of the present approach is to implement an optimization procedure that must be the most unconstrained as possible. Indeed, only in this way is it possible to identify what kind of geometry and loading conditions lead to a better strain field for material parameters identification purposes.

Thus, the optimization process defined in this chapter must be based on a model with a free geometry and a loading path evolution. For that, two optimization strategies were adopted. The first one, named as “Test design using rigid tools” corresponds to a one-step procedure where the initial specimen shape and loading path, imposed by using a tool, can be both subjected to design optimization. The main advantage of this strategy is the resemblance with the experimental reality, since a rigid tool is used for applying the displacement in a similar way as standard testing machines. The second strategy, called as “Test design based on local displacements”, consists of a sequential incremental technique that designs by optimization the loading path, locally, on the overall free boundary of the specimen shape. In this strategy, the optimization of the specimen shape was taken into account in the first step of the sequential optimization process while the loading path is subjected to optimization in the several sequential steps. Although this strategy seems unrealistic from an experimental point of view, its main purpose is to understand the effect of a complex loading path, in terms of multisteps as well as local displacements, on the achievement of rich strain fields. Alternatively, this strategy consists of the most unconstrained optimization procedure developed in this work since (i) initial specimen shape, (ii) boundary conditions by means of local displacements and (iii) complex loading path by sequential steps are all designed by optimization.

As a starting point, before implementing the above-mentioned optimization strategies, a shape optimization process for a rectangular specimen used in simple shear tests was developed. The reason of this work was the fact that for high strength steels, such as DP980 steel, premature rupture of the shear specimen occurs near the grips. For this material, just a shear strain value of 0.42 was reached experimentally. Then, it was proposed to re-design the geometry of the shear specimen in order to avoid this premature rupture. Therefore, the geometry of the shear sample was subjected to design optimization with the aim of maximizing the shear strain. An optimization process searching for the best design of the specimen boundaries which delay the rupture and, consequently, maximize the shear strain was performed. This optimization process is detailed in appendix C. Though such an optimization work did not deal with the design of a heterogeneous test, it consisted of an introductory way to conceive the optimization strategies for the design of the heterogeneous test. Indeed, it was the starting basis for the development of the following optimization strategies.

8.2.1 Test design using rigid tools

The current optimization strategy is based on a symmetric model with the specimen geometry defined by curve interpolation and the loading path imposed by a rigid tool. Figure 8.1 presents a schematic view of this optimization strategy. The symmetry was used as a starting point, in order to limit the degrees of freedom of the problem.

The curve interpolation method was considered in this strategy since it uses polynomials to represent the specimen geometry. As a result, it allows for a reduced number of design variables

because only a few points, designated as control points, are needed to define the polynomials. Therefore, the shape of the specimen is controlled by 7 control points (red points in Figure 8.1) defined radially at every 15°. The position of these control points may change and, by means of the polynomials, the specimen geometry is modified and can be optimized during the optimization process. The arrows in Figure 8.1 illustrate the variation allowed for the position of the control points and it can be seen that the radial length between the control points and the specimen center x_i, i = 1,…, 7 corresponds to the design variables for the specimen shape. In this optimization strategy, cubic splines were used to define the specimen shape. A different cubic spline is created between consecutive control points, which leads to a boundary shape definition composed by 6 continuous cubic splines. This polynomial curve type is described in appendix D.

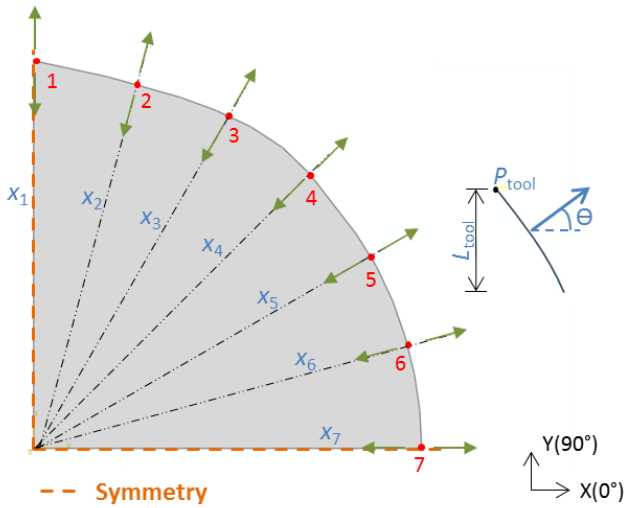

Figure 8.1 – Illustration of the sample shape and rigid tool.

Concerning the loading path optimization, a rigid tool was used. The shape of the rigid tool must be coincident with the specimen shape in each evaluation of the optimization process. This is mandatory, since the specimen geometry is continuously updated during the optimization process and concordance between both shapes is required for a proper contact definition in the model. However, the size of the tool L_{tool} as well as the orientation of the tool displacement Θ are optimized during the process. The position of the tool P_{tool} corresponding to one or the other extremity of the tool is not subjected to design. It is initially fixed at any location of the specimen boundary. The position, size and orientation of the tool displacement were defined in angular measurement then P_{tool} can be fixed for any angular value between 0° and 90°. In this way, the tool shape is defined with the fixed position P_{tool} and with its updated size L_{tool} by considering the corresponding cubic splines shape previously created for the specimen geometry. Figure 8.1 also displays the design variables used for the tool.

The loading path is applied in a single step procedure up to rupture. For that, the numerical simulation is carried out until reaching W_{CL}^{f} parameter. Thereby, just the orientation Θ of the tool displacement needs to be updated, whereas the displacement value was defined large enough to always lead to rupture.

Therefore, 9 design variables **r** were considered in this optimization strategy, namely, 7 radial displacements of the control points, L_{tool} and Θ of the tool. The tensor **r** can be written as

$$\mathbf{r} = \begin{bmatrix} x_1 & x_2 & x_3 & x_4 & x_5 & x_6 & x_7 & L_{\text{Tool}} & \theta \end{bmatrix}. \tag{8.1}$$

During the optimization process these design variables are updated in order to maximize the strain field information by increasing the indicator I_T. This optimization process is illustrated in Figure 8.2.

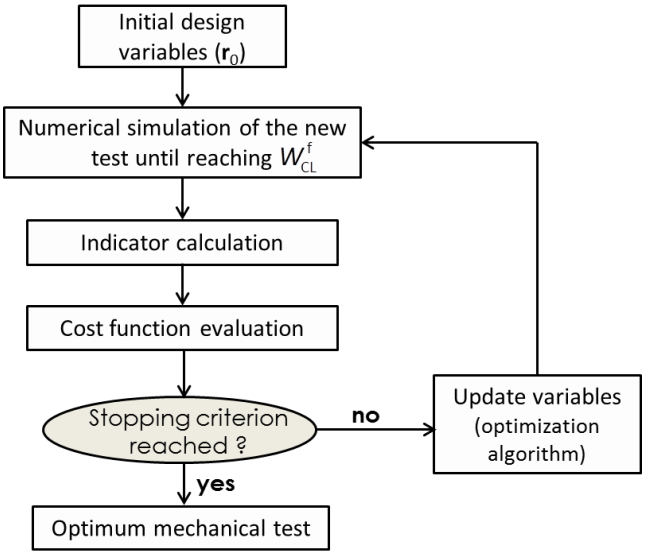

Figure 8.2 – General optimization procedure.

8.2.1.1 Automatic model generation

Usually, the main problem in shape optimization is to warrantee a reliable mesh definition. Indeed, since this optimization strategy can generate complex specimen shapes that may not allow a structured mesh, it is required to create the model with a robust parametrization.

The computational analysis was carried out by using ABAQUS/Standard FE code. Therefore, the most straightforward way to create the numerical model is through an ABAQUS script developed in Python (Abaqus, 2012). These scripts are very useful when automatic repetitive tasks, as the iterative modification of the model geometry, are needed. In the case of this design strategy, the use of a Python script presents many advantages since it constitutes an easy and automatic method to (i) change the geometry of the model, (ii) define properly the mesh and also (iii) vary the size of the rigid tool in each evaluation. The main structure of the ABAQUS script is depicted in Figure 8.3.

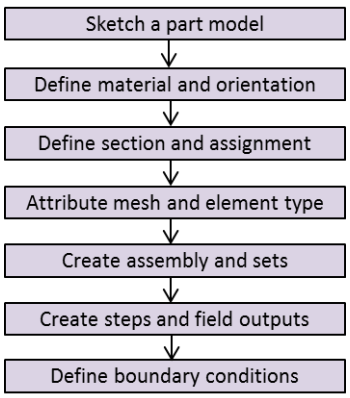

Figure 8.3 – Python script structure for the creation of a numerical model developed in ABAQUS.

As can be seen in Figure 8.3, the Python script follows the usual steps of a numerical model development when using ABAQUS software. This script allows obtaining different specimen shapes by just changing the position of the 7 design control points, as shown in Figure 8.4. By this figure, it can also be stressed out the important role of the cubic splines in the optimization strategy due to the large diversity of different shapes which can be generated.

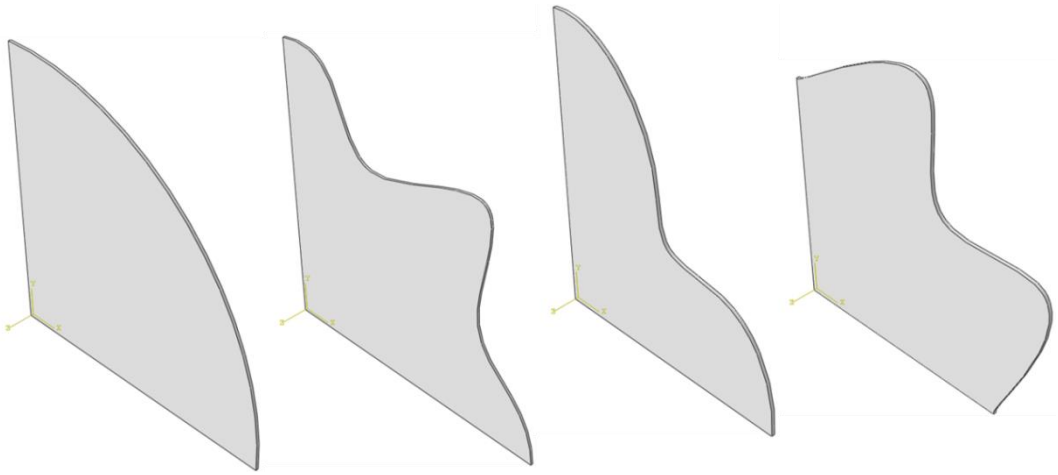

Figure 8.4 – Illustration of initial specimen shape variation by using the ABAQUS script developed in Python.

In addition, the position P_{tool} and size L_{tool} of the rigid tool can be easily parameterized in order to optimize the loading path. Figure 8.5 illustrates some examples of the tool position and size variation allowed by the implemented script code. Nevertheless, it must be highlighted that during the optimization procedure the position of the tool was fixed.

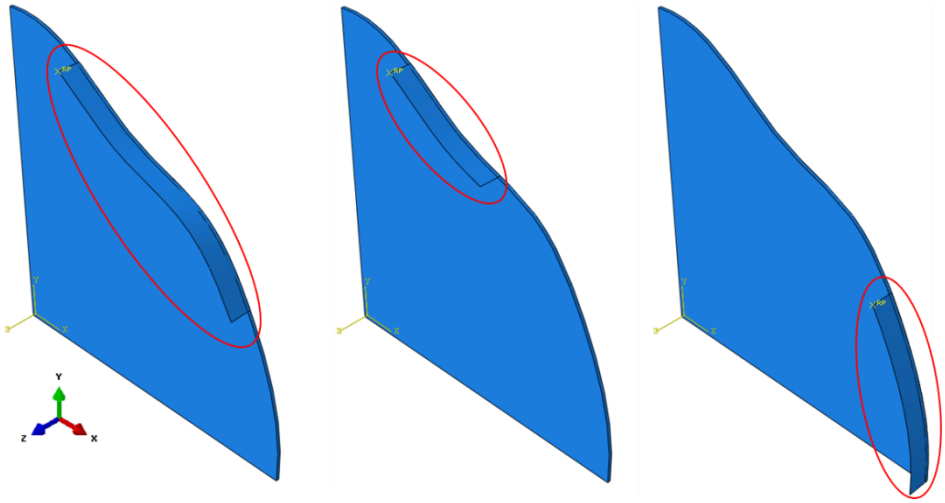

Figure 8.5 – Illustration of position and size variation of the rigid tool by using the ABAQUS script.

Although the parametrization of the design variables constitutes the focus for the optimization of the model, the definition of a reliable unstructured mesh is one of the great benefits of the use of this script code. In fact, it is mandatory to have a reliable mesh definition in order to get accurate results coming from the numerical simulation. Moreover, a new mesh must

be generated automatically by the script code for each evaluation of the optimization process due to the continuous updating of the specimen shape. As demonstrated in Figure 8.6, the script code creates reliable unstructured meshes and is also able to define different mesh refinements. Independently of the complexity of the generated specimen geometry, the mesh size must always be defined with 3 elements/mm. Indeed, it corresponds to the mesh size used for the uniaxial tensile test to calibrate the CL fracture parameter. Since the loading path was applied up to rupture, W_{CL}^{f} is used as a condition to stop the numerical simulation and, therefore, a mesh refinement of the model similar to the one used for the calibration of CL parameter is required.

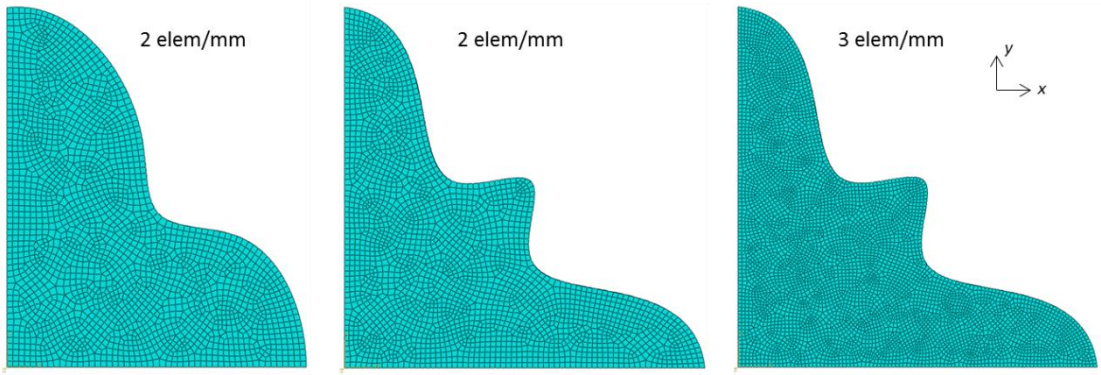

Figure 8.6 – Several mesh generation of the model using the ABAQUS script.

In this design optimization strategy, a tridimensional model was created by the ABAQUS script and only one eighth of the model was defined by considering material and process symmetries. The symmetry simplification adopted for the numerical specimen geometry, applying both symmetries in x- and y-directions (as shown in Figure 8.1) and also along the thickness, allows for the reduction of the number of design variables and saving calculation time in every evaluation of the optimization process. The specimen was meshed with 3D 8-node linear isoparametric elements with reduced integration (C3D8R) and hourglass control, while the tool was defined as analytical rigid using 3D 4-node rigid elements (R3D4). A tie contact was assumed between tool and specimen boundary in order to apply the loading path. The specimen was defined with an approximated mesh density of 3 elements/mm in the sheet plane and with 2 elements along the thickness by extrusion of the 2D mesh. The numerical simulations were carried out using the material parameters identified for *Yld2004-Mixed*$_{Mod}$ model. In addition, a rupture zone centered in the node with the maximum W_{CL} value consisting of a region of 1x1.5 mm^2 is used for determining W_{CL}^{f}, as considered for its calibration, and the entire specimen surface was taken into account for the calculation of the indicator.

8.2.1.2 Optimization framework

The optimization process was implemented in an interface program developed using Matlab. The interface program consists of a Matlab script that links ABAQUS code, used to carry out the numerical simulations, and the Python script, used to create the numerical model as well as to post-process some output data coming from the numerical simulation. The Matlab script also defines the specimen boundary and tool shapes by cubic splines interpolation, calculates the cost

function and updates the design variables by using the optimization toolbox available in this environment. Figure 8.7 illustrates the flow diagram of the optimization methodology developed.

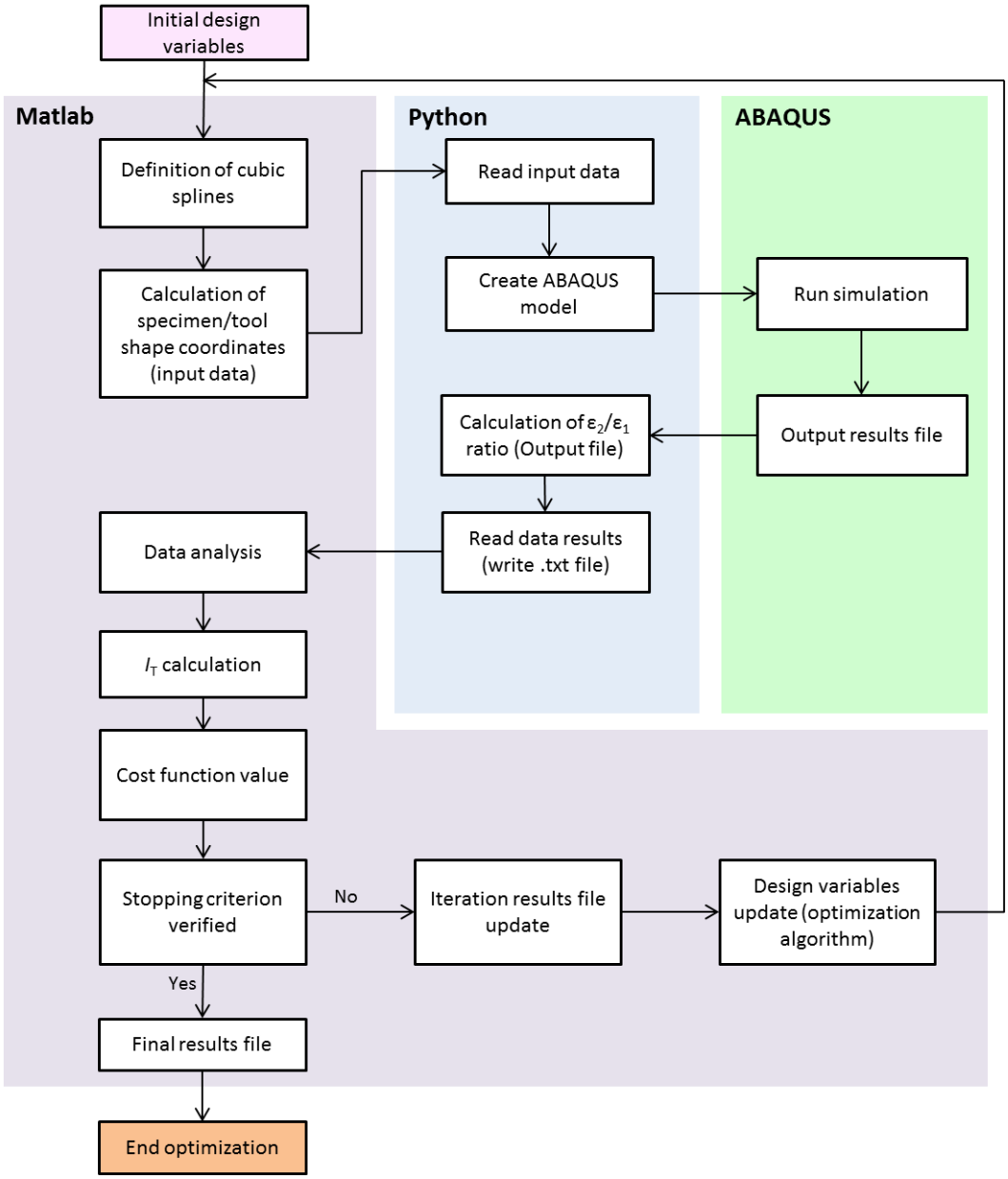

Figure 8.7 – Flow diagram of the optimization procedure developed for the design strategy using rigid tools.

The optimization procedure starts by introducing the initial guess of the design variables in the Matlab script. Then, the script determines the cubic splines defining the specimen outer shape from the 7 design control points. By means of interpolation, the Cartesian coordinates of the specimen boundary are calculated for each decimal degree of the angular space between 0° and 90°. After that, taking into account the position and the size of the tool, the angular range occupied by the tool is calculated and the tool is converted into Cartesian coordinates by using the cubic splines which define the specimen boundary. Figure 8.8 shows an example of specimen boundary and tool shape defined in Cartesian coordinates. The coordinates are written by the

Matlab script in two different files, with respect to the specimen and tool shapes, and are read by the Python script. Indeed, before starting creating the ABAQUS model, the Python script opens the coordinates files and records these data as construction points of the specimen and tool, respectively. Then, the ABAQUS model is created and the numerical simulation is carried out up to rupture. At the end of the numerical simulation, another Python script is used for post-processing the results. For instance, it is used to determine the $\varepsilon_2/\varepsilon_1$ ratio over the specimen surface and also to read and record the numerical results required for the calculation of the several terms of the indicator I_T. These data are analyzed by the Matlab script and, consequently, the indicator as well as the cost function are determined. When a stopping criterion is reached, the optimization process stops, the optimum strain field is found and an automatic file summarizing the optimization is created. In opposition, if the stopping criterion is not reached, the optimization file recording the evolution of the design variables as well as the cost function during the optimization is automatically re-written, the design variables are updated by the optimization algorithm and the process is repeated until achieving the stopping criterion or reaching the maximum number of evaluations. This optimization process is conducted using the Nelder-Mead direct search algorithm, as introduced in chapter 3.

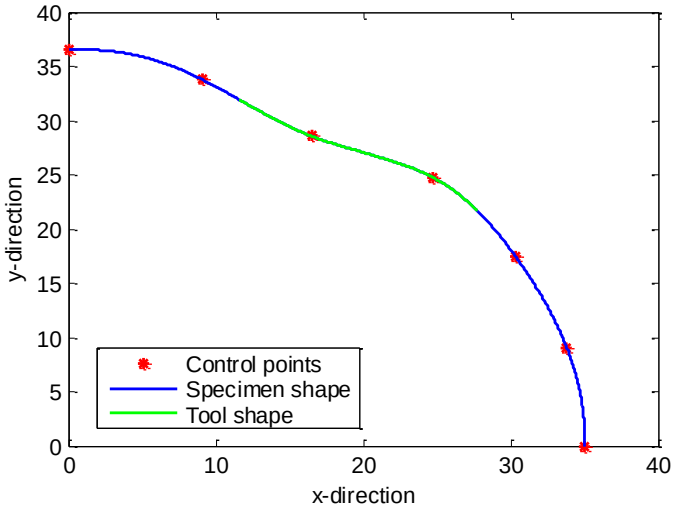

Figure 8.8 – Example of specimen boundary and tool shape obtained using Matlab script.

8.2.1.3 Cost function definition

As the goal of the developed strategy is the maximization of the strain field information, the indicator must increase during the optimization process. However, the optimization methods were conceived to proceed to the minimization of the cost function. Therefore, the cost function must be defined in order that its minimization means the maximization of the indicator I_{T_Op}, defined in Table 8.1. A simple way to achieve this goal is defining the cost function as

$$S_{cost}(\mathbf{r}) = 2 - I_{T\_Op}\,, \tag{8.2}$$

where the difference between 2 and I_{T_Op} ensures the required condition. Note that due to its formulation, theoretically, the maximum I_{T_Op} value that can be reached is the unity and then, the value 2 was just chosen as an upper limit.

From preliminary design tests, it was observed that abrupt variations for the design variables values of consecutive control nodes occur during the optimization process. It tends to promote (i) the generation of unrealistic specimen shapes, which leads to the impossible definition of the specimen shape and mesh by the Python script or (ii) specimen configurations leading to premature strain localization and rupture. Therefore, by introducing optimization constraints, the optimization algorithm can be instructed to avoid such kinds of solutions.

The optimization constraints were defined based on the admissible range values for each one of the 7 design control points. Thus, it was assumed that the design control point 1 can vary between the lower and upper limits (L_{Bound} and U_{Bound}) chosen for the optimization process, while the following control points were lower and upper constrained in function of the previous control point value. It can be written as

$$\begin{gathered} L_{\text{Bound}} \le x_1 \le U_{\text{Bound}} \\ (1-a_{\text{v}})x_1 \le x_2 \le (1+a_{\text{v}})x_1 \\ \vdots \\ (1-a_{\text{v}})x_{k-1} \le x_k \le (1+a_{\text{v}})x_{k-1} \\ \vdots \\ (1-a_{\text{v}})x_6 \le x_7 \le (1+a_{\text{v}})x_6, \end{gathered} \tag{8.3}$$

where a_v is the parameter value defining the admissible variation and x_{k} represents the design control point. For example, a_v = 0.15 means that the admissible value for design control point 2 is between 0.85 and 1.15 of the value of the design control point 1. The inequalities imposed by Equation 8.3 are analyzed in each evaluation of the optimization process and are quantified as

$$g_{\text{U},i}(\mathbf{r}) = x_{i+1} - (1+a_{\text{v}})x_i \tag{8.4}$$

and

$$g_{\text{L},i}(\mathbf{r}) = (1-a_{\text{v}})x_i - x_{i+1}, \tag{8.5}$$

where i = 1, ..., 6. Taking into account the several values obtained in Equations 8.4 and 8.5, a penalty function *Res* was defined in order to penalize the cost function when these inequalities are not respected during the optimization. The penalty function *Res* is calculated by

$$Res = \sum_{i=1}^{6} \alpha \left(\left[\max\left(g_{\text{L},i}(\mathbf{r}),0\right) \right]^2 + \left[\max\left(g_{\text{U},i}(\mathbf{r}),0\right) \right]^2 \right) \tag{8.6}$$

with

$$\alpha = \frac{1}{\left(U_{\text{Bound}} - L_{\text{Bound}}\right)^2}, \tag{8.7}$$

where α is a penalty coefficient that defines the importance of the constraints during the optimization process. It must be noted that the *Res* function leads to a quadratic penalization[6].

The penalty function *Res* was introduced in Equation 8.2 and an augmented objective function was defined as

$$S_{\text{cost}}(\mathbf{r}) = 2 - I_{\text{T\_Op}} + Res\ . \tag{8.8}$$

This cost function is the one used to guide the optimization process.

In addition, the weighting factors of I_T were also adjusted in order to improve the optimized results. It was also observed on the preliminary optimization processes that an increase of importance of the I_T terms relative to the strain level group promoted the global deformation of the specimen and reduced premature strain localization effects. Thus, the set of weighting factors was modified to avoid solutions promoting premature rupture. Therefore, the adjusted weighting factors listed in Table 8.1 are used in the formulation of I_{T_op}. The relative weights were changed taking into account that the maximum I_{T_Op} value that can be reached in the test is 1.

Table 8.1 – Adjusted weighing factors used for I_{T_Op} formulation in the optimization process.

w_{a1}	w_{a2}	w_{a3}	w_{a4}	w_{a5}
1	4	0.25	0.8	0.4
w_{r1}	w_{r2}	w_{r3}	w_{r4}	w_{r5}
0.13	0.02	0.25	0.35	0.25

8.2.1.4 Optimization conditions

Several conditions related to the optimization process as well as the design strategy must be defined. Thus, concerning the optimization process, the stopping criterion corresponds to a stagnation value of $1x10^{-4}$, in terms of the cost function value between two consecutive evaluations. Alternatively, the maximum number of evaluations allowed for Nelder-Mead algorithm was 200.

In the case of the conditions imposed to the design strategy, it must be stressed out that P_{tool} was fixed for the angular value of 90°. As a result of this choice, the orientation of the displacement Θ was also fixed at 90°, due to the symmetry condition. Note that horizontal displacement of the elements on the vertical symmetry is not allowed and, then, a numerical conflict could exist for the control point 1. Then, just the 7 control points x_i and the size of the tool L_{tool} were subjected to design by optimization. The admissible variation between consecutive control points was defined in the penalty function with $a_v = 0.25$. Furthermore, taking into account that the results obtained by the optimization algorithm may depend on the starting guess, three different sets of initial design variables were considered.

Additionally, the optimization strategy was adapted in order to include one more rigid tool. Hence, an optimization process using two rigid tools was also performed. The goal of this approach was to promote the optimization of a multiaxial loading path such as occurs, for

[6] It means that for a control point value out of the admissible variation but close to the imposed limit, just a smooth penalty is obtained. However, for a control point value far away of the imposed limit, a huge penalty is applied.

example, for the biaxial tensile test. Thereby, the tools were fixed, respectively, for $P_{tool1} = 90°$ and $P_{tool2} = 0°$. As a result, the orientation of the displacement was also fixed at $\Theta_1 = 90°$ and $\Theta_2 = 0°$ due to both symmetries. Also three different starting guesses were considered and a total of 9 design variables were used, namely, the 7 control points x_i and the sizes L_{tool1} and L_{tool2} of both tools. In this case, the admissible variation between consecutive control points was considered less restrictive, with $a_v = 0.55$.

8.2.1.5 Results

The different design variable sets selected as starting guesses for both optimization processes using 1 and 2 rigid tools are represented in Figure 8.9. It can be seen that distinct initial specimen shapes were purposely chosen aiming at decreasing the possibility of the optimization algorithm to start the process directly into a local minimum of the cost function.

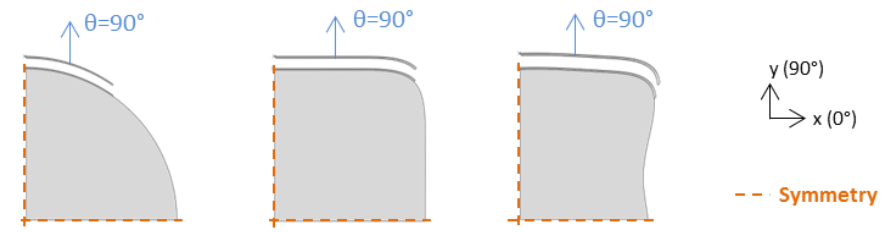

a) 1 tool

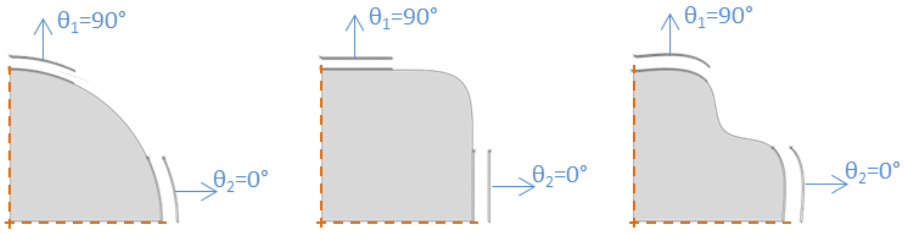

b) 2 tools

Figure 8.9 –Specimen geometries using the initial design variable sets defined for the optimization process. A gap between the tool and specimen was inserted in the models for an easy visualization.

Although three optimization processes were performed for each approach, only the best design solution is presented. Table 8.2 shows (i) the initial and optimal design variables, (ii) the initial and final S_{cost}, *Res* and I_{T_Op} values and (iii) the number of evaluations as well as time spent in both design optimization processes. The variation allowed for the design control points was defined between 10 and 60 mm and the initial values were chosen, approximately, in the middle of this range for both design cases. Concerning the bounds imposed to the size of the tools, these ones were defined leading to a minimum tool size of 10° and a maximum size lower than the angular range covered by the specimen shape boundary, *i*. *e*. 90° for one tool and 45° when using two tools, to avoid symmetry conflicts. Analyzing I_{T_Op} values, it can be seen that the design test using 2 tools gives the best result. Moreover, an increase of I_{T_Op} about of 153% and 92% were obtained, respectively, in the optimization processes using 1 and 2 tools. It revealed the ability of the optimization algorithm to find a solution that maximizes the strain field information. Additionally, the optimum solutions presented slight *Res* values. On the one hand, it means that some design control points did not fully respect the optimization constraints imposed. However,

these design control points are in the vicinity of the inequalities since the *Res* values were very small compared to S_{cost}. On the other hand, it confirms the trend of the optimization process to search for abrupt variations between the design control points which leads to unfeasible solutions.

The evolution of S_{cost} for both optimization process is depicted in Figure 8.10. It should be mentioned that the optimization algorithm tried some design variable sets leading to unfeasible specimen shapes and, consequently, impossibility of generating the model. For these cases the value of S_{cost} is equal to 2, since calculations are not performed and, consequently, $I_{T\_Op} = 0$. Such sets were mainly observed before 50 evaluations (particularly for the test design using 2 tools). After that, the Nelder-Mead algorithm tested almost only feasible solutions. The type of S_{cost} evolution obtained, with several peaks, also points out the non-smoothness of the problem, justifying the reason for the choice of a direct search algorithm.

Table 8.2 – Optimized results obtained for both design tests using 1 and 2 rigid tools.

	Test using 1 tool		Test using 2 tools			
Variables	Initial	Optimal	Initial	Optimal	L_{Bound}/U_{Bound}	Units
x_1	35.0	32.90	36.0	39.91		
x_2	35.0	31.89	37.75	39.18		
x_3	35.0	42.56	37.25	38.23		
x_4	35.0	29.27	31.0	24.57	10/60	mm
x_5	35.0	37.15	37.25	38.49		
x_6	35.0	35.78	37.75	39.52		
x_7	35.0	34.03	36.0	37.18		
L_{Tool}	35.0	37.0	-	-	10/80	Deg
L_{Tool1}	-	-	28.0	29.2	10/40	Deg
L_{Tool2}	-	-	28.0	29.6	10/40	Deg
S_{cost}	1.873	1.672	1.813	1.640	-	-
I_{T_Op}	0.127	0.334 (+153%)	0.187	0.359 (+92%)	-	-
Res	0.0	0.0058	0.0	$7x10^{-5}$	-	-
Evaluations		200		200		-
Time[7]		39.7		44.2		hours

The two optimization processes started respectively with a circular and a cross specimen shapes and led to the optimized geometries illustrated in Figure 8.11. This figure shows that the optimal shape obtained for the approach using 1 tool corresponds to a butterfly specimen. Whereas, in the case of the approach using 2 tools, a typical specimen shape of biaxial tension was obtained. As previously stated in chapter 7, the cruciform specimen shape seems to be the best shape for promoting a rich mechanical information when biaxial loading path is applied. Therefore, it must be stressed out that the design optimization process was able to achieve this kind of result, revealing the consistency of the optimization strategy proposed. Even if the conditions defined could favor the achievement of the cruciform specimen shape, it must be highlighted that the indicator was effective in guiding the optimization to such a shape. The designed tests are further called butterfly and cruciform, respectively.

[7] The optimizations were carried out in a Intel(R) Core(TM) i7-3630QM CPU using 4 processors.

In Table 8.3, the values of the several contributions to I_T are listed. It was verified that the butterfly test presents a larger $(\varepsilon_2/\varepsilon_1)_R$ value than the cruciform one. Hence, a larger strain state range is covered and more strain states are reproduced by the butterfly test. However, it must be highlighted that these states, with exception to uniaxial and plane strain tension, were characterized only for strain values lower than 0.01, as shown by the different $\bar{\varepsilon}^p$ values reached for each strain state. Nonetheless, these results demonstrate that the optimization process converge for solutions that favor the existence of multi-strain states. It can also be observed by Table 8.3 that a similar value of deformation heterogeneity $Std(\bar{\varepsilon}^p)$ was obtained for the two designed tests, while the cruciform test presents a better result in terms of global deformation $Av_{\bar{\varepsilon}^p}$.

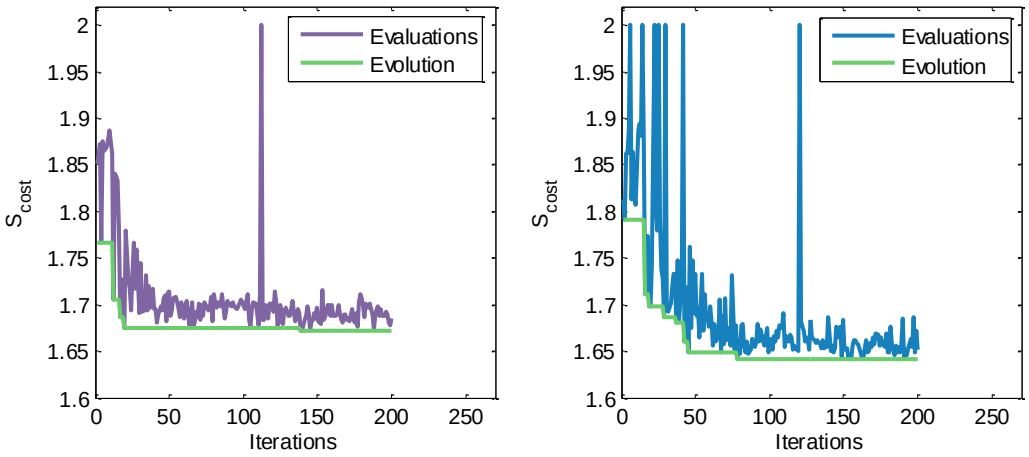

a) 1 tool b) 2 tools

Figure 8.10 – Evolution of the cost function for the optimization processes.

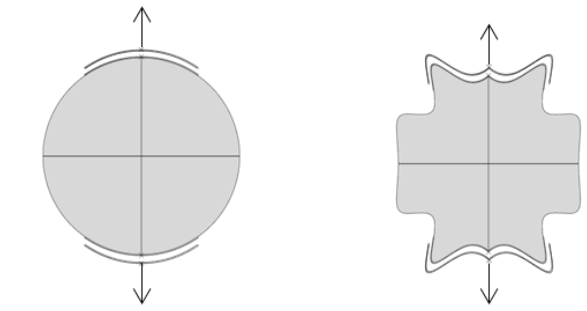

a) 1 tool – Butterfly test

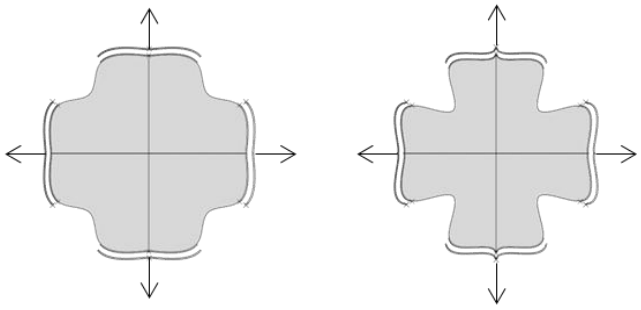

b) 2 tools – Cruciform test

Figure 8.11 – Initial (left) and optimal (right) specimen shapes obtained in the optimization process.

Comparing the I_T contributions of both designed tests (Table 8.3) with the ones listed in Table 7.3 of similar tests (shear-like and biaxial tests), it can been verified that the designed tests present better performance.

Figure 8.12 shows the distribution of $\bar{\varepsilon}^P$ and $\varepsilon_2/\varepsilon_1$ at rupture. Concerning $\bar{\varepsilon}^P$ distribution, both designed tests reached almost the same maximum value, although the cruciform test was generally more deformed. In relation to the $\varepsilon_2/\varepsilon_1$ distribution, the cruciform test leads to the characterization of $\varepsilon_2/\varepsilon_1$ range between biaxial to uniaxial strain states. While the butterfly test covers, in the most part of the sample, near shear to plane strain states. Note that it is without considering the remaining zone covering compression states, since this one presents a very small deformation level (*cf*. Figure 8.12 a)).

Strain states above plane strain tension were not developed by the butterfly test and, in opposition, strain states below uniaxial tension were not developed by the cruciform test. It seems, therefore, that the current optimization strategy is not performant enough to find an experiment promoting the characterization of the full strain state range. To this end, eventually, design optimization strategies using more tools or with increased complexity of the specimen configuration, adding holes or slits, can be explored.

Table 8.3 – Contributions to I_T for the optimized butterfly and cruciform tests.

	Butterfly	Cruciform
$\mathrm{Mean}\left[\mathrm{Std}\left(\varepsilon_2/\varepsilon_1\right)\right]$	0.318	0.336
$\left(\varepsilon_2/\varepsilon_1\right)_R$	2.269	1.681
$\mathrm{Mean}\left[\mathrm{Std}\left(\bar{\varepsilon}^P\right)\right]$	0.076	0.078
$\bar{\varepsilon}^P_{test}$	0.869	0.843
$\bar{\varepsilon}^P_{tens}$	0.229	0.305
$\bar{\varepsilon}^P_{shear}$	0.003	0
$\bar{\varepsilon}^P_{plane}$	0.047	0.054
$\bar{\varepsilon}^P_{biaxial}$	0	0.037
$\bar{\varepsilon}^P_{comp}$	0.005	0
$Av_{\bar{\varepsilon}^P}$	0.192	0.222

In order to quantitatively compare both designed tests with the ones evaluated in section 7.5.2, the ranking classifying all the tests through I_T was updated. Thereby, Figure 8.13 presents a classification of the different tests and it can be seen that both designed tests achieved better results than the other ones. Note that I_T values of the designed tests displayed on the ranking scale were calculated using the same weighting factors (listed in Table 7.1) as the other tests. These values are different of the ones obtained by the optimization process and consist of I_T = 0.261 and I_T = 0.271 for the butterfly and cruciform test, respectively. It must be pointed out that the butterfly specimen reached almost the same I_T value than the cruciform test. However, this

test only involves the use of uniaxial loading path. From the experimental point of view, its reproduction requires less effort since can be made by a universal standard testing machine.

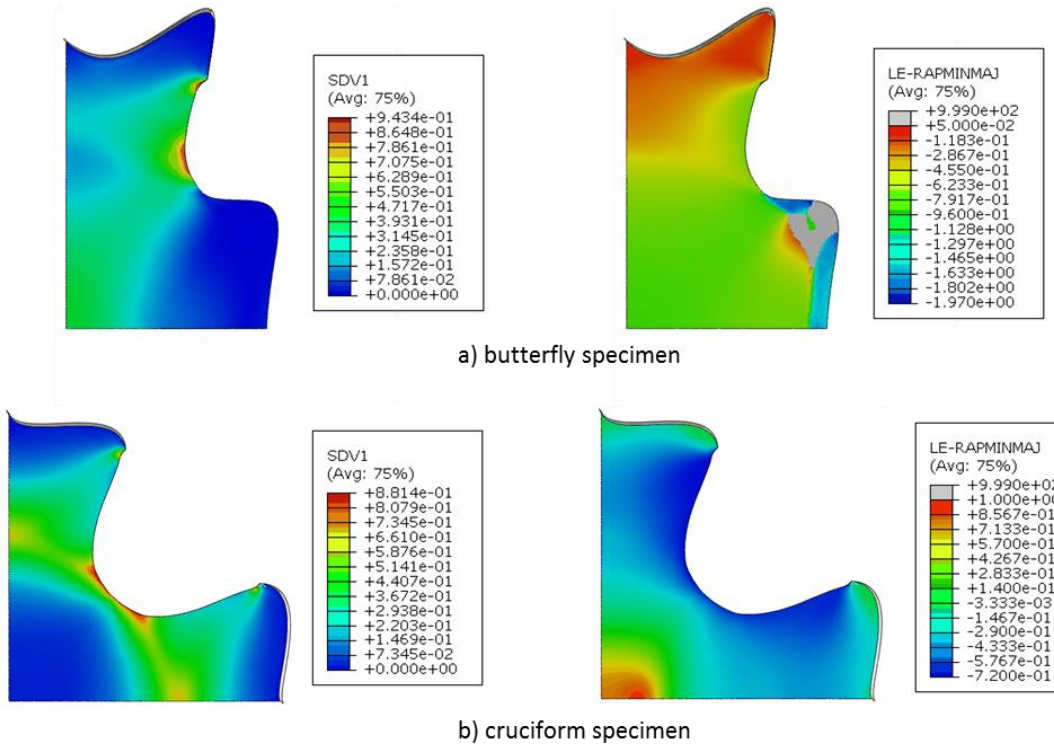

Figure 8.12 – Distributions of $\bar{\varepsilon}^P$ (left) and $\varepsilon_2/\varepsilon_1$ (right) for the two tests. Grey zones on $\varepsilon_2/\varepsilon_1$ contour means that $\bar{\varepsilon}^P < 10^{-3}$ and that this ratio was not calculated. SDV1 and LE-RAPMINMAJ stands for $\bar{\varepsilon}^P$ and $\varepsilon_2/\varepsilon_1$, respectively.

The ranking shows that with the optimization strategy developed it was possible to design experiments with enhanced mechanical information. Therefore, it appears that such a methodology is effective for finding mechanical tests promoting a better mechanical characterization of the material.

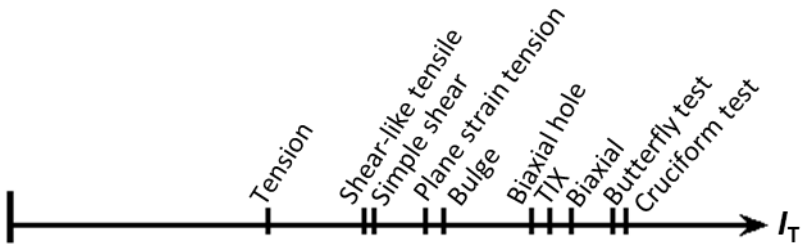

Figure 8.13 – I_T ranking for the tests evaluated in section 7.5.2 and the designed ones (butterfly and cruciform tests).

8.2.2 Test design based on local displacements

The local displacements strategy consists of a sequential design optimization technique applied to a symmetric model. In this strategy, the specimen geometry is defined by curve interpolation and

the loading path is imposed by local displacements over the specimen boundary shape. A schematic view of this design strategy is illustrated in Figure 8.14.

Similarly to the optimization strategy using rigid tools, the specimen geometry is controlled by the radial length of 7 design control points and the specimen center (red points 1 to 7 in Figure 8.14) and cubic splines are used to generate the boundary shape. However, in the case of the loading path, instead of using rigid tools, local displacements $\mathbf{u}_i$, $i = 1,\ldots, 7$ of coordinates $\mathbf{u}_i(u_{x,i}, u_{y,i})$ were applied directly to the control points, as shown in Figure 8.14. Hence, the position and displacement of the control points are the design variables **r** in the design process. Then, the tensor **r** can be written as

$$\mathbf{r} = \left[x_1 \;\; x_2 \;\; x_3 \;\; x_4 \;\; x_5 \;\; x_6 \;\; x_7 \;\; u_{y1} \;\; u_{x2} \;\; u_{y2} \;\; u_{x3} \;\; u_{y3} \;\; u_{x4} \;\; u_{y4} \;\; u_{x5} \;\; u_{y5} \;\; u_{x6} \;\; u_{y6} \;\; u_{x7}\right]. \qquad (8.9)$$

Concerning the loading path, the purpose of this strategy is to apply individual displacements for each point belonging to the outer boundary of the specimen. As a consequence, the displacement field for all these points (later discretized as nodes) must be calculated. To do that, the numerical deformed shape of the specimen must be known. Therefore, the displacements $\mathbf{u}_i$ are applied on the control points and a new spline taking into account the updated position of the control points is calculated, as shown in Figure 8.14. This new spline corresponds to the deformed shape of the specimen obtained in the numerical simulation. Thus, the displacements for the remaining points (black points in Figure 8.14) of the outer boundary of the specimen can be determined by calculating the difference between their position in the initial and new (deformed) spline shape, as exemplified by u_A. It must be highlighted that the updated cubic spline between control points is equally spaced in order to accurately determine the updated position of the remaining points (black points).

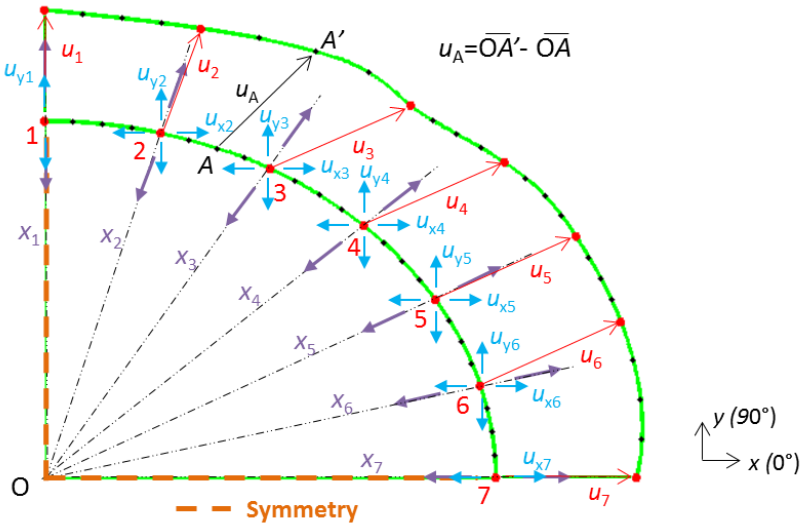

Figure 8.14 – Scheme of the test design based on local displacements.

In this way, all displacements for the control and remaining points can be defined and introduced as boundary conditions in the numerical model. It consists, thereby, of a loading path applied locally on the overall outer boundary of the specimen.

The current optimization strategy was applied as a sequential incremental technique since the loading path evolution was designed considering several steps. In other words, instead of just optimizing a one-step displacement leading to a loading path evolution up to rupture, the loading path was optimized in multistep displacements where the rupture, by reaching W_{CL}^{f} , is achieved in the last one. As a result, in the first step, both specimen shape and loading path are subjected to optimization by designing the initial position and displacement of the control points whereas, in the following steps, just the loading path is designed through the control points displacement. This kind of approach consists of a dynamic optimization design problem because the optimum values of the previous step are required in the following step. Indeed, the optimum deformed shape of the specimen in the previous step corresponds to the initial specimen shape in the following step.

During each optimization step, the design variables are found with the aim of maximizing the value of the indicator I_{T_Op} and, consequently, maximizing the strain field information of the test. Figure 8.15 shows the general design optimization process for the local displacements strategy.

This strategy involves the design optimization of (i) the initial specimen shape, (ii) boundary conditions by means of local displacements and (iii) a complex loading path in sequential steps. With this optimization procedure, it is expected to evaluate the effect of a complex loading path, in terms of multisteps as well as local displacements over the outer boundary of the specimen, on the achievement of a rich strain field. Although the optimized results may lead to an unfeasible loading path evolution from the experimental point of view, these results will allow to understand what kind of loading path evolution promotes a better mechanical information.

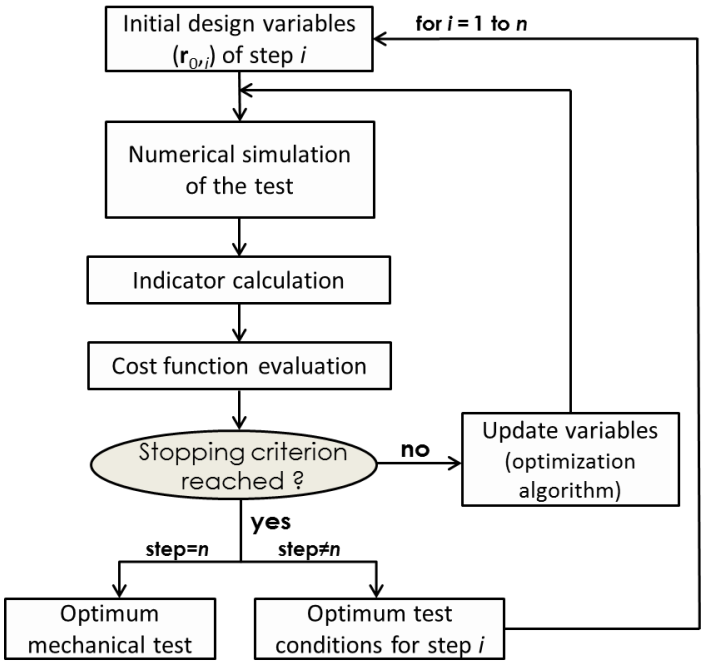

Figure 8.15 – Design optimization process for n steps of the local displacements strategy.

8.2.2.1 Automatic model generation

Such as for the design optimization using a rigid tool, in this strategy, a similar Python script generating the model was used. However, some differences on the definition of the script must

be pointed out. For instance, (i) all the points belonging to the outer boundary must be controlled in order to apply the displacements and (ii) the boundary must be meshed with 3 elements per mm along the edge, in order to respect the mesh density used to calibrate CL fracture parameter.

Nevertheless, in the first step of the design optimization process, the initial specimen geometry is always changing since this one is successively updated. Then, based on the arc length of the specimen boundary obtained for each evaluation, the Python script meshes the boundary shape with a number of nodes leading to a mesh definition of 3 elements/mm in-between the control points. These nodes are also controlled by the script in order to apply locally the boundary conditions concerning the updated loading path.

Concerning the following steps of the design optimization process, only the loading path is subjected to optimization. As a consequence, the specimen mesh remains the same and just the displacement values imposed on each node belonging to the specimen boundary are changed for each evaluation. Therefore, it is mandatory to parametrize the boundary conditions applied to each one of these nodes and, then, a parametrized input ABAQUS file is required for these optimization steps.

In addition, as the sequential steps of the optimization process are dependent on the final (and optimum) deformed shape of the previous step, it is also mandatory to retrieve this information. Therefore, all the information of each step is stored and, for the following step, the calculation is re-started from the end of the previous step with new boundary conditions. In this way, it is possible to carry out a dynamic multistep optimization since the previous designed deformation of the specimen is considered as the initial shape of the specimen in the following design optimization step and the displacement field for all the nodes of the outer boundary can be calculated.

A tridimensional model with both symmetries in x- and y-directions and also along the thickness is generated to be used by this design strategy. The specimen shape was meshed using C3D8R elements with hourglass control and a mesh density of 3 elements/mm in the sheet plane and 2 elements along the thickness was defined. The numerical simulations were carried out using *Yld2004-Mixed*$_{\text{Mod}}$ model and a zone of 1x1.5 mm^2 for determining W_{CL}^{f}. For the optimization of the strain field, the indicator was calculated taking into account the entire specimen surface in the sheet plane.

8.2.2.2 Optimization framework

The optimization procedure implemented for the design strategy based on local displacements is depicted in Figure 8.16. This design procedure involves a Matlab interface linked to ABAQUS code and to a Python script. Due to the loading path design in multistep displacements, this optimization procedure is repeated *n* times, until rupture is reached.

In the first step, specimen geometry as well as local displacements are subjected to design. Therefore, for step 1, the optimization process starts with an initial guess of design variables composed by the position and displacement of the 7 control points (*cf*. Equation 8.9).

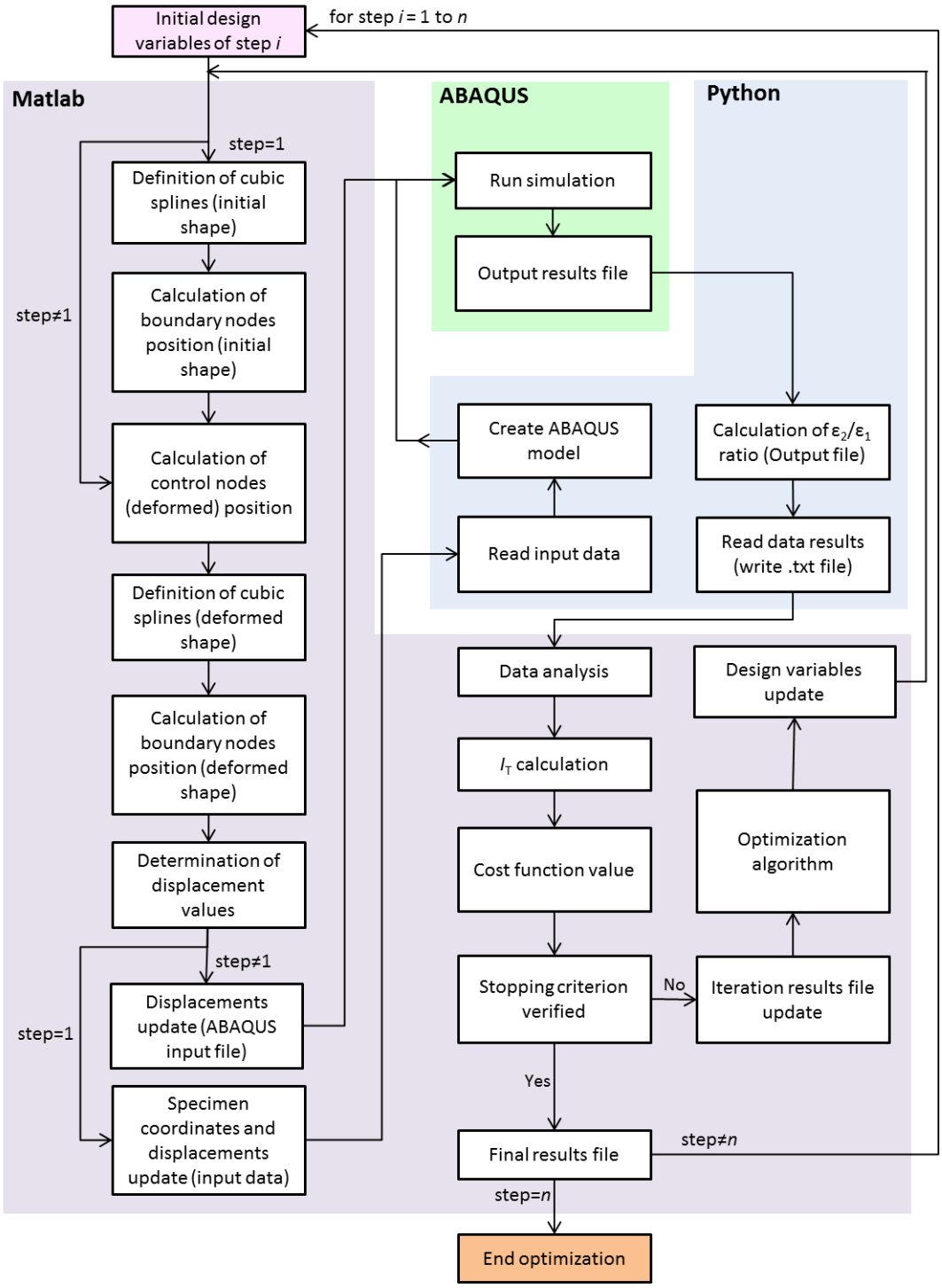

Figure 8.16 – Flow diagram of the multistep design process based on local displacements.

The Matlab script then determines the cubic splines defining the specimen shape from the position of the control points and, by calculating the arc length of this global spline, determines the number of nodes needed on the outer boundary of the specimen in order to respect the mesh density. Knowing the number of nodes required, their position on the boundary is further calculated by curve interpolation in Cartesian coordinates. At this stage, the initial shape of the specimen and position of the boundary nodes are defined. After that, the design variables

consisting of the control points displacements are added to the initial position of the control nodes. In this way, the position of the control points concerning the deformed shape of the specimen is calculated. Using these values, the deformed boundary shape is then determined by means of cubic splines and, applying curve interpolation, the position of the boundary nodes on the deformed state of the specimen are obtained. Note that the deformed boundary shape defined here corresponds to the final specimen shape that will be achieved by the numerical simulation. Hence, the loading path applied to the numerical simulation results of the difference between the boundary nodes position for the deformed and initial boundary shape. Such difference gives the individual displacements for each node of the outer boundary of the specimen, as illustrated in Figure 8.14. As a consequence, it is possible to impose a complex loading path on the overall specimen boundary.

Since the initial specimen shape in Cartesian coordinates and the displacements imposed to the boundary nodes (loading path) were defined, the Matlab script writes these values in files that are used by the Python script for generating the numerical model. For instance, the coordinates data are used as building points for the cubic splines that define the part model of the specimen, while the displacements data are directly applied as boundary conditions defining the loading path of the model.

With the model created, the numerical simulation is carried out with ABAQUS software and, subsequently, another Python script is used for post-processing the numerical results. The post-processing includes the determination of the $\varepsilon_2/\varepsilon_1$ ratio over the whole surface of the specimen and the numerical data needed for the indicator calculation. Using these data, the Matlab script determines the indicator as well as the cost function. In the case of the stopping criterion is reached, (i) the design process for this step ends, (ii) the final results file related to the optimization process of this step is written and (iii) the optimization process for the following step starts. In the case of the non-verification of the stopping criterion, (i) the optimization file recording the evolution of the design variables as well as the cost function during the optimization is automatically re-written, (ii) the design variables are updated by using the Nelder-Mead algorithm and (iii) the process is repeated until the stopping criterion is verified or the optimization process achieves the maximum number of evaluations.

For the optimization steps between 2 to *n*, the same design procedure is followed with the exception of the definition of the initial specimen shape. In these optimization steps, just the loading path evolution is designed since the specimen geometry was previously found in the starting optimization step. In fact, these following optimization steps consist of sequential designs of the loading path evolution leading to a more informative specimen deformation. Thereby, the displacement design variables are calculated taking into account the deformed state of the specimen obtained on the previous step, which is considered as the initial shape of the specimen in the following step. As a result, the following design step starts directly by the calculation of the deformed position of control nodes, adding the respective displacement design variables to the 'initial' position of the control nodes. Moreover, a new model does not need to be created, the geometric model is the one achieved in the first optimization step and just a parametrized input ABAQUS file is required for running the numerical simulation. However, it must be highlighted that it consists of an incremental design of the loading path. Therefore, the numerical simulation

of the model must be continued (and not restarted) from the first to the last step and all the numerical information must be continuously stored.

8.2.2.3 Cost function definition

Due to the fact that this design strategy is a sequential optimization process, the cost function was defined differently for the first and the following optimization steps.

In the case of the first optimization step, the cost function ($S_{\text{cost},1}$) is the one given by Equation 8.8. The same features described in section 8.2.1.3 were considered since this optimization step also involves optimizing the specimen geometry. Similarly, the weighting factors listed in Table 8.1 are used in the formulation of the indicator $I_{\text{T\_Op}}$. However, here, the displacements are constraints to a maximum value, never reaching rupture.

In the case of the following optimization steps, the Bellman's principle of optimality[8] (Sniedovich, 1986) was applied in the definition of the cost function. The Bellman's principle constitutes a necessary condition when dynamic optimization is used since it allows to break the optimization problem into simpler sub-problems. Thus, the principle of optimality is formulated in relation to a sequential decision model characterized by its cost function being dependent only on the final state of the process. In the case of the proposed design strategy, it means that the indicator value obtained by the optimum strain field of the previous step must be related with the one calculated during the optimization of the current step. Then, for an optimization step *i* comprised between 2 to *n*, the cost function is defined by

$$S_{\text{cost},i}(\mathbf{r}) = S_{\text{cost},i-1} - \Delta I_{\text{T\_Op},i}\,, \tag{8.10}$$

where $\Delta I_{\text{T\_Op},i} = I_{\text{T\_Op},i} - I_{\text{T\_Op},i\text{-}1}$ is the incremental variation of the indicator at the increment *i*.

8.2.2.4 Optimization conditions

The optimization procedure was performed considering 4 sequential steps. For each design step, a stagnation value between consecutive evaluations of the cost function of $1\text{x}10^{-4}$ was defined as the stopping criterion. Additionally, the maximum number of evaluations allowed for Nelder-Mead algorithm was 350 for the first and 200 for the remaining optimization steps. The reason for defining more evaluations in the first optimization step is related to the larger number of design variables. Concerning the penalty function used in this optimization step, the parameter value defining the admissible variation between consecutive control points was defined as $a_v = 0.55$.

The displacements of the control points were defined in terms of Cartesian system by their horizontal and vertical values ($u_{\text{x},i}$, $u_{\text{y},i}$). Hence, 19 design variables were used in the first step of this optimization strategy, namely: (i) the radial length of the 7 design control points to the specimen center, (ii) the 6 vertical and (iii) the 6 horizontal displacements of the control points. For the following steps, only the 6 vertical and 6 horizontal displacements of the control points were designed, leading to a total value of 12 design variables. It must be noted that for the control points 1 and 7 (Figure 8.14) it can be only applied, respectively, vertical and horizontal

[8] The principle of Bellman states that an optimal sequence of decisions in a multistage decision process problem has the property that whatever the initial state and decisions are, the remaining decisions must constitute an optimal policy with regard to the state resulting from the first decisions.

displacement, due to the symmetry conditions defined on the model. Therefore, for these control points the conditions $u_{x,1} = 0$ and $u_{y,7} = 0$ were imposed.

8.2.2.5 Results

Due to the complexity of this design strategy, a preliminary approach just considering the design of the loading path was first applied. Its main goal was to define a suitable number of steps and maximum local displacements for investigating the loading path evolution. This preliminary approach has shown that rupture can be reached in 4 steps and the maximum displacements should be around 1.5 mm. Therefore, 4 steps are considered for this design strategy.

On a second preliminary approach, the effect of the predefined specimen shape on the achievement of more informative loading path was analyzed. Therefore, the multistep loading path evolution was designed considering 3 different initial specimen geometries. These geometries are shown in Figure 8.17. The obtained results of this preliminary analysis revealed that the loading path of the rectangular specimen shape led to larger mechanical information of the test. Therefore, this rectangular shape was chosen as initial specimen shape to be subjected to optimization in the multistep design strategy.

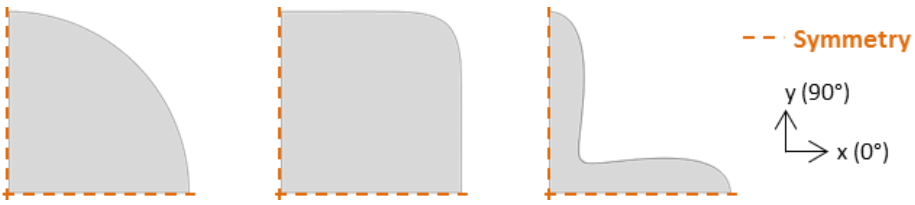

Figure 8.17 – Specimen geometries used for investigating the effect of the starting specimen shape on the multistep loading path evolution.

Table 8.4 lists (i) the initial and optimal design variables, (ii) the S_{cost}, I_{T_Op} and *Res* values and (iii) the number of evaluations as well as the time spent for the 4 steps of the optimization process. Concerning the first step, where specimen shape and loading path were simultaneously subjected to optimization, it was defined a variation of position of the control points between 10 and 60 mm and a variation of the displacement variables between 0 and 1.5 mm. For steps 1 to 3, the later range was used and the initial displacement values were 0.75 mm. However, for step 4 (last one) the initial displacement values were set equal to 1.5 mm and the bound values allowed were defined as 0 and 3 mm. Large displacements were allowed for this last step in order to ensure the achievement of rupture. Analyzing the optimum design variables, it can be seen that the design control points did not present significant variations comparatively to the initial values chosen. However, in the case of the displacement variables, different values from the initial ones were obtained in the different steps. By I_{T_Op} and S_{cost} values, it can be seen that a considerable increase of the mechanical information of the test is obtained when a multistep loading path is adopted, since an I_{T_Op} value of 0.497 was reached at the last step. In addition, no active constraints were verified, obtaining a null value for *Res*.

Figure 8.18 shows the evolution of S_{cost} for the different optimization steps. It can be seen that, for step 1, the Nelder-Mead algorithm tested some design variable sets leading to unfeasible specimen shapes and, consequently, impossibility of generating the model (evaluations with $S_{cost} = 2$). For the remaining steps, such a situation was not observed since only the loading path

was subjected to design. Figure 8.19 illustrates the initial and final specimen geometry as well as the deformed shapes of the specimen at the end of each optimization step. It can be seen that the designed specimen shape obtained was not substantially different from the initial one and, in addition, it can also be observed the slight differences between the achieved deformed shapes.

Table 8.4 – Results obtained for the multistep design test.

Variables	Initial	Optimal				L_{Bound}	U_{Bound}	Units
		Step 1	*Step 2*	*Step 3*	*Step 4**			
x_1	35.0	33.28	-	-	-	10	60	mm
x_2	36.2	36.07	-	-	-	10	60	mm
x_3	40.4	39.59	-	-	-	10	60	mm
x_4	45.7	46.35	-	-	-	10	60	mm
x_5	40.4	39.93	-	-	-	10	60	mm
x_6	36.2	36.51	-	-	-	10	60	mm
x_7	35.0	38.50	-	-	-	10	60	mm
u_{y1}	0.75/1.5*	0.684	0.731	1.006	0.898	0	1.5/3.0*	mm
u_{x2}	0.75/1.5*	0.80	1.039	0.135	1.063	0	1.5/3.0*	mm
u_{y2}	0.75/1.5*	0.769	0.682	0.407	0.959	0	1.5/3.0*	mm
u_{x3}	0.75/1.5*	0.793	0.878	1.282	0.835	0	1.5/3.0*	mm
u_{y3}	0.75/1.5*	0.645	0.998	1.094	0.945	0	1.5/3.0*	mm
u_{x4}	0.75/1.5*	0.85	0.937	1.277	0.844	0	1.5/3.0*	mm
u_{y4}	0.75/1.5*	0.721	0.898	0.430	1.117	0	1.5/3.0*	mm
u_{x5}	0.75/1.5*	0.846	0.996	1.385	1.087	0	1.5/3.0*	mm
u_{y5}	0.75/1.5*	0.856	0.750	1.477	0.955	0	1.5/3.0*	mm
u_{x6}	0.75/1.5*	0.786	1.285	0.001	0.806	0	1.5/3.0*	mm
u_{y6}	0.75/1.5*	1.125	0.020	1.422	1.107	0	1.5/3.0*	mm
u_{x7}	0.75/1.5*	0.665	0.448	1.411	1.039	0	1.5/3.0*	mm
I_{T_Op}	0.114	0.153	0.271	0.420	0.497			-
S_{cost}	1.886	1.847	1.729	1.580	1.503			-
Res	0	0	-	-	-			-
Evaluations		350	200	200	200			-
Time[9]		45.59	22.6	23.3	20.3			hours

Table 8.5 presents the values of the several contributions used in I_T formulation. It can be observed that the strain state range $(\varepsilon_2/\varepsilon_1)_R$ as well as the diversity of the mechanical information $Std(\varepsilon_2/\varepsilon_1)$ did not always increase during the multistep optimization. It reveals that the strain state range covered varied for each step as can be proven by the $\bar{\varepsilon}^P$ values reached for each strain state. In fact, for step 1, shear and compression strain states were not covered while, for step 3, all the strain states were reproduced. Concerning the average deformation $Av_{\bar{\varepsilon}^P}$ as well as the deformation heterogeneity $Std(\bar{\varepsilon}^P)$, it can be seen that these values increased continuously during the multistep optimization. It was due to the fact that these values deal with plastic strain, which increased up to rupture in the last step.

[9] The optimization was carried out in a Intel(R) Core(TM) i7-3630QM CPU using 4 processors.

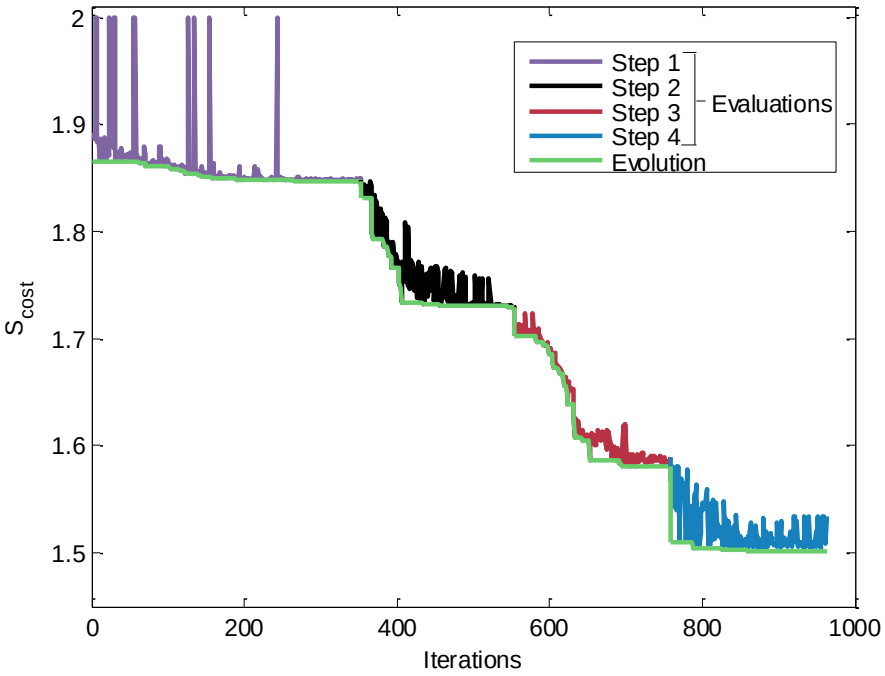

Figure 8.18 – Evolution of the cost function for the multistep design process.

Figure 8.20 shows the distribution of $\bar{\varepsilon}^P$ and $\varepsilon_2/\varepsilon_1$ at the end of each step. Analyzing $\bar{\varepsilon}^P$ distribution, it can be seen that the large strains occur in the vicinity of the specimen boundary and that the maximum equivalent plastic strain value achieved in the step 4 was about of 1.34. It appears that by applying a loading path based on local displacements, large deformation can be reached compared with the tool displacement approach. Concerning $\varepsilon_2/\varepsilon_1$ distribution, it can be seen that the strain state range was mainly covered between uniaxial ($\varepsilon_2/\varepsilon_1 = -0.62$) to equibiaxial tension ($\varepsilon_2/\varepsilon_1 = 1$). However, uniaxial compression ($\varepsilon_2/\varepsilon_1 = -1.59$) and/or simple shear ($\varepsilon_2/\varepsilon_1 = -1$) were also covered in steps 3 and 4. These results show that it is possible to cover all the strain state range using a multistep design optimization approach.

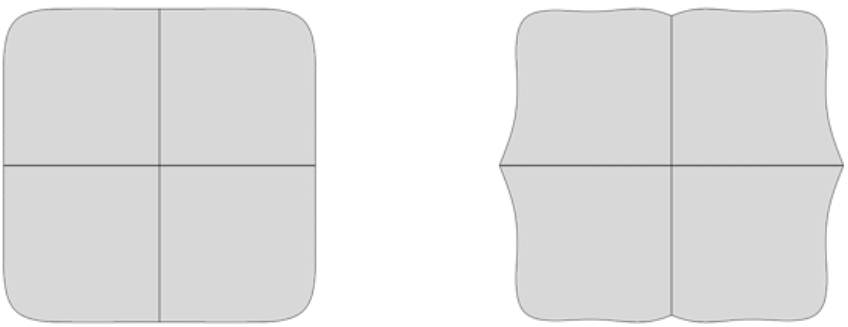

a) Initial geometry b) Designed geometry (end of step 1)

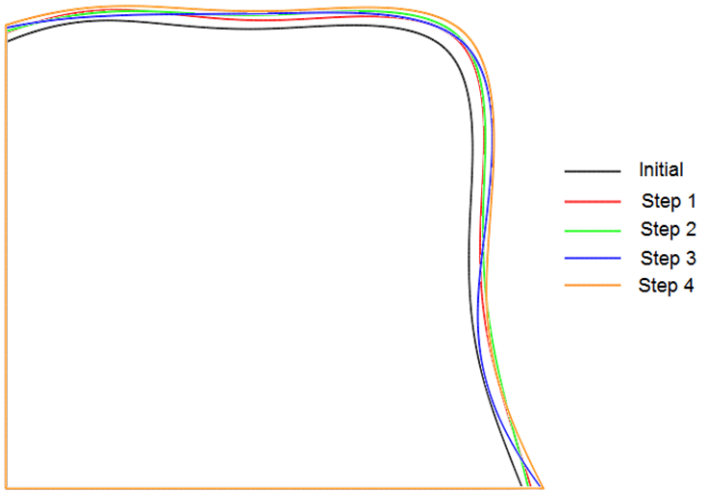

c) Initial and deformed specimen shapes at the end of each step

Figure 8.19 – Several sample geometries after each step.

Table 8.5 – Values obtained for the contributions of I_T on the different steps of the multistep test.

	Step 1	*Step 2*	*Step 3*	*Step 4*
$\mathrm{Mean}\left[\mathrm{Std}\left(\varepsilon_2/\varepsilon_1\right)\right]$	0.443	0.411	0.4684	0.503
$\left(\varepsilon_2/\varepsilon_1\right)_R$	1.633	2.305	2.629	1.998
$\mathrm{Mean}\left[\mathrm{Std}\left(\bar{\varepsilon}^P\right)\right]$	0.012	0.037	0.079	0.115
$\bar{\varepsilon}^P_{test}$	0.226	0.728	1.328	1.366
$\bar{\varepsilon}^P_{tens}$	0.196	0.494	0.178	0.493
$\bar{\varepsilon}^P_{shear}$	0	0.339	0.717	0.960
$\bar{\varepsilon}^P_{plane}$	0.081	0.076	0.083	0.145
$\bar{\varepsilon}^P_{biaxial}$	0.053	0.054	0.055	0.083
$\bar{\varepsilon}^P_{comp}$	0	0	0.413	0
$Av_{\bar{\varepsilon}^P}$	0.093	0.282	0.463	0.508

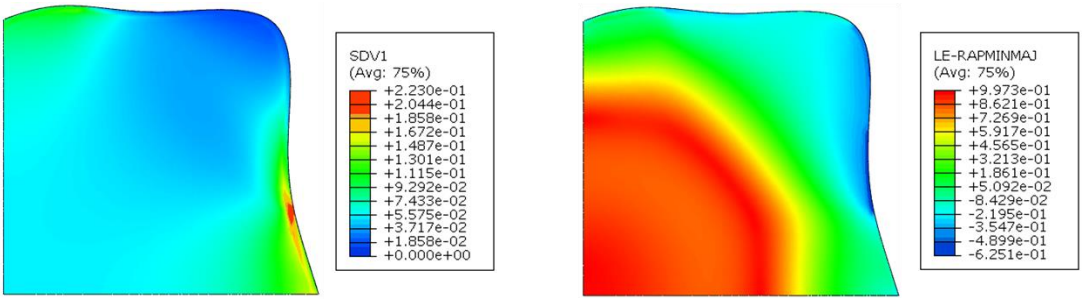

a) Step 1

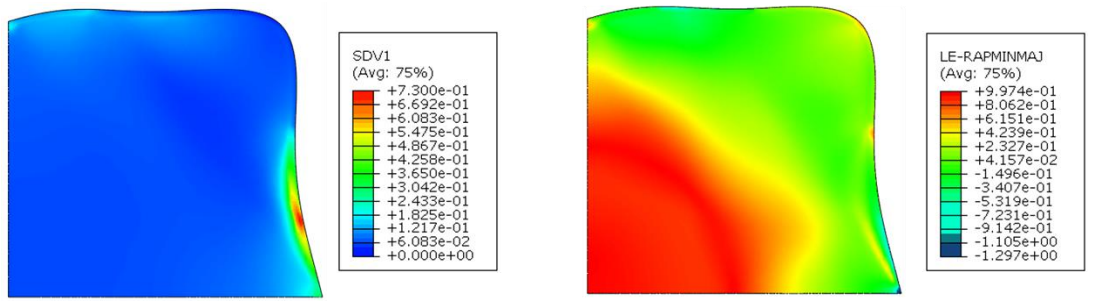

b) Step 2

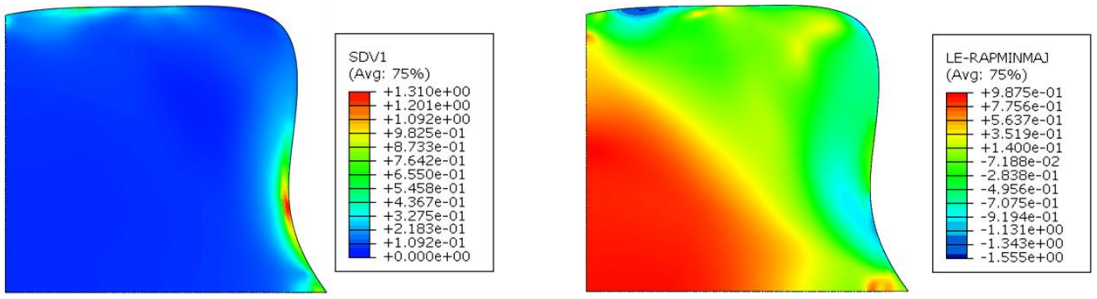

c) Step 3

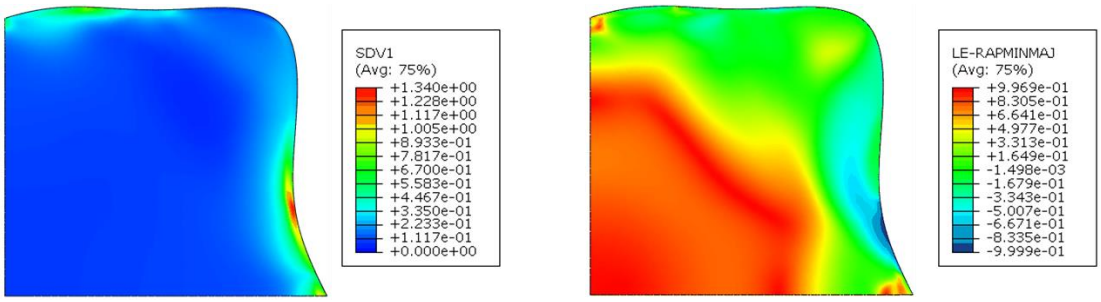

d) Step 4

Figure 8.20 – Distribution of $\bar{\varepsilon}^{P}$ and $\varepsilon_2/\varepsilon_1$ over the specimen surface at the end of the different steps.

The multistep test was included in the I_T ranking classifying all the tests, as shown in Figure 8.21. Its I_T value was calculated using the weighting factors listed in Table 7.1. Thus, the indicator value was different of the one (I_{T_Op}) obtained on the optimization process and consists of $I_T = 0.46$.

Figure 8.21 – I_T ranking for the classical and heterogeneous tests evaluated in section 7.5.1, the ones designed using 1 and 2 rigid tools and the multistep test.

From Figure 8.21, it can be observed that the multistep test achieved a quite higher I_T value than the remaining tests. By this result, it was proved that a complex loading path evolution in terms of sequential steps as well as local displacements is able to promote a considerable

improvement of the mechanical information given by a test. However, from an experimental point of view such kind of test seems hard to carry out, mainly due to the boundary conditions applied by means of global displacement of the free boundary specimen shape. Nonetheless, it should be emphasized that the main purpose of this design optimization strategy was to understand the effect of a complex loading path on the achievement of informative strain fields.

8.3 Parameters identification using a heterogeneous test

The butterfly test obtained in section 8.2.1.5 was used in order to evaluate its performance for material parameters identification purposes. Among the designed mechanical tests, this one was chosen due to the fact that its experimental reproduction seems to be straightforward, since it can be carried out using a standard testing machine.

However, experimental tests with this specimen were not performed. Instead, for this material parameter identification study, the virtual DC04 mild steel identified from the conventional tests was considered as the reference material. In this way, the reference data used as experimental results was virtually generated by considering the parameters set of Table 5.2 for *Yld2004-Mixed* model.

Since the butterfly test corresponds to a heterogeneous experiment, a non-homogeneous identification approach was considered. Therefore, an evaluation of the strain fields was carried out for the identification of the material parameters. Then, the objective function $S_{\text{obj}}(\mathbf{x})$ defined by Equation 2.19 was used. Hence, both load and strain data were taken into account. For instance, the specimen surface was analyzed up to a tool displacement of 10 mm, which corresponds to a maximum equivalent plastic strain of 0.65, comparing 5 strain fields ($n_{\text{im}} = 5$). The strain fields, in terms of minor ε_2 and major ε_1 strain values in the sheet plane were compared for the tool displacements $d = 0.2$, 1, 2, 6 and 10 mm. In the case of the load data, the tool force-displacement curve was considered.

Further, the parameters identification framework previously developed in chapter 5 and described in Figure 5.1 was used to identify the material parameters. However, a Python script was included to read the strain field results.

It was observed, by a preliminary identification process, that using only the butterfly test, the parameters set identified was not the most accurate, leading to some differences in the prediction of the experimental curves of the uniaxial tensile and simple shear tests mainly oriented at 77° and 90° to RD. Therefore, another butterfly test with a rotation of 90° of the material orientation was introduced and was also used for identifying the material parameters. Thus, $S_{\text{obj-T}}(\mathbf{x})$ was defined as

$$S_{\text{obj-T}}(\mathbf{x}) = \sum_{i=1}^{n_{\text{test}}} S_{\text{obj},\,i}(\mathbf{x}), \tag{8.11}$$

where n_{test} is equal to 2 and stands for the butterfly test without and with a rotation (of 90°) of the material orientation.

8.3.1 Numerical model of the butterfly test

The numerical model of the butterfly test was already described in section 8.2.1.1. However, since the optimized butterfly test was generated with an unstructured mesh, a re-meshing of the specimen surface was carried out in order to create a structured mesh. The reason for that was to acquire the strain field data by a similar approach as the one using DIC technique to output the experimental results. Figure 8.22 shows the original mesh, obtained in the design of the butterfly test, and the structured mesh, for the identification process. It must be emphasized that both meshes present approximately a mesh density of 3 elements/mm and the structured mesh leads to a similar I_T value for the test. Thereby, no influence of the re-meshing was evidenced on the achievement of more (or less) mechanical information from the test.

In addition, such as for DIC technique, a ROI for the specimen surface was defined as shown in Figure 8.22 b) (red zone). Only the strain field information coming from the ROI was used for identifying the material parameters. The outer ROI was not considered due to the local effects related to the tool contact and also, because, from an experimental point of view, DIC technique may present some difficulty to accurately measure data in this region.

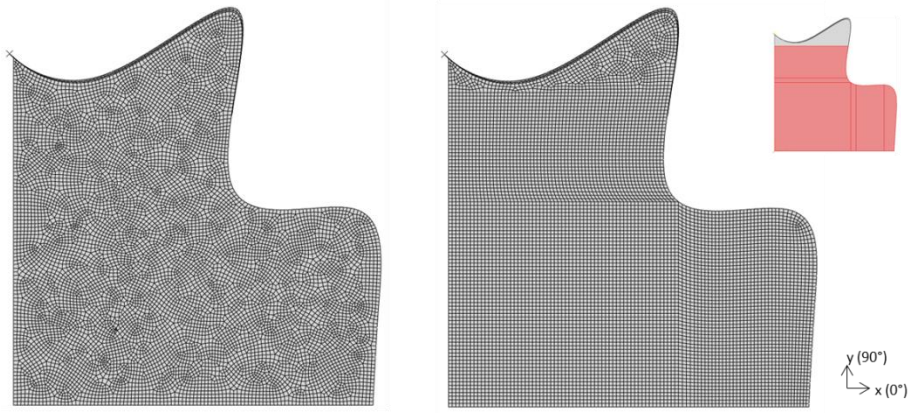

a) unstructured mesh b) structured mesh

Figure 8.22 – Meshes for the butterfly test used in the parameters identification process. The red zone consists in the ROI of the sample.

8.3.2 Process parameters

The parameters identification process was defined considering a stagnation value of 10^{-12}, in terms of the objective function value between two consecutive evaluations, as the stopping criterion. Moreover, the derivatives of the objective function were calculated numerically through a forward finite difference scheme with a perturbation value of $5x10^{-3}$ and the L-M algorithm was used with a maximum number of evaluations limited to 250. It was observed for the parameters identification processes using the classical tests (section 5.3) that this number of evaluations could be enough to obtain a reliable material parameters set.

As for the parameters identification processes of chapter 5, the elastic parameters E and υ, the exponent a as well as the anisotropic coefficients $c_{44}^{(k)}$ and $c_{55}^{(k)}$, with $k = 1, 2$, of the *Yld2004-18p* yield function were not considered as parameters to be identified. In addition, the kinematic hardening parameters were considered constant values and equal to the reference ones since the butterfly test does not involve reverse loading.

8.3.3 Results

Table 8.6 shows the initial, reference and optimal identified parameters, the initial and final values of the objective function and the number of evaluations carried out by the identification process. The initial values as well as the bounds for the material parameters were set equal to the ones used in the identification of the virtual DC04 mild steel behavior (reference material). Hence, both identification processes started in similar conditions.

Table 8.6 - Material parameters identified from the butterfly tests and the experimental database.

		Yld2004-Mixed			
Parameters	Initial	Reference	Identified	Limits	Units
$c_{12}^{(1)}$	1.0	1.264	1.317 (+4.2%)	-2.2 / 2.2	-
$c_{13}^{(1)}$	1.0	0.974	1.021 (+4.8%)	-2.2 /2.2	-
$c_{21}^{(1)}$	1.0	1.242	0.973 (-21.7%)	-2.2 / 2.2	-
$c_{23}^{(1)}$	1.0	1.049	1.049	-2.2 /2.2	-
$c_{31}^{(1)}$	1.0	0.579	0.769 (+32.8%)	-2.2 / 2.2	-
$c_{32}^{(1)}$	1.0	0.708	0.721 (+1.8%)	-2.2 /2.2	-
$c_{66}^{(1)}$	1.0	1.365	1.064 (-22.1%)	-2.2 / 2.2	-
$c_{12}^{(2)}$	1.0	0.792	0.936 (+18.2%)	-2.2 /2.2	-
$c_{13}^{(2)}$	1.0	0.672	0.828 (+23.2%)	-2.2 / 2.2	-
$c_{21}^{(2)}$	1.0	0.838	0.894 (+6.7%)	-2.2 /2.2	-
$c_{23}^{(2)}$	1.0	0.929	1.101 (+18.5%)	-2.2 / 2.2	-
$c_{31}^{(2)}$	1.0	0.996	0.889 (-10.7%)	-2.2 /2.2	-
$c_{32}^{(2)}$	1.0	0.768	0.662 (-13.8%)	-2.2 /2.2	-
$c_{66}^{(2)}$	1.0	0.678	1.067 (+57.4%)	-2.2 /2.2	-
σ_0	141.2	100.0	106.4 (+6.4%)	100.0 / 170.0	MPa
σ_∞	261.0	210.3	185.9 (-11.6%)	160.0 / 800.0	MPa
δ	10.5	5.92	7.069 (+19.4%)	1.0 / 100.0	-
β	160.0	102.8	180.1 (+75.2%)	100.0 / 900.0	MPa
$Xsat_1$		44.57	-		MPa
γ_1		22.85	-		-
$Xsat_2$		106.2	-		MPa
γ_2		258.38	-		-
$Xsat_3$		5629.7	-		MPa
γ_3		0.0258	-		-
$S_{obj\text{-}T}(\mathbf{x})$	0.141	-	5.207×10^{-4} (-99.6%)		-
Evaluations		-	233		-

Comparing the identified and the reference parameters, it can be seen that these parameters sets are rather different. It results from the fact that multiple solutions can be obtained on the search of parameters of non-linear elastoplastic constitutive models. Moreover,

the identified parameter set was found after performing 233 evaluations, while the reference parameter set was identified after performing 500 evaluations. However, comparing the initial and final objective function values, given at the bottom of Table 8.6, it can be observed that a reduction of 99.6% was obtained. Therefore, though the reference and identified parameters sets are different, these ones must predict similar results and reproduce the behavior of the material.

Figure 8.23 depicts the evolution of the objective function value during the identification process of the identified parameters set. For the first 19 evaluations, individual perturbations of each material parameter were performed in order to calculate numerically the Jacobian of the objective function (sensitivity matrix) and, before 50 evaluations, S_{obj_T} value was significantly decreased. In the following evaluations, a stabilization of S_{obj_T} value was observed till the verification of the stopping criterion after 233 evaluations.

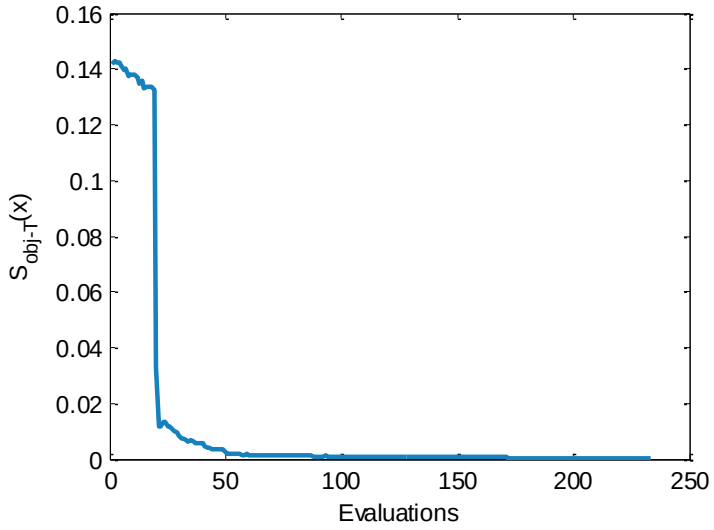

Figure 8.23 – Evolution of the objective function S_{obj_T} during the material parameters identification process using both butterfly tests.

Figure 8.24 depicts the load-displacement curves obtained for the butterfly tests without and with rotation of the material orientation using both reference and identified parameter sets. Concerning the load-displacement curve of the butterfly test without rotation of the material orientation, it can be seen that the identified parameter set led to a smooth over-prediction of the reference result. However a good reproduction of this curve was achieved. In the case of the load-displacement curve of the butterfly test with rotation of the material orientation, a very reliable prediction of this curve was obtained since both reference and identified parameter sets led to similar results.

Figures 8.25 to 8.28 show the major and minor strain distribution obtained in the butterfly tests for the tool displacements $d = 2$ mm and $d = 10$ mm, using both reference and identified parameters set. It can be seen that a good agreement was obtained between the reference and the predicted results. Concerning the major and minor strain distributions for $d = 2$ mm (Figures 8.25 and 8.27), identical strain fields were obtained. In the case of the major and minor strain distributions for $d = 10$ mm (Figures 8.26 and 8.28), slight differences can be observed mainly for the strain field of the butterfly test without rotation of the material orientation, however, the

global strain distribution was almost identical. Taking into account the observed objective function reduction during the identification process, it was expected to obtain similar strain field distributions. Indeed, the strain distributions depicted confirmed this expectation.

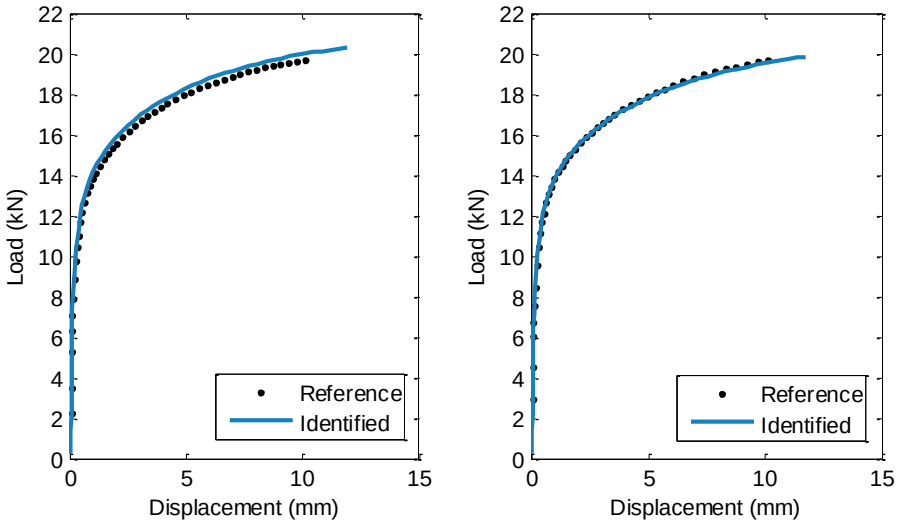

Figure 8.24 – Load-displacement curves obtained using the reference and the identified parameters sets for the butterfly test a) without and b) with rotation of the material orientation.

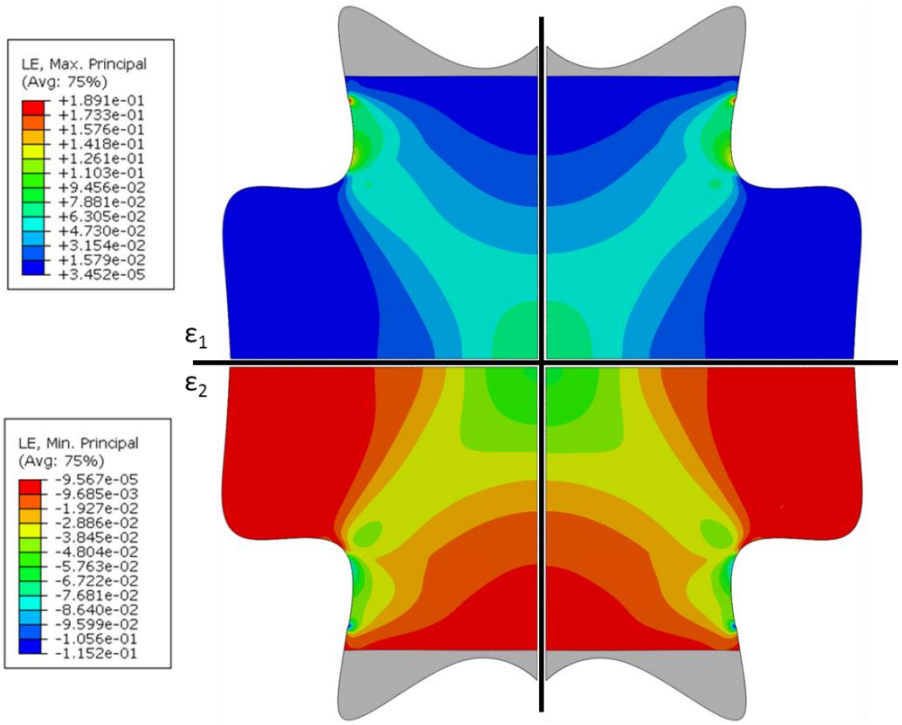

Figure 8.25 – Major ε_1 and minor ε_2 strain distribution for a displacement $d = 2$ mm of the butterfly test without rotation of the material orientation.

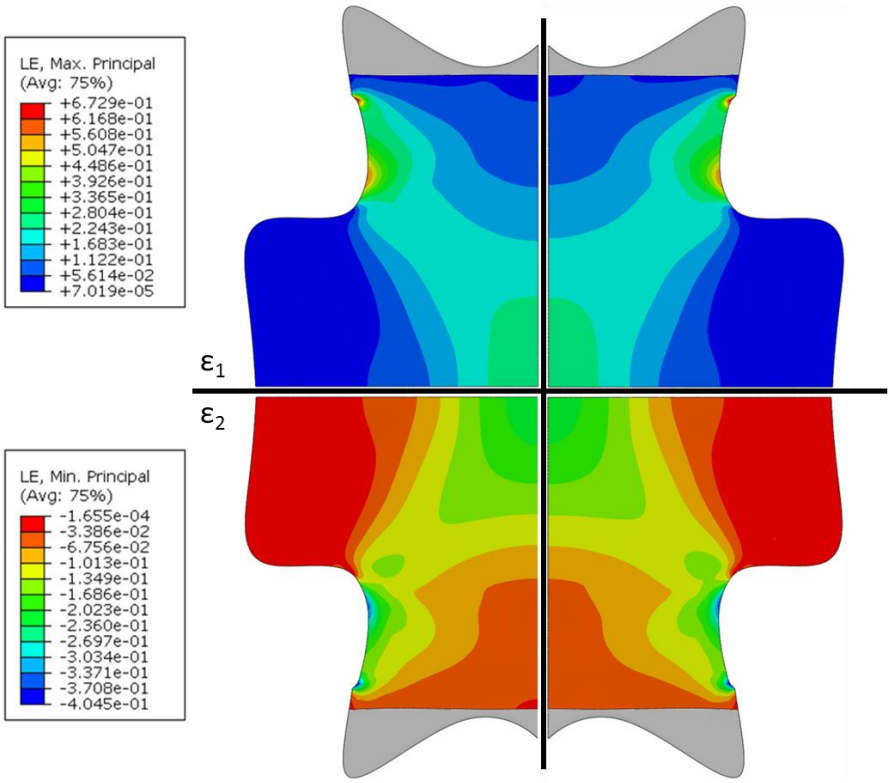

a) Reference set b) Identified set

Figure 8.26 – Major ε_1 and minor ε_2 strain distribution for a displacement $d = 10$ mm of the butterfly test without rotation of the material orientation.

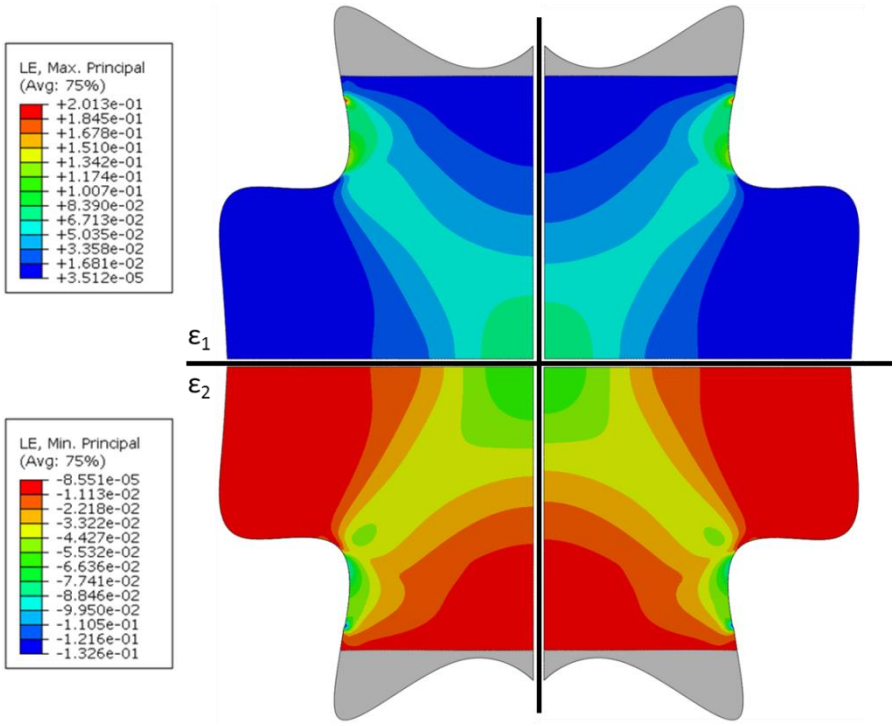

a) Reference set b) Identified set

Figure 8.27 – Major ε_1 and minor ε_2 strain distribution for a displacement $d = 2$ mm of the butterfly test with rotation of the material orientation.

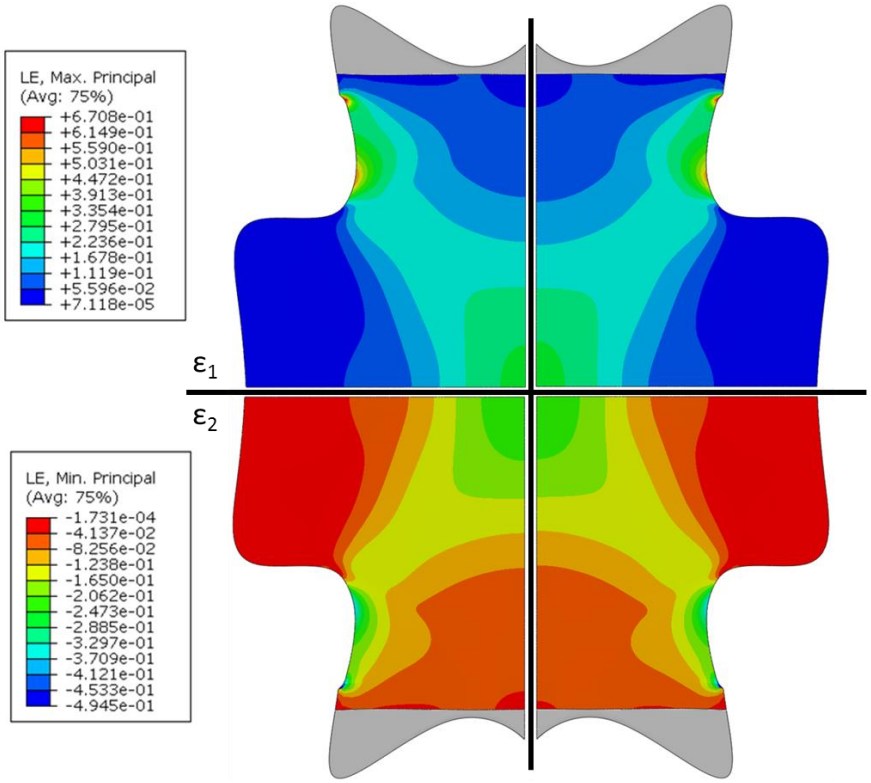

a) Reference set b) Identified set

Figure 8.28 – Major ε_1 and minor ε_2 strain distribution for a displacement $d = 10$ mm of the butterfly test with rotation of the material orientation.

8.3.4 Numerical reproduction of the experimental data

In order to assess the quality of the material parameters set identified from the butterfly test, the experimental database composed by the several classical tests used in chapter 5 was reproduced. Figures 8.29 and 8.30 show the experimental and numerical, obtained with the reference and identified parameters sets, stress-strain curves for simple shear/uniaxial tension and ε_{11}-ε_{22} curves for uniaxial tension in the five different orientations to RD. Figure 8.29 also includes the experimental and numerical results for bulge test.

From Figure 8.29, it can be observed that a reliable reproduction of the experimental uniaxial tension and simple shear curves was obtained using the identified parameters set. In fact, both identified and reference parameters sets led to similar numerical predictions. In the case of the bulge test, an under-estimation of the hardening evolution was verified using the identified parameters set. Nonetheless, it must be emphasized that the butterfly test does not cover the equibiaxial stress state (*cf*. Table 8.3). Moreover, identical numerical and experimental ε_{11}-ε_{22} curves were obtained for both uniaxial and biaxial tension.

Concerning the numerical reproductions of the stress level in uniaxial tension and simple shear as well as ε_{11}-ε_{22} curves at 22° and 45° to RD, depicted in Figures 8.30 a) and b), it can be seen that the identified parameters led to almost identical stress-strain curves to the ones obtained with the reference parameters set. However, the numerical ε_{11}-ε_{22} curves at 22° and 45° using the identified parameters set were not accurately predicted. These curves tended to deviate from the experimental behavior with the increase of deformation.

In the case of the uniaxial tension and simple shear curves as well as ε_{11}-ε_{22} curves at 77° and 90° to RD, shown in Figures 8.30 c) and d), very reliable predictions were obtained. The experimental and numerical curves using the identified and reference parameters sets were similar.

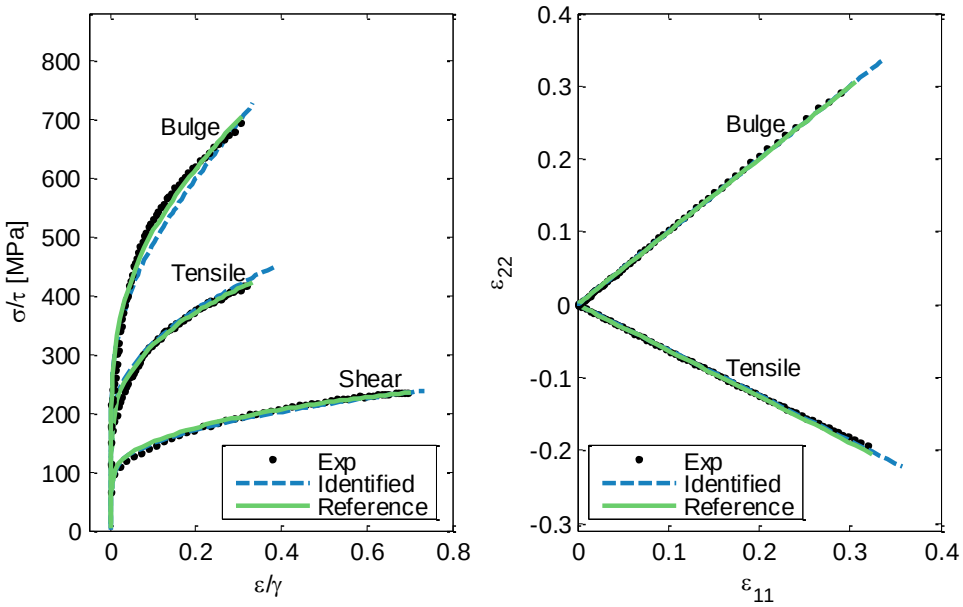

Figure 8.29 – Experimental and numerical (i) τ-γ curve for simple shear and σ-ε curves for bulge and uniaxial tension to 0°/RD and (ii) ε_{11}- ε_{22} curves for bulge and uniaxial tension to 0° to RD.

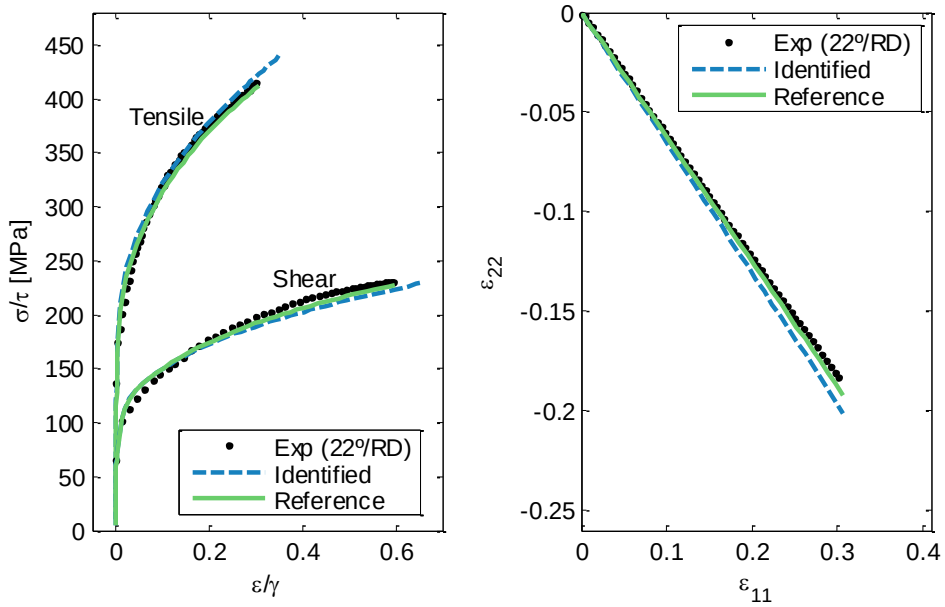

a) 22° to RD

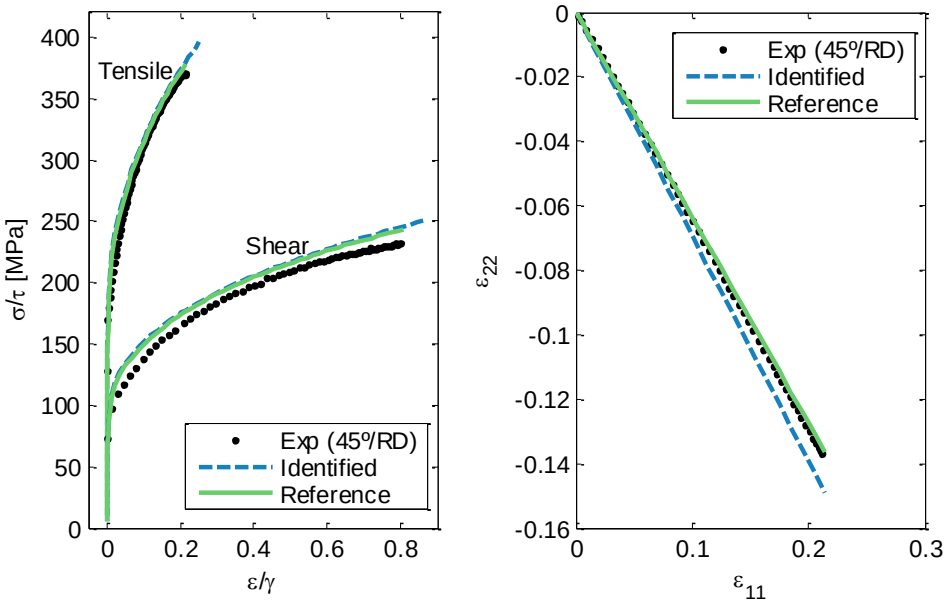

b) 45° to RD

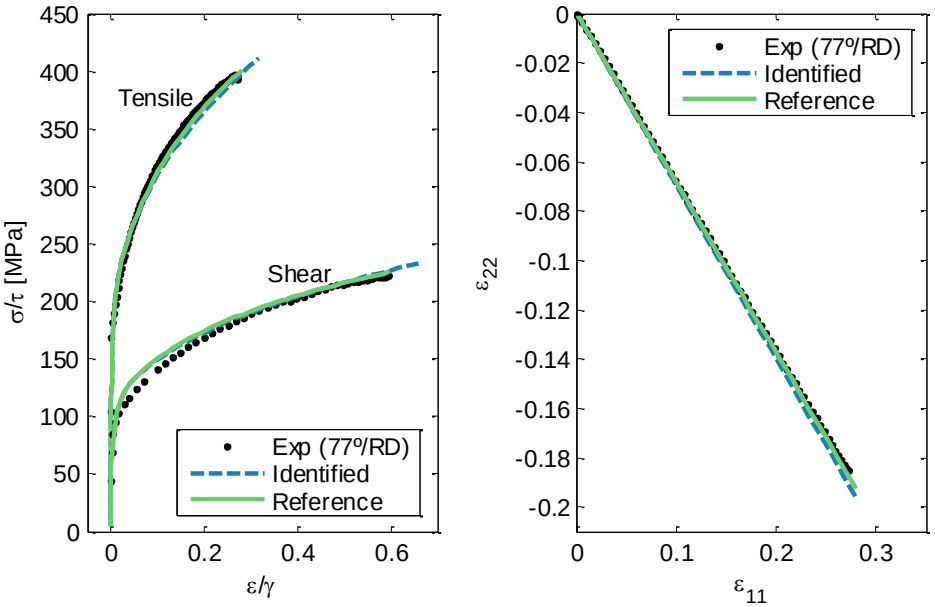

c) 77° to RD

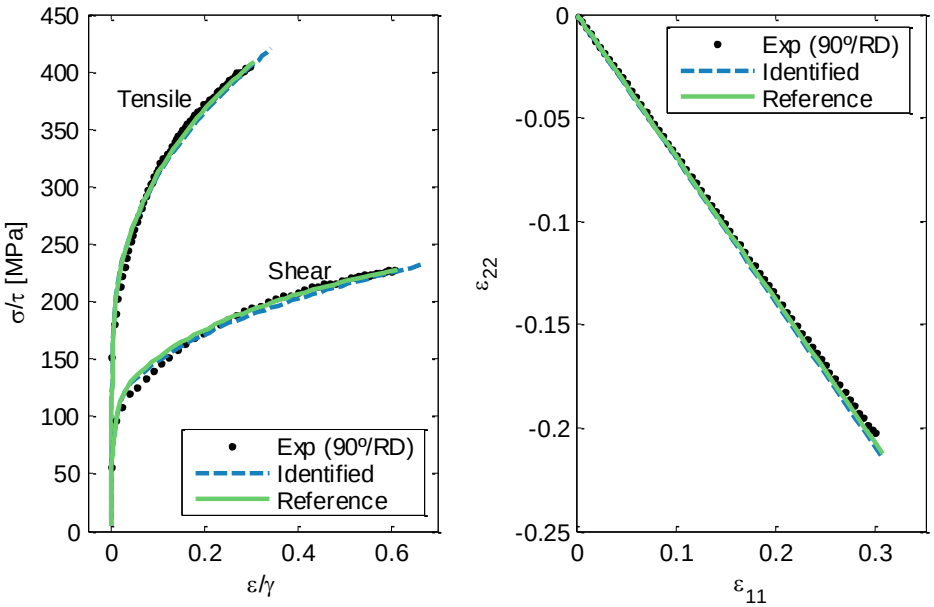

d) 90° to RD

Figure 8.30 – Experimental and numerical (i) τ-γ curves for simple shear and σ-ε curves for uniaxial tension and (ii) ε_{11}- ε_{22} curves for uniaxial tension.

In addition, the normalized projection of the yield surface in the plane ($\sigma_{XX}/\sigma_Y(0)$, $\sigma_{YY}/\sigma_Y(0)$) is illustrated in Figure 8.31 for the identified and reference material parameters set. It can be seen that the one obtained with the identified parameters set was not able to reach the equibiaxial stress point, however, it was close to this experimental value. Nonetheless, it can be seen that a general agreement was verified between the yield projections obtained using the reference and identified parameters set

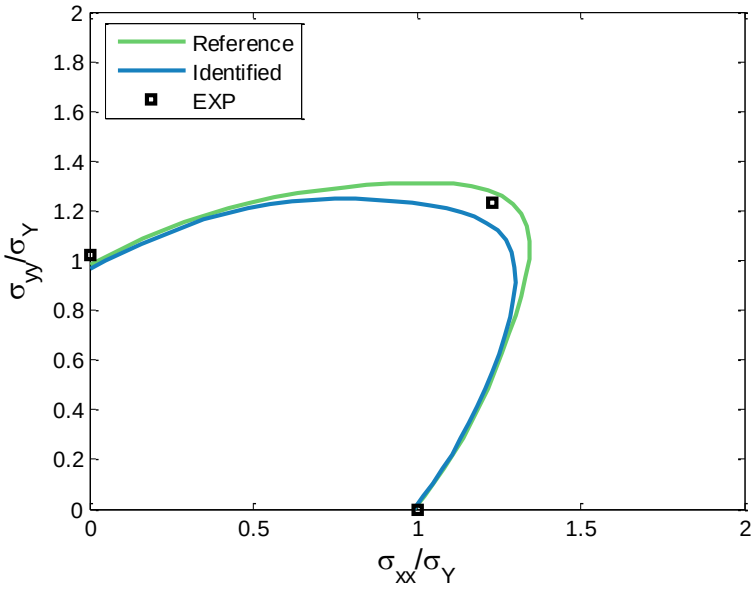

Figure 8.31 – Projection of the *Yld2004* yield surface in the plane ($\sigma_{XX}/\sigma_Y(0)$, $\sigma_{YY}/\sigma_Y(0)$) for the reference and identified material parameters sets.

From the numerical predictions using the identified parameters set, it appears that interesting results can be obtained for material parameters identification considering the butterfly test. These predictions revealed that this heterogeneous test performed in both 0° and 90° to RD is able to characterize the mechanical behavior of sheet metals under several stress and strain states and amplitudes. Concerning the phenomenological model chosen in this work, only two butterfly tests led to similar numerical predictions to the ones obtained from 5 uniaxial tension and 5 simple shear tests at different orientations to RD as well as 1 bulge test. However, the biaxial stress state was not accurately predicted. Nevertheless, it was also pointed out that a heterogeneous test performed in uniaxial loading path can also be very effective to identify all the material parameters of a complex phenomenological model involving large number of parameters.

8.4 Conclusion

The main goal of this chapter was the development of an innovative methodology for designing heterogeneous tests which promote a more complete mechanical characterization of sheet metals. Two different design optimization strategies based on a direct search method and on the quantitative indicator I_T, proposed in chapter 7, were developed for this purpose.

On the one hand, a one-step procedure designing both specimen shape and loading path by using rigid tools was defined. The main advantage of this strategy is the resemblance with the experimental reality, since a rigid tool is used for applying the displacement similarly to standard testing machines. Heterogeneous tests were designed using one and two rigid tools in order to also investigate the effect of uniaxial and biaxial loading path on the achievement of strain fields with enhanced mechanical information. The optimization processes started with a circular and a cross specimen shapes and led to a butterfly and cruciform specimens, respectively, using one and two rigid tools. The obtained results suggested that when a uniaxial loading path is applied, the design optimization process tends to search for a specimen shape developing a strain state range between simple shear to plane strain tension. While, when a biaxial loading path is applied, a cruciform specimen shape, such as the typical one of biaxial tensile tests, tends to promote larger mechanical information.

On the other hand, a sequential incremental technique that designs the loading path, locally, on the overall outer boundary of the specimen shape was also defined. In this strategy, the design optimization of the specimen shape was taken into account in the first step of the sequential optimization process while the loading path was subjected to design optimization on the several sequential steps. Despite such a strategy may be experimentally unfeasible, its main purpose was to evaluate the effect of a complex loading path, through multisteps and local displacements, on the achievement of richer strain fields. The heterogeneous test designed revealed that it was possible to cover all the strain state range and to improve considerably the mechanical information using this kind of multistep optimization approach.

From the I_T results obtained for the designed tests, it was demonstrated that both optimization methodologies proposed were able to find mechanical tests promoting a better mechanical characterization of the material. Nonetheless, the proposed indicator I_T may present some limitations since it was not possible to cover successfully all the principal strain states,

mainly in the case of the optimization methodology using rigid tools. However, it must be stressed out that these are very first results and the optimization procedure developed can be very efficient for designing a mechanical test leading to a complete mechanical characterization of thin metallic sheets.

Moreover, a material parameters identification process using the butterfly test i) without and ii) with rotation of the material orientation was carried out considering the virtual DC04 mild steel identified from the conventional tests as a reference material. The identified material parameters from this heterogeneous test were used to predict the experimental data of the conventional tests and reliable numerical reproductions were obtained. It revealed that the two butterfly tests are necessary to (i) characterize the mechanical behavior of sheet metals under several stress and strain paths, (ii) give identical numerical predictions to the ones obtained from 5 uniaxial tension and 5 simple shear tests at different orientations to RD as well as 1 bulge test and (iii) promote an effective material parameters identification for complex phenomenological models involving a large number of parameters.

V – Final remarks

Chapter 9

Conclusions and future works

9.1 General conclusions

The present work was proposed since the material parameters identification of modern constitutive models demands for a large number of classical quasi-homogeneous tests and, as a consequence, leads to expensive and time consuming identification procedures. Therefore, the main goal of the present work was the computational design of heterogeneous tests for material parameters identification purposes. The inhomogeneous strain fields developed by these tests should be close to the ones encountered in sheet metal forming processes, concerning the variety of stress and strain states as well as strain levels.

Regarding this, in the current work, a first introduction to the different strategies, namely, both homogeneous and non-homogeneous inverse approaches, for material parameters identification of constitutive models was performed. Also in this topic, the classical and heterogeneous tests used, respectively, by these approaches were introduced.

Moreover, both types of optimization problems covered in this thesis, namely, material parameters identification and shape optimization, were defined and discussed. One the one hand, the shape optimization was the main goal of the present work due to the development of an innovative optimization methodology for the computational design of heterogeneous tests. On the other hand, the material parameters identification problem was also considered due to the need of characterizing numerically the mechanical behavior of DC04 mild steel in order to become the virtual material in the shape optimization problem.

Therefore, an inverse methodology for material parameters identification was developed with the purpose of identifying parameters from classical as well as heterogeneous tests. This inverse methodology was used to identify the parameters for initial anisotropy and evolution of hardening of DC04 mild steel from a complex phenomenological model (*Yld2004-Mixed*) composed by the non-quadratic *Yld2004-18p* yield criterion combined with a mixed isotropic-kinematic hardening law. A large experimental database composed by (i) uniaxial tensile and simple shear tests at 0°, 22°, 45°, 77° and 90° to RD, (ii) bulge test and (iii) three shear-

Bauschinger tests reversed at 0.13, 0.21 and 0.33 of pre-strain was used. The implemented optimization process was able to identify a set of material parameters leading to a global accurate characterization of DC04 mechanical behavior. Nonetheless, some discrepancy was obtained in the prediction of the rounded yield point and work hardening stagnation of shear-Bauschinger tests since the kinematic hardening law chosen does not take into account such a kind of mechanical phenomena. Additionally, the Cockroft and Latham (CL) uncoupled fracture criterion was adopted for calibrating the macroscopic rupture behavior of DC04 mild steel from a uniaxial tensile test up to rupture. Such a calibration was required to define the rupture as an end condition to stop the numerical optimization approach used on the design of the heterogeneous mechanical tests. The calibration of CL criterion was performed considering an experimental-numerical approach based on experimental data acquired by using DIC technique. The numerical simulations of this experiment presented some difficulty in describing perfectly the cross shape in the fracture zone. However, the CL parameter achieved larger values at the center of the sample, predicting accurately the fracture zone.

The reliability of the material parameters identified for *Yld2004-Mixed* model and the critical parameter of CL criterion was evaluated with a deep drawing test leading either to full drawing or rupture of the blank. Strain fields at several stages of the deep drawing experiments were recorded by DIC technique. In the case of the experiment leading to full drawing, a reliable reproduction of the experimental data was obtained, validating the material parameters set identified of *Yld2004-Mixed* model. While, for the experiment leading to premature rupture of the blank, some differences between the experimental data and numerical results were observed. However, these numerical results described accurately the experimental fracture zone and led to a good prediction of the experimental strain distributions with exception to the fracture zone, where the major strain was underestimated. The critical parameter of CL criterion was under-predicted with a relative gap of 13% comparatively to the reference value obtained by the uniaxial tensile test up to rupture. Although, it was considered that such a difference remained acceptable mainly due to the substantial difficulty in reproducing properly the experimental friction conditions of the cylindrical cup test leading to rupture and also regarding the different stress triaxiality range of both uniaxial tensile and cylindrical cup tests.

For the computational design of heterogeneous tests a suitable analysis of the inhomogeneous strain field was mandatory in order to find optimized tests exhibiting several stress and strain states as distinctly as possible. Thus, a quantitative indicator I_T able to distinguish, rate and rank mechanical tests was formulated. This indicator was designed to include the analysis of the strain state range covered by the test, the deformation heterogeneity of the specimen as well as the strain level achieved up to rupture. Its performance was numerically investigated for classical mechanical tests as well as modern heterogeneous tests using the virtual behavior of the DC04 mild steel. The qualitative analysis of these mechanical tests indicated that the ones developing multiaxial stress states as well as larger heterogeneity must provide a more complete mechanical characterization of sheet metals and the quantitative I_T results confirmed this trend. These results pointed out that I_T was able to accurately quantify the mechanical information provided by the tests. Moreover, to validate I_T, a material parameter sensitivity study was performed and it was shown that the proposed indicator consists of an efficient strategy for choosing the more appropriate heterogeneous test when it comes to identification of material

properties. Thereby, I_T was used for guiding the design of the computational mechanical tests in order to find an ideal strain field able to promote better mechanical characterization of the material behavior.

Finally, concerning the computational design of heterogeneous mechanical tests for thin metallic sheets, an optimization methodology approach was developed. Within this approach, two different strategies, namely (i) a one-step procedure designing both specimen shape and loading path by using a tool and (ii) a sequential incremental technique designing the specimen shape and the loading path of the specimen considering local displacements, were proposed.

In the case of the first optimization strategy, heterogeneous tests were designed using one and two rigid tools with the aim of investigating the effect of uniaxial and biaxial loading path on the achievement of richer strain fields. The optimized results led to a butterfly and cruciform specimens, respectively, using one and two rigid tools. These results suggested that when uniaxial loading path is applied, the optimization process tends to search for a specimen shape exhibiting a strain state range between simple shear to plane strain tension. While when biaxial loading path is applied, a cruciform specimen shape such as the typical one of biaxial tensile tests tends to be the specimen configuration providing more mechanical information. Such a result revealed that the optimization procedure and, mostly, the indicator can be very effective in finding the best specimen configurations since it appears that the cruciform specimen shape is indeed the best shape for promoting richer mechanical information when a biaxial loading path is applied.

In the case of the sequential incremental optimization strategy, it was observed that the heterogeneous test designed covered all the strain state range and reached an I_T result revealing a significant improvement of the mechanical information given by the test, compared with the ones of the first optimization strategy. It demonstrated the potential of using a complex loading path, through multisteps and local displacements, on the achievement of richer strain fields.

Additionally, the optimized butterfly test i) without and ii) with rotation of the material orientation was used for identifying the material parameters of the DC04 mild steel of *Yld2004-Mixed* model. By this way, it was possible to investigate the reliability of identified material parameters sets coming from an experimental database composed by several quasi-homogeneous tests and heterogeneous tests. A non-homogeneous inverse approach was defined and the virtual DC04 mild steel identified from the conventional tests was considered as the reference material. The identified material parameters obtained with this heterogeneous approach were used to predict the experimental data of the conventional tests and reliable numerical reproductions were obtained. These results were interesting since it was observed that the two butterfly tests, with and without rotation of the material orientation, are able to (i) characterize the mechanical behavior of sheet metals under several stress and strain paths, (ii) give identical numerical predictions to the ones obtained from 5 uniaxial tension and 5 simple shear tests at different orientations to RD as well as 1 bulge test and (iii) promote an effective material parameters identification for complex phenomenological models involving a large number of parameters.

Generally speaking, in this work, an innovative methodology for designing heterogeneous tests which promote a better mechanical characterization of sheet metals was presented. The obtained results consist of very first results, however, it was observed that such an innovative

optimization methodology can be very efficient for designing a mechanical test leading to a complete mechanical characterization of thin metallic sheets.

9.2 Future works

Considering the work presented, future developments may be outlined. According to the obtained results as well as their validation, it was shown that the global procedure developed for material parameters identification of sheet metals by including initial anisotropy, evolution of hardening and macroscopic rupture can be very useful for a more complete characterization of the mechanical behavior of sheet metals. Therefore, this efficient identification procedure can be extended to other materials. However, integrating the rupture test in tension in the optimization of material parameters in order to seek for a better description of necking could be very interesting.

Concerning the indicator I_T proposed, this one was essentially formulated for monotonic loading experiments. However, since in sheet metal forming operations the material can be subjected to different strain path changes affecting the work-hardening behavior, reverse and orthogonal strain path experiments are commonly studied. Therefore, I_T formulation can be enhanced to detect strain path changes during the test, accounting for the mechanical phenomena inherent to these multistep tests. In addition, it could be very interesting to compare numerical and experimental evaluations of I_T for a certain mechanical test with the aim of validating experimentally this indicator. Note that the several contributions of I_T have physical meaning because they were based only on strain deformations. Therefore, I_T can be determined experimentally by using, for example, DIC technique to output the strain field over the specimen surface during the test.

Besides evolutionary algorithms tend to be very time consuming due to the large number of evaluations required, they are very robust avoiding local minima of the objective function. Thereby, this type of algorithm could be used on the optimization approach for designing heterogeneous tests in order to investigate their influence on the achievement of more informative strain fields. In addition, the innovative methodology for designing the heterogeneous tests can be further developed without considering symmetry conditions. Indeed, non-symmetric experiments may provide more mechanical information than symmetric ones. Alternatively, in the case of the optimization strategy using a rigid tool, the optimization methodology could be extended to include more tools or to increase the complexity of the specimen configuration adding holes and/or slits. In this way, the effect of multi-axial loading paths as well as perforated specimens on the full characterization of the strain state range could be studied.

Interesting results were obtained using the butterfly test for material parameters identification purposes and its experimental reproduction could be carried out. Though it involves additional devices for the cross heads of the standard testing machine, this butterfly test may promote a suitable material parameters identifications for complex phenomenological models with large number of parameters.

Finally, the innovative methodology proposed in this thesis was a completely distinct approach to the common ones used to design heterogeneous mechanical tests, which are based

on trial-and-error attempts or geometrical parametric studies of existent tests. Hence, this kind of optimization approach may be adopted in future developments of heterogeneous tests with enhanced inhomogeneous strain fields.

Appendix A

Kinematic hardening implementation in a UMAT subroutine

A.1 General equations

The constitutive model *Yld2004-Mixed* but with only one term for the kinematic contribution was already implemented in a UMAT[10] subroutine by Grilo *et al.* (2013b). This constitutive model was implemented considering a fully-implicit backward-Euler stress integration algorithm based on the multi-stage return mapping procedure (Yoon *et al.*, 1999). This kind of integration algorithm uses the control of the potential residual and integrates the constitutive equations at any instant of time (pseudo-time), during a deformation process. More detailed information can be found in Grilo *et al.* (2013b).

To formulate material constitutive models it is necessary take into account the integration of the material state variables at each integration point within the continuum medium, at any instant of time (pseudo-time), during the deformation process. This integration of the material state variables is carried out by the return-mapping method, also called as predictor-corrector method. This kind of integration method is based on an elastic predictor phase, when a purely elastic trial stress is evaluated, and a plastic corrector phase.

Considering the assumption that the system is in global equilibrium and the stress and all state variables are known at the beginning of the time step, the trial stress state ($\boldsymbol{\sigma}^{TR}$) can be formulated under the assumption that the total strain increment is entirely elastic. Then**,**

$$\boldsymbol{\sigma}_{n+1}^{TR} = \boldsymbol{\sigma}_n + \mathbf{D} : \boldsymbol{\Delta\varepsilon}^{t}, \tag{A.1}$$

where n is reported to the values at the beginning of the time step and $\boldsymbol{\sigma}^{TR}$ is evaluated at the configuration n+1. If the trial stress is within the yield surface in the principal stress space (F≤0), the previous assumption is correct and the material point belongs to an elastic state. However, if the trial stress is outside the yield surface, the yield condition is violated and the plastic corrector phase is required to numerically ensure the consistency condition. In other words, the plastic

[10] The commercial FE code ABAQUS allows the introduction of constitutive models by means of a user material subroutine (UMAT).

corrector is responsible to bring the stress onto the subsequent yield surface. The consistency condition is defined as

$$F = \overline{\eta}(\boldsymbol{\eta}_n + \boldsymbol{\Delta\eta}) - \sigma_{\mathrm{Y}}(\bar{\varepsilon}_n^{\mathrm{p}} + \lambda) = 0, \tag{A.2}$$

where the following relations can be established by:

$$\boldsymbol{\Delta\eta} = \boldsymbol{\Delta\sigma} - \boldsymbol{\Delta\alpha}, \tag{A.3}$$

$$\boldsymbol{\Delta\sigma} = \mathbf{D} : \boldsymbol{\Delta\varepsilon}^{\mathrm{e}}, \tag{A.4}$$

$$\boldsymbol{\Delta\varepsilon}^{\mathrm{e}} = \boldsymbol{\Delta\varepsilon}^{\mathrm{t}} - \boldsymbol{\Delta\varepsilon}^{\mathrm{p}}, \tag{A.5}$$

$$\boldsymbol{\Delta\varepsilon}^{\mathrm{p}} = \lambda \mathbf{a} \tag{A.6}$$

and

$$\boldsymbol{\Delta\alpha} = \left(\frac{C_1}{\overline{\eta}}\boldsymbol{\eta} - \gamma_1\boldsymbol{\alpha}_1\right)\lambda + \left(\frac{C_2}{\overline{\eta}}\boldsymbol{\eta} - \gamma_2\boldsymbol{\alpha}_2\right)\lambda + \left(\frac{C_3}{\overline{\eta}}\boldsymbol{\eta} - \gamma_3\boldsymbol{\alpha}_3\right)\lambda. \tag{A.7}$$

Note that the kinematic hardening model is modified in $\boldsymbol{\Delta\alpha}$, relatively to initial formulation, by adding two more backstress tensors.

In order to carry out the plastic correction, it is required consider an assumption for the deformation path. In the case of this implementation, the state variables used in the returning procedure are evaluated at the current configuration, which is unknown. This kind of strategy is designed as backward-Euler methodology. Despite the backward-Euler methodology is quite complex due to the consideration of the variation of the normal to the yield surface (flow direction **a**), it presents several advantages, such as: (i) provides great accuracy even for large time steps, (ii) is more appropriated for the implicit integration scheme and (iii) follows the minimum plastic work path which is based on the incremental deformation theory.

Using the backward-Euler method, Equation A.2 is solved in *N*-sub-steps through

$$F(\lambda_k) = \overline{\eta}(\boldsymbol{\eta}_n + \boldsymbol{\Delta\eta}_k) - \sigma_{\mathrm{Y}}(\bar{\varepsilon}_n^{\mathrm{p}} + \lambda_k) = F_k, \tag{A.8}$$

where the residual F_k, for each sub-step k=1, …, N, has a prescribed value, and $F_1 > F_2 > \ldots > F_k > \ldots > F_N$, ($F_N \approx 0$). In the following the iterative procedure for the k^{th} sub-step on the backward-Euler procedure is given. The following auxiliary residuals for the sub-step k can be defined by:

$$g_{1_k}(\lambda_k) = \overline{\eta}(\boldsymbol{\eta}_k) - \sigma_{\mathrm{Y}}(\bar{\varepsilon}_n^{\mathrm{p}} + \lambda_k) - F_k = 0, \tag{A.9}$$

$$\mathbf{g}_{2_k}(\lambda_k) = \mathbf{D}^{-1} : \left(\boldsymbol{\sigma}_k - \boldsymbol{\sigma}^{\mathrm{TR}}\right) + \lambda_k \mathbf{a}_k = \mathbf{0}, \tag{A.10}$$

$$\mathbf{g}_{3_k}(\lambda_k) = \boldsymbol{\alpha}_{\mathbf{1}_k} - \boldsymbol{\alpha}_{\mathbf{1}_n} - \left(\frac{C_1}{\overline{\eta}}\boldsymbol{\eta} - \gamma_1 \boldsymbol{\alpha}_{\mathbf{1}_k}\right)\lambda_k = \mathbf{0}, \tag{A.11}$$

$$\mathbf{g}_{4_k}(\lambda_k) = \boldsymbol{\alpha}_{2_k} - \boldsymbol{\alpha}_{2_n} - \left(\frac{C_2}{\overline{\eta}}\boldsymbol{\eta} - \gamma_2 \boldsymbol{\alpha}_{2_k}\right)\lambda_k = \mathbf{0}, \tag{A.12}$$

$$\mathbf{g}_{5_k}(\lambda_k) = \boldsymbol{\alpha}_{3_k} - \boldsymbol{\alpha}_{3_n} - \left(\frac{C_3}{\overline{\eta}}\boldsymbol{\eta} - \gamma_3 \boldsymbol{\alpha}_{3_k}\right)\lambda_k = \mathbf{0}. \tag{A.13}$$

Equation A.9 is obtained from Equation A.8 considering that $\boldsymbol{\Delta\eta}_k = \boldsymbol{\eta}_k - \boldsymbol{\eta}_n$, Equation A.10 is determined from Equations A.3-A.6 and A.1, and Equations A.11-A.13 are formulated through Equation A.7 considering that $\boldsymbol{\Delta\alpha}_k = \boldsymbol{\alpha}_k - \boldsymbol{\alpha}_n$. When the convergence of the constitutive equations is achieved, the auxiliary residuals must be approximately zero, within a given tolerance. These residuals are non-linear functions of the plastic multiplier which are linearized, at each iteration, around the current values of the state variables to obtain the increment of the plastic multiplier. The linearization of the auxiliary residuals is performed using the Taylor series expansion (where only the linear terms were considered). For each iteration of the sub-step *k*, the auxiliary residuals are given as:

$$g_{1_k} + \mathbf{a}_k : \boldsymbol{\Delta\sigma}_k - \mathbf{a}_k : \boldsymbol{\Delta\alpha}_k - H_k \Delta\lambda_k = 0, \tag{A.14}$$

$$\mathbf{g}_{2_k}(\lambda_k) + \left(\mathbf{D}^{-1} + \lambda_k \frac{\partial \mathbf{a}_k}{\partial \boldsymbol{\eta}_k}\right) : \boldsymbol{\Delta\sigma}_k - \left(\lambda_k \frac{\partial \mathbf{a}_k}{\partial \boldsymbol{\eta}_k}\right) : \boldsymbol{\Delta\alpha}_k + \mathbf{a}_k \Delta\lambda_k = \mathbf{0}, \tag{A.15}$$

$$\mathbf{g}_{3_k} + \boldsymbol{\Delta\alpha}_{1_k} + \gamma_1 \lambda_k \boldsymbol{\Delta\alpha}_{1_k} - \left(\frac{C_1}{\overline{\eta}_k}\boldsymbol{\eta}_k - \gamma_1 \boldsymbol{\alpha}_{1_k}\right)\Delta\lambda_k - \frac{C_1 \lambda_k}{\overline{\eta}_k}\left(1 - \frac{\mathbf{a}_k : \boldsymbol{\eta}_k}{\overline{\eta}_k}\right)(\boldsymbol{\Delta\sigma}_k - \boldsymbol{\Delta\alpha}_k) = \mathbf{0}, \tag{A.16}$$

$$\mathbf{g}_{4_k} + \boldsymbol{\Delta\alpha}_{2_k} + \gamma_2 \lambda_k \boldsymbol{\Delta\alpha}_{2_k} - \left(\frac{C_2}{\overline{\eta}_k}\boldsymbol{\eta}_k - \gamma_2 \boldsymbol{\alpha}_{2_k}\right)\Delta\lambda_k - \frac{C_2 \lambda_k}{\overline{\eta}_k}\left(1 - \frac{\mathbf{a}_k : \boldsymbol{\eta}_k}{\overline{\eta}_k}\right)(\boldsymbol{\Delta\sigma}_k - \boldsymbol{\Delta\alpha}_k) = \mathbf{0}, \tag{A.17}$$

$$\mathbf{g}_{5_k} + \boldsymbol{\Delta\alpha}_{3_k} + \gamma_3 \lambda_k \boldsymbol{\Delta\alpha}_{3_k} - \left(\frac{C_3}{\overline{\eta}_k}\boldsymbol{\eta}_k - \gamma_3 \boldsymbol{\alpha}_{3_k}\right)\Delta\lambda_k - \frac{C_3 \lambda_k}{\overline{\eta}_k}\left(1 - \frac{\mathbf{a}_k : \boldsymbol{\eta}_k}{\overline{\eta}_k}\right)(\boldsymbol{\Delta\sigma}_k - \boldsymbol{\Delta\alpha}_k) = \mathbf{0}. \tag{A.18}$$

From the mathematical manipulation of Equations A.16-A.18 which can be rewritten as:

$$\boldsymbol{\Delta\alpha}_{1_k} = \frac{-\mathbf{g}_{3_k} + \left(\frac{C_1}{\overline{\eta}_k}\boldsymbol{\eta}_k - \gamma_1 \boldsymbol{\alpha}_{1_k}\right)\Delta\lambda_k + \frac{C_1 \lambda_k A_{1_k}}{\overline{\eta}_k}(\boldsymbol{\Delta\sigma}_k - \boldsymbol{\Delta\alpha}_k)}{A_{g3}}, \tag{A.19}$$

$$\Delta\boldsymbol{\alpha}_{2_k} = \frac{-\mathbf{g}_{4_k} + \left(\frac{C_2}{\overline{\eta}_k}\boldsymbol{\eta}_k - \gamma_2\boldsymbol{\alpha}_{2_k}\right)\Delta\lambda_k + \frac{C_2\lambda_k A_{1_k}}{\overline{\eta}_k}(\Delta\boldsymbol{\sigma}_k - \Delta\boldsymbol{\alpha}_k)}{A_{\mathrm{g4}}}, \tag{A.20}$$

$$\Delta\boldsymbol{\alpha}_{3_k} = \frac{-\mathbf{g}_{5_k} + \left(\frac{C_3}{\overline{\eta}_k}\boldsymbol{\eta}_k - \gamma_3\boldsymbol{\alpha}_{3_k}\right)\Delta\lambda_k + \frac{C_3\lambda_k A_{1_k}}{\overline{\eta}_k}(\Delta\boldsymbol{\sigma}_k - \Delta\boldsymbol{\alpha}_k)}{A_{\mathrm{g5}}}, \tag{A.21}$$

and considering the relation $\Delta\boldsymbol{\alpha} = \Delta\boldsymbol{\alpha}_1 + \Delta\boldsymbol{\alpha}_2 + \Delta\boldsymbol{\alpha}_3$, the equation that describes the evolution of the backstress tensor can be determined. This equation presents the following form,

$$\Delta\boldsymbol{\alpha}_k = \frac{\Delta\boldsymbol{\sigma}_k A_{2_k}\left(\frac{C_1}{A_{\mathrm{g3}}} + \frac{C_2}{A_{\mathrm{g4}}} + \frac{C_3}{A_{\mathrm{g5}}}\right) + \Delta\lambda_k A_{\mathrm{g3}}\boldsymbol{\beta} - A_{\mathrm{g3}}\left(\frac{\mathbf{g}_{3_k}}{A_{\mathrm{g3}}} + \frac{\mathbf{g}_{4_k}}{A_{\mathrm{g4}}} + \frac{\mathbf{g}_{5_k}}{A_{\mathrm{g5}}}\right)}{A_{\mathrm{g3}} + A_{2_k}\left(\frac{C_1}{A_{\mathrm{g3}}} + \frac{C_2}{A_{\mathrm{g4}}} + \frac{C_3}{A_{\mathrm{g5}}}\right)}, \tag{A.22}$$

with

$$\boldsymbol{\beta} = \frac{1}{A_{\mathrm{g3}}}\left(\frac{C_1}{\overline{\eta}_k}\boldsymbol{\eta}_k - \gamma_1\boldsymbol{\alpha}_{1_k}\right) + \frac{1}{A_{\mathrm{g4}}}\left(\frac{C_2}{\overline{\eta}_k}\boldsymbol{\eta}_k - \gamma_2\boldsymbol{\alpha}_{2_k}\right) + \frac{1}{A_{\mathrm{g5}}}\left(\frac{C_3}{\overline{\eta}_k}\boldsymbol{\eta}_k - \gamma_3\boldsymbol{\alpha}_{3_k}\right). \tag{A.23}$$

The evolution equation of the stress tensor is obtained by using Equations A.15 and A.22 and is defined by

$$\Delta\boldsymbol{\sigma}_k = -\mathbf{E}^{-1} : \left[\mathbf{g}_{2_k} + \lambda_k \frac{\partial \mathbf{a}_k}{\partial \boldsymbol{\eta}_k} : A_{\mathrm{g3}} A_{3_k}\left(\frac{\mathbf{g}_{3_k}}{A_{\mathrm{g3}}} + \frac{\mathbf{g}_{4_k}}{A_{\mathrm{g4}}} + \frac{\mathbf{g}_{5_k}}{A_{\mathrm{g5}}}\right) + \mathbf{A}_{5_k}\Delta\lambda_k\right]. \tag{A.24}$$

The substitution of the Equations A.22 and A.24 into Equation A.9 allows to define the increment of the plastic multiplier, which is formulated as

$$\Delta\lambda_k = \frac{g_{1_k} - \mathbf{a}_k : \mathbf{E}^{-1} : \mathbf{A}_{6_k} A_{4_k} + \mathbf{a}_k : A_{3_k} A_{\mathrm{g3}}\left(\frac{\mathbf{g}_{3_k}}{A_{\mathrm{g3}}} + \frac{\mathbf{g}_{4_k}}{A_{\mathrm{g4}}} + \frac{\mathbf{g}_{5_k}}{A_{\mathrm{g5}}}\right)}{\mathbf{a}_k : \mathbf{E}^{-1} : \mathbf{A}_{5_k} A_{4_k} + H_k + \mathbf{a}_k : A_{3_k} A_{\mathrm{g3}}\boldsymbol{\beta}}. \tag{A.25}$$

In addition, the auxiliary variables used in Equations A.22-A.25 are given by:

$$A_{\mathrm{g3}} = 1 + \gamma_1\lambda_k, \tag{A.26}$$

$$A_{\mathrm{g4}} = 1 + \gamma_2\lambda_k, \tag{A.27}$$

$$A_{1_k} = 1 - \frac{\mathbf{a}_k : \boldsymbol{\eta}_k}{\overline{\eta}_k}, \tag{A.28}$$

$$A_{2_k} = \frac{\lambda_k A_{1_k} A_{g3}}{\overline{\eta}_k}, \tag{A.29}$$

$$A_{3_k} = \frac{1}{A_{g3} + A_{2_k}\left(\frac{C_1}{A_{g3}} + \frac{C_2}{A_{g4}} + \frac{C_3}{A_{g5}}\right)}, \tag{A.30}$$

$$A_{4_k} = 1 - A_{2_k} A_{3_k}\left(\frac{C_1}{A_{g3}} + \frac{C_2}{A_{g4}} + \frac{C_3}{A_{g5}}\right), \tag{A.31}$$

$$\mathbf{A}_{5_k} = \mathbf{a}_k - \lambda_k \frac{\partial \mathbf{a}_k}{\partial \boldsymbol{\eta}_k} : A_{g3} A_{3_k}\left[\frac{1}{A_{g3}}\left(\frac{C_1}{\overline{\eta}_k}\boldsymbol{\eta}_k - \gamma_1 \boldsymbol{\alpha}_{1_k}\right) + \frac{1}{A_{g4}}\left(\frac{C_2}{\overline{\eta}_k}\boldsymbol{\eta}_k - \gamma_2 \boldsymbol{\alpha}_{2_k}\right) + \frac{1}{A_{g5}}\left(\frac{C_3}{\overline{\eta}_k}\boldsymbol{\eta}_k - \gamma_3 \boldsymbol{\alpha}_{3_k}\right)\right], \tag{A.32}$$

$$\mathbf{A}_{6_k} = \mathbf{g}_{2_k} - \lambda_k \frac{\partial \mathbf{a}_k}{\partial \boldsymbol{\eta}_k} : A_{g3} A_{3_k}\left(\frac{\mathbf{g}_{3_k}}{A_{g3}} + \frac{\mathbf{g}_{4_k}}{A_{g4}} + \frac{\mathbf{g}_{5_k}}{A_{g5}}\right), \tag{A.33}$$

$$\mathbf{E} = \mathbf{D}^{-1} + \lambda_k \frac{\partial \mathbf{a}_k}{\partial \boldsymbol{\eta}_k} A_{4_k}. \tag{A.34}$$

At the end of each iteration *i*, the plastic multiplier, the backstress and stress tensors are updated as:

$$\lambda_k^{i+1} = \lambda_k^i + \Delta\lambda_k, \tag{A.35}$$

$$\boldsymbol{\alpha}_k^{i+1} = \boldsymbol{\alpha}_k^i + \Delta\boldsymbol{\alpha}_k, \tag{A.36}$$

$$\boldsymbol{\sigma}_k^{i+1} = \boldsymbol{\sigma}_k^i + \Delta\boldsymbol{\sigma}_k. \tag{A.37}$$

The iterative procedure is continuously performed until the auxiliary residuals are within a prescribed tolerance. When this situation occurs, the convergence is achieved and the following conditions are taken into account for the determination of the elastoplastic consistent tangent modulus matrix, for instance: (i) $\overline{\eta}_k = \mathbf{a}_k : \boldsymbol{\eta}_k$ and, consequently, A_{1_k} is equal to 0; (ii) the auxiliary residuals g_{1_k}, $\mathbf{g}_{2_k}$, $\mathbf{g}_{3_k}$, $\mathbf{g}_{4_k}$ and $\mathbf{g}_{5_k}$ are equal to 0 and (iii) the variation of the flow direction **a** must be considered. Respecting these conditions, the increments of backstress and stress tensors are, respectively,

$$\boldsymbol{\Delta\alpha} = \Delta\lambda\left[\frac{1}{A_{g3}}\left(\frac{C_1}{\overline{\eta}}\boldsymbol{\eta} - \gamma_1\boldsymbol{\alpha}_1\right) + \frac{1}{A_{g4}}\left(\frac{C_2}{\overline{\eta}}\boldsymbol{\eta} - \gamma_2\boldsymbol{\alpha}_2\right) + \frac{1}{A_{g5}}\left(\frac{C_3}{\overline{\eta}}\boldsymbol{\eta} - \gamma_3\boldsymbol{\alpha}_3\right)\right] \tag{A.38}$$

and

$$\boldsymbol{\Delta\sigma} = \mathbf{E}^{-1} : \left(\boldsymbol{\Delta\varepsilon}^{\mathrm{t}} - \mathbf{A}_5^{*}\Delta\lambda\right). \tag{A.39}$$

It must be mentioned that $\boldsymbol{\Delta\alpha}$ is obtained from Equation A.22 and Δσ from Equations A.4, A.5, A.38 and also considering the variation of the flow direction **a** by the differentiation

$$\boldsymbol{\Delta\varepsilon}^{\mathrm{p}} = \Delta\lambda\mathbf{a} + \lambda\frac{\partial\mathbf{a}}{\partial\boldsymbol{\eta}}\left(\boldsymbol{\Delta\sigma} - \boldsymbol{\Delta\alpha}\right). \tag{A.40}$$

Additionally, $\mathbf{E}^{*}$ and $\mathbf{A}_5^{*}$ are the specific values of the auxiliary variables **E** and $\mathbf{A}_5$ after convergence and are defined as

$$\mathbf{A}_5^{*} = \mathbf{a} - \lambda\frac{\partial\mathbf{a}}{\partial\boldsymbol{\eta}} : \left[\frac{1}{A_{\mathrm{g3}}}\left(\frac{C_1}{\overline{\eta}}\boldsymbol{\eta} - \gamma_1\boldsymbol{\alpha}_1\right) + \frac{1}{A_{\mathrm{g4}}}\left(\frac{C_2}{\overline{\eta}}\boldsymbol{\eta} - \gamma_2\boldsymbol{\alpha}_2\right) + \frac{1}{A_{\mathrm{g5}}}\left(\frac{C_3}{\overline{\eta}}\boldsymbol{\eta} - \gamma_3\boldsymbol{\alpha}_3\right)\right] \tag{A.41}$$

and

$$\mathbf{E}^{*} = \mathbf{D}^{-1} + \lambda\frac{\partial\mathbf{a}}{\partial\boldsymbol{\eta}}. \tag{A.42}$$

With the aim of determining the increment of the plastic multiplier Δλ, Equations A.38 and A.39 are replaced in the consistency condition and the following equation is given,

$$\Delta\lambda = \frac{\mathbf{a} : \left(\mathbf{E}^{*}\right)^{-1} : \boldsymbol{\Delta\varepsilon}^{\mathrm{t}}}{\mathbf{a} : \left(\mathbf{E}^{*}\right)^{-1} : \mathbf{A}_5^{*} + \mathbf{a} : \left[\frac{1}{A_{\mathrm{g3}}}\left(\frac{C_1}{\overline{\eta}}\boldsymbol{\eta} - \gamma_1\boldsymbol{\alpha}_1\right) + \frac{1}{A_{\mathrm{g4}}}\left(\frac{C_2}{\overline{\eta}}\boldsymbol{\eta} - \gamma_2\boldsymbol{\alpha}_2\right) + \frac{1}{A_{\mathrm{g5}}}\left(\frac{C_3}{\overline{\eta}}\boldsymbol{\eta} - \gamma_3\boldsymbol{\alpha}_3\right)\right] + H}. \tag{A.43}$$

Finally, the elastoplastic consistent tangent modulus $\hat{\mathbf{D}}^{\mathrm{ep}}$, for the backward-Euler stress integration method, can be obtained by replacing Equation A.43 into Equation A.39,

$$\hat{\mathbf{D}}^{\mathrm{ep}} = \left(\mathbf{E}^{*}\right)^{-1} - \frac{\left(\mathbf{E}^{*}\right)^{-1} : \mathbf{A}_5^{*} \otimes \mathbf{a} : \left(\mathbf{E}^{*}\right)^{-1}}{\mathbf{a} : \left(\mathbf{E}^{*}\right)^{-1} : \mathbf{A}_5^{*} + \mathbf{a} : \left[\frac{1}{A_{\mathrm{g3}}}\left(\frac{C_1}{\overline{\eta}}\boldsymbol{\eta} - \gamma_1\boldsymbol{\alpha}_1\right) + \frac{1}{A_{\mathrm{g4}}}\left(\frac{C_2}{\overline{\eta}}\boldsymbol{\eta} - \gamma_2\boldsymbol{\alpha}_2\right) + \frac{1}{A_{\mathrm{g5}}}\left(\frac{C_3}{\overline{\eta}}\boldsymbol{\eta} - \gamma_3\boldsymbol{\alpha}_3\right)\right] + H}. \tag{A.44}$$

A.2 Validation of kinematic hardening model

The numerical validation of the implemented kinematic hardening model is performed comparing tension-compression and/or shear- Bauschinger tests for two different cases. In the first case, the performance of the implemented kinematic hardening model is analyzed considering an anisotropic material behavior combined with the Swift isotropic and the Armstrong-Frederick kinematic hardening model (only one backstress tensor). The reference data is presented in Grilo *et al.* (2013a) and consists of shear-Bauschinger curves with reverse direction after a pre-strain of 0.1, 0.2 and 0.3 obtained using a virtual material. Table A.1 depicts the material parameter values of this reference data.

For this virtual material, both reference shear-Bauschinger curves, presented in Grilo *et al.* (2013a), and the ones obtained by the new kinematic formulation, implemented in the UMAT, are illustrated in Figure A.1. This comparison allows to verify if the kinematic hardening behavior and the anisotropic yield criterion are accurately linked in the new UMAT formulation.

Table A.1 - Reference parameter values of the virtual material (Grilo *et al.*, 2013a).

Virtual material	$c_{12}^{(1)}$	$c_{13}^{(1)}$	$c_{21}^{(1)}$	$c_{23}^{(1)}$	$c_{31}^{(1)}$	$c_{32}^{(1)}$	$c_{44}^{(1)}$	$c_{55}^{(1)}$	$c_{66}^{(1)}$
	1.241	1.078	1.216	1.223	1.093	0.889	0.501	0.557	1.349
	$c_{12}^{(2)}$	$c_{13}^{(2)}$	$c_{21}^{(2)}$	$c_{23}^{(2)}$	$c_{31}^{(2)}$	$c_{32}^{(2)}$	$c_{44}^{(2)}$	$c_{55}^{(2)}$	$c_{66}^{(2)}$
	0.775	0.922	0.765	0.793	0.918	1.027	1.115	1.112	0.589
	a	ε_0	K (MPa)	n	C (MPa)	γ	E (GPa)	υ	
	8	$4.78\text{x}10^{-3}$	500.8	0.20	150.0	2.2	69.0	0.33	

Comparing the results depicted in Figure A.1, it can be verified that an identical reproduction of the shear-Bauschinger curves between the reference data and the new kinematic formulation of the UMAT is achieved. Hence, it leads to the conclusion that the linking between kinematic hardening formulation and anisotropic yield criterion was correctly implemented in the new UMAT.

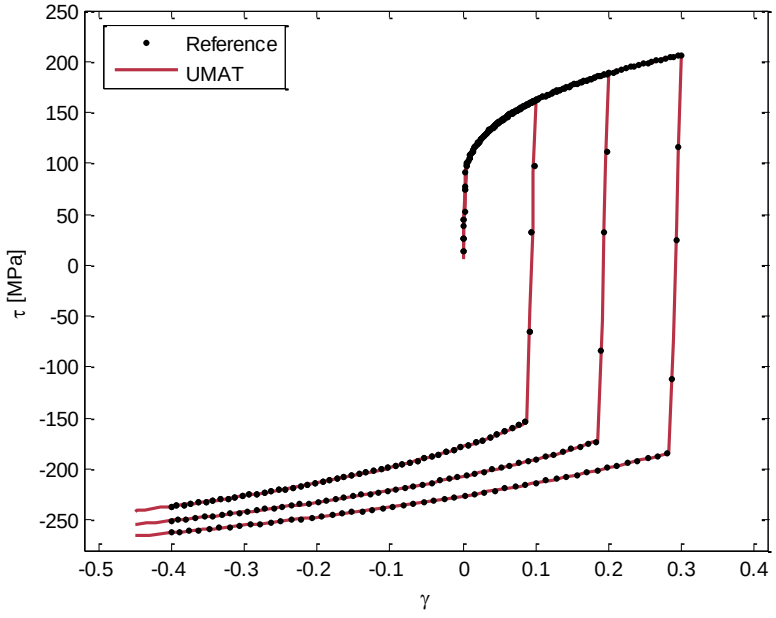

Figure A.1 – Shear-Bauschinger curves obtained with the reference data (Grilo *et al.*, 2013a) and the new kinematic formulation implemented in the UMAT, using the virtual material parameter values of Table A.1.

In the second case, shear-Bauschinger and tension-compression curves obtained considering material isotropy combined with the isotropic hardening law of Equation 4.15 and the implemented kinematic hardening model (with three backstress tensors) are evaluated. For this purpose, a numerical model composed by the von Mises yield criterion and the additive

contribution of three Armstrong-Frederick kinematic terms is defined in ABAQUS software and is used as reference data. Concerning the UMAT, this material model can also be reproduced since the isotropic yield criterion is easily obtained reducing all the parameters of *yld*2004-18p yield criterion to 1 and defining the exponent parameter *a* equal to 2 or 4 (Barlat *et al.*, 2005). Thus, shear-Bauschinger and tension-compression results obtained by two different ways, namely, ABAQUS library model and UMAT, can be compared. Such comparison investigates if the implemented kinematic hardening model works correctly in the new UMAT formulation. Table A.2 shows the material parameter values used in this second case.

Figures A.2 and A.3 show, respectively, the shear-Bauschinger curves with reverse direction after 0.1, 0.2 and 0.3 of pre-strain and the tension-compression curves with reverse direction after 0.06, 0.1 and 0.16 of pre-strain obtained by both ABAQUS library and UMAT models.

Table A.2 - Material parameter values adopted for the constitutive model composed by the von Mises yield criterion with the isotropic hardening law and the kinematic model for three backstresses.

E (GPa)	υ	σ_0 (MPa)	σ_∞ (MPa)	δ	β (MPa)	C_1 (MPa)	γ_1	C_2 (GPa)	γ_2	C_3 (MPa)	γ_3
176.0	0.29	141.2	242.3	1.089	81.2	100	0.02	30.0	300.0	2250	90.0

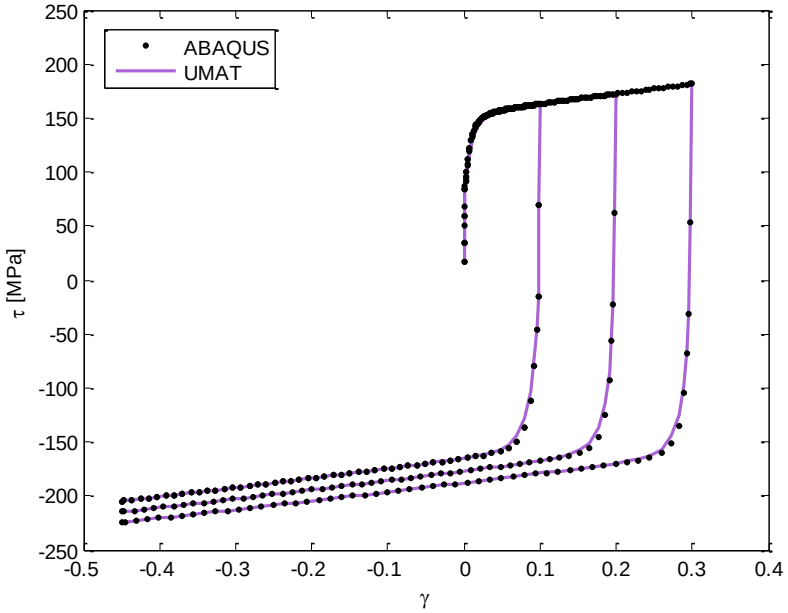

Figure A.2 – Shear-Bauschinger curves with reverse direction after 0.1, 0.2 and 0.3 of pre-strain obtained with the constitutive models implemented in ABAQUS library and UMAT, using the material parameter values of Table A.2.

By analyzing Figures A.2 and A.3, it is observed that a reliable reproduction of the ABAQUS shear-Bauschinger and tension-compression curves is achieved by using the new UMAT formulation. Therefore, these results validate the implementation of the kinematic hardening model with three additive Armstrong-Frederick terms.

Based on the results obtained for both cases of study, it may be concluded that the kinematic hardening model composed by three additive Armstrong-Frederick terms was successfully implemented in the UMAT subroutine.

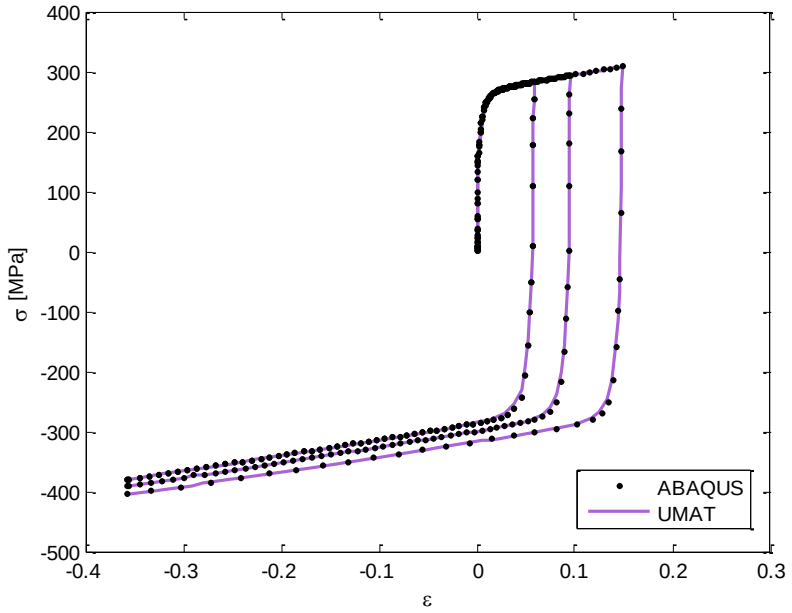

Figure A.3 – Tension-compression curves with reverse direction after 0.06, 0.1 and 0.16 of pre-strain obtained with the constitutive models implemented in ABAQUS library and UMAT, using the material parameter values of Table A.2.

Appendix B

Bulge test analysis

B.1 Numerical model for the bulge test

In order to clarify the validity of the assumption made for bulge test, numerical results with (i) a single element (1-element) and (ii) whole bulge were compared using the identified parameters of Table 5.2.

The whole bulge test is numerically modeled with ABAQUS/Standard considering a tridimensional model defined by one-fourth of the geometry, due to the symmetry conditions. The geometric dimensions of this experiment are shown in Figure B.1. The pressure fluid is applied on the surface of the blank as a linear increasing normal surface load. The boundary conditions defined can be seen in Figure 7.5. The blank is modeled with 8 node elements with linear interpolation and reduced integration (C3D8R). A mesh refinement with 3 layers of elements in the thickness and a total number of 3096 elements was defined. The dimension of the apex element in the undeformed configuration was 0.33 x 0.33 mm.

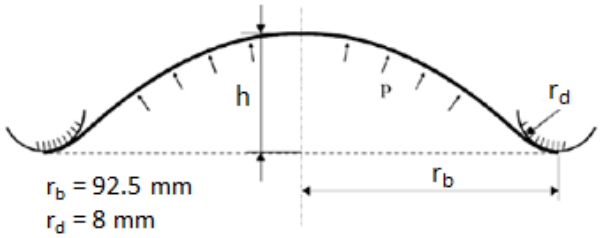

Figure B.1 – Experimental set-up of the bulge test.

Figures B.2 and B.3 show the experimental and numerical σ-ε_{11}, ε_{11}-ε_{22} and σ_{11}-σ_{22} curves obtained by both 1-element and whole bulge test models, using the identified parameter sets for *Yld2004-Iso* and *Yld2004-Mixed*, respectively. On the whole bulge test model, stress and strain components are recorded at the apex, as illustrated in Figure B.2. In addition, the numerical σ-ε_{11} curves are plotted using σ_{11} stress component.

From Figures B.2 and B.3, it can be seen that both simplified 1-element and whole bulge test models perform an identical reproduction of the experimental σ-ε_{11} curve (data used in the

parameters identification procedure). It can also be observed that a similar reproduction between experimental and numerical ε_{11}-ε_{22} and σ_{11}-σ_{22} curves was achieved with exception to the whole bulge ε_{11}-ε_{22} curve of *Yld2004-Mixed* model, which presents a slight deviation. These results pointed out that the membrane theory assumption ($\sigma_1 \approx \sigma_2$) is respected by the simplified 1-element model.

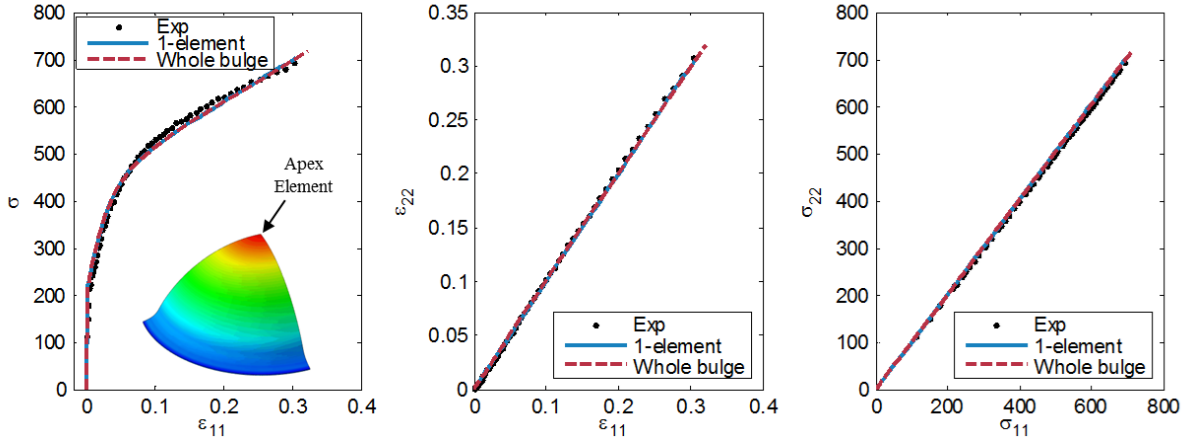

Figure B.2 – Experimental and numerical a) σ-ε_{11}, b) ε_{11}-ε_{22} and c) σ_{11}-σ_{22} curves obtained by 1-element and whole bulge models using the identified parameters of *Yld2004-Iso*.

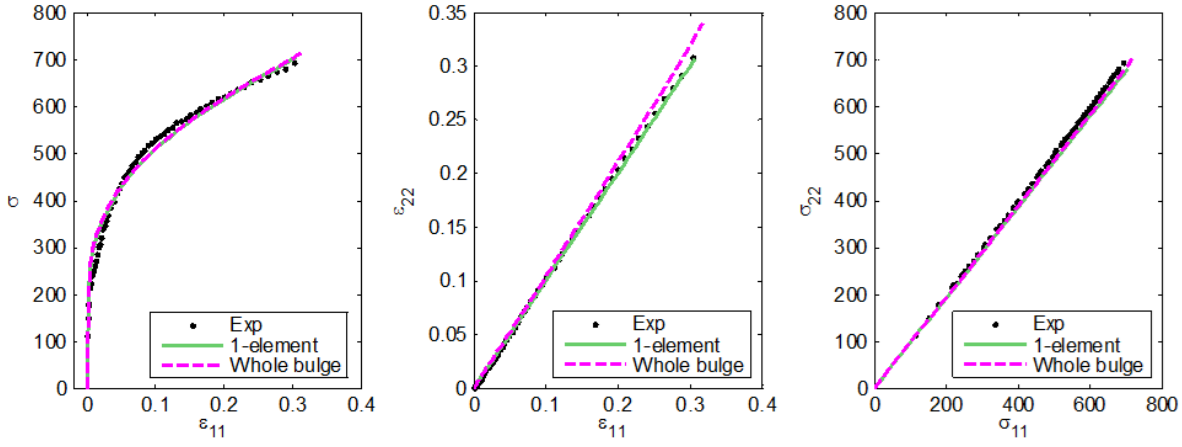

Figure B.3 – Experimental and numerical a) σ-ε_{11}, b) ε_{11}-ε_{22} and c) σ_{11}-σ_{22} curves obtained by 1-element and whole bulge models using the identified parameters of *Yld2004-Mixed*.

Therefore, it was demonstrated that (i) the assumption adopted (1-element model) to save calculation time leads to similar results to the ones obtained by using the whole bulge model and (ii) a good agreement between experimental behavior and numerical results was observed.

Mention that, comparing the calculation time required for each numerical model adopted for bulge experiment, the numerical simulation of one-fourth of bulge specimen was performed in approximately 8 minutes while the numerical simulation using 1-element was performed in less than 20 seconds. Due to this fact, the numerical simulation of the bulge test considering 1-element model was adopted in the parameters identification process.

B.2 Validation of the stress calculation

As stated in section 2.2.1.4, Aretz and Keller (2011) pointed out that the membrane theory assumption may not be longer valid when using anisotropic materials exhibiting r_b value significantly different from unity, while Yoshida (2013) concluded that the stress state at the apex can deviate by 1-5% from the equibiaxial stress state due to the material anisotropy.

The identified parameter sets lead to r_b values of 0.91 and 1.43 for *Yld2004-Iso* and *Yld2004-Mixed* models, respectively. These values were determined from the numerical simulation of a disk compression test.

Though the material was anisotropic, the bulge stress component was calculated according to isotropic relationship. Therefore, the equibiaxial stress state imposed by the membrane theory assumption must be checked numerically by using the whole bulge model. In this way, the evolution of σ_{11}, σ_{22}, ε_{11} and ε_{22} with $\bar{\varepsilon}^p$ for both *Yld2004-Iso* and *Yld2004-Mixed* models is presented in Figures B.4 and B.5.

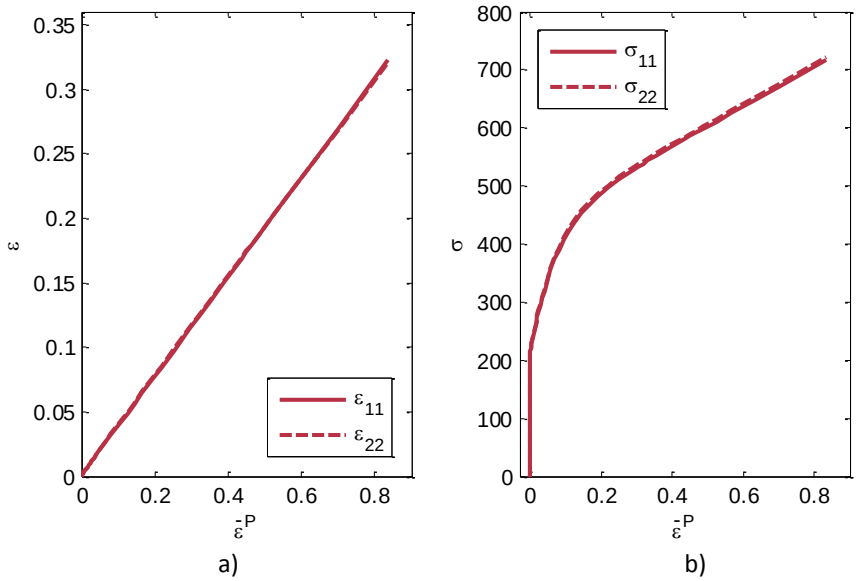

Figure B.4 – Numerical evolution of a) ε_{11} and ε_{22} and b) σ_{11} and σ_{22} with $\bar{\varepsilon}^p$ obtained at the apex of bulge test using *Yld2004-Iso* model.

Figure B.4 shows that a similar evolution for ε_{11} and ε_{22} components as well as σ_{11} and σ_{22} occurs during the numerical simulation of the whole bulge test using the identified parameters of *Yld2004-Iso* model. In Figure B.5, a slight difference between σ_{11} and σ_{22} values during the numerical simulation of the bulge using the identified parameters of *Yld2004-Mixed* model was detected. Nevertheless, this difference remains very small as demonstrated by Figure B.6, which represents the evolution of the biaxial deviation $(\sigma_{11}-\sigma_{22})/\sigma_{11}$ during the numerical simulation of the bulge test. It can be seen that an average relative gap of 3% between the stress components in RD and transverse directions were recorded for *Yld2004-Mixed* model. In the case of *Yld2004-Iso* model, an average relative gap lower than 1% was achieved.

From an experimental point of view, it should be emphasized that the size of the area used to calculate the radius of curvature at the apex was small compared to the gauge diameter of the bulge test (185 mm), as proposed by Yoshida (2013). Hence, taking it into account as well as the

very small recorded deviations from the equibiaxial stress state, it was shown that the theoretical formulation on bulge stress remains acceptable in this work.

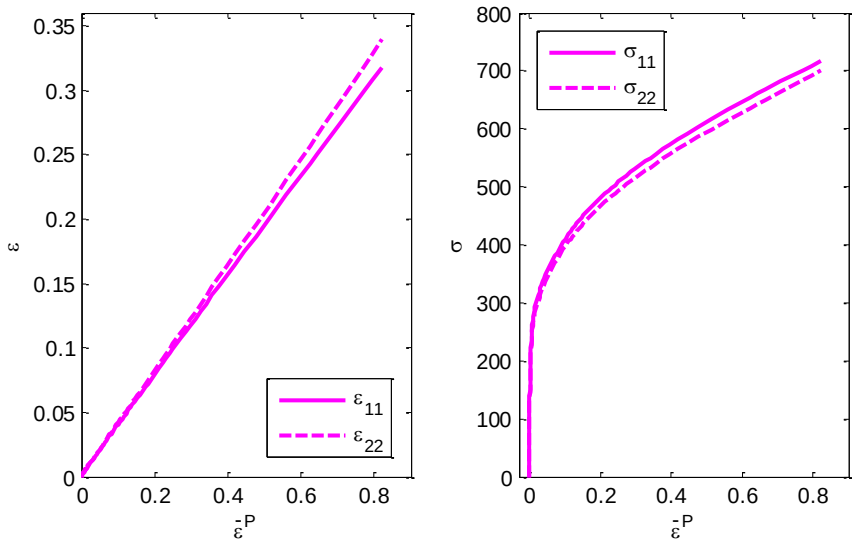

Figure B.5 – Numerical evolution of a) ε_{11} and ε_{22} and b) σ_{11} and σ_{22} with $\bar{\varepsilon}^P$ obtained at the apex of bulge test using *Yld2004-Mixed* model.

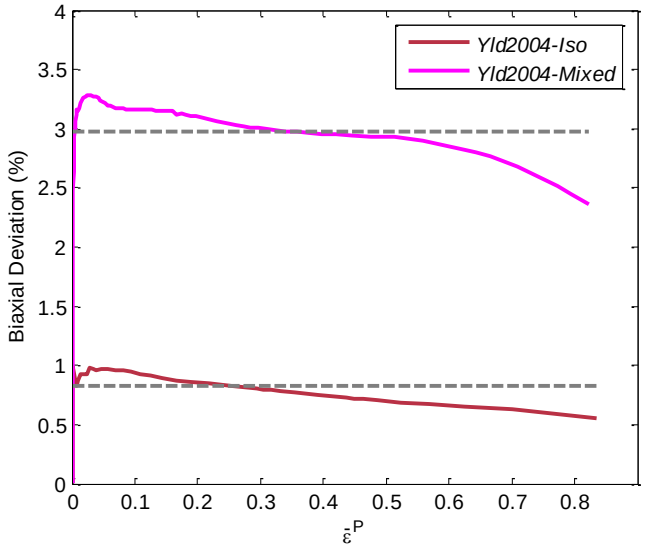

Figure B.6 – Numerical biaxial deviation on the bulge test using the identified parameter sets of both *Yld2004-Iso* and *Yld2004-Mixed* models. Dashed lines correspond to the average values.

Appendix C

Shape optimization of the rectangular shear specimen

The planar simple shear is a loading path particularly interesting for evaluating the mechanical properties of sheet metals. Actually, shear tests using rectangular specimen are widely used by the scientific community for characterizing the material behavior due to the large strains that can be obtained. Nevertheless, for high strength steels, such as dual-phase steel DP980, premature rupture occurs in the vicinity of the grips. For this material, the maximum shear strain achieved using the rectangular specimen geometry was 0.425. Due to this fact, the shape of the shear specimen is redesigned with the aim of maximizing the deformation achieved in the central part of the specimen without the occurrence of rupture near the grips.

Dunand and Mohr (2011) performed a parametric study for evaluating the influence of some geometric parameters of a butterfly specimen applied to fracture testing. The butterfly specimen and the evaluated geometric parameters are depicted in Figure C.1.

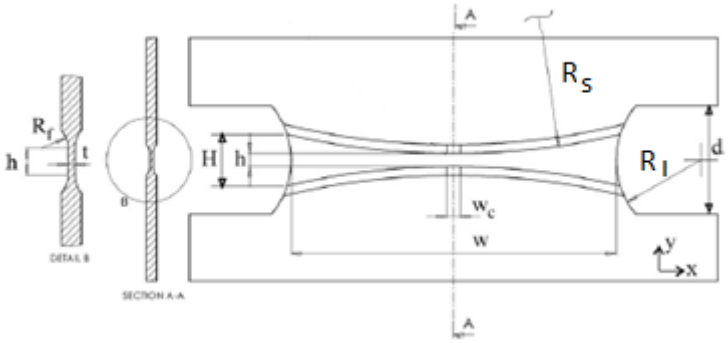

Figure C.1 – Schematic of the butterfly specimen proposed by Dunand and Mohr (2011).

By using different values for the geometric parameters R_s and R_I, it was observed that (i) the homogeneity of the strain distribution can be improved by increasing the shoulder radius R_s, (ii) a concave ($R_I > 0$), in opposition to rectangular ($R_I = \infty$) and convex ($R_I < 0$) geometry of the lateral boundaries, leads to the reduction of strain concentrations near the specimen shoulders and (iii) the maximum value of the equivalent plastic strain along the lateral boundary can be reduced by varying the concave geometry of the lateral boundaries. This study consisted only of punctual testing of some different values of geometric parameters and was applied on a different specimen

type. However, considering their results and knowing that the rupture occurs at the corners of the rectangular shear specimen, in this work, just the lateral boundaries of the sample were subjected to shape optimization.

C.1 Material and numerical validation

Initially, shear tests were carried out on rectangular specimens of dimension 50 x 17 x 1.75 mm^3. Nonetheless, sliding of the sample was verified during the experiments, as shown in Figure C.2 a). It is due to the hardness and considerable thickness of the specimen. Then, the sample geometry was modified and the shear tests were performed using the geometry depicted in Figure C.2 b) (Mishra, 2013). The reduction of the gauge area of the sample led to a significant decrease of the clamping load and, as a result, sliding was avoided. The numerical reproduction of DP980 mechanical behavior was carried out considering a phenomenological model composed by the anisotropic yield criterion of Hill48 combined with a linear isotropic hardening law identified from tensile tests (Mishra *et al.*, 2011).

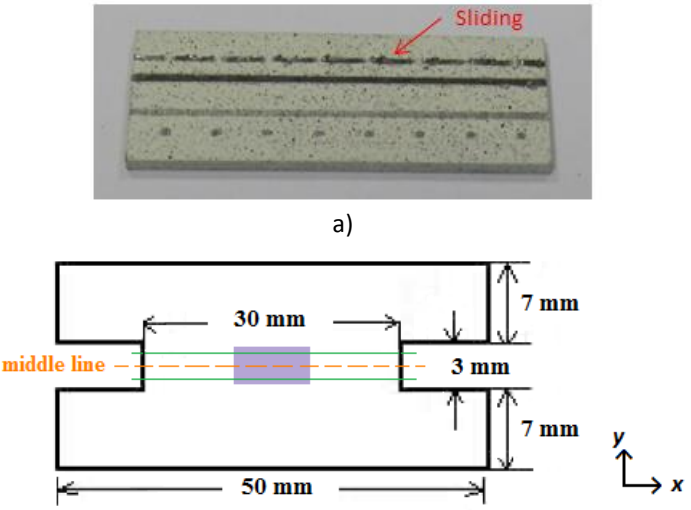

Figure C.2 – Shear specimen with a) rectangular and b) modified geometry.

Table C.1 lists the anisotropic coefficients and the elastic properties of the material while Figure C.3 (left) presents the experimental and numerical shear stress-strain curves obtained. The results depicted in Figure C.3 (left) reveal a good agreement between the numerical and experimental behavior of DP980 steel. Additionally, the shear strain distribution along the lines parallel to the shear direction in the gauge area of the sample was also evaluated for the shear test at the RD. The shear strain distribution along the middle line and the lines at + 1 mm and - 1 mm from the specimen center (shown in Figure C.2 b)), for an average shear strain of 0.35, are depicted in Figure C.3 b), a) and c), respectively. Note that the positions of 0 and 30 mm correspond to the lateral boundaries of the gauge area. Excepting the shear strain distribution for the line at +1 mm (Figure C.3Figure C a)) where the numerical reproduction exhibits some discrepancy, for the two remaining shear strain distributions reliable reproductions were

obtained. Thereby, these numerical results allow a good description of the DP980 mechanical behavior.

Table C.1 – Plastic anisotropy and elastic coefficients of DP980 steel.

	r_0	r_{45}	r_{90}	E [Pa]	υ
DP980	0.63	0.95	0.82	180×10^9	0.3

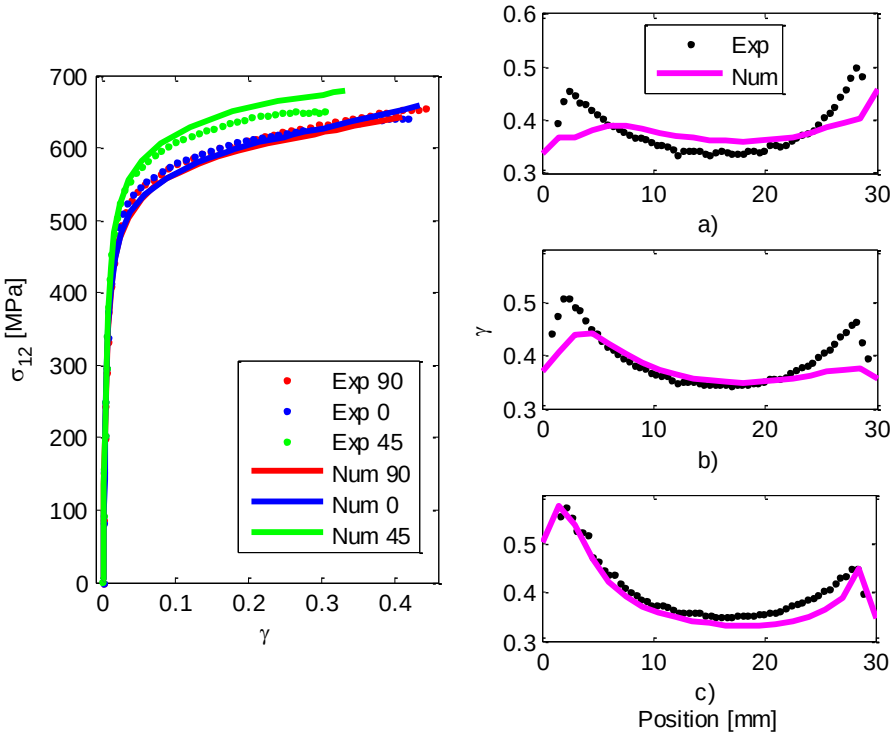

Figure C.3 – Experimental and numerical (i) shear stress-strain curves at 0°, 45° and 90° to the RD (left) and (ii) shear strain distribution along the lines at a) +1 mm, b) middle and c) -1 mm of the specimen center for DP980 steel.

C.2 Numerical modeling and rupture criterion

The shape optimization is carried out by using a bidimensional numerical model that consists of the gauge area of the modified shear specimen.

In shape optimization, it is essential to proceed to the parametrization of the specimen geometry in order to control the nodes position and also to obtain a reliable mesh definition when FE method is used. The commercial FE code ABAQUS is chosen for this purpose. The specimen geometry is parametrized on the ABAQUS input file considering mesh refinement in the boundaries of the sample. This local mesh refinement is required since the critical rupture is reached on the boundaries. Figure C.4 shows the different mesh regions defined on the numerical model of the shear sample. The zones A consist of an area of 3×3 mm^2 at each opposite side of the specimen with a mesh definition of 6 elements/mm, while the zone B was defined with 6 elements/mm along *y*-direction and 2 elements/mm along *x*-direction. This mesh is structured

with 4-node plane stress quadrilateral elements (CPS4). Moreover, ALE[11] adaptative meshing was also included in the numerical model. This kind of formulation makes possible to maintain a high-quality mesh throughout an analysis, even when large deformation or loss of material occurs, by allowing the mesh to move independently of the material. Additionally, this formulation does not alter the element connectivity of the mesh (Abaqus, 2009).

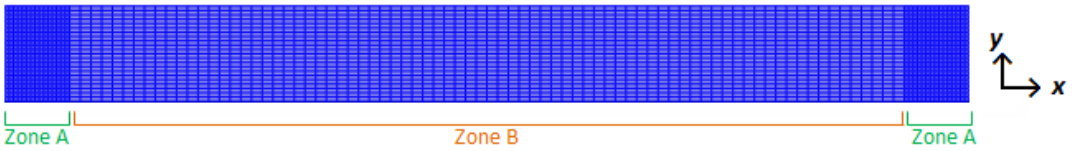

Figure C.4 – Different zones defined over the numerical model of the shear sample, for mesh refinement.

The definition of the boundaries is performed using curve interpolation with cubic splines. In this way, a reduced number of design variables is used.

For evaluating the rupture in the specimen geometry, RT (Rice and Tracey, 1969) macroscopic rupture criterion was implemented in a user-defined output variable subroutine (UVARM) for ABAQUS code.

Mishra (2013) calibrated the RT criterion for DP980 steel through a uniaxial tensile test subjected to rupture and the critical value obtained was W_{RT}^{C} =1.31. Moreover, RT criterion was compared for tension and bending tests, with triaxiality ratio of the order of 0.33 up to 0.66, and it was observed that this rupture criterion gives a good prediction of the rupture strain over all the stress triaxiality range (Mishra, 2013). Latter, it is shown that the stress triaxiality ratio for simple shear, near the free edges, reaches a value of 0.46 which is in the range used to validate the rupture criterion.

For calibrating the rupture behavior in the shear test, a numerical reproduction up to the experimental rupture average strain ($\gamma = 0.425$) was carried out using the specimen geometry shown in Figure C.2 b). The critical RT rupture value obtained was 1.41. By comparing this rupture value with the one calibrated by Mishra (2013) using uniaxial tensile test, a discrepancy of about 7% was obtained. Since such discrepancy is less than 10%, it was considered that the critical rupture value calibrated for the shear test remains acceptable. Therefore, it was considered that an accurate reproduction of the experimental reality is achieved with this model and, consequently, the critical rupture value obtained (1.41) was used as reference W_{RT}^{C} parameter in the shape optimization process.

C.3 Shape optimization process

As referred above, the aim of this work is to maximize the shear strain achieved on the shear sample before rupture takes place. For this purpose, the shape optimization process developed consists of finding the best geometry of the specimen boundaries that delay the rupture and, consequently, maximize the average shear strain. To do this, the numerical simulation of the

[11] Arbitrary Lagrangian Eulerian.

shear test is performed until the end criterion W_{RT}^{C} is reached, while the specimen boundary shape is iteratively updated in order to maximize the average value of shear strain.

The success of the optimization process depends on a suitable definition of the objective function. This objective function must be formulated to represent the shape optimization problem and to satisfy the optimization approach considered. Therefore, the objective function $S_{obj}(\mathbf{x})$ is defined as

$$S_{obj}(\mathbf{x}) = (2 - \gamma_{ave})^2, \tag{C.1}$$

where $\mathbf{x}$ is the design variables set and γ_{ave} is the average shear strain obtained for a region of 2x1mm^2 in the center of the specimen (shown in Figure C.6) when the reference critical rupture value is reached.

The optimization process is conducted by an interface program developed in Matlab. This interface program is linked with the FE code ABAQUS to perform the numerical simulations and with a Fortran script to read the numerical results. Figure C.5 illustrates the flow diagram of the optimization methodology implemented. The objective function is minimized by using the Nelder-Mead optimization algorithm (Coleman *et al.*, 1999; González, 2001).

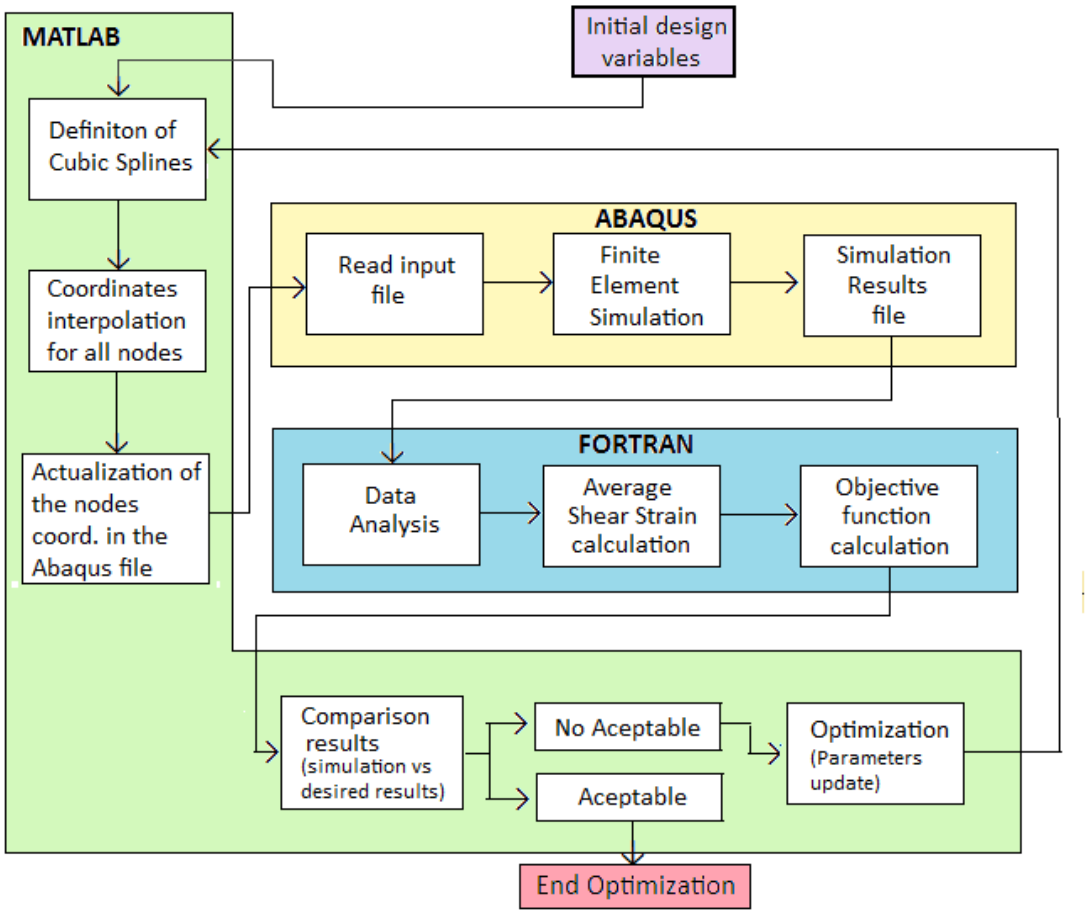

Figure C.5 – Flow diagram of the optimization methodology implemented in this work.

The optimization process is repeated iteratively until a stagnation criterion of $1x10^{-15}$ between two consecutive evaluations of the objective function is obtained or a maximum of 200 evaluations is reached. In addition, the Nelder-Mead optimization algorithm used is available in Matlab by the *fminsearch* function (Coleman *et al.*, 1999).

In order to simplify the optimization problem, some conditions were defined: (i) it was considered that diagonal symmetry exists in the sample. Therefore, the geometric shape of the lateral boundaries is identical, however, inverted relatively to the other boundary side. Thus, just the design variables of one lateral boundary need to be optimized. It is illustrated in Figure C.6 by considering 5 design variables; (ii) the vertical position y of the design variables is fixed whereas the horizontal position x is subjected to optimization; (iii) the design variables (1 and 5) of the extremities are not subjected to optimization since a previous study considering these control points as variables revealed that no significant variations occur. These control points maintained almost the same initial value. Moreover, the imposition of this condition avoids eventual variations in the length of the gauge area and additional effort on manufacturing the optimized specimen geometry; (iv) different number of design variables are considered in the optimization process, namely, 3, 5 and 7 control points. These control points are equally spaced on the lateral boundary. The use of different number of design variables allow to evaluate the influence of the cubic splines interpolation in the obtained results; and (v) three optimization processes using different starting values were carried out for each optimization process (with 3, 5 or 7 design variables) because the Nelder-Mead algorithm, besides effective, does not avoid local minima of the objective function.

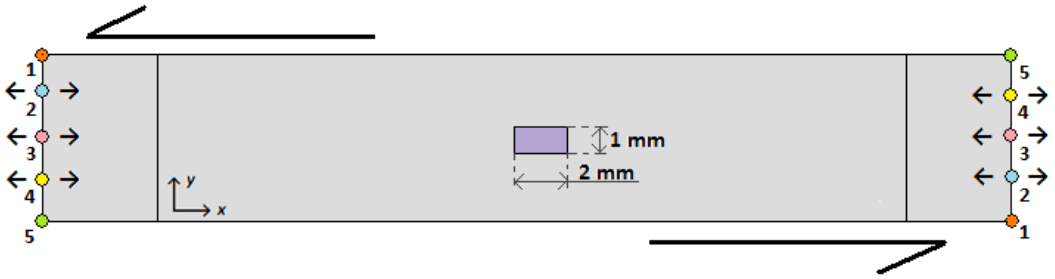

Figure C.6 – Schematic representation of the shear specimen boundaries subjected to optimization. The average shear strain is calculated in the region with 2 x 1 mm^2.

C.4 Results and discussion

Table C.2 shows the initial and optimal design variables and objective function values as well as the number of evaluations performed and the average shear strain obtained for each set of design variables. In addition, the deformed optimal shapes showing the RT distribution (UVARM1) are also depicted. Though three optimization processes were carried out for each set of design variables, just the one that achieved best results is presented in Table C.2. The best obtained shapes using 3, 5, and 7 design variables allow to reach 0.83, 1.03 and 1.05 of average strain. These results show that by optimizing the shear specimen shape it is possible to achieve substantial average shear strain up to rupture, when comparing with the average shear strain of 0.425 that was experimentally obtained. In addition, it is also observed that a larger number of

design variables leads to an optimal geometry with larger average shear strain. However, for 5 and 7 design variables the average shear strain value obtained is quite similar.

The initial and best geometries using 3, 5 and 7 design variables are illustrated in Figure C.7 a), b) and c), respectively, and these best geometries are compared in Figure C.7 d).

Table C.2 – Optimization results obtained using 3, 5 and 7 design variables.

Opt.	Variables	Initial (mm)	Optimal (mm)	
3 control points	$x1$	0.0	0.0	
	$x2$	0.5	0.49	
	$x3$	0.0	0.0	
	Iterations		45	
	S_{obj} initial		1.49	
	S_{obj} final		1.36	
	γ_{ave}		**0.83**	
5 control points	$x1$	0.0	0.0	
	$x2$	0.4	0.33	
	$x3$	0.6	0.57	
	$x4$	0.4	0.46	
	$x5$	0.0	0.0	
	Iterations		137	
	S_{obj} initial		1.25	
	S_{obj} final		0.92	
	γ_{ave}		**1.03**	
7 control points	$x1$	0.0	0.0	
	$x2$	0.1	0.23	
	$x3$	0.25	0.41	
	$x4$	0.31	0.50	
	$x5$	0.25	0.41	
	$x6$	0.1	0.18	
	$x7$	0.0	0.0	
	Iterations		157	
	S_{obj} initial		1.65	
	S_{obj} final		0.88	
	γ_{ave}		**1.05**	

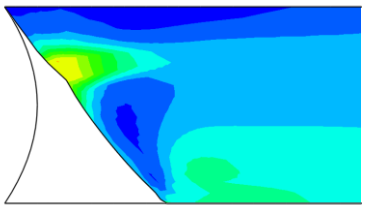

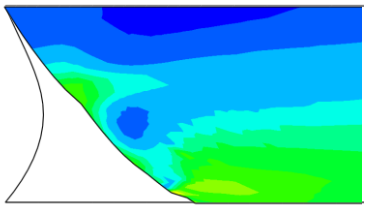

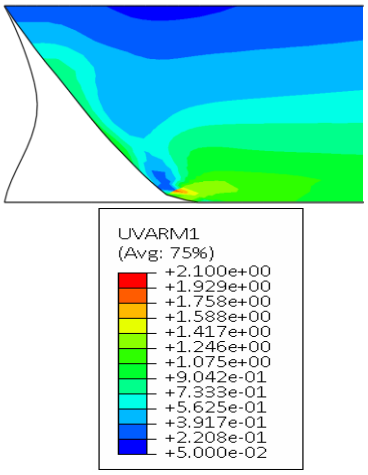

By Figure C.7, it can be seen that the best geometry corresponds to a concave shape for the three optimization processes. It leads to the conclusion that this kind of specimen shape is the one more effective for delaying rupture in shear experiments.

In this work, the best geometry shape was achieved using 7 design variables and the stress triaxiality ($\chi=\sigma_H/\sigma_{eq}$) was evaluated for this specimen geometry. A maximum value of 0.46 was obtained near the free edges in this stress analysis. This value is in agreement with the range used to validate the rupture criterion.

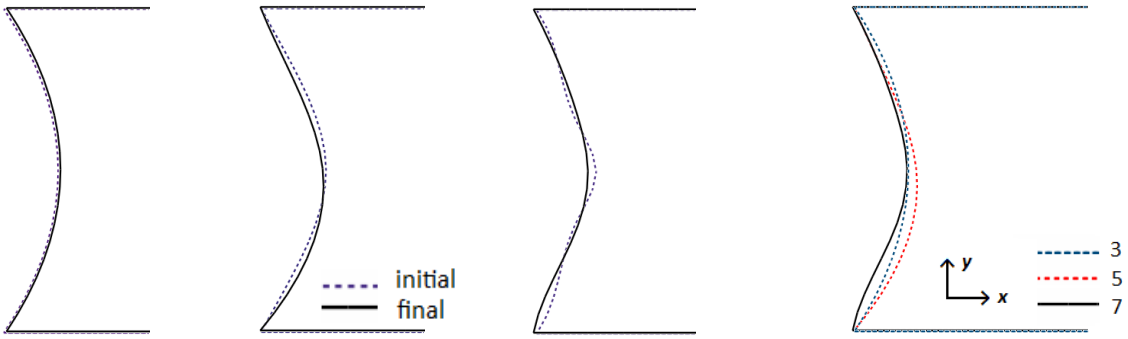

(a) (b) (c) (d)

Figure C.7 – Initial and best boundary shapes using a) 3, b) 5 and c) 7 design variables; d) best boundary shapes using 3, 5 and 7 design variables.

C.5 Conclusion

The aim of this work is the optimization of the conventional simple shear specimen in order to obtain a large level of deformation. This work comes from the fact that hard materials, such as DP 980 steel, reach premature rupture in shear near the grips. In the case of this material, the experimental rupture was obtained for an average shear strain of 0.425.

A shape optimization process based on RT macroscopic rupture criterion was defined to solve this problem. Cubic splines were applied for describing the boundary geometries and the Nelder-Mead algorithm was used for minimizing the objective function. The optimization results show that concave shape is the most effective one to delay the rupture. In addition, when a larger number of design variables is used, the higher is the average shear strain achieved. The best geometry allows reaching an average shear strain value of 1.05. However, this shear strain value was obtained numerically and experimental results using this optimized geometry shape are required for validating the accuracy of this value and, consequently, of this shape optimization process.

Appendix D

Cubic splines definition

The curve interpolation is a useful technique to interpolate between known data points in order to design and control the shape of smooth complex curves and surfaces. The main principle of this technique consists in using the mathematical representation of polynomials defined by a sequence of a few points to construct a complex curve whose shape follows this sequence. The points are called control points.

The interpolation methods used in curve interpolation technique are, usually, divided into two main categories: global interpolation and piecewise interpolation (Lyche and Mørken, 2008).

The global interpolation method deals with the construction of a single mathematical equation fitting all the control points. This single mathematical equation corresponds to a high degree polynomial. In fact, a polynomial of degree n is needed to interpolate n+1 control points. This kind of interpolation method results in smooth curves when no abrupt changes along the sequence of control points exist. However, for complex shapes such as the ones used on several engineering applications, the global interpolation is not well suited due to the fact that a high degree polynomial catches all oscillations at least until n-1 derivatives leading to estimation and round off errors and then, severe oscillation and overshoot at intermediate points (Knott, 2000; Lyche and Mørken, 2008).

The piecewise interpolation is based on the construction of a complex curve shape applying a lower degree polynomial between each pair of control points. Splines, B-splines or Bézier are some types of polynomial curves used in piecewise interpolation (de Boor, 1978; Knott, 2000; Lyche and Mørken, 2008). The splines defined with second or third degree polynomials are called, respectively, quadratic or cubic splines. The cubic spline is the one most typically chosen for constructing interpolation curves since (i) it is the lowest degree polynomial that can support an inflection, allowing defining flexible curves and (ii) it behaves well numerically promoting a smooth and continuous curve. It is due to the fact that the cubic splines are formulated considering continuous and smooth connections between consecutive control points. In addition, since cubic splines are defined by a lower degree polynomial, the oscillations captured are kept to a minimum and, generally, high approximations of the curve shape behavior are provided (Knott, 2000; Lyche and Mørken, 2008).

In Figure D.1, the performance between a polynomial of degree 6, quadratic and cubic splines used for the definition of a curve shape using 7 control points can be compared. It can be easily seen that the cubic spline leads to a better representation of the curve shape.

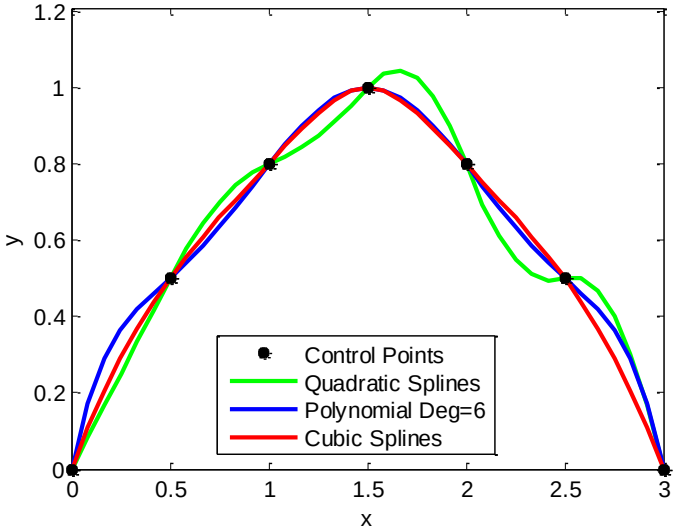

Figure D.1 – Curve shapes obtained using quadratic splines, a polynomial function of degree 6 and cubic splines.

A cubic spline is defined mathematically for given n control points, $(x_1,y_1),\ldots,(x_n,y_n)$, by a piecewise function of the form (Matlab):

$$\begin{aligned} S_1(x) &= y_1 + b_1(x-x_1) + c_1(x-x_1)^2 + d_1(x-x_1)^3 \qquad \text{for } x \in [x_1, x_2] \\ S_2(x) &= y_2 + b_2(x-x_2) + c_2(x-x_2)^2 + d_2(x-x_2)^3 \qquad \text{for } x \in [x_2, x_3] \\ &\vdots \\ S_{n-1}(x) &= y_{n-1} + b_{n-1}(x-x_{n-1}) + c_{n-1}(x-x_{n-1})^2 + d_{n-1}(x-x_{n-1})^3 \qquad \text{for } x \in [x_{n-1}, x_n], \end{aligned} \tag{D.1}$$

where b_i, c_i and d_i with $i = 1,\ldots, n\text{-}1$ are chosen to satisfy the interpolation constraints and also some smoothness constraints. For instance, the continuity (C^0) between each curve segment at the control points is enforced by

$$S_i(x_{i+1}) = S_{i+1}(x_{i+1}) = y_{i+1} \tag{D.2}$$

and at the right value of x, $S_{n-1}(x_n)=y_n$. Additionally, C^1 and C^2 continuity imposing that the shapes and curvatures of curve segments connected by the same control points is also considered by

$$S_i'(x_{i+1}) = S_{i+1}'(x_{i+1}) \tag{D.3}$$

and

$$S_i''(x_{i+1}) = S_{i+1}''(x_{i+1}). \tag{D.4}$$

Finally, two more constraints are needed to define uniquely the cubic splines. These ones consist of defining that the third derivatives match at x_2 and x_{n-1} control points. Such constraints are designated as “Not-A-Knot” condition and are written as (Matlab)

$$S_1'''(x_2) = S_2'''(x_2) \tag{D.5}$$

and

$$S_{n-2}'''(x_{n-2}) = S_{n-1}'''(x_{n-2}). \tag{D.6}$$

References

Abaqus, 2009. ABAQUS/Standard - User's manual. Dassault Systèmes Simulia.

Abaqus, 2012. Abaqus 6.12 - Scirpting User's Manual. Dassault Systèmes Simulia.

Abbassi, F., Belhadj, T., Mistou, S., Zghal, A., 2013. Parameter identification of a mechanical ductile damage using Artificial Neural Networks in sheet metal forming. Materials and Design 45, 605–615.

Adams, D.F., Walrath, D.E., 1986. Further Development of the Iosipescu Shear Test Method. Experimental Mechanics 27, 113-119.

An, Y.G., Vegter, H., Heijne, J., 2009. Development of simple shear test for the measurement of work hardening. Journal of Materials Processing Technology 209, 4248–4254.

Andrade-Campos, A., 2011. Development of an Optimization Framework for Parameter Identification and Shape Optimization Problems in Engineering. International Journal of Manufacturing, Materials, and Mechanical Engineering 1, 57-79.

Andrade-Campos, A., .de-Carvalho, R., Valente, R.A.F., 2012. Novel criteria for determination of material model parameters. International Journal of Mechanical Science 54, 294–305.

Andrade-Campos, A., Thuillier, S., Pilvin, P., Teixeira-Dias, F., 2007. On the Determination of Material Parameters for Internal Variable Thermoelastic–Viscoplastic Constitutive Models. International Journal of Plasticity 23, 1349-1379.

Aretz, H., Keller, S., 2011. On the Non-Balanced Biaxial Stress State in Bulge-Testing, Steel research international, Special edition: 10th international conference on technology of plasticity. ICTP, pp. 738–743.

ASTM, 1993. Standard Test Method for Shear Properties of Composite Materials by the V-Notched Beam Method, American Society for Testing and Materials.

ASTM B831, 2005. Standard Test Method for Shear Testing of Thin Aluminum Alloy Products, Annual Book of ASTM Standards.

ASTM E8-04, 2004. Standard Test Methods for Tension Testing of Metallic Materials, ASTM International.

Avril, S., Bonnet, M., Bretelle, A.-S., Grédiac, M., Hild, F., Ienny, P., Latourte, F., Lemosse, D., Pagano, S., Pagnacco, E., Pierron, F., 2008a. Overview of Identification methods of mechanical parameters based on full-field measurements. Experimental Mechanics 48, 381-402.

Avril, S., Pierron, F., Pannier, Y., Rotinat, R., 2008b. Stress Reconstruction and Constitutive Parameter Identification in Plane-Stress Elasto-plastic Problems Using Surface Measurements of Deformation Fields. Experimental Mechanics 48, 403–419.

Ayres, R.A., Brazier, W.G., Sajewski, V.F., 1978. Evaluating the GMR-Limiting Dome Height Test as a new measure of press formability near plane strain. Journal of Applied Metalworking 1, 41-49.

Azzouna, M.B., Périé, J.-N., Guimard, J.-M., Hild, F., Roux, S., 2011. On the identification and validation of an anisotropic damage model by using full-field measurements International Journal of Damage Mechanics 20, 1130-1150.

Banabic, D., 2007. Advanced Methods in Material Forming. Springer Berlin Heidelberg.

Banabic, D., 2010. Sheet Metal Forming Processes: Constitutive Modelling and Numerical Simulation. Springer-Verlag, Berlim.

Banabic, D., Balan, T., Comsa, D.S., 2000a. A new yield criterion for orthotropic sheet metals under plane-stress conditions, 7th Conference 'TPR2000', Cluj Napoca, pp. 217–224.

Banabic, D., Barlat, F., Cazacu, O., Kuwabara, T., 2010. Advances in anisotropy and formability. International Journal of Material Forming 3, 165-189.

Banabic, D., Bunge, H.-J., Pölandth, K., Tekkaya, A.E., 2000b. Formability of Metallic Materials. Springer-Verlag, Berlim.

Bao, Y., Wierzbicki, T., 2004. On fracture locus in the equivalent strain and stress triaxiality space. International Journal of Mechanical Sciences 46, 81-98.

Barlat, F., Aretz, H., Yoon, J.W., Karabin, M.E., Brem, J.C., Dick, R.E., 2005. Linear transfomation-based anisotropic yield functions. International Journal of Plasticity 21, 1009–1039.

Barlat, F., Brem, J.C., Yoon, J.W., Chung, K., Dick, R.E., Lege, D.J., Pourboghrat, F., Choi, S.-H., Chu, E., 2003. Plane stress yield function for aluminum alloy sheets—part 1: theory. International Journal of Plasticity 19, 1297–1319.

Barlat, F., Lege, D.J., Brem, J.C., 1991. A six-component yield function for anisotropic materials. International Journal of Plasticity 7, 693–712.

Belhabib, S., Haddadi, H., Gaspérini, M., Vacher, P., 2008. Heterogeneous tensile test on elastoplastic metallic sheets: Comparison between FEM simulations and full-field strain measurements. International Journal of Mechanical Sciences 50, 14–21.

Belytschko, T., Liu, W.K., Moran, B., 2001. Nonlinear Finite Elements for Continua and Structures. John Wiley & Sons.

Besson, J., 2010. Continuum Models of Ductile Fracture: A Review. International Journal of Damage Mechanics 19, 3-52.

Björklund, O., Govik, A., Nilsson, L., 2014. Prediction of fracture in a dual-phase steel subjected to non-linear straining. Journal of Materials Processing Technology 214, 2748–2758.

Björklund, O., Larsson, R., Nilsson, L., 2013. Failure of high strength steel sheets: Experiments and modelling. Journal of Materials Processing Technology 213, 1103– 1117.

Boger, R.K., Wagoner, R.H., Barlat, F., Lee, M.G., Chung, K., 2005. Continuous, large strain, tension/compression testing of sheet material. International Journal of Plasticity 21, 2319-2343.

Bouvier, S., Haddadi, H., Levée, P., Teodosiu, C., 2006. Simple shear tests: Experimental techniques and characterization of the plastic anisotropy of rolled sheets at large strains. Journal of Materials Processing Technology v.172, 96–103.

Bron, F., Besson, J., 2004. A yield function for anisotropic materials application to aluminum alloys. International Journal of Plasticity 20, 937–963.

Brosius, A., Yin, Q., Güner, A., Tekkaya, A.E., 2011. A New Shear Test for Sheet Metal Characterization. Steel Research International 82, 323–328.

Brown, W.F., Thompson, F.C., 1949. Strength and Failure Characteristics of Metal Membranes in Circular Bulging. Transactions of ASM 71, 575-586.

Brozzo, P., Deluca, B., Rendina, R., 1972. A new method for the prediction of formability limits of metal sheets, Seventh Biennial Congress of International Deep Drawing Research Group. Sheet Metal Forming and Formability, Netherlands.

Bui, H.D., Constantinescu, A., Maigre, H., 2004. Numerical identification of linear cracks in 2d elastodynamics using the instantaneous reciprocity gap. Inverse Problems 20, 993–1001.

Cailletaud, G., Pilvin , P., 1993. Identification, Problémes Inverse: un Concept Modulaire, In: 2ième Colloque National en Calcul des Structures, Giens, pp. pp. 770–787.

Cailletaud, G., Pilvin , P., 1994. Identification and Inverse Problems Related to Material Behaviour, Proceedings of the International Seminar on Inverse Problems, Clamart, pp. 79–86.

Cao, J., Lee, W., Cheng, H.S., Seniw, M., Wang, H.-P., Chung, K., 2009. Experimental and numerical investigation of combined isotropic-kinematic hardening behavior of sheet metals. International Journal of Plasticity 25, 942–972.

Carbonnière, J., Thuillier, S., Sabourin, F., Brunet, M., Manach, P.Y., 2009. Comparison of the work hardening of metallic sheets in bending-unbending and simple shear. International Journal of Mechanical Sciences 51, 122-130.

Chaboche, J.L., 2008. A review of some plasticity and viscoplasticity constitutive theories. International Journal of Plasticity 24, 1642-1693.

Chaboche, J.L., Nouailhas, D., Savalle, S., 1991. Logiciel pour l'Identification Interactive Graphique des Lois de Comportement. La Recherche Aérospaciale v.3, pp. 59-76.

Chaboche, J.L., Rousselier, G., 1983. On the plastic and viscoplastic constitutive equations, Parts I and II. International Journal of Pressure Vessels and Piping 105, 153–158. 159–164.

Chaparro, B.M., Thuillier, S., Menezes, L.F., Manach, P.Y., Fernandes, J.V., 2008. Material parameters identification: Gradient-based, genetic and hybrid optimization algorithms. Computational Materials Science 44, 339–346.

Chong, E., Zak, S., 2001. An Introduction to Optimization. John-Wiley & Sons Inc.

Choung, J.M., Cho, S.R., 2008. Study on true stress correction from tensile tests. Journal of Mechanical Science and Technology 22, 1039-1051.

Chung, K., Lee, M.-G., Kim, D., Kim, C., Wenner, M.L., Barlat, F., 2005. Spring-back evaluation of automotive sheets based on isotropic-kinematic hardening laws and non-quadratic anisotropic yield functions Part I: theory and formulation. International Journal of Plasticity 21, 861–882.

Claire, D., Hild, F., Roux, S., 2004. A finite element formulation to identify damage fields: the equilibrium gap method. International Journal Numerical Methods in Engenieering 61, 189–208.

Claire, D., Hild, F., Roux, S., 2007. Identification of a Damage Law by Using Full-field Displacement Measurements. International Journal of Damage Mechanics 16, 179–197.

Cockroft, M.G., Latham, D.J., 1968. Ductility and the workability of metals. Journal of the Institute of Metals 96, 33-39.

Coër, J., 2013. Mise en forme par emboutissage en temperature d'un alliage d'alluminium. Université de Bretagne-Sud, France.

Coleman, T., Branch, M.A., Grace, A., 1999. Optimization Toolbox - for use with Matlab. MathWorks Inc.

Cooreman, S., 2008. Identification of the plastic material behaviour through full-field displacement measurements and inverse methods. Vrije Universiteit Brussel, Belgium.

Cooreman, S., Lecompte, D., Sol, H., Vantomme, J., Debruyne, D., 2008. Identification of Mechanical Material Behavior Through Inverse Modeling and DIC. Experimental Mechanics 48, 421–433.

de-Carvalho, R., Silva, S., Valente, R.A.F., Andrade-Campos, A., 2012. Blank optimization in a stamping process - Influence of the geometry definition. Finite Elements in Analysis and Design 61, 75–84.

de-Carvalho, R., Valente, R.A.F., Andrade-Campos, A., 2011. Optimization Strategies for Non-Linear Material Parameters Identification in Metal Forming Problems. Computers and Structures 89, 246-255.

de Boor, C., 1978. A Practical Guide to Splines. Springer-Verlag.

DIN EN 10 002, 2001. Tensile testing of metallic materials - Part 1: method of test at ambient temperature, German Institute for Standardization.

Dudderar, T.D., Koch, F.B., Doerries, E.M., 1977. Measurement of the Shapes of Foil Bulge-test Samples. Experimental Mechanics 17, 133-140.

Dunand, M., Mohr, D., 2011. Optimized butterfly specimen for the fracture testing of sheet materials under combined normal and shear loading. Engineering Fracture Mechanics 78, 2919–2934.

Dunne, F., Petrinic, N., 2005. Introduction to computational plasticity, 6th Edition ed. Oxford University Press.

Fleury, C., 1989. First and second order convex approximation strategies in structural optimization. Structural optimization 1, 3-10.

Florentin, E., Lubineau, G., 2010. Identification of the parameters of an elastic material model using the constitutive equation gap method. Computational Mechanics 46, 521–531.

Foecke, T., Iadicola, M.A., Lin, A., Banovic, S.W., 2007. A Method for Direct Measurement of Multiaxial Stress-Strain Curves in Sheet Metal. Metallurgical and Materials Transactions 38, 306-313.

Fourment, L., Balan, T., Chenot, J.L., 1996. Optimal design for non-steady-state metal forming processes - II. Application of shape optimization in forging. International Journal Numerical Methods in Engenieering 39, 51–65.

Fourment, L., Chenot, J.L., 1996. Optimal design for non-steady-state metal forming processes - I. Shape optimization method. International Journal Numerical Methods in Engenieering 39, 33–50.

Furukawa, T., Yagawa, G., 1997. Inelastic Constitutive Parameter Identification using an Evolutionary Algorithm with Continuous Individuals. International Journal Numerical Methods in Engenieering 40, 1071–1090.

G'Sell, C., Boni, S., Shrivastava, S., 1983. Application of the simple shear test for determination of the plastic behaviour of solid polymers at large strains. Journal of Materials Science 18, 903-918.

Gau, J.-T., Kinzel, G.L., 2001. A new model for springback prediction in which the Bauschinger effect is considered. International Journal of Mechanical Sciences 43, 1813–1832.

Gelin, J.C., Ghouati, O., 1996. An Inverse Solution Procedure for Material Parameters Identification in Large Plastic Deformation. Communications in Numerical Methods in Engineering v.12, pp. 161–173.

Genevois, P., 1992. Etude expérimental et modélisation du comportement plastique anisotrope de tôles d'acier en grandes déformations. Institut National Polytecnique de Grenoble, France.

Geng, L., Wagoner, R.H., 2002. Role of plastic anisotropy and its evolution on springback. International Journal of Mechanical Sciences 44, 123–148.

Geymonat, G., Pagano, S., 2003. Identification of mechanical properties by displacement field measurement: a variational approach. Meccanica 38, 535–545.

Golongrac, F., 1975. Gerat zur kontinuierlichen aufnahme von fließkurven an blechwerkstoffen im hydraulischen tiefungsversuch. Industrie Anzeiger 97, 937-938.

GOM, 2009. ARAMIS: User Manual - Software. GOM mbH, Germany.

González, J.L.M., 2001. Parameter optimisation and adjustment by the simplex method (Nelder-Mead), 1st Meeting of EcosimPro Users. UNED, Madrid, pp. 1-11.

Gosling, M., Brosius, A., Tekkaya, A.E., 2008. Study on the accuracy of springback predictions by finite element analysis, NUMISHEET 2008, Interlaken, Switzerland, pp. 509-513.

Grédiac, M., 2004. The use of full-field measurement methods in composite material characterization: interest and limitations. Composites: Part A 35, 751–761.

Grédiac, M., Hild, F., 2013. Full-field measurements and identification in solid mechanics. ISTE and John Wiley & Sons.

Grédiac, M., Pierron, F., 2006. Applying the Virtual Fields Method to the identification of elasto-plastic constitutive parameters. International Journal of Plasticity 22, 602–627.

Grédiac, M., Pierron, F., 2012. Identifying constitutive parameters from heterogeneous strain fields using the Virtual Fields Method. Procedia IUTAM 4, 48-53.

Grédiac, M., Pierron, F., Avril, S., Toussaint, E., 2006. The Virtual Fields Method for Extracting Constitutive Parameters From Full-Field Measurements: a Review. Strain 42, 233–253.

Grilo, T.J., Souto, N., Valente, R.A.F., Andrade-Campos, A., Thuillier, S., Sousa, R.J.A.d., 2013a. On the development and computational implementation of complex constitutive models and parameters' identification procedures. Key Engineering Materials 554-557, 936-948.

Grilo, T.J., Valente, R.A.F., Sousa, R.J.A.d., 2013b. Assessment on the performance of distinct stress integration algorithms for complex non-quadratic anisotropic yield criteria. International Journal of Material Forming.

Grilo, T.J., Valente, R.A.F., Sousa, R.J.A.d., 2013c. On the study of distinct algorithmic strategies in the implementation of advanced anisotropic models with mixed hardening. Key Engineering Materials 554-557, 1174-1183.

Güner, A., Soyarslan, C., Brosius, A., Tekkaya, A.E., 2012. Characterization of anisotropy of sheet metals employing inhomogeneous strain fields for Yld2000-2D yield function. International Journal of Solids and Structures 49, 3517-3527.

Gutscher, G., Wu, H.-C., Ngaile, G., Altan, T., 2004. Determination of flow stress for sheet metal forming using the viscous pressure bulge (VPB) test. Journal of Materials Processing Technology 146, 1–7.

Habraken, A., 2004. Modelling the Plastic Anisotropy of Metals. Archives of Computacional Methods in Engineering v.11, pp. 3-96.

Haddadi, H., Belhabib, S., 2012. Improving the characterization of a hardening law using digital image correlation over an enhanced heterogeneous tensile test. International Journal of Mechanical Sciences 62, 47-56.

Hannon, A., Tiernan, P., 2008. A review of planar biaxial tensile test systems for sheet metal. Journal of Materials Processing Technology 198, 1–13.

Hill, R.G., 1948. A theory of the yielding and plastic flow of anisotropic metals. Proceedings of the Royal Society London A 193, :281–297.

Hosford, W.F., 1979. On yield loci of anisotropic cubic metals, 7th North American Metalworking Conference (NMRC), Dearborn, pp. 191–197.

Hosford, W.F., Caddell, R.M., 2007. Metal Forming: Mechanics and Metallurgy. Cambridge University Press.

Hu, Z., Rauch, E.F., Teodosiu, C., 1992. Work-hardening behavior of mild steel under stress reversal at large strains. International Journal of Plasticity 8, 839–856.

Ikehata, M., 1993. An inverse problem for the plate in the Love-Kirchhoff Theory,. SIAM Journal on Numerical Analysis 53, 942–970.

Iosipescu, N., 1967. New Accurate Procedure for Single Shear Testing of Metals. Journal of Materials 2, 537-566.

ISO 6892-1, 2009. Metallic materials — Tensile testing - Part 1: Method of test at room temperature, International Organization for Standardization.

Johnson, W., Duncan, J.L., 1965. The use of the biaxial test extensometer. Sheet Metal Industries 42, 271–275.

Kajberg, J., Lindkvist, G., 2004. Characterisation of materials subjected to large strains by inverse modelling based on in-plane displacement fields. International Journal of Solids and Structures 41, 3439–3459.

Karafillis, A.P., Boyce, M.C., 1993. A general anisotropic yield criterion using bounds and a transformation weighting tensor. Journal of the Mechanics and Physics of Solids 41, 1859–1886.

Kim, J.-H., Serpantié, A., Barlat, F., Pierron, F., Lee, M.-G., 2013. Characterization of the post-necking strain hardening behavior using the virtual fields method. International Journal of Solids and Structures 50, 3829–3842.

Kleinermann, J., 2000. Identification Paramétrique et Optimisation des Procedes de Mise a Forme par Problemes Inverses. Université de Liège, Liège.

Kleinermann, J., Ponthot, J., 2003. Parameter identification and shape/process optimization in metal forming simulation. Comp. Methods in Applied Mechanics and Engineering 139, 521–526.

Knott, G.D., 2000. Interpolating Cubic Splines. Progress in Computer Science and Applied Logic.

Koç, M., Billur, E., Cora, Ö.N., 2011. An experimental study on the comparative assessment of hydraulic bulge test analysis methods. Materials and Design 32, 272–281.

Koh, C.W., 2008. Design of a hydraulic bulge test apparatus. Massachusetts Institute of Technology.

Kuwabara, T., 2007. Advances in experiments on metal sheets and tubes in support of constitutive modeling and forming simulations. International Journal of Plasticity 23, 385–419.

Kuwabara, T., Kumano, Y., Ziegelheim, J., Kurosaki, I., 2009. Tension–compression asymmetry of phosphor bronze for electronic parts and its effect on bending behavior. International Journal of Plasticity 25, 1759–1776.

Ladeveze, P., Nedjar, D., Reynier, M., 1994. Updating of finite element models using vibration tests. AIAA Journal 32, 1485-1491.

Lagarias, J.C., Reeds, J.A., Wright, M.H., Wright, P.E., 1998. Convergence properties of the Nelder-Mead simplex method in low dimensions. SIAM Journal Optimization 9, 112-147.

Latourte, F., Chrysochoos, A., Pagano, S., Wattrisse, B., 2008. Elastoplastic Behavior Identification for Heterogeneous Loadings and Materials. Experimental Mechanics 48, 435–449.

Le Port, A., 2012. Caractérisation et Prédiction des Défauts d'Aspect sur les Ouvrants Automobiles. Université de Bretagne-Sud, France.

Lebedev, A.A., Muzyka, N.R., 1998. Design of cruciform specimens for fracture toughness tests in biaxial tension (review). Strength of Materials 30, 243-254.

Levenberg, K., 1944. A method for the solution of certain problems in least squares. Quarterly of Applied Mathematics 2, 164–168.

Li, H., Fu, M.W., Lu, J., Yang, H., 2011. Ductile fracture: Experiments and computations. International Journal of Plasticity 27, 147–180.

Li, K.P., Carden, W.P., Wagoner, R.H., 2002. Simulation of springback. International Journal of Mechanical Sciences 44, 103–122.

Logan, R.W., Hosford, W.F., 1980. Upper-Bound Anisotropic Yield Locus Calculations Assuming (111)-Pencil Glide. International Journal of Mechanical Sciences v.22, pp. 419-430.

Lubineau, G., 2009. A goal-oriented field measurement filtering technique for the identification of material model parameters. Computational Mechanics 44, 591-603.

Lyche, T., Mørken, K., 2008. Spline Methods Draft. Centre of Mathematics for Applications, University of Oslo.

Makinde, A., Thibodeau, L., Neale, K.W., 1992. Development of an Apparatus for Biaxial Testing Using Cruciform Specimens. Experimental Mechanics 32, 138-144.

Makris, A., Vandenbergh, T., Ramault, C., Hemelrijck, D.V., Lamkanfi, E., Paepegem, W.V., 2010. Shape optimisation of a biaxially loaded cruciform specimen. Polymer Testing 29, 216–223.

Maniatty, A.M., Chen, M.F., 1996. Shape sensitivity analysis for steady metal-forming processes. International Journal Numerical Methods in Engenieering 39, 1199–1217.

Maniatty, A.M., Zabaras, N., 1989. Method for solving inverse elastoviscoplatic problems. Journal of Engineering Mechanics 115, 2216–2231.

Maniatty, A.M., Zabaras, N., 1994. Investigation of regularization parameters and error estimating in inverse elasticity problems. International Journal Numerical Methods in Engenieering 37, 1039–1052.

Marciniak, Z., 1961. Influence of the sign change of the load on the strain hardening curve of a copper test subject to torsion. Archiwum Mechaniki Stosowanj 13, 743-751.

Marciniak, Z., Duncan, J.L., Hu, S.J., 2002. Mechanics of Sheet Metal Forming. Butterworth-Heinemann.

Marquardt, D., 1963. An algorithm for least-squares estimation of nonlinear parameters. SIAM Journal on Applied Mathematics 11, 431–441.

Matlab, Cubic splines and Matlab. http://people.whitman.edu/~hundledr/courses/M467/CubicSplines.pdf.

Mattiasson, K., Sigvant, M., 2004. Material Characterization and Modeling for Industrial Sheet Forming Simulations, NUMIFORM. AIP Conference Proceedings, pp. 875-880.

Merklein, M., Biasutti, M., 2011. Forward and reverse simple shear test experimentsfor material modeling in forming simulations, Steel research international, Special edition: 10th international conference on technology of plasticity. ICTP 2011, pp. 702–707.

Merklein, M., Kuppert, A., 2009. A method for the layer compression test considering the anisotropic material behavior. International Journal of Material Forming 2, 483–486.

Merzouki, T., Nouri, H., Roger, F., 2014. Direct identification of nonlinear damage behavior of composite materials using the constitutive equation gap method. International Journal of Mechanical Sciences 89, 487-499.

Meuwissen, M.H.H., 1998. An inverse method for the mechanical characterisation of metals. Eindhoven University of Technology, Netherlands.

Meuwissen, M.H.H., Oomens, C.W.J., Baaijens, F.P.T., Petterson, R., Janssen, J.D., 1998. Determination of the elasto-plastic properties of aluminium using a mixed numerical–experimental method. Journal of Materials Processing Technology 75, 204–211.

Mishra, A., 2013. Experimental investigation and numerical prediction of forming limits in bending of metallic sheets. PhD thesis at Université de Bretagne-Sud, France.

Mishra, A., Leguen, C., Thuillier, S., Marie, E., 2011. Investigation of ductile damage in DP 980 steel sheets using mechanical tests and x-ray microtomography, 14th International ESAFORM Conference on Material Forming: ESAFORM 2011. AIP Conference Proceedings, pp. 1464-1469.

Mishra, A., Thuillier, S., 2014. Investigation of the rupture in tension and bending of DP980 steel sheet. International Journal of Mechanical Sciences 84, 171–181.

Miyauchi, K., 1984. A proposal of a planar simple shear test in sheet metals. Sci. Papers RIKEN 78, 27-42.

Mohr, D., Oswald, M., 2008. A New Experimental Technique for the Multi-axial Testing of Advanced High Strength Steel Sheets. Experimental Mechanics 48, 65–77.

Morestin, F., Boivin, M., Silva, C., 1996. Elasto plastic formulation using a kinematic hardening model for springback analysis in sheet metal forming. Journal of Materials Processing Technology 56, 619-630.

Moussawi, A., Lubineau, G., Florentin, E., Blaysat, B., 2013. The constitutive compatibility method for identification of material parameters based on full-field measurements. Comp. Methods in Applied Mechanics and Engineering 265, 1-14.

Nocedal, J., Wright, S.J., 2006. Numerical Optimization, 6th Edition ed. Springer-Verlag.

Oyane, M., Sato, T., Okimoto, K., Shima, S., 1990. Criteria for ductile fracture and their applications. Journal of Mechanical Working Technology 4, 65–81.

Ozturk, F., Lee, D., 2004. Analysis of forming limits using ductile fracture criteria. Journal of Materials Processing Technology 147, 397–404.

Pannier, Y., Avril, S., Rotinat, R., Pierron, F., 2006. Identification of Elasto-Plastic Constitutive Parameters from Statically Undetermined Tests Using the Virtual Fields Method. Experimental Mechanics 46, 735–755.

Papirno, R., 1961. Stress and Strain in Thin Films Bulged over Circular Openings. Journal of Applied Physics 32, 1175-1176.

Park, J.J., Rebelo, N., Kobayashi, S., 1983. A new approach to preform design in metal forming with the finite element method. International Journal of Machine Tool Design and Research 23, 71-79.

Peirs, J., Verleysen, P., Paepegem, W.V., Degrieck, J., 2011. Determining the stress-strain behaviour at large strains from high strain rate tensile and shear experiments. International Journal of Impact Engineering 38, 406-415.

Périé, J.N., Leclerc, H., Roux, S., Hild, F., 2009. Digital image correlation and biaxial test on composite material for anisotropic damage law identification. International Journal of Solids and Structures 46, 2388–2396.

Pierron, F., Avril, S., Tran, V.T., 2010. Extension of the virtual fields method to elasto-plastic material identification with cyclic loads and kinematic hardening. International Journal of Solids and Structures 47, 2993–3010.

Pijlman, H.H., 2001. Sheet material characterisation by multi-axial experiments. University of Twente.

Pöhlandt, K., Banabic, D., Lange, K., 2002. Equi-biaxial anisotropy coefficient used to describe the plastic behavior of sheet metal, ESAFORM Conference, Krakow, Poland, pp. 723-726.

Polak, E., 1997. Optimization - Algorithms and consistent aproximations. Springer-Verlag, New York.

Ponthot, J., Kleinermann, J., 2006. A Cascade Optimization Methodology for Automatic Parameter Identification and Shape/Process Optimization in Metal Forming Simulation. Comp. Methods in Applied Mechanics and Engineering 195, 5472-5508.

Pottier, T., 2010. Identification paramétrique par recalage de modèles éléments finis couplée à des mesures de champs cinématiques et thermiques. University of Savoie.

Pottier, T., Vacher, P., Toussaint, F., 2011a. Contribution of heterogeneous strain field measurements and boundary conditions modelling in inverse identification of material parameters. European Journal of Mechanics A/Solids 30, 373-382.

Pottier, T., Vacher, P., Toussaint, F., Louche, H., Coudert, T., 2011b. Out-of-plane Testing Procedure for Inverse Identification Purpose: Application in Sheet Metal Plasticity. Experimental Mechanics, 1-13.

Pourboghrat, F., Chu, E., 1995. Springback in plane strain stretch/draw sheet forming. International Journal of Mechanical Sciences 36, 327-341.

Prater, T.A., Read, H.J., 1949. The Strength and Ductility of Electrodeposited Metals -The Hydraulic Bulge Test. Plating 38, 1221-1226

Prates, P.A., Oliveira, M.C., Fernandes, J.V., 2014. A new strategy for the simultaneous identification of constitutive laws parameters of metal sheets using a single test. Computational Materials Science 85, 102–120.

Ranta-Eskola, A.J., 1979. Use of the hydraulic bulge test in biaxial tensile testing. International Journal of Mechanical Sciences 21, 457–465.

Rao, S.S., 1996. Engineering Optimization: Theory and Practice, 3rd Edition. John Wiley & Sons.

Rauch, E.F., 1998. Plastic Anisotropy of Sheet Metals Determined by Simple Shear Tests. Materials Science and Engineering A 241, 179–183.

Rauch, E.F., G'Shell, C., 1989. Flow localisation induced by a change in strain path in mild steel Materials Science and Engineering A 111, 71-80.

Rice, J.R., Tracey, D.M., 1969. On the ductile enlargement of voids in triaxial stress fields. Journal of the Mechanics and Physics of Solids 17, 201-217.

Roll, K., 2007. Advanced Simulation Techniques - Exceeding Reality?, Proceedings of Materials & Technology Conference, Detroit, USA.

Rossi, M., Pierron, F., 2012. Identification of plastic constitutive parameters at large deformations from three dimensional displacement fields. Computational Mechanics 49, 53–71.

Saito, R., Iizuka, E., Kuwabara, T., 2010. Material modelling of 980 MPa dual-phase steel sheet based on biaxial tensile test and in-plane stress reversal test, International Deep Drawing Research Group: IDDRG 2010 International Conference IDDRG 2010.

Schmit, L.A., 1960. Structural Design by Systematic Synthesis, 2nd Conference on Electronic Computation. ASCE, New York, pp. 105–122.

Schmitt, J.H., Aernoudt, E., Baudelet, B., 1985. Yield loci for polycrystalline metals without texture. Materials Science and Engineering A 75, 13–20.

Schnur, D., Zabaras, N., 1992. An Inverse Method for Determining Elastic Material Properties and Material Interface. International Journal Numerical Methods in Engenieering v.32, pp. 2039-2057.

Shiratori, E., Ikegami, K., 1967. A new biaxial testing machine with flat specimens. Bulletin of the Tokyo Institute of Technology 82, 105–118.

Shouler, D.R., Allwood, J.M., 2010. Design and use of a novel sample design for formability testing in pure shear. Journal of Materials Processing Technology 210, 1304–1313.

Simo, J.C., 1988. A Framework for Finite Strain Elastoplasticity based on Maximum Plastic Dissipation and the Multiplicative Decomposition. Comp. Methods in Applied Mechanics and Engineering 66, 199-219.

Sniedovich, M., 1986. A New Look at Bellman's Principle of Optimality. Journal of Optimization Theory and Applications 49, 161-176.

Soare, S., 2007. On the use of homogeneous polynomials to develop anisotropic yield functions with applications to sheet metal forming. University of Florida.

Sousa, R.J.A.d., Yoon, J.W., Cardoso, R.P.R., Valente, R.A.F., Grácio, J.J., 2007. On the use of a reduced enhanced solid-shell (RESS) element for sheet forming simulations. International Journal of Plasticity 23, 490–515.

Souto, N., Andrade-Campos, A., Thuillier, S., 2015. Material parameter identification within an integrated methodology considering anisotropy, hardening and rupture. Journal of Materials Processing Technology 220, 157-172.

Svanberg, K., 1987. The method of moving asymptotes. A new method for structural optimization. International Journal Numerical Methods in Engenieering 24, 359–373.

Takuda, H., Mori, K., Hatta, N., 1999. The application of some criteria for ductile fracture to the prediction of the forming limit of sheet metals. Journal of Materials Processing Technology 95, 116–121.

Tardif, N., Kyriakides, S., 2012. Determination of anisotropy and material hardening for aluminium sheet metal. International Journal of Solids and Structures 49, 3496-3506.

Tarigopula, V., Hopperstad, O.S., Langseth, M., Clausen, A.H., Hild, F., Lademo, O.-G., Eriksson, M., 2008. A Study of Large Plastic Deformations in Dual Phase Steel Using Digital Image Correlation and FE Analysis. Experimental Mechanics 48, 181-196.

Teaca, M., Charpentier, I., Martiny, M., Ferron, G., 2010. Identification of sheet metal plastic anisotropy using heterogeneous biaxial tensile tests. International Journal of Mechanical Sciences 52, 572–580.

Thuillier, S., Manach, P.Y., 2008. Comparison of the Work-Hardening of Metallic Sheets using Tensile and Shear Strain Paths. International Journal of Plasticity 25, 733-751.

Thuillier, S., Manach, P.Y., Menezes, L.F., 2010. Occurence of strain path changes in a two-stage deep drawing process. Journal of Materials Processing Technology 210, 226-232.

Tiernan, P., Hannon, A., 2014. Design optimisation of biaxial tensile test specimen using finite element analysis. International Journal of Material Forming 7, 117-123.

Valente, R.A.F., Andrade-Campos, A., Carvalho, J.F., Cruz, P.S., 2010. Parameter Identification and Shape Optimization: An Integrated Methodology in Metal Forming and Structural Applications. Optimization and Engineering 12, 129-152.

Valente, R.A.F., Sousa, R.A.d., Andrade-Campos, A., Caseiro, J.F., 2014. Computational Methods in Metal Forming Simulation - Finite Element Formulations and Optimization Strategies. Springer.

van Riel, M., van den Boogaard, A.H., 2007. Stress-strain responses for continuous orthogonal strain path changes with increasing sharpness. Scripta Materialia 57, 381-384.

Vegter, H., van den Boogaard, A.H., 2006. A plane stress yield function for anisotropic sheet material by interpolation of biaxial stress states. International Journal of Plasticity 22, 557-580.

von Mises, R., 1913. Mechanics of solids in plastic state. Göttinger Nachrichten Mathematical Physics 4, 582–592 (in German).

Vrh, M., Halilovic, M., Stock, B., 2011. Characterization of Mechanical Behaviour of Sheet Metal: Hardening at Large Strains and Anisotropy Identification, 14th International ESAFORM Conference on Material Forming: ESAFORM 2011. AIP Conference Proceedings, pp. 1441-1446.

Wagoner, R.H., 1981. Comparison of Plane-Strain and Tensile Work Hardening in Two Sheet Steel Alloys. Metallurgical Transactions 12, 877-882.

Wattrisse, B., Chrysochoos, A., Muracciole, J.-M., Némoz-Gaillard, M., 2001. Analysis of Strain Localization during Tensile Tests by Digital Image Correlation. Experimental Mechanics 41, 29-39.

Weise, T., 2008. Global Optimization Algorithms – Theory and Application, 6th Edition ed. www.it-weise.de.

Wierzbicki, T., Bao, Y.B., Lee, Y.W., Bai, Y.L., 2005. Calibration and evaluation of seven fracture models. International Journal of Mechanical Science 47, 719–743.

Xue, L., 2008. Constitutive modeling of void shearing effect in ductile fracture of porous materials. Engineering Fracture Mechanics 75, 3343–3366.

Yin, Q., Brosius, A., Tekkaya, A.E., 2011. Modified plane torsion tests for sheet metal characterization, Steel research international, Special edition: 10th international conference on technology of plasticity. ICTP 2011, pp. 696-701.

Yin, Q., Soyarslan, C., Guner, A., Brosius, A., Tekkaya, A.E., 2012. A cyclic twin bridge shear test for the identification of kinematic hardening parameters. International Journal of Mechanical Sciences 59, 31-43.

Yin, Q., Zillmann, B., Suttner, S., Gerstein, G., Biasutti, M., Tekkaya, A.E., Wagner, M.F.-X., Merklein, M., Schaper, M., Halle, T., Brosius, A., 2014. An experimental and numerical investigation of different shear test configurations for sheet metal characterization. International Journal of Solids and Structures 51, 1066-1074.

Yoon, J.W., Barlat, F., Dick, R.E., Karabin, M.E., 2006. Prediction of six or eight ears in a drawn cup based on a new anisotropic yield function. International Journal of Plasticity 22, 174-193.

Yoon, J.W., Barlat, F., Grácio, J., Rauch, E., 2005. Anisotropic Strain Hardening Behavior in Simple Shear for Cube Textured Aluminum Alloy Sheets. International Journal of Plasticity v.21, pp. 2426-2447.

Yoon, J.W., Yang, D.Y., Chung, K., 1999. Elasto-plastic finite element method based on incremental deformation theory and continuum based shell elements for planar anisotropic sheet materials. Comp. Methods in Applied Mechanics and Engineering 174, 23-56.

Yoshida, F., Hamasaki, H., Uemori, T., 2013. A user-friendly 3D yield function to describe anisotropy of steel sheets. International Journal of Plasticity 45, 119–139.

Yoshida, F., Uemori, T., Fujiwara, K., 2002. Elastic-plastic behavior of steel sheets under in-plane cyclic tension -compression at large strain. International Journal of Plasticity 18, 633-659.

Yoshida, K., 2013. Evaluation of Stress and Strain Measurement Accuracy in Hydraulic Bulge Test with the Aid of Finite-element Analysis. ISIJ International 33, 86-95.

Young, R.F., Bird, J.E., Duncan, J.L., 1981. An Automated Hydraulic Bulge Tester. Journal of Applied Metalworking 2, 11-18.

Zang, S.L., Thuillier, S., Port, A.L., Manach, P.Y., 2011. Prediction of anisotropy and hardening for metallic sheets in tension, simple shear and biaxial tension. International Journal of Mechanical Sciences 53, 338–347.

Zhalehfar, F., Hosseinipour, S.J., Nourouzi, S., Gorji, A.H., 2013. A different approach for considering the effect of non-proportional loading path on the forming limit diagram of AA5083. Materials and Design 50, 165–173.

Zhang, S., 2014. Characterization of anisotropic yield criterion with biaxial tension test. PhD thesis at Université de INSA Rennes.

Zhang, S., Léotoing, L., Guines, D., Thuillier, S., Zang, S., 2014. Calibration of anisotropic yield criterion with conventional tests or biaxial test. International Journal of Mechanical Sciences 85, 142-151.

Zidane, I., Guines, D., Léotoing, L., Ragneau, E., 2010. Development of an in-plane biaxial test for forming limit curve (FLC) characterization of metallic sheets. Measurement Science and Technology 21, 1-11.

Zienkiewicz, C., Campbell, J.S., 1973. Shape optimization and sequential linear programming, Optimum Structural Design. Willey.